Rapid and Semi-Automated Estimation of Flow Domains and Solute Transport Parameters in Fractured Media

Development of the Flow And Transport - Multi Domain (FAST-MD) Procedure from Tracer Transport Measurements at the Hidden Lane Landfill Superfund Site (Washington, D.C., USA)

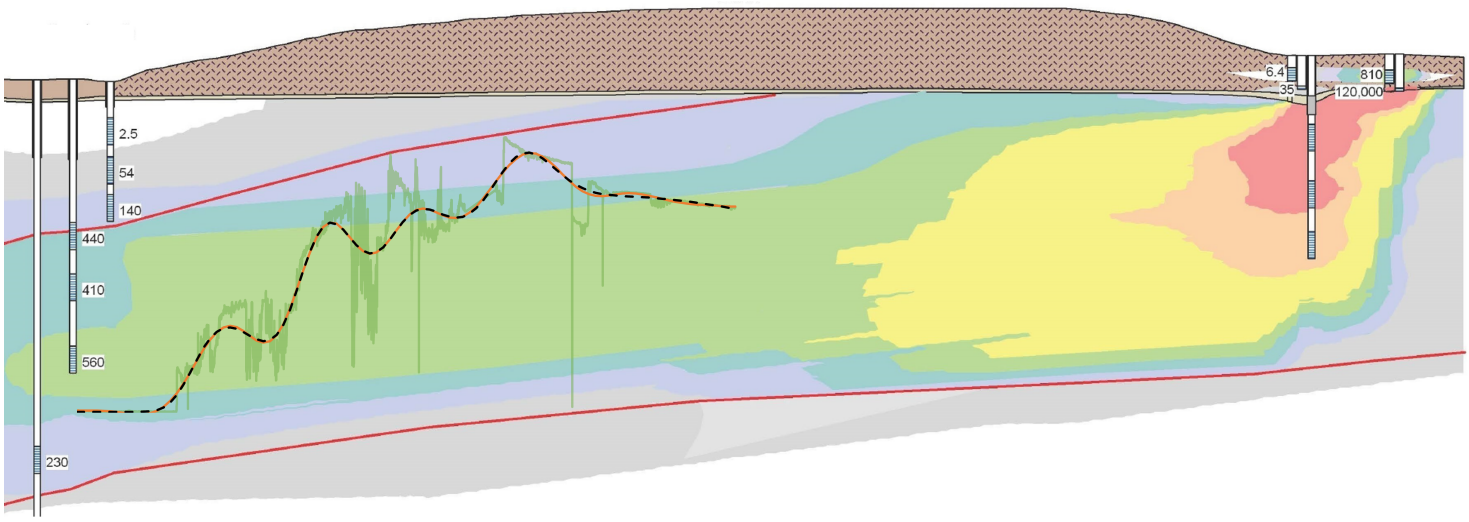

Master's Thesis
Nicolai Wortmann Svendsen
Water and Environmental Engineering
Aalborg University
California State University Long Beach
June 9th 2022

AALBORG
UNIVERSITY

Department of the Built Environment
Water and Environmental Engineering
Thomas Manns Vej 23
9220 Aalborg Ø
https://www.en.build.aau.dk/

Title:

Rapid and Semi-Automated Estimation of Flow Domains and Solute Transport Parameters in Fractured Media

Project:

Master's Thesis

Project period:

September 1st 2021 - June 9th 2022

Participiants:

Nicolai Wortmann Svendsen

Supervisors:

Per Møldrup
Feike J. Leij

Number of pages: 146
Nr. of appendixes: 4
Ended: 09/06/2022

Table of Contents

Preface

This Master's Thesis was done by Nicolai Wortmann Svendsen during the 9^{th}-10^{th} semester as part of the master's education in Water and Environmental Engineering at the Department of the Built Environment, in collaboration with California State University Long Beach as part of an exchange program.
The report is written under the assumption that the reader has knowledge of common principles and relevant subjects within water and environmental engineering.
References to figures, equations, and tables are first referred to with a chapter- or appendix number followed by a number in chronological order. The Harvard method is used for references.
Intermediate results are calculated using all significant figures. However, these are rounded in the report for clarity. The number of significant figures depends on the specific situation.
Figures are developed in QGIS, Microsoft Excel, and Microsoft PowerPoint unless otherwise implied.

I would like to express gratitude towards my supervisors, Per Møldrup and Feike Leij; they have been a great support, not only with the Master's Thesis but also with the exchange program as a whole; I truly appreciate it. Thanks to Malcolm Field for providing the tracer experiment data and helping with any questions I may have had regarding it and the Hidden Lane Landfill Superfund Site. Thanks to Kathy Fox and Christopher Vallone for helping with additional information regarding the Hidden Lane Landfill Superfund Site.

Nicolai Wortmann Svendsen
nsvend17@student.aau.dk

1 Introduction

This thesis aims to develop a procedure for solute transport modeling in porous media with multiple flow domains using complex tracer data. The results from the procedure will then be compared to models of pollution and geology at one of the most polluted sites in the United States of America.

The project location of this thesis is the Hidden Lane Landfill Superfund Site, referred to as the HLLSS. Superfund Sites are defined as some of the most polluted sites in the United States of America [EPA]. The site was an unpermitted landfill during the early '70s and was closed in the mid-'80s. In 1989 trichloroethylene (TCE) was found in drinking wells near the HLLSS [Field, 2020]. Concentration was measured, which was 24000 times higher than the legal maximum contaminant level [Field, 2020]. TCE is harmful to humans and can cause life-threatening illnesses such as kidney cancer [Minnesota Department of Health]. As part of the United States Environmental Protection Agency's remedial strategy, a tracer test was conducted to obtain more knowledge of the movement of fluids at the HLLSS. The main aquifer at the HLLSS is located within a fractured bedrock layer, which makes the movement of fluids more complex due to its multi-domain properties [Field, 2020]. This resulted in some relatively complex tracer data with a significant amount of peaks and fluctuation.

Polluted sites are a major problem in both the United States of America and Denmark, as they can pose serious threats to the health of the surrounding environment and its inhabitants [EPA]. Currently, 133 Superfund Sites are assessed as "not under control" in terms of the Human Exposure Environmental Indicator set by the United States Environmental Protection Agency, meaning a potential for humans to be exposed to unsafe levels of contamination [EPA, d]. According to U.S. Census data, in 2007, more than 25 million people lived within 10 miles of sites assessed as "not under control", according to the Center for Public Integrity, more than a 100 schools were located within 1 mile; back then, 114 sites were assessed as "not under control" [The Center for Public Integrity]. In 2022 the United States Environmental Protection Agency added an additional 12 sites to the Superfund National Priorities List. Furthermore, 3.5 billion USD was invested into the Superfund Remedial Program, and the Superfund chemical excise taxes were reinstated, making it one of the biggest investments into legacy pollution in American history [EPA, a]. In 2020 the Danish government announced that it would invest approximately 90 million USD into a cleanup of the 10 most polluted sites in the country. This was only the estimated cost of the first phase of the cleanup [Miljøstyrelsen].

Some of these sites also have soil types with multi-domain properties, like the HLLSS, and will therefore have similar complex fluid movement; an example is the GMH Electronics EPA Superfund Site [EPA, b] or the Hanford Site [Martin, 2011]. Aquifers within fractured media are especially challenging cause the fracturing is not continuous. A monitoring well may intersect multiple significant fractures for water and solute transport. However, another well a meter away may not intersect any, and these wells can be quite expensive to establish. Furthermore, fracture size can vary from a human hair to sizes which can clearly be spotted in samples [Delvin, 2020] and [Field, 2020].

Tracer tests are therefore often used for these complex soil types, such as fractured bedrock, due to the high variations in soil properties within the soil type. Thereby, an average estimate of the hydrogeology over the scale of the tracer test is described instead [Enviroforensics]. Due to the velocity variations caused by these discontinuous fractures, the tracer data may lead to multiple peaks and fluctuations. Hydrogeologists are then tasked with the complex challenge of evaluating this tracer data and using it to obtain solute transport parameters, which are then used for a remediation strategy for these pollution sites. Therefore, a simple tool for data treatment, assessing the number of domains required to describe the tracer data, and solute transport modeling of it, would be valuable to hydrogeologists when dealing with complex tracer data from fractured media.

1.1 Objectives

Four main objectives were identified for this Master's thesis.

To identify the most promising wells and screens for tracer data analyses by making a geohydrological overview of the Hidden Lane Landfill Superfund Site (HLLSS) and using the available experimental data to identify governing flow direction and estimate levels of tracer recovery.

Develop a robust, rapid, objective, and semi-automated procedure (FAST-MD) for analyzing tracer data focusing on identifying dominating individual flow domains and their key transport parameters.

To use literature values for unimodal soil systems as an initial validation of the concept by comparing with the parameter values obtained by FAST-MD.

Apply the obtained network of parameter values within the main tracer recovery area of the HLLSS to evaluate existing models for geology and TCE concentrations.

The Hidden Lane Landfill Superfund Site 2

The Hidden Lane Superfund Site (HLLSS) is a pollution site located in the United States of America. The HLLSS is part of the United States Environmental Protection Agency's (EPA) fund program that aims to clean up some of the most contaminated sites in the United States of America [EPA].

2.1 Site Description and Landfill History

The HLLSS is located in Virginia in Loudoun County, approximately 70 kilometers northwest of the nation's capital, Washington, D.C. The HLLSS covers 59.56 ha and borders the Potomac River to the north, the residential areas Broad Run Farms and Countryside to the west and east, respectively, and more residential areas to the south. In figure 2.1 the location of the HLLSS is shown.

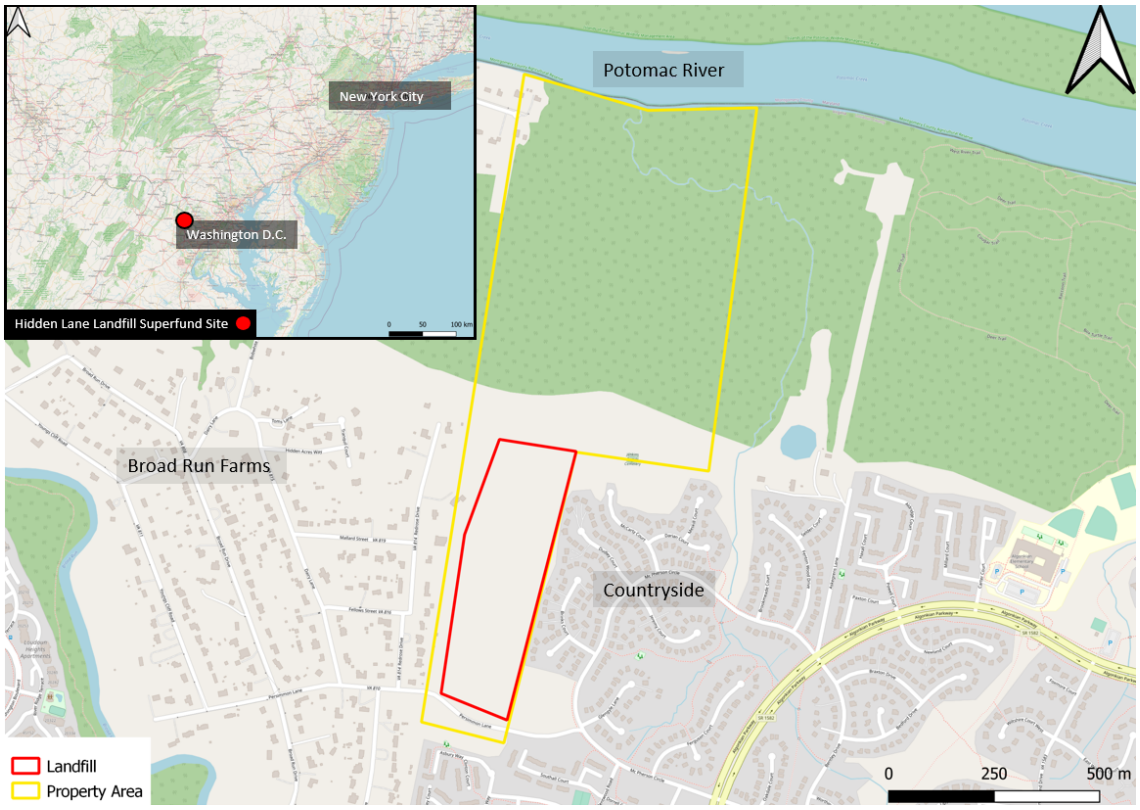

Figure 2.1: Location of the HLLSS.

The site was an unpermitted landfill during the early '70s storing construction debris, cars, scrap metal, and more. In 1973 the Bureau of Solid Waste and Vector Control investigated the landfill, noting that garbage and hazardous material were also being brought [Field, 2020]. A picture of the landfill in 1973 is shown in figure 2.2.

Figure 2.2: Edge of the HLLSS in 1973 [EPA, 2015a].

Multiple fires also occurred at the landfill, an example of which is shown in figure 2.3.

Figure 2.3: Fire at the HLLSS, date unknown [EPA, 2015a].

In 1976 another inspection was done where containers marked "poison and toxic" were found.
In 1984 the landfill was closed by court order.
In 1986 the landfill was covered by a 61 cm thick clay cover intended to make the surface of the landfill impermeable and thereby minimizing the movement of possible contaminants located in the landfill [Field, 2020].
In 1989 trichloroethylene (TCE) was found in drinking water wells of the Broad Run Farms community, located west of the HLLSS, with concentrations way higher than the maximum threshold set by the EPA.
In 2005 local water treatment systems were installed at private wells, particularly exposed to the TCE [Field, 2020]. Prolonged exposure to TCE can cause kidney and liver cancer, affect fetal development during pregnancy, and more [Minnesota Department of Health], which is why the EPA conducted an remedial investigation so a remediation plan for the TCE can be developed.

2.2 EPA Remedial Investigation

TCE is a chemical solvent used for cleaning metal parts, and does not naturally occur in the environment. It has, however, been found in both underground and surface water due to improper disposal [Wexler, 2014]. TCE is a DNAPL, dense non-aqueous phase liquid. Dense refers to it having a higher density than water, meaning it will usually sink until it reaches an impermeable or low permeability surface, and non-aqueous liquid means it will not dissolve in water. TCE can be found in three forms DNAPL, dissolved, and gas. This makes it difficult to determine its fate and transport compared to single-phase chemicals. The DNAPL plume of the TCE is especially problematic, in terms of groundwater pollution. This is because the DNAPL plume is not quickly dissolved in the groundwater; instead, it will slowly be dissolved and spread through dispersion and dilution. This causes the TCE to act as a long-term source of contamination, which is very problematic due to the already described consequences of prolonged exposure [Huling and Weaver, 1991].

In 2018 the EPA conducted measurements of TCE at the different monitoring wells at the HLLSS and, based on these measurements, estimated the TCE's movement and concentration through the aquifer. The results are shown in figure 2.4.

The TCE plume is moving from the southeast corner of the landfill northwest towards the Broad Run Farms and the Potomac River, indicating that the general flow direction is northwest from the landfill, which is also shown by the dashed black arrow on the figure.

The EPA defined a Source Area and Treatability Study Area based on these results. The Source Area is located at the southeast corner of the landfill. High concentrations of TCE were found in both the soil and groundwater in this area. Over the years, samples have been taken at the monitoring well RI-27S, established by the EPA, within the Source area. The concentrations were 120 000 μg/L in 2018, 42 000 μg/L in 2019, and 41 000 μg/L in 2020 [Field, 2020].

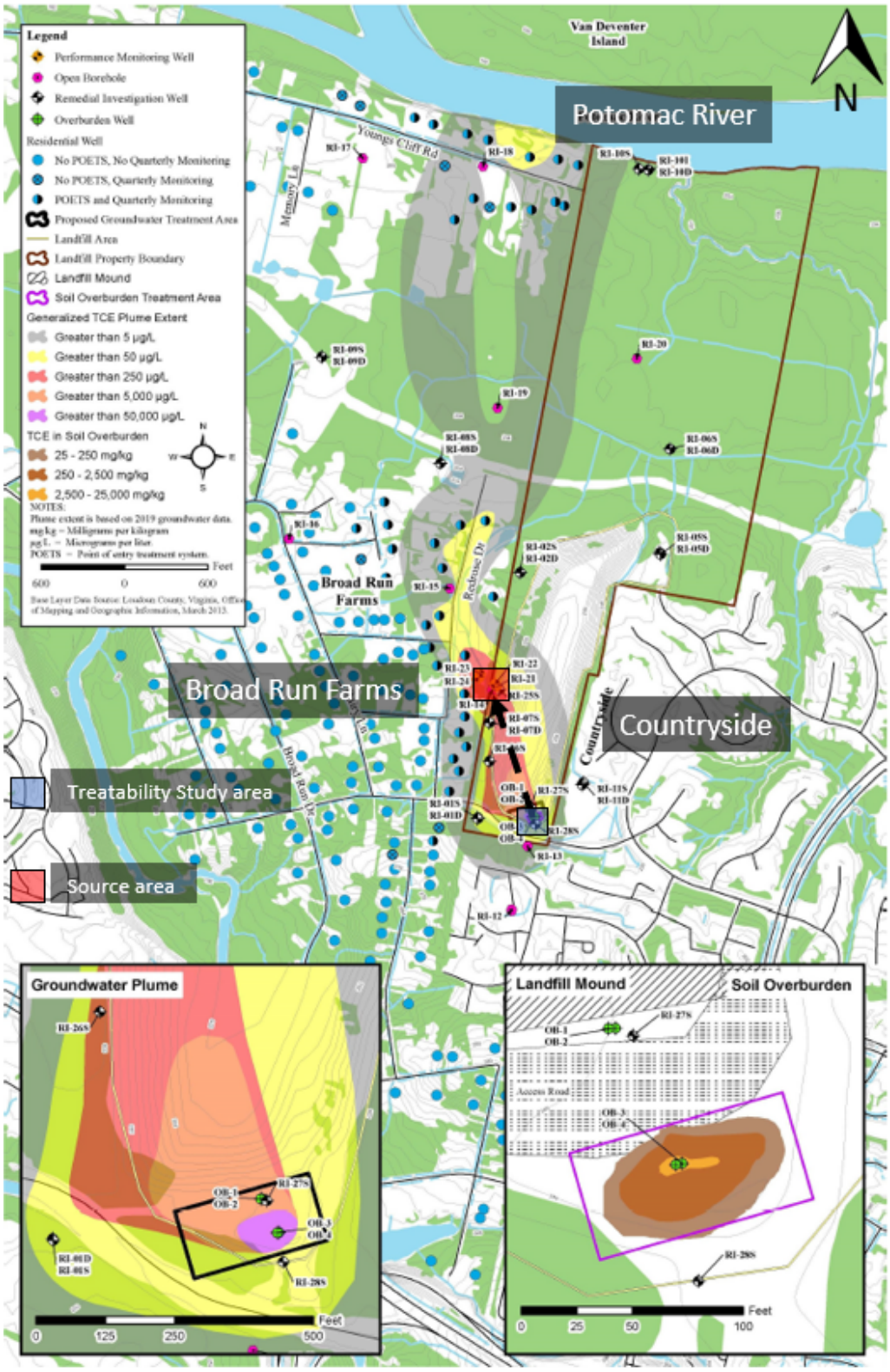

Figure 2.4: Aerial overview of TCE concentrations based on measurements in 2018. The black arrow is an estimated flow path based on the TCE concentration distribution. Modified from [EPA, 2019].

The Treatability Study Area is located in the eastern part of the Broad Run Farms community on the border of the landfill property line. This area was chosen as the

Treatability Study Area based on its proximity to affected drinking water wells and being seemingly located within the main transport path of the TCE based on measurements. The EPA installed five remedial investigation wells within the Treatability Study area named RI-21 through to RI-25 [EPA, 2019].

In 2019 the EPA conducted groundwater samples for contaminating chemicals, TCE being the primary concern. In total, 68 samples were taken, and out of those 64 detected TCE concentrations, of those 40 had concentrations higher than the MCL [EPA, 2019]. The MCL is defined as the maximum contaminant level, a standard set by the EPA for drinking water quality. It is the legal threshold for the concentration allowed in public water systems, as defined by the Safe Drinking Water Act. The MCL for TCE is 5 μg/L[Field, 2020]. The maximum concentration found through sampling was 75 000 μg/L.

A cross-sectional profile from the Treatability Study area to the Source area, based on groundwater measurements in 2018, is shown in figure 2.5.

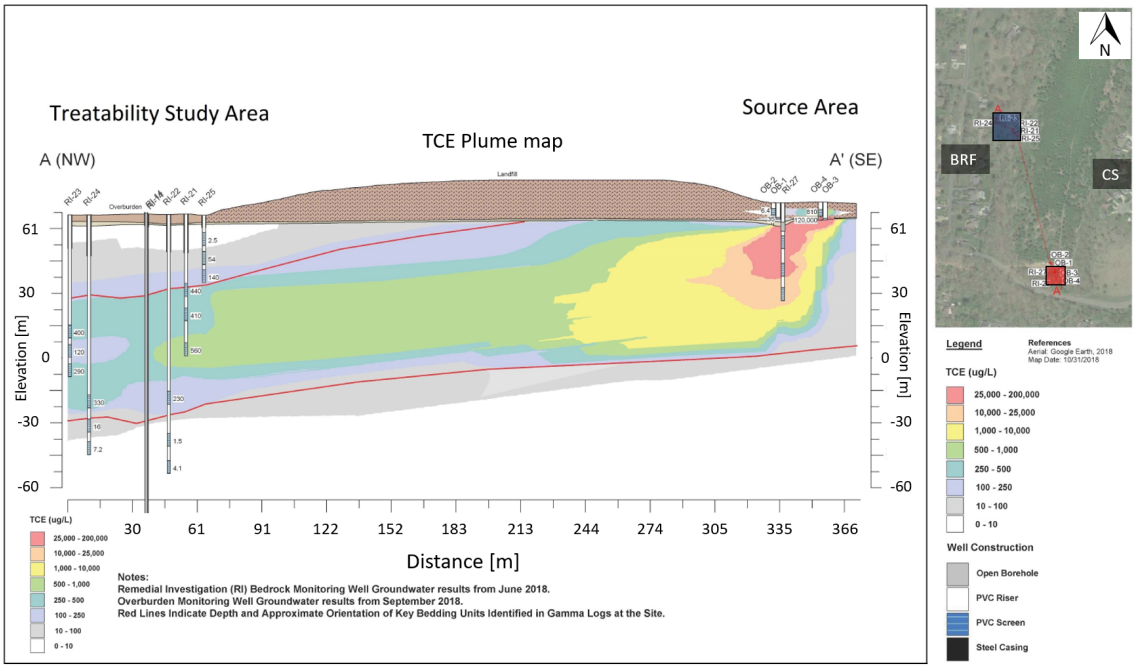

Figure 2.5: Cross-sectional profile of the TCE concentration from the Source area to the Treatability Study Area based on measurements in 2019. The blue square indicates the Treatability Study Area, and the red square indicates the Source Area. The abbreviations BRF and CS are Broad Run Farms and Countryside, respectively. Modified from [EPA, 2019].

From the cross-sectional profile in figure 2.5, it is shown that the TCE spreads mainly horizontally towards the Treatability Study area from underneath the landfill, following the orientation of the key bedding units identified by the red line. The key bedding units are located within a fractured bedrock layer, which will be further described in section 2.3. The TCE plume is mainly being transported through the wells with shallower screenings at the Treatability Study area, which are RI-21 and RI-23.

This project will mainly focus on the area from the Source Area to the Treatability Study Area since understanding the transport path in this area will be essential for stopping the pollution of the affected residential area, Broad Run Farms. The transport of TCE is

dependent on the hydrogeological conditions of the HLLSS; these will be further explored in the following sections.

2.3 Geology at the HLLSS

The site's geology mainly consists of an overburden layer and bedrock. A geological cross-sectional profile was created in both the estimated flow direction (Source area to the Treatability Study area) in figure 2.6, as well as perpendicular to it in 2.7. These figures were created from geological boring logs [EPA, 2015b] near the Source area and the Treatability Study area and topographical data using the software QGIS [QGIS].

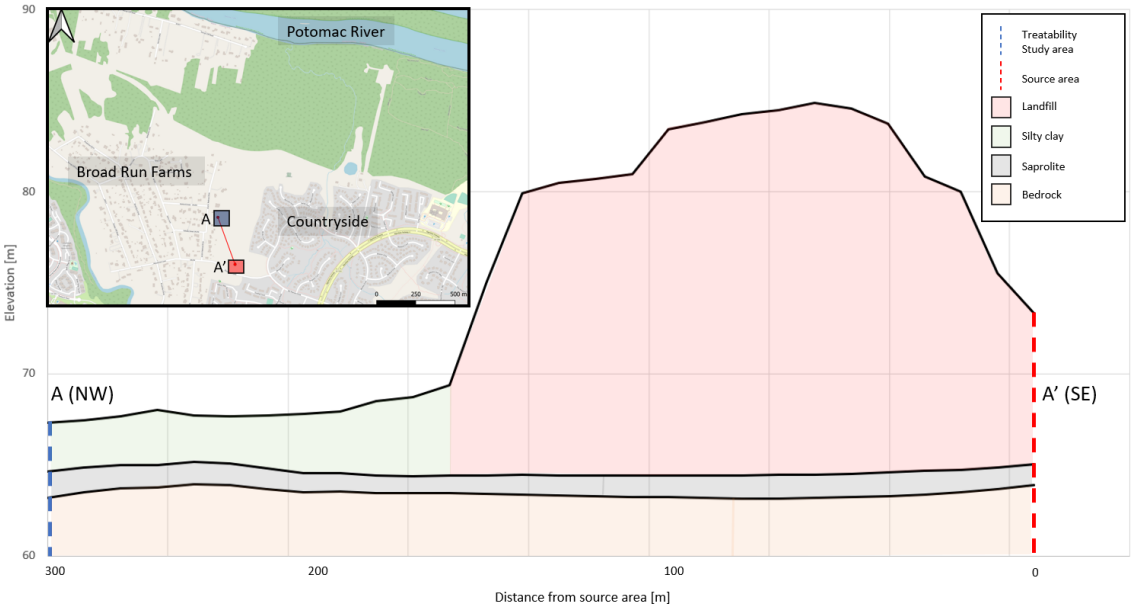

Figure 2.6: Geological cross-sectional profile in the estimated flow direction (Source Area to the Treatability Study Area). The blue square indicates the Treatability Study Area and the red square indicates the Source Area. Data from [EPA, 2015b] and [QGIS].

The top layer of the HLLSS either consists of the landfill or a silty clay layer. The silty clay layer is approximately 5 meters thick. The geology of the landfill will be further described below. Underneath the top layers, a small saprolite layer of 1-2 meters in thickness occurs. Finally, underneath the saprolite layer, the previously mentioned bedrock layer occurs. The layers are relatively constant in elevation and thickness except for the landfill.

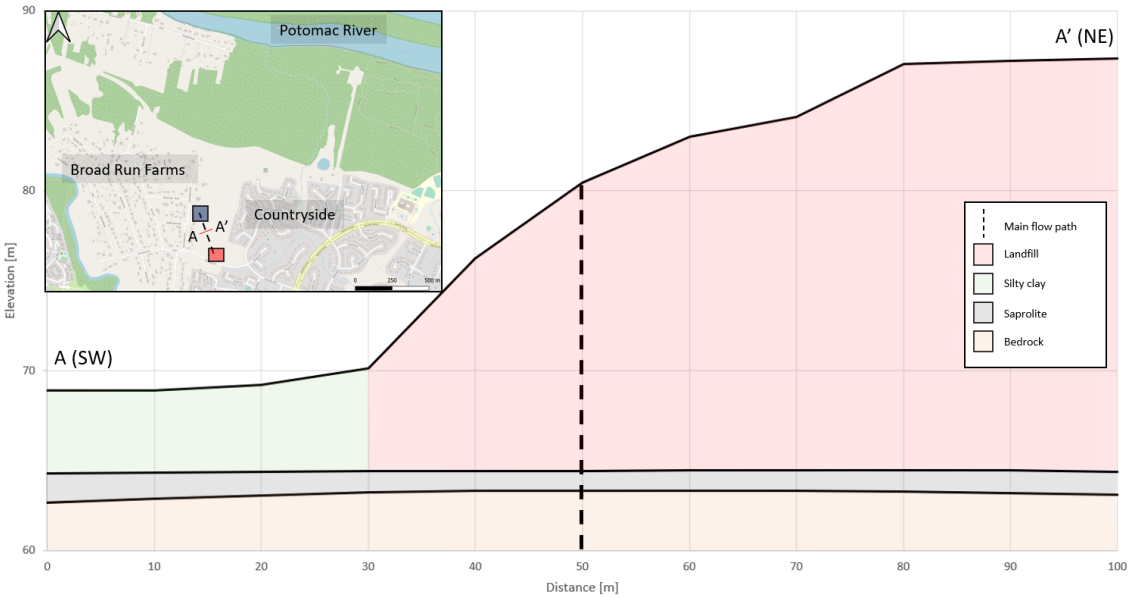

Figure 2.7: Geological cross-sectional profile perpendicular to the estimated flow direction (main flow path) halfway between the Source Area and the Treability Study Area. The blue square indicates the Treatability Study area and the red square indicates the Source Area. Data from [EPA, 2015b] and [QGIS].

The geology at the landfill is a bit more complex consisting of many discontinuous layers. A cross-sectional area of the source area is shown in figure 2.8.

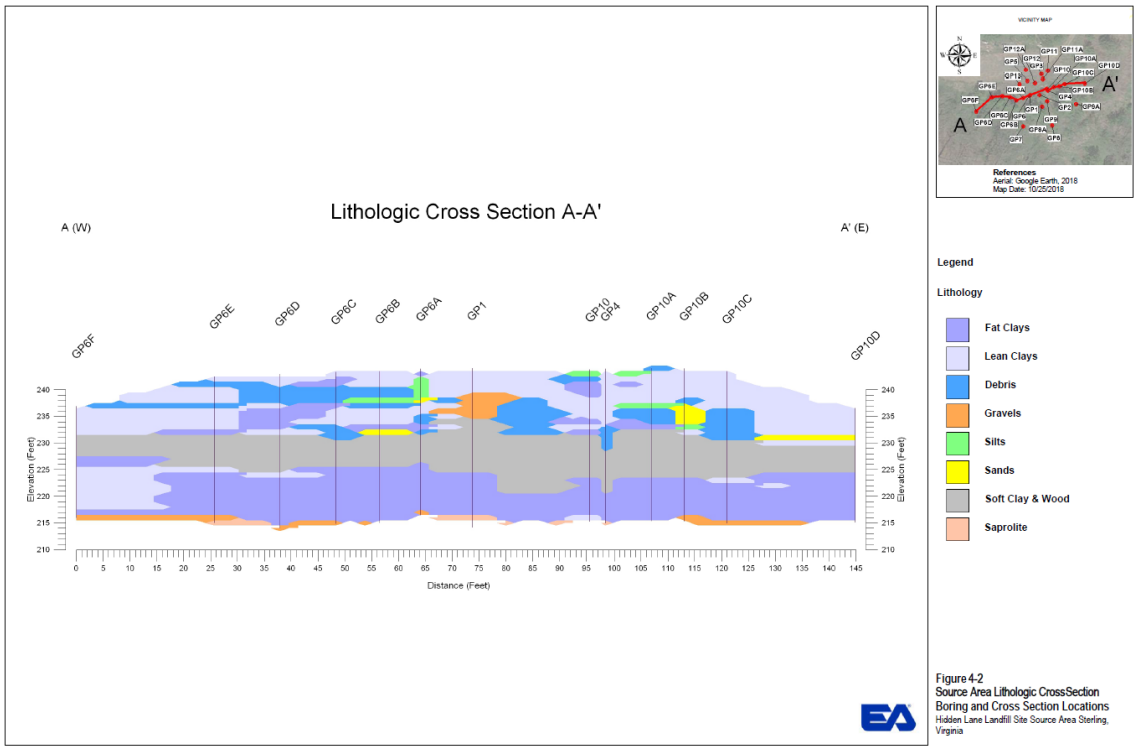

Figure 2.8: Geological cross-sectional profile of the Source area [EPA, 2019].

The geology in the landfill varies a lot with many different soil types and a significant amount of leftover debris. However, it mainly consists of different clay types. These types

of soils generally have a low permeability [EPA, 2015a].

In figure 2.9 a topographical map of the HLLSS is shown as well as the bedrock elevation near the Source area and Treatability Study area; the layers are based on the same data as the geological cross-sectional profiles [EPA, 2015b] and [QGIS].

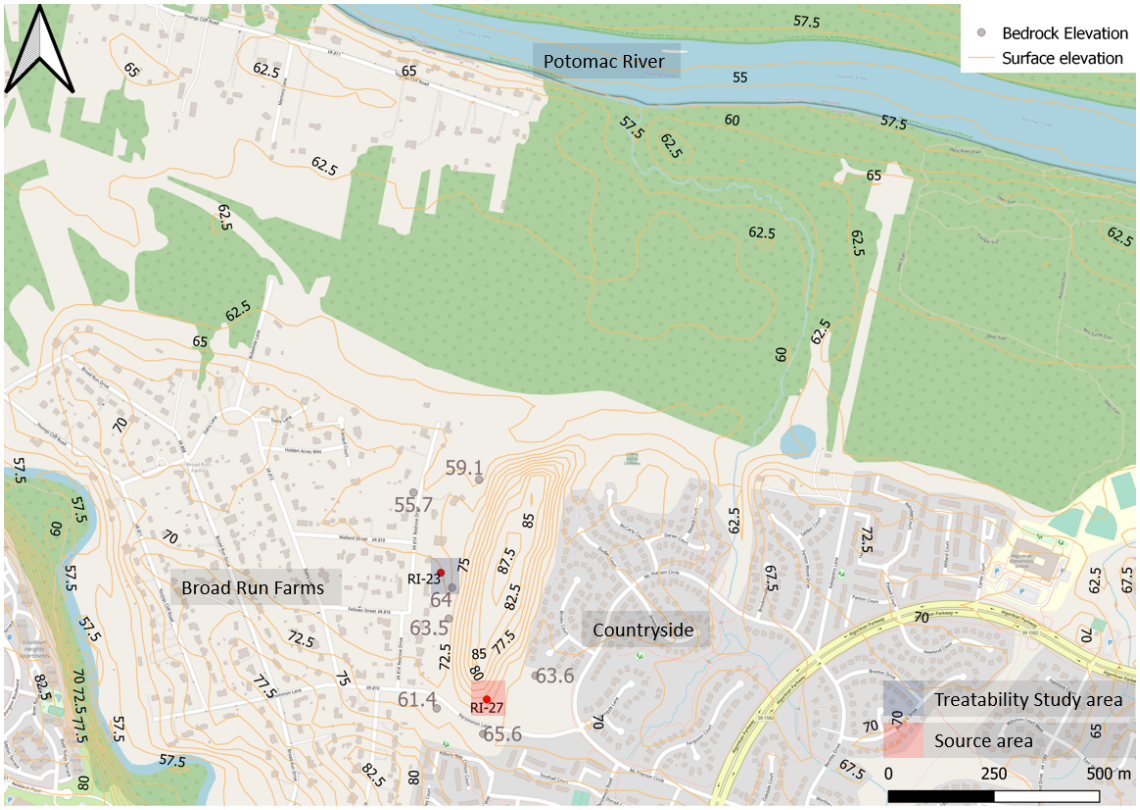

Figure 2.9: Topography and bedrock elevation for the HLLSS. Data from [EPA, 2015b] and [QGIS].

The landfill is identified with a high increase in elevation from the topographical map. The elevation, in general, is higher in the south and decreases to the north towards the Potomac River. The bedrock is located approximately 5-10 meters below the surface and seemingly decreases in elevation towards the Potomac River. The bedrock layer mainly consists of a fluvial and lacustrine layer separated by a fault. This fault has created fractures in the bedrock, which is significant for water and chemical transport. The fractures are significant because they are very permeable, creating pathways for fast water and chemical movement than their non-fractured counterparts. While the fault does not directly intersect the HLLSS, it is close to it, causing fractures in the underlying bedrock of the HLLSS. [Field, 2020] In figure 2.10 samples of the bedrock at HLLSS are shown, which clearly illustrates the fractures in the bedrock.

Figure 2.10: Bedrock samples from the HLLSS illustrating the fractures [Field, 2020].

These fractures are paramount for chemical and water transport and, thereby, TCE movement at the HLLSS. The EPA conducted gamma logging measurements at the site to determine the location and orientation of major fractures. In figure 2.11 a cross-sectional profile of stratification's based on these measurements is shown and in figure 2.11 the transect line used to develop this cross sectional profile is shown.

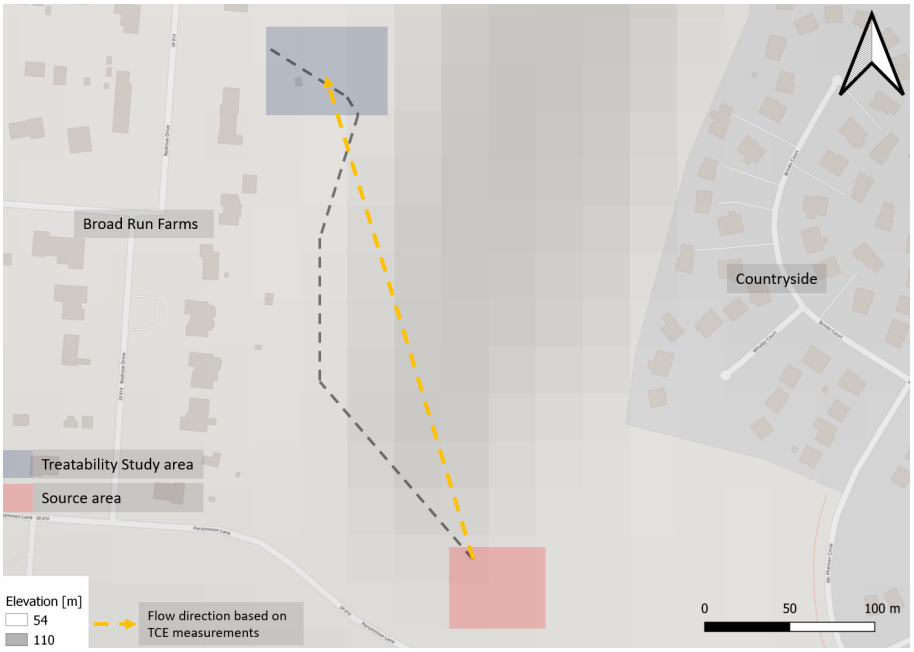

Figure 2.11: Aerial overview of the HLLSS. The dashed gray line is the transect line used to develop figure 2.12. The location of the landfill is clearly indicated by the change in elevation.

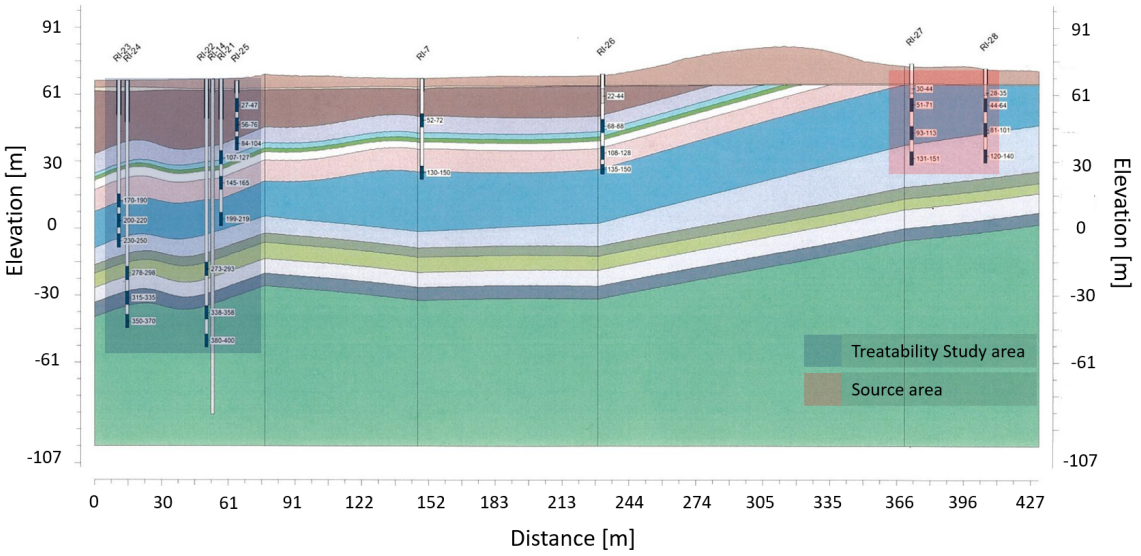

Figure 2.12: Cross-sectional profile of the different stratifications in the bedrock from the Source Area to the Treatability Study Area. The cross-sectional profile is based on the dashed gray transect line shown in figure 2.11. Modified from [Field, 2020].

The figure shows that the fracture orientation from the Source Area is mainly horizontal. The horizontal movement fits fairly well with the concentration measurements of TCE shown in the cross-sectional profile in figure 2.5. The dark blue stratification is connected to the Source area and Treatability Study area. Furthermore, comparing the cross-sectional profile of the TCE measurements, the high concentrations of TCE in the Treatability Study area are within the area of the dark blue layer, indicating that this may be a significant layer for transport of TCE.

2.4 Hydrogeology at the HLLSS

The aquifers at HLLSS can generally be divided into two parts, upper and lower. The upper aquifer is located within the overburden, and the lower aquifer is in the bedrock [EPA, 2015a].

The upper aquifer is present seasonally in periods with high precipitation and only in areas with low permeability, such as the landfill. The water movement in the upper aquifer tends to follow the topographic gradient generally northbound towards the Potomac River.

The lower aquifer is located within the fractured bedrock. The movement of the water in the lower aquifer is dominated by second porosity such as fractures and bedding planes. This aquifer is essential as the TCE is transported through the bedrock layer, as shown in figure 2.5.

Measurements from 2011 and 2012 of the potentiometric surface in the lower aquifer are shown in figure 2.13 and 2.14.

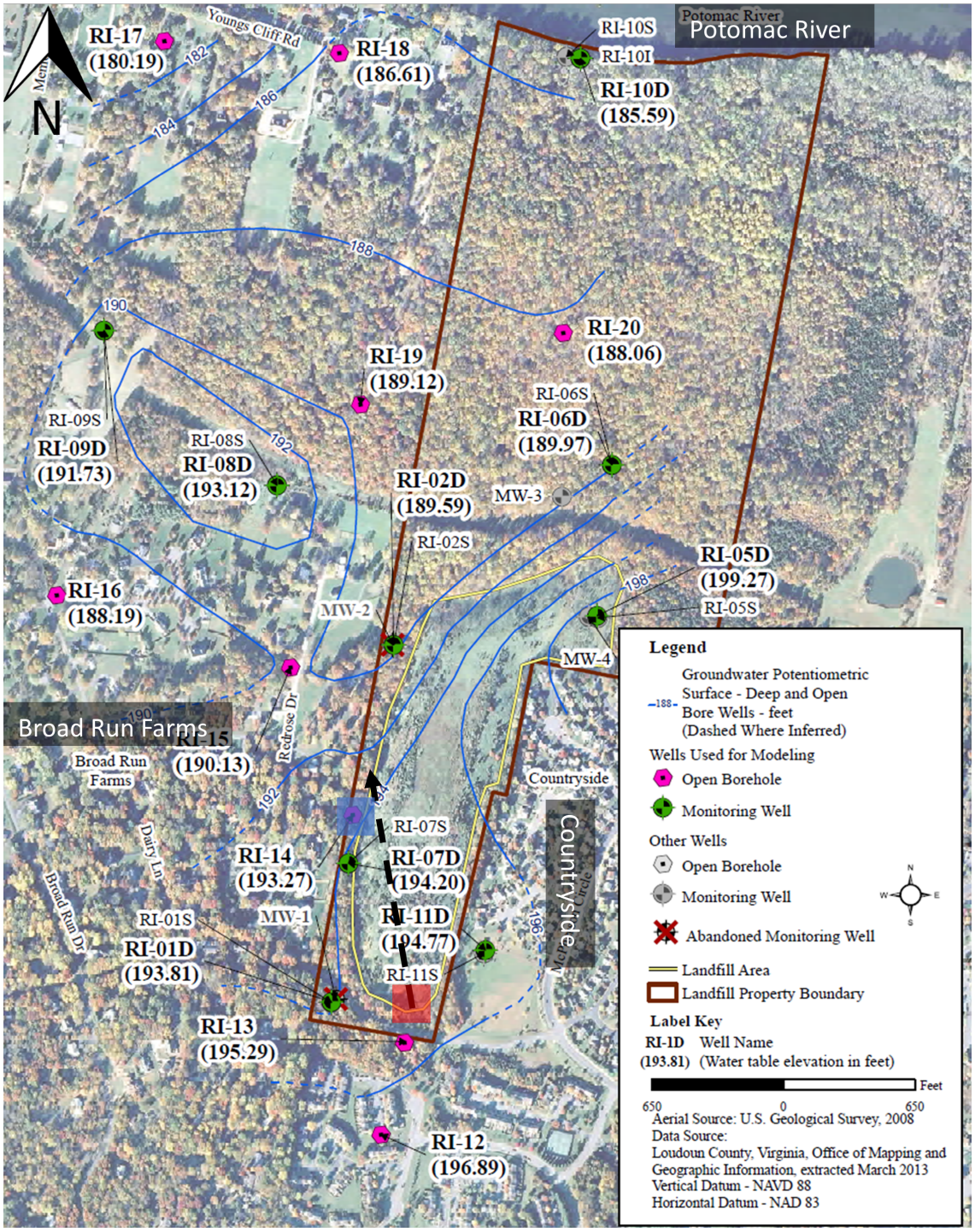

Figure 2.13: Potentiometric surface measurements for the HLLSS, June 2011. The red square indicates the Source area, and the blue square indicates the Treatability Study area. The dashed black arrow indicates an assessed overall flow direction of the groundwater of the entire mapped area based on both potentiometric maps. Modified from [EPA, 2015a].

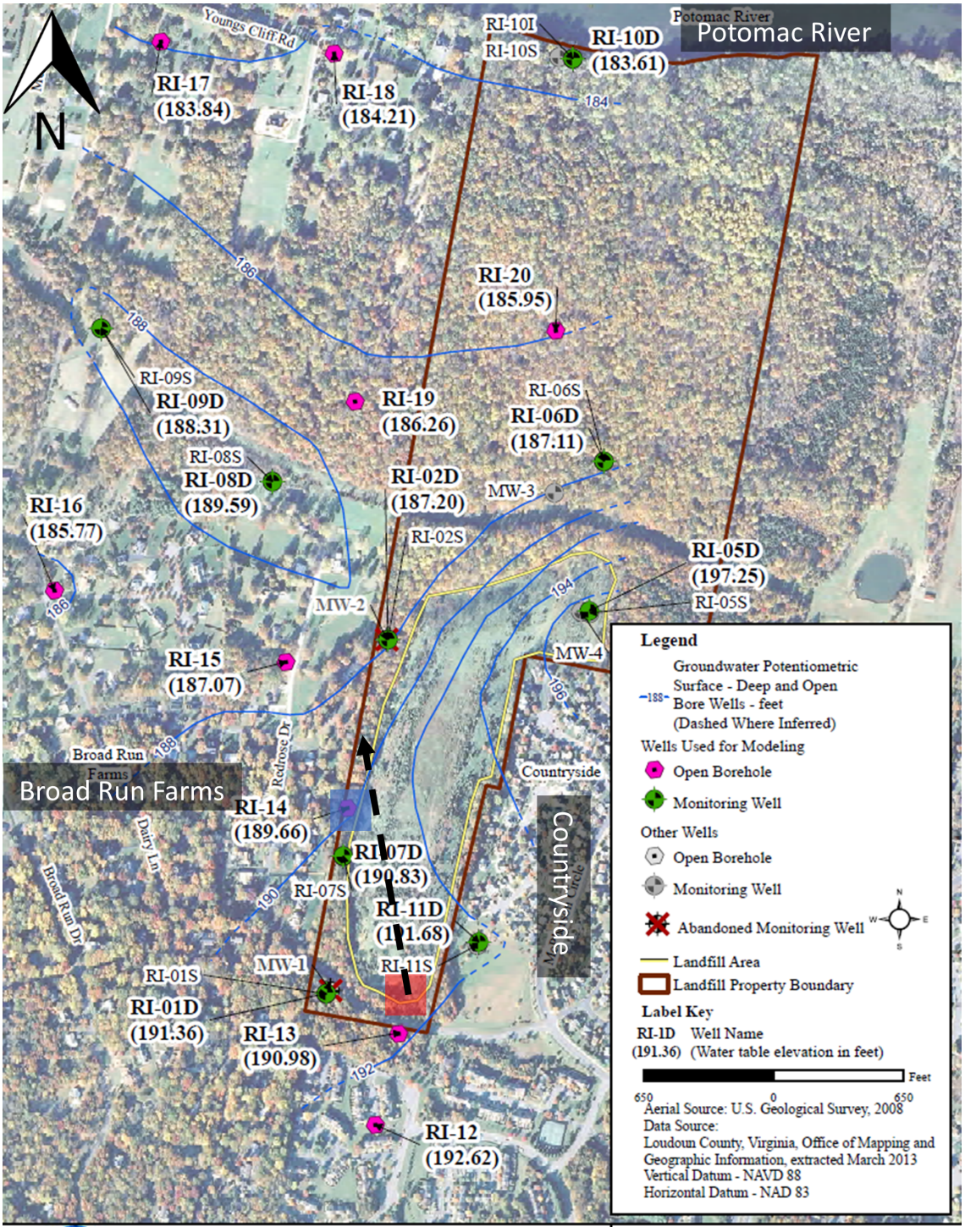

Figure 2.14: Potentiometric surface measurements for the HLLSS, June 2012. The red square indicates the Source area, and the blue square indicates the Treatability Study area. The dashed black arrow indicates an assessed overall flow direction of the groundwater of the entire mapped area based on both potentiometric maps. Modified from [EPA, 2015a].

Through the measurements of the potentiometric surface, a flow direction for the HLLSS and the surrounding area was assessed. The arrow on the figures indicates it. The flow direction was based on the assumption that the flow direction is perpendicular to the potentiometric surface measurements. The direction of the groundwater movement is

assessed as northwest, which is towards the Broad Run Farms and the Potomac River from the Source area. This flow direction is similar to the direction based on the TCE concentrations previously described in the chapter, however slightly more northward. An average hydraulic gradient, dh/dx, for the HLLSS and the surrounding area is assessed based on the two measurement points furthest away from each other (RI-12 and RI-10) and their distance. The results are shown in table 2.1

Table 2.1: Estimated distance between measurement points, dx, change in potentiometric surface, dh, and hydraulic gradient.

dh [m change in head]	dx [m porous media]	dh/dx [$\frac{\text{m change in head}}{\text{m porous media}}$]
3.1	1637	0.002

Summary

A general overview of the HLLSS and its contamination problems was introduced throughout this chapter. The TCE movement was found to be through mainly horizontally oriented fractured bedrock. Based on the information collected above, some considerations regarding the transport processes that affect the dissolved TCE phase are made. These are sorption, biodegradation, and vapor migration.
Vapor migration was assessed as unlikely by the EPA since the TCE is being transported in a fractured bedrock layer, where the fractures have very low porosities causing little chemical exchange [EPA, 2015a].
Biodegradation within the interested transport path from the Source area to the Treatability Study area is assessed to be negligible due to the high concentrations, causing toxic conditions for the microorganisms that would cause biodegradation.
TCE is a non-polar volatile organic compound [NIST]. Because of this, the degree of adsorption of TCE is dependent on the amount of organic matter in the soil since organic matter is generally less polar than water [Loll and Moldrup, 2000]. Through a correspondence with EPA, it was found that groundwater measurements showed concentrations around the detection limit for most measurements of total organic carbon. Therefore, it is assessed that the sorption of TCE would be low. Based on these considerations, it is expected that the dissolved TCE plume is largely controlled by groundwater movement, further emphasizing that the hydrogeological conditions at the HLLSS are essential for understanding the movement of the TCE.

An average hydraulic gradient for the HLLSS was defined based on potentiometric surface measurements and is 0.002. A Source area and a Treatability Study area were defined. Flow directions were estimated based on both TCE, and potentiometric surface measurements were also established. Figure 2.15 shows the defined areas and flow directions.

Figure 2.15: Source area and Treatability Study area, and estimated flow directions based on TCE and potentiometric surface measurements. The location of the landfill is clearly indicated by the change in elevation.

Both flow directions are northwest-trending towards the Treatability Study area, the TCE flow direction being slightly more westward. The bedrock at the HLLSS showed clear fracture tendencies in soil samples. These fractures will cause multiple transport paths for water and chemical transport. This information is not enough to obtain a detailed overview of the complex fractured bedrock system underneath the HLLSS. Therefore, the EPA conducted a tracer experiment, which will be further described in the following chapter.

Tracer Experiment 3

In 2019 the EPA initiated a tracer test to gain more knowledge of the groundwater movement through the fractured bedrock from the Source area of the TCE contamination to the Treatability Study Area.

3.1 Experimental Setup

A tracer test aims to have a fluid containing a tracer in a solution, then have it displaced through a porous medium by the same fluid but without the tracer. This leads to a concentration distribution versus time of the tracer at a given measurement point [Nielsen and Biggar, 1961]. This distribution is also called a breakthrough curve. A breakthrough curve is a plot of the duration of a given test as a function of an effluent concentration of the chemical being tested [Gao, 2022] and is frequently used for solute transport in porous mediums [Biggar and Nielsen, 1962].

The tracer test was a natural gradient test. The test usually provides the most representative solute-transport parameters as the movement in the aquifer remains unaffected, however, it requires an extensive monitoring network and a long sampling time. The alternative would be a forced gradient test with a pump, but those are not allowed at Superfund Sites [Field, 2020].

As described in chapter 2 TCE is quite a complex chemical, and therefore a tracer will not be able to mimic its movement entirely due to its distinct multi-phase properties. However, the movement of the dissolved TCE was assessed in chapter 2 as being mainly controlled by groundwater movement. The goal of the tracer is therefore to describe the groundwater movement from the Source area to the Treatability Study area so that it can be used to describe hydrogeological conditions within this area, which is then beneficial information for evaluating the fate and transport of the dissolved TCE.

Therefore an evaluation of which injection well to use must be considered. The injection well and screening for the tracer test was RI-27S. It is located within the approximated Source area, and showed very high concentrations of TCE as mentioned in chapter 2. It has a screening in the bedrock just below the landfill, which, as described in chapter 2 is the main transport layer for the TCE contamination [Field, 2020].

The tracer chosen for the test was sodium fluorescein, also known as uranine. This tracer dye was chosen as it is significantly more fluorescent than typical tracer dyes. The more fluorescent the tracer is, the lower the detection limit becomes, meaning more reliable measurements at lower concentrations. Furthermore, the tracer also has a small sorption compared to most tracers [Field, 2020]. Vapor migration is deemed unlikely for the same reasons as described for TCE in chapter 2. The tracer was also found to not be readily biodegradable, meaning biodegradation of the tracer is unlikely to occur [ECHA]. Both the low sorption and biodegradation is beneficial since the goal is to mimic groundwater movement. The tracer is also almost nontoxic and easy to use since its available in liquid form [Field, 2020]. The tracer is highly water-soluble and has a bright yellow hue, and has been used in several tracer studies such as [Kresic and Stevanovic, 2009], [Pan et al., 1991], and [Cascarano, 2018].

A research projected on uranine as a tracer in the vadose zone was conducted, where it was concluded that the tracer is promising based on the following characteristics [Gerke et al., 2013]:

- Good water solubility
- Visibility under UV light that is easily discernible in any soil and has no background concentrations
- Low toxicity
- Inexpensive compared to other fluorescent dyes (factor of 10)
- Sorption characteristics for forest soils comparable to brilliant blue (BB FCF) (one of the most common tracers [Jarai Mon and B.Harsh, 2006])

A successful tracer test requires an adequate mass to ensure detection at the furthest downgradient monitoring well while still minimizing the chances of visible water colorization. The sampling of the tracer test was done in situ with Cyclops-7 sensors collecting data every 30 minutes. The concentration detection limit was $0.01\,\mu g/L$. [Field, 2020] The software EHTD [Field, 2003] was used to estimate the tracer mass using estimated input parameters such as porosity, discharge, retardation, distance, concentration, and decay rate. The tracer mass was estimated to 5.37 kg [Field, 2020].

For each monitoring well and screening, a background concentration of the tracer dye was estimated based on the measurements' mean concentration before the tracer test, while considering potential faulty measurements and outliers, which is then subtracted from the eventual tracer data.

For the tracer injection, water was injected prior to the actual tracer to minimize the change in flow behavior when the tracer was injected. First, water was injected at a slow rate of 0.0360 $\frac{L}{min}$ for 6 minutes. Afterward, continuous water injection at a rate of 2.69 $\frac{L}{min}$ for two hours was conducted. After this, the diluted tracer dye was released as quickly as possible to mimic an instantaneous injection [Field, 2020]. Post-water flush was done to ensure that the water flow through the aquifer was unchanged, so the tracer was transported as naturally as possible into the aquifer. Post-water flush was conducted until the tracer was no longer visible in the well and lasted approximately three days [Field, 2020]. In figure 3.1 the injection of tracer is shown.

Figure 3.1: Injection of the diluted tracer [Field, 2020].

Using the sampled data from the Cyclops-7 sensors, breakthrough curves were developed for each monitoring well and screening. Data was collected over a 233 days sampling period leading to approximately 11000 data points for each screening.

3.2 Tracer Data Overview

No tracer data was collected at the actual injection screening (RI-27S (I)), but data were collected in the other screenings within the same casing. The wells named RI were installed as part of the remedial investigation and use slotted screens [EPA, 2015a]. The well called OB-3 is an open hole with no screening. The last letter after its assigned number in the RI screen names (e.g., RI-27S) is based on the location of the screening in terms of depth; there are four different screening depths:

- O: Open hole
- S: Shallow
- I: Intermediate
- D: Deep

The screenings with intermediate or strong tracer recovery have been given more relatable names in parenthesis. These abbreviations are based on the distance and depth from the injection screening and are as follows:

- I: Screening where the injection of tracer occurred
- E: Early
- M: Middle
- L: Late
- F: Final
- Numeration relates to the depth of the screening and is from shallow to deep

An aerial and cross-sectional profile of the location of the monitoring wells and screenings is shown in figures 3.2 and 3.3

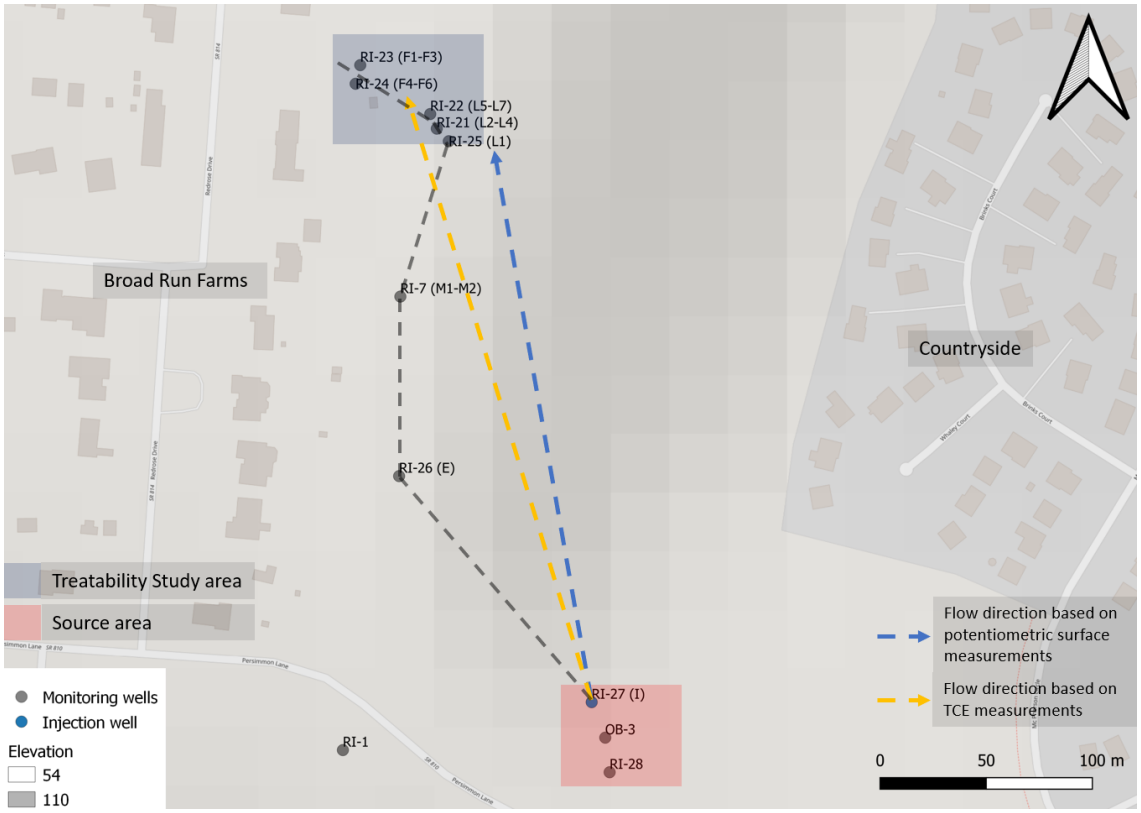

Figure 3.2: Aerial overview of the tracer test. The dashed gray line is a transect line used to develop figure 3.19. The location of the landfill is clearly indicated by the change in elevation.

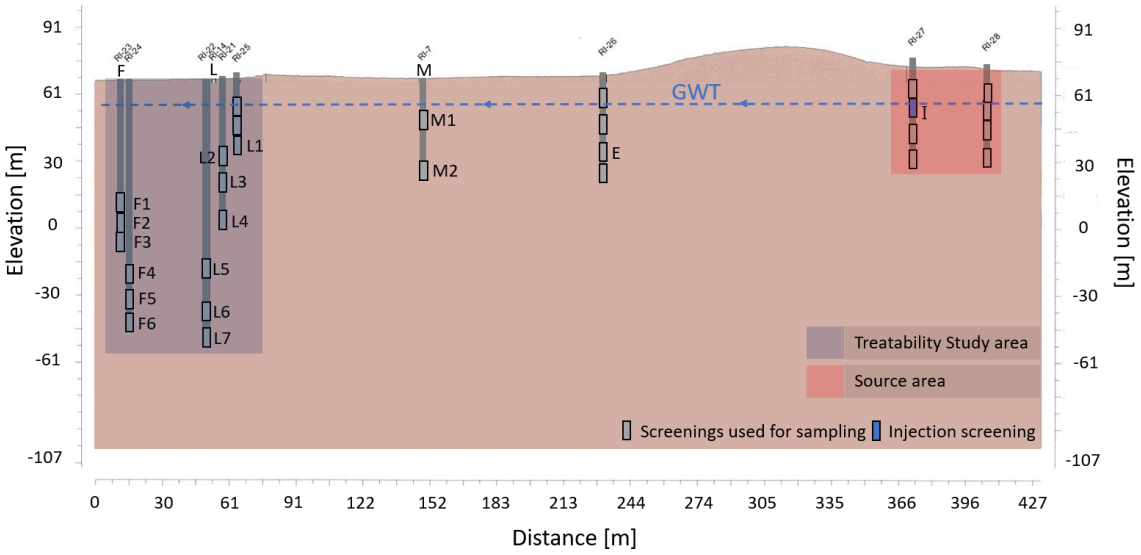

Figure 3.3: Cross-sectional overview of the tracer test. The cross-sectional profile is based on the dashed gray transect line shown in figure 3.18. For the screenings not assigned more relatable names the following order always applies from most shallow screening to deepest: O (Open hole), S (Shallow), I (Intermediate), D (Deep).

In table 3.1 the depth and distance from the injection screening to each screening is shown. The relative location to the injection screening, is based on the estimated flow directions defined in chapter 2.

Table 3.1: Depth and distance from the screenings to the injection screening. The parameters in order from left to right is: The distance from injection to monitoring well, the change in depth from injection to screening (using the center of the screening), and location relative to the injection screening. The depth of the injection screening is 16-22 meters.

Location		L	$\Delta depth$	Relative location
RI name	Given name	[m]	[m]	[-]
RI-28O	-	34	-9.4	Upgradient
RI-28S	-	34	-3	Upgradient
RI-28I	-	34	8	Upgradient
RI-28D	-	34	20	Upgradient
OB-3	-	23	-11	Upgradient
RI-27O	-	0	-7	Same casing
RI-27I	-	0	13	Same casing
RI-27D	-	0	24	Same casing
RI-01S	-	132	1.3	Downgradient
RI-01D	-	132	11	Downgradient
RI-26O	-	142	-	Downgradient
RI-26S	-	142	5	Downgradient
RI-26I	E	142	17	Downgradient
RI-26D	-	142	25	Downgradient
RI-7S	M1	211	0.42	Downgradient
RI-7D	M2	211	24	Downgradient
RI-25D	L1	271	10	Downgradient
RI-21S	L2	277	17	Downgradient
RI-21I	L3	277	29	Downgradient
RI-21D	L4	277	45	Downgradient
RI-22S	L5	283	68	Downgradient
RI-22I	L6	283	87	Downgradient
RI-22D	L7	283	100	Downgradient
RI-23S	F1	317	36	Downgradient
RI-23I	F2	317	45	Downgradient
RI-23D	F3	317	55	Downgradient
RI-24S	F4	308	69	Downgradient
RI-24I	F5	308	80	Downgradient
RI-24D	F6	308	91	Downgradient

3.2.1 Tracer Recovery Types

The tracer test results were categorized into three tracer recovery types:

- Strong tracer recovery
- Intermediate tracer recovery
- Weak tracer recovery

The categorization of the tracer recovery was based on two main factors.

1. If the tracer did not have a continuous tracer concentration after the first breakthrough, the tracer recovery is considered weak.
2. The magnitude of the tracer concentration is also considered.
   Three different scenarios are used to describe the different recovery types:
   a) If the tracer concentration is 100 times above the detection limit, which is equal to a concentration of 1 μg/L, for the majority of the tracer test, the tracer recovery is considered strong.
   b) If the tracer recovery is 10 times above the detection limit, which is equal to a concentration of 0.1 μg/L, for the majority of the tracer test, the tracer recovery is considered intermediate.
   c) If the tracer recovery is lower than 10 times the detection limit for the majority of the tracer test, the tracer recovery is considered weak.

An example of a strong tracer recovery is shown in figure 3.4.

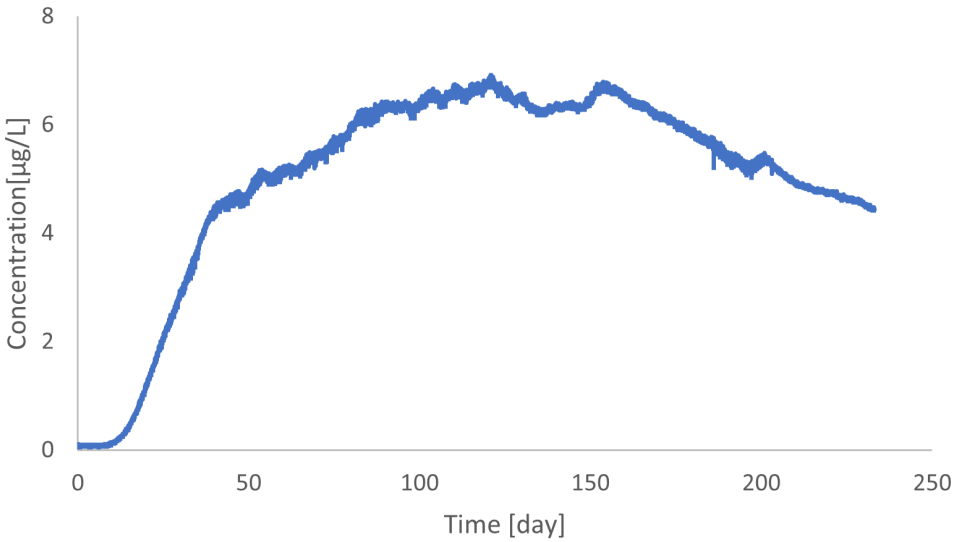

Figure 3.4: Tracer data results for well RI-21S (L2), as an example of a strong tracer recovery. An aerial and cross-sectional overview of the screening locations and tracer recovery is shown in figures 3.18 and 3.19.

The concentrations recovered are way above the detection limit of 0.01 μg/L; hence it being assessed as a strong tracer recovery.

An example of an intermediate tracer recovery is shown in figure 3.5.

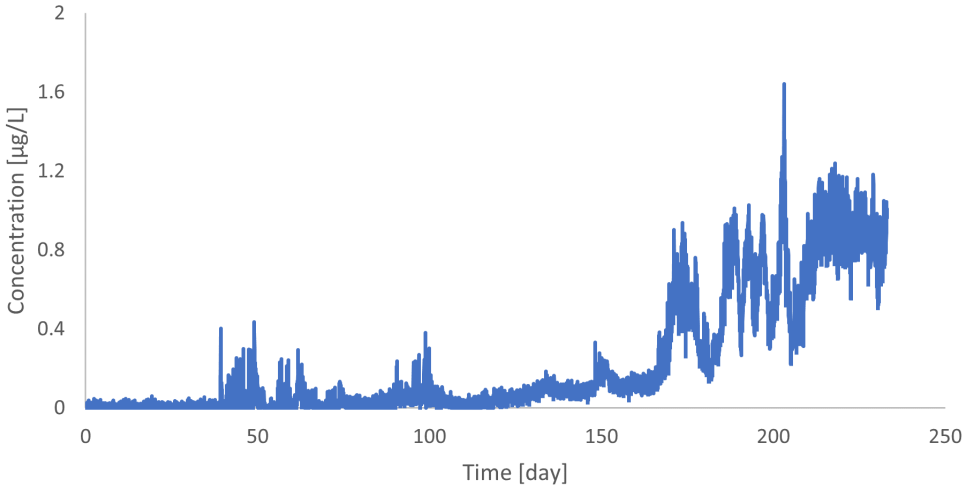

Figure 3.5: Tracer data results for well RI-7D (M2), as an example of a intermediate tracer recovery. An aerial and cross-sectional overview of the screening locations and tracer recovery is shown in figures 3.18 and 3.19.

The concentrations recovered are somewhat low, presumably causing some of the significant fluctuation seen, due to measurement uncertainty. However, after approximately 150 days, the data reaches a somewhat high concentration that exceeds the detection limit by more than a factor 10 for a substantial amount of time. Therefore the tracer recovery is assessed as intermediate.

An example of a weak tracer recovery is shown in figure 3.6.

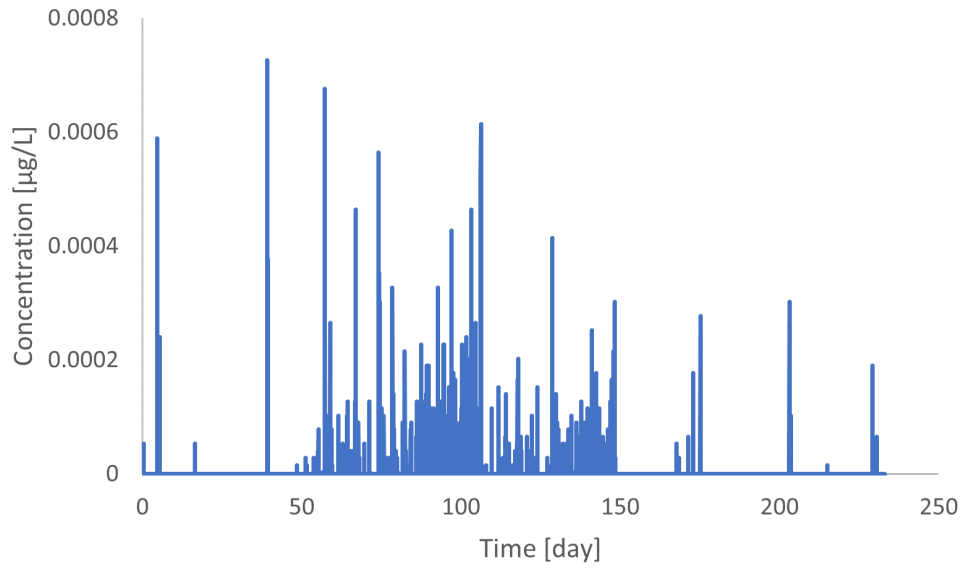

Figure 3.6: Tracer data results for well RI-26S, as an example of a weak tracer recovery. An aerial and cross-sectional overview of the screening locations and tracer recovery is shown in figures 3.18 and 3.19.

The concentrations recovered at this screening were very low. At no point did the concentrations exceed the detection limit of 0.01 μg/L, meaning the reliability of these

results is questionable at best and is therefore considered a weak tracer recovery.

In the following sections, the tracer data for each well is shown. First, the tracer data from the screenings within the same casing as the injection screening will be shown. After that, the wells will be shown in the order of furthest upstream to furthest downstream well.

RI-27

As mentioned above, the tracer data for RI-27 are from screenings located within the same casing as the injection screening, RI-27S (I). The recoveries are shown in figure 3.7.

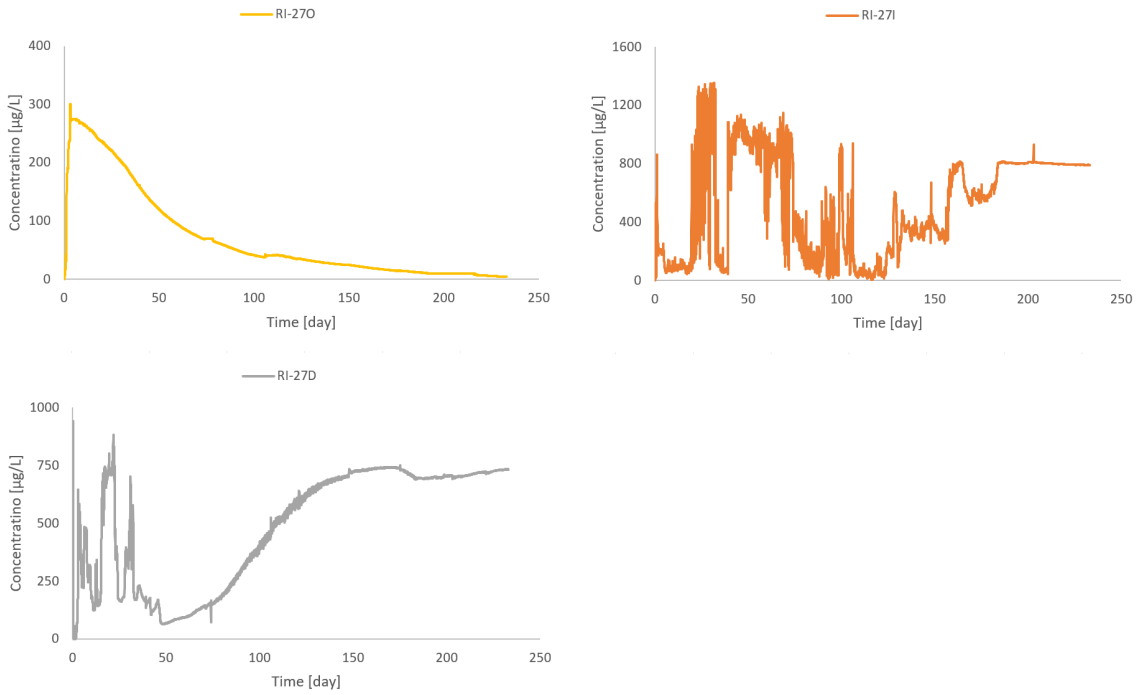

Figure 3.7: Tracer data results for well RI-27. An aerial and cross-sectional overview of the screening locations and tracer recovery is shown in figures 3.18 and 3.19.

The tracer data for the open hole shows a relatively rapid decrease in concentration after injection. The intermediate and deep screenings still have high concentrations of tracer when the tracer test was ended, indicating that a longer sampling period may have been ideal.

RI-28

RI-28 is located south of the injection well and is the furthest upstream monitoring well, located 34 meters from the injection well. Therefore, good tracer recoveries were not expected. The breakthrough curves for RI-28 are shown in figure 3.8

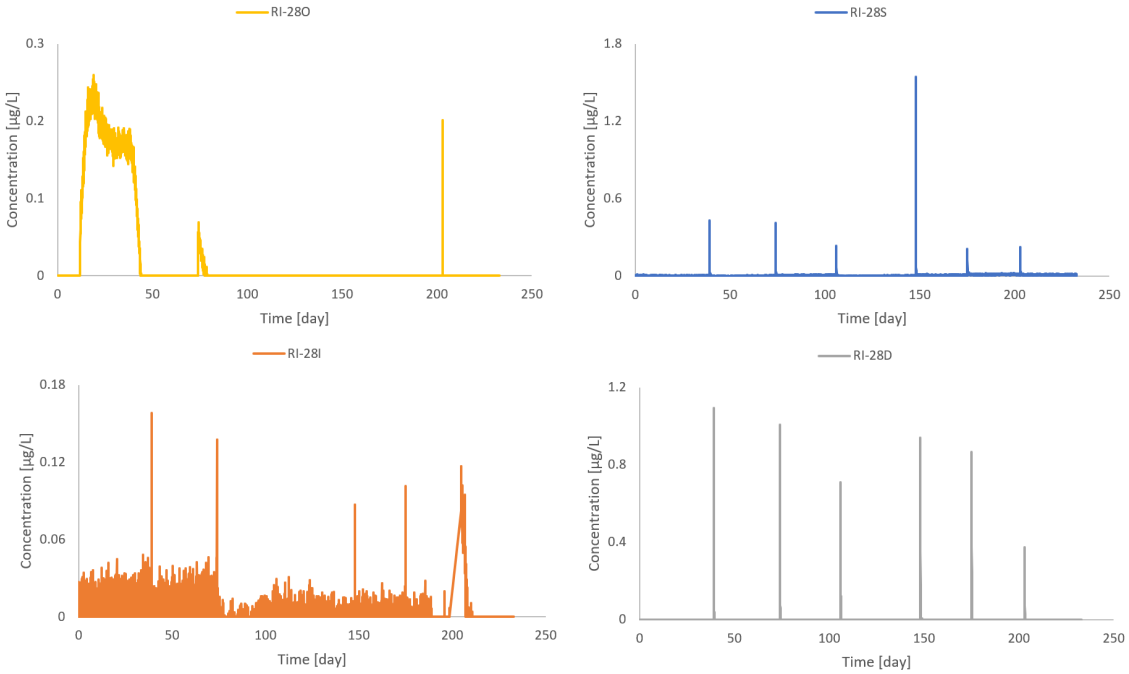

Figure 3.8: Tracer data results for well RI-28. An aerial and cross-sectional overview of the screening locations and tracer recovery is shown in figures 3.18 and 3.19.

Almost no tracer was collected, except a few peaks and low concentration just above the detection limit of 0.01 μg/L was found. Therefore, as expected, are all screenings within well RI-28 assessed as weak tracer recoveries.

OB-3

OB-3 is located between RI-27 and RI-28, upstream of the injection well and within the overburden, as it is a open hole. Therefore, good tracer recoveries were not expected either. The breakthrough curve for OB-3 is shown in figure 3.9.

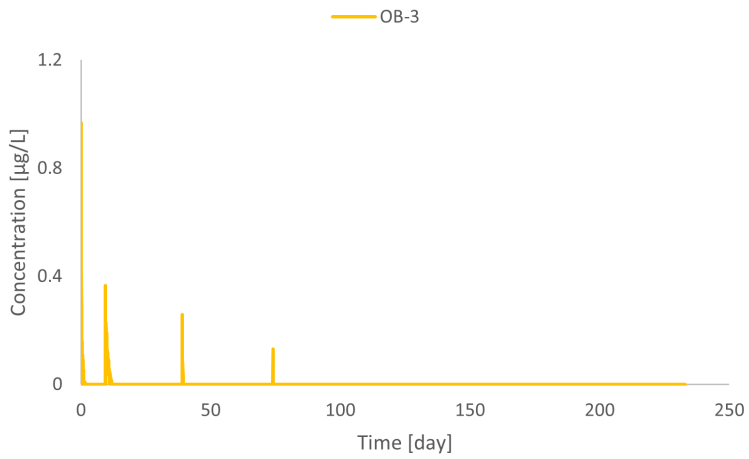

Figure 3.9: Tracer data results for well OB-3. An aerial and cross-sectional overview of the screening locations and tracer recovery is shown in figures 3.18 and 3.19.

Almost no tracer was recovered, and only a few brief peak concentrations were measured. Therefore, the tracer recovery is considered weak.

RI-1

RI-1 is located a bit upstream and west of the injection well. Based on the estimated flow directions, strong tracer recoveries were not expected. The breakthrough curves for RI-1 are shown in figure 3.10.

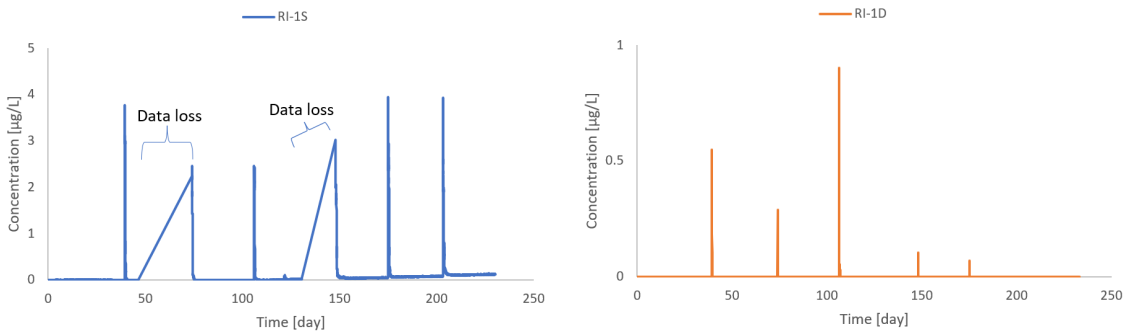

Figure 3.10: Tracer data results for well RI-1. An aerial and cross-sectional overview of the screening locations and tracer recovery is shown in figures 3.18 and 3.19.

Very little tracer was collected at RI-1. Except for a few spikes in concentration, the concentration was 0 for most of the sampling period. Also, a few data loss periods occurred for screening RI-1S. Therefore, the tracer recovery was assessed as weak.

RI-26 (E)

RI-26 (E) is the closest downstream monitoring well. It is located 142 meters northwest of the injection well. It is located more west than the estimated flow directions, so strong recoveries were not expected; however, stronger recoveries than the upstream monitoring wells were expected. The breakthrough curves for RI-26 (E) are shown in figure 3.11.

RI-26S and RI-26D have very low concentration recoveries, and the data primarily consists of spikes in concentration. Therefore, these screenings are considered weak recoveries. RI-26O has a period of approximately 40 days where concentrations above 0.1 μg/L were measured, which was the criterion for an intermediate tracer recovery. However, it is over a relatively short period, and the tracer recovery is considered weak. RI-26I (E) shows concentrations higher than the 0.1 μg/L threshold from around 180 days to the end of the tracer test. Furthermore, small concentration recoveries were found from the start of the tracer test until around 100 days into the tracer test, where the concentration then becomes 0. While the tracer recovery is not entirely continuous, and the concentrations are somewhat low, the tracer is still assessed as an intermediate recovery. Partly also due to its unique location compared to other monitoring wells.

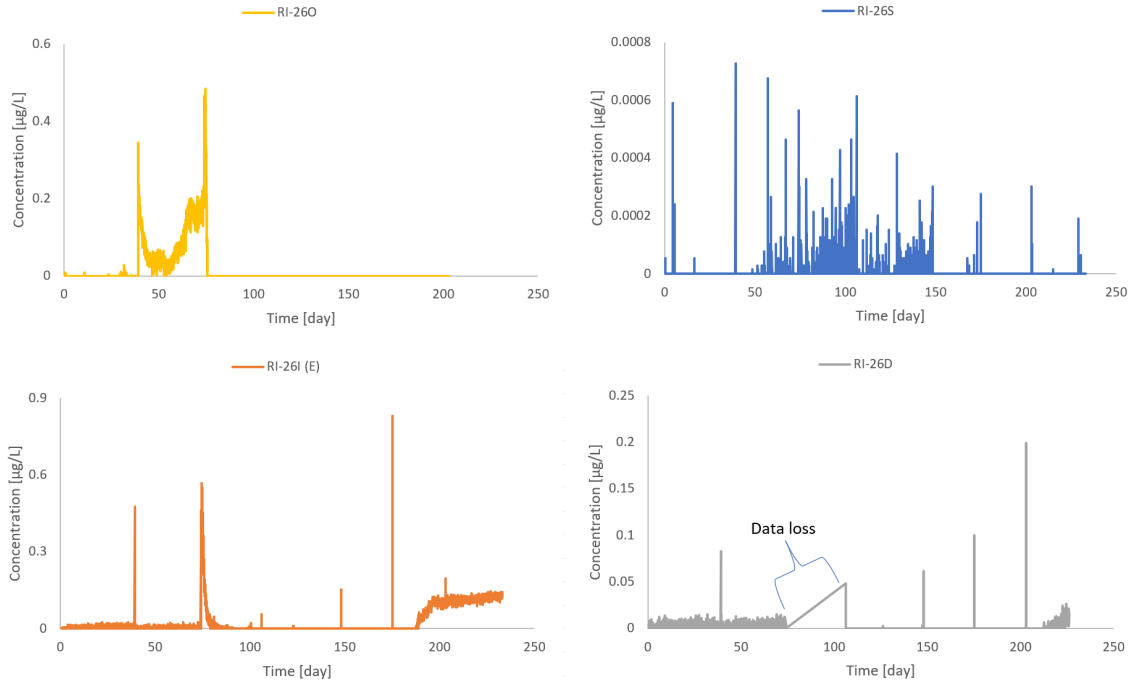

Figure 3.11: Tracer data results for well RI-26 (E). An aerial and cross-sectional overview of the screening locations and tracer recovery is shown in figures 3.18 and 3.19.

RI-7 (M1-M2)

RI-7 (M1-M2) is located 211 meters downstream from the injection well. Based on the estimated flow directions, it is located somewhat close to the expected flow direction. Therefore, moderately strong recoveries were expected. The breakthrough curves for RI-7 (M1-M2) are shown in figure 3.12.

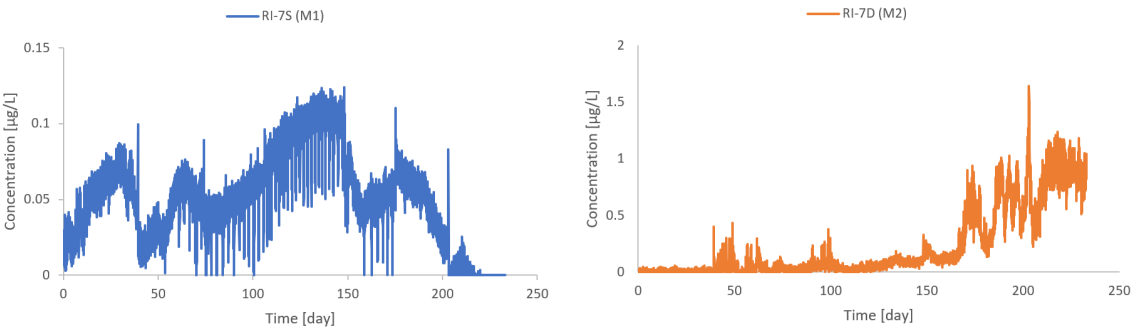

Figure 3.12: Tracer data results for well RI-7 (M1-M2). An aerial and cross-sectional overview of the screening locations and tracer recovery is shown in figures 3.18 and 3.19.

The concentration for both screenings was above the threshold of 0.1 μg/L for intermediate tracer recoveries during most of the sampling time. However, the concentrations were also below the criterion of 1.0 μg/L for strong tracer recoveries except for a few sporadic peaks. Therefore, the tracer recovery for both screenings was considered intermediate.

RI-25 (L1)

RI-25 (L1) is located just inside the eastern part of the Treatability Study area. It is therefore located within the estimated flow directions. However, its screenings are relatively shallow, especially when considering the distance to the injection well, which is 271 meters. The deepest screening is located only 10 meters below the injection screening. Therefore, both strong and weak recoveries could be found at RI-25 (L1). The breakthrough curves for RI-25 (L1) are shown in figure 3.13.

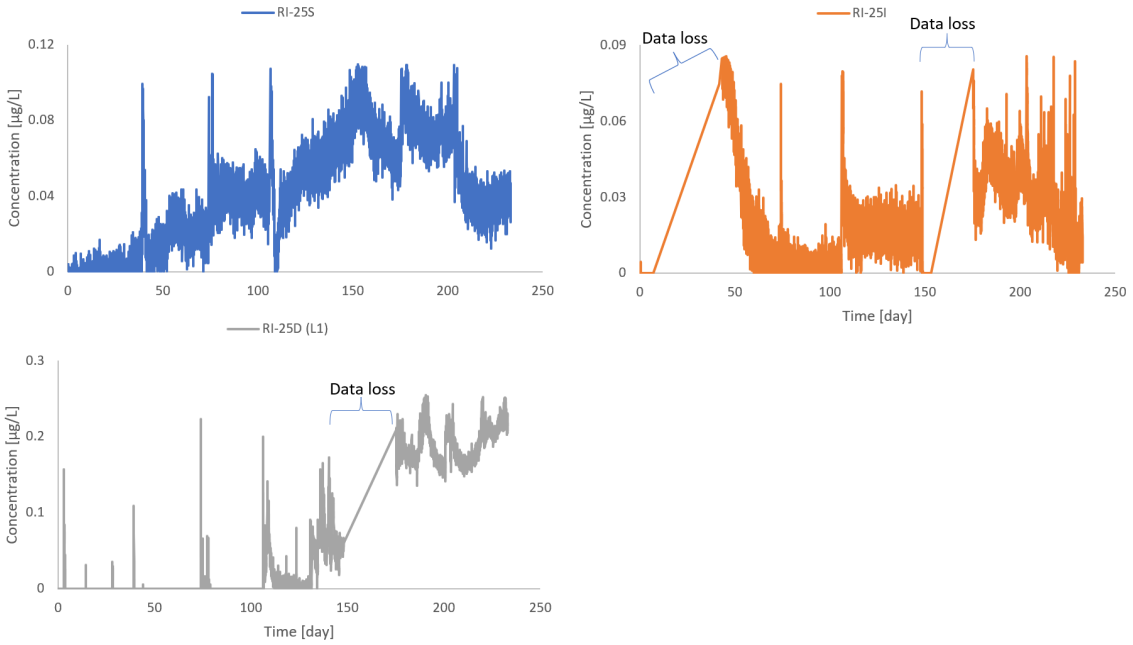

Figure 3.13: Tracer data results for well RI-25 (L1). An aerial and cross-sectional overview of the screening locations and tracer recovery is shown in figures 3.18 and 3.19.

For the two more shallow screenings, RI-25S and RI-25I, the recoveries were below the 0.1 μg/L threshold for almost the entirety of the tracer test, and are therefore considered weak recoveries. RI-25D (L1) had almost no tracer recoveries except a few peak concentrations until approximately 100 days, when tracer recovery started to occur. The concentrations after 175 days until the end of the tracer were above the 0.1 μg/L threshold. An unfortunate data loss occurred between days 150-175. Presumably, the tracer concentration were gonna increase during this period towards the levels detected after the data loss. The recovery for RI-25D (L1) is considered intermediate.

RI-21 (L2-L4)

RI-21 (L2-L4) is also located within the eastern part of the Treatability Study area just north of RI-25 (L1). It is located within the estimated flow directions and with deeper screenings than RI-25 (L1). Therefore, strong recoveries were expected. Furthermore, this was one of the wells showing high concentrations of TCE in the cross-sectional profile shown in chapter 2 figure 2.5. The breakthrough curves for RI-21 (L2-L4) are shown in figure 3.14.

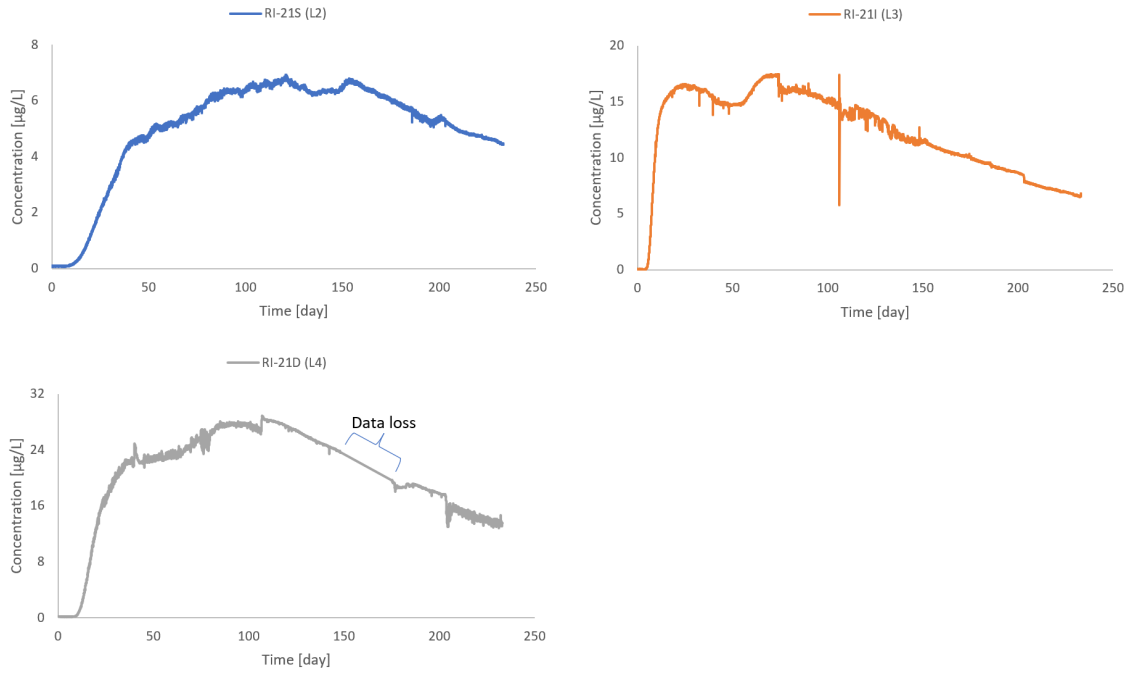

Figure 3.14: Tracer data results for well RI-21 (L2-L4). An aerial and cross-sectional overview of the screening locations and tracer recovery is shown in figures 3.18 and 3.19.

All screenings had concentrations way above the 1.0 μg/L threshold and are therefore considered strong recoveries. For RI-21D (L4), a small data loss is shown. The concentration was seemingly declining during the data loss, so the data loss is not assessed as being that significant.

RI-22 (L5-L7)

RI-22 (L5-L7) is located within the Treatability Study area, north of RI-21 (L2-L4), but with deeper screenings. Therefore, strong recoveries were expected. The breakthrough curves for RI-22 (L5-L7) are shown in figure 3.15.

Screenings RI-22S (L5) and RI-22I (L6) had concentrations above the 1.0 μg/L threshold and are therefore considered strong recoveries. It should be noted that the concentrations are, in general, not as high as for RI-21 (L2-L4), indicating that the main tracer mass may have passed the screenings due to their depth, as was also the tendency for the TCE concentrations in the cross-sectional profile. Screening RI-22D (L7) had lower concentrations than the 1.0 μg/L threshold except for very brief periods. This is also the deepest screening used for the tracer test, and therefore indicates that the main tracer mass was transported above the screening. The concentration was still above the threshold of 0.1 μg/L, and it is therefore assessed that the tracer recovery at RI-22D (L7) was intermediate.

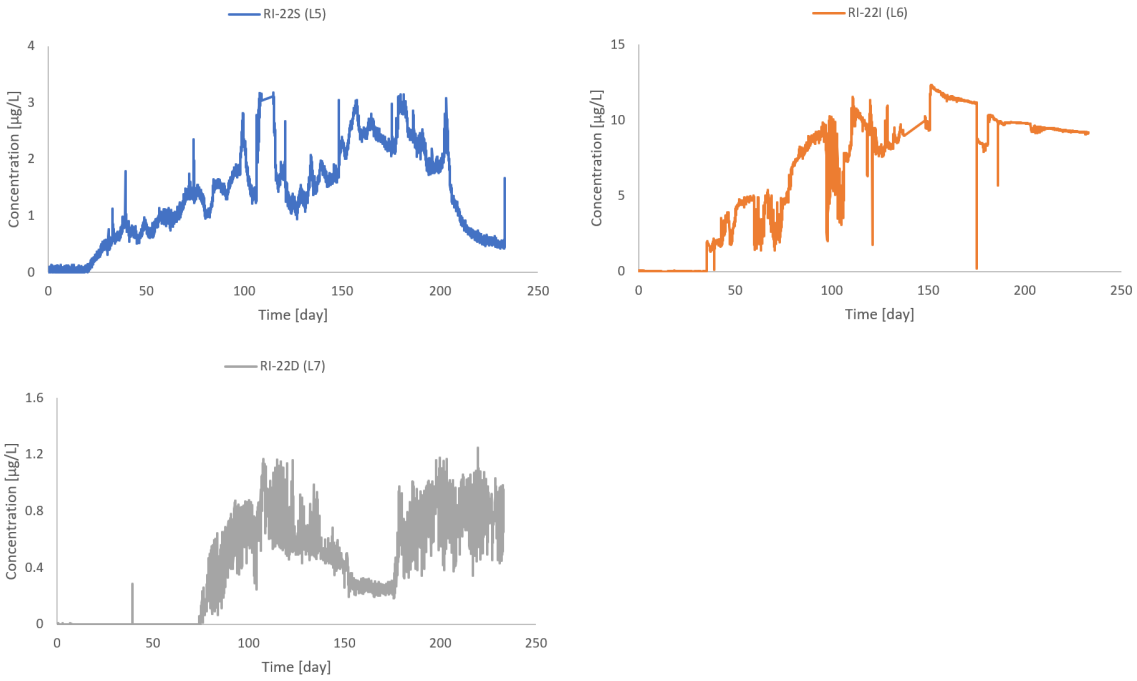

Figure 3.15: Tracer data results for well RI-22 (L5-L7). An aerial and cross-sectional overview of the screening locations and tracer recovery is shown in figures 3.18 and 3.19.

RI-23 (F1-F3)

RI-23 (F1-F3) is located within the western part of the Treatability Study area. Therefore, it is located within the estimated flow directions. It has screenings somewhat close to the same depth as RI-21 (L2-L4) and showed the same tendencies in terms of the TCE cross-sectional profile. Therefore, strong recoveries were expected. The breakthrough curves for RI-23 (F1-F3) are shown in figure 3.16.

The concentrations for screenings RI-23S (F1) and RI-23D (F3) had recoveries above the 1.0 μg/L threshold and are therefore considered strong recoveries. RI-23D (F3) had an unfortunate data loss after 175 days which lasted approximately 25 days. Much like RI-21D (L4), the concentration was seemingly declining during the data loss, so the data loss is not assessed as being that significant. For RI-23I (F2), surprisingly low concentrations were found. At no point did the concentration exceed the threshold of 1.0 μg/L, but it was above the threshold of 0.1 μg/L and is therefore considered an intermediate tracer recovery. Interestingly when comparing with the TCE cross-sectional profile a dip in concentration is also seen around RI-23I (F2), indicating that perhaps some fracture orientations are causing a significant amount of mass of both TCE and tracer to bypass the screening.

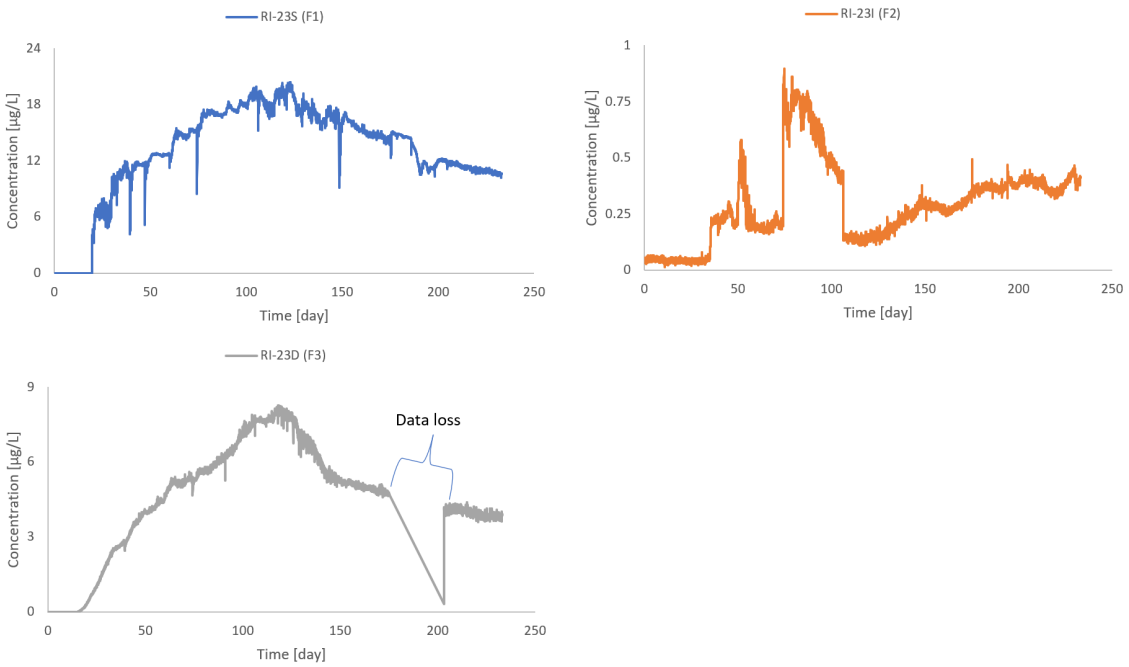

Figure 3.16: Tracer data results for well RI-23 (F1-F3). An aerial and cross-sectional overview of the screening locations and tracer recovery is shown in figures 3.18 and 3.19.

RI-24 (F4-F6)

The final well, RI-24 (F4-F6), is located next to RI-23 (F1-F3) but with deeper screenings. Therefore, it is expected to obtain strong recoveries, however, following the same tendency as RI-21 (L2-L4) and RI-22 (L5-L7), being that the deeper screenings, in general, have a lower tracer recovery. The breakthrough curves for RI-23 (F1-F3) are shown in figure 3.17.

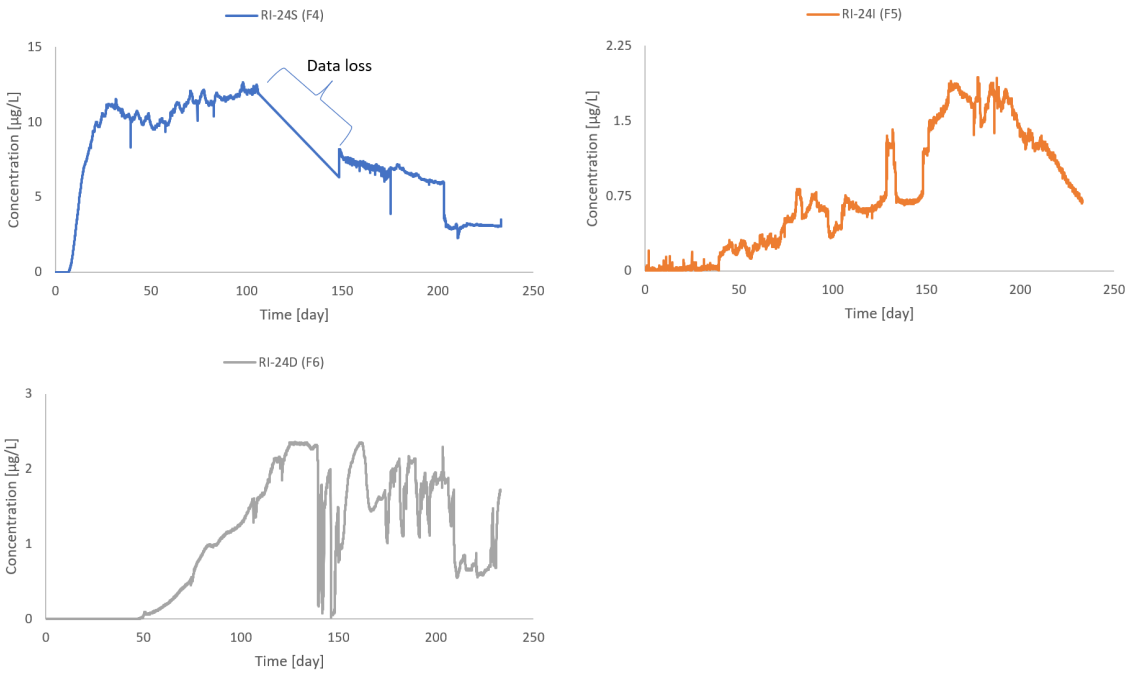

Figure 3.17: Tracer data results for well RI-24 (F4-F6). An aerial and cross-sectional overview of the screening locations and tracer recovery is shown in figures 3.18 and 3.19.

The recoveries for RI-24I (F5) and RI-24D (F6) follow the expected tendency of high recoveries but are lower than the recoveries found at RI-23 (F1-F3) (excluding RI-23I (F2)). They are both considered strong recoveries. RI-24S (F4) has somewhat surprisingly high tracer concentrations but also a significant data loss from approximately days 110 to 150. The data loss is during the peak concentration, which is quite unfortunate as it could continue increasing or start to decrease. The screening is still considered a strong recovery.

3.3 Tracer Recovery Overview

A general tendency seen in the tracer data for the intermediate and strong recoveries is that the breakthrough curve was still developing when the tracer test was ended. Indicating that the tracer was still being transported, which was also indicated by the screenings within the injection well. This introduces some uncertainties in interpreting the tracer data after the sampling period, for the models introduced in the following chapter. A few screenings had some unfortunate data losses, but most of the data losses were not that significant. Either because a clear tendency in the data was shown, or the data was a weak tracer recovery.

A summary of the tracer test recoveries based on their breakthrough curves is shown in figures 3.18 and 3.19.

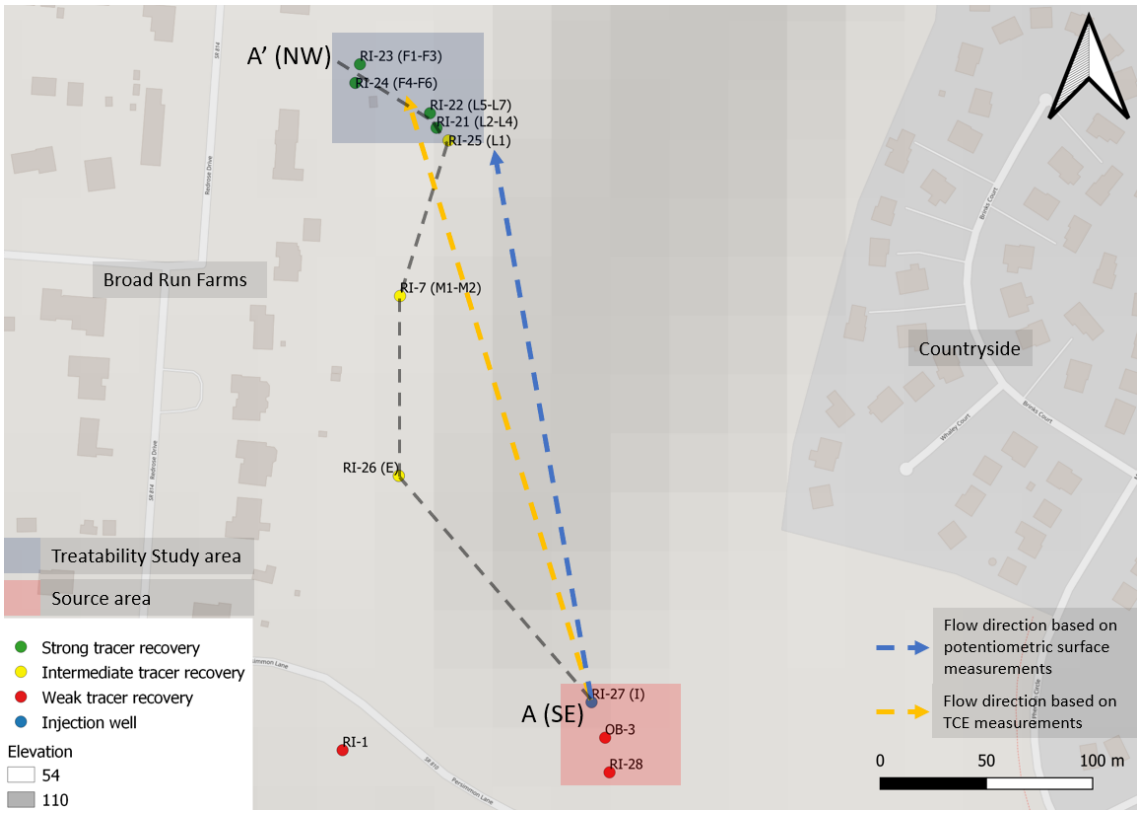

Figure 3.18: Aerial overview of the tracer test recovery assessment. The dashed gray line is a transect line used to develop figure 3.19. The location of the landfill is clearly indicated by the change in elevation.

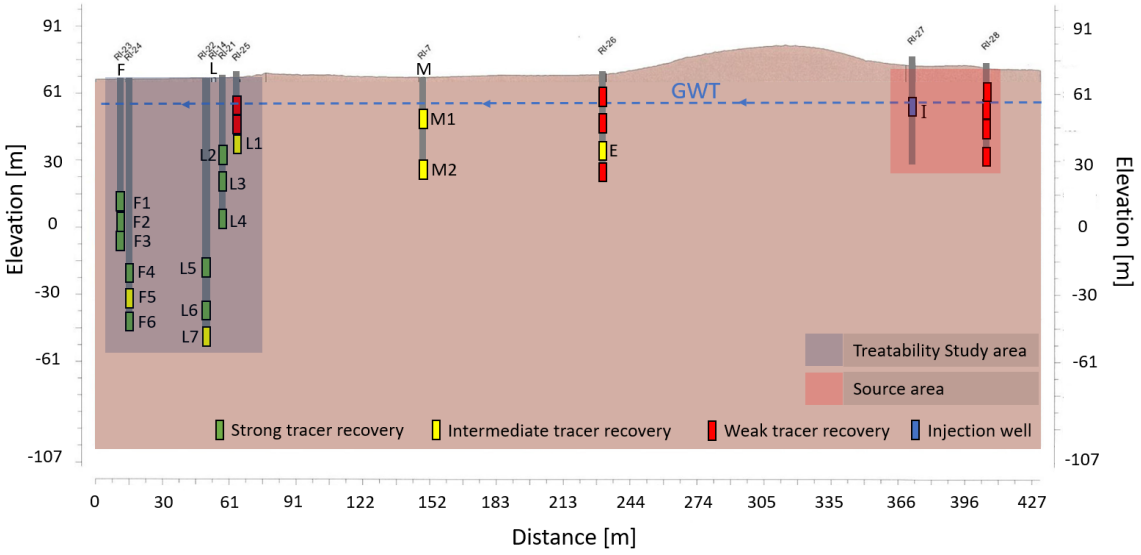

Figure 3.19: Cross-sectional overview of the tracer test recovery assessment. The cross-sectional profile is based on the dashed gray transect line shown in figure 3.18. For the screenings not assigned more relatable names the following order always applies from most shallow screening to deepest: O (Open hole), S (Shallow), I (Intermediate), D (Deep).

As shown in the figures, the monitoring wells located within the Treatability Study Area almost all had a strong recovery, while those outside it had an intermediate or weak recovery. This indicates that the tracer had a similar transport path as expected based on the estimated flow directions from the TCE and the potentiometric surface measurements described in chapter 2. The screenings inside the Treatability Study area without a strong recovery are the ones that are either shallow or deep screenings (with the exception of RI-23I (F2)), indicating that the tracer may have mainly been transported between the two. This was also the case when comparing these results to the cross-sectional profile of the TCE measurements in chapter 2.

It should be noted that no monitoring wells east or straight north of the injection well were used for the tracer test, leaving little knowledge as to whether or not the tracer may have been transported in those directions. It would not be expected that the tracer were to travel east due to no significant TCE concentrations being found in the Countryside drinking wells [Field, 2020]. However, a monitoring well placed within the landfill northeast of the injection well, would be of interest to have further confirmation, or the opposite, in the estimated flow direction.

The breakthrough curves with weak tracer recoveries will not be used for further analysis, as they have already fulfilled their purpose in indicating where the tracer was not transported. Furthermore, the measurements' magnitude is too small, approaching the detection limit, making the uncertainty too big to be used for further analysis.

Some of the breakthrough curves with a strong recovery were shaped like a typical breakthrough curve, which is a right-skewed histogram [Gao, 2022]. However, some were quite different from a typical breakthrough having many peaks in concentration. This was also expected because of the fractured bedrock layer, which the tracer was transported through. Some tracer will end up in fractures; some will not be transported through

the fractures, and some will do a combination of both. This causes multiple peaks in concentration, due to different properties in the soil causing velocity variations. This is also known as a multi-domain soil system, which means that very different soil properties can be found within the same characterized soil [Grenier et al., 2005].

An illustration of a dual and multi-domain breakthrough curve is shown in figure 3.20.

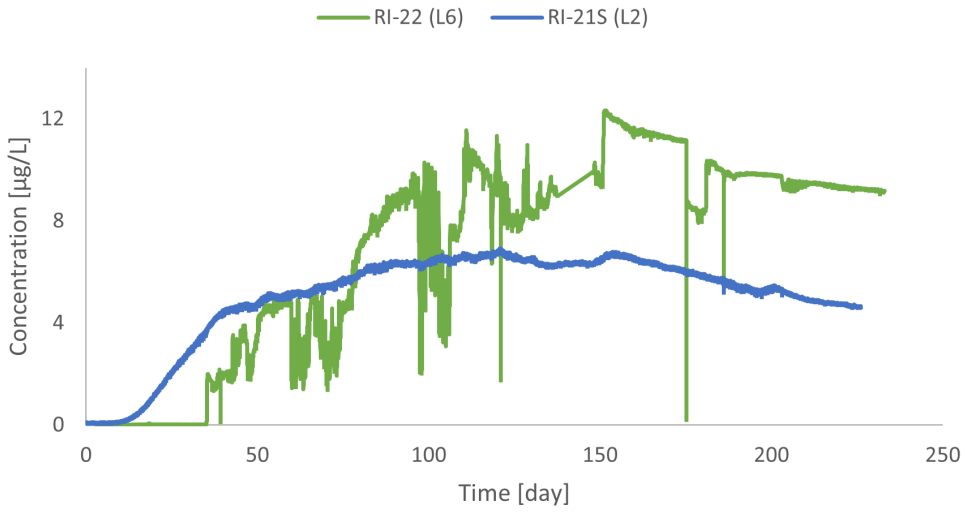

Figure 3.20: Breakthrough curve for RI-21S (L2) showing a dual-domain breakthrough curve, and RI-22I (L6) showing a multi-domain breakthrough curve. An aerial and cross-sectional overview of the screening locations are shown in figures 3.21 and 3.22.

The dual-domain breakthrough curve (RI-21S (L2)) has a steep slope from its initial breakthrough, around 15 days until 50 days. After the slope decrease until it reaches its peak at around 125 days. These two concentration tendencies are considered caused by two different domains. A small dip in concentration is shown afterward, which may be considered a third domain but is hard to assess.

The multi-domain breakthrough curve (RI-22I (L6)) tracer shows a high amount of fluctuation, and it is hard even to assess the number of domains, but it is clearly a multi-domain breakthrough curve.

As already illustrated by these two tracer recovery curves, assessing the number of domains for a given tracer data set quickly becomes subjective. Therefore, a more objective way of categorizing the tracer data's complexity was desired. This was developed in the FAST-MD procedure, further explained in chapter 5.

Summary

An overview of the tracer test experiment conducted by the EPA was described. From the tracer test, three categories for tracer recovery were chosen. The strong and intermediate tracer recoveries will be used for further analysis, while the weak recoveries will not be used further. In figures 3.21 and 3.22 an aerial and cross-sectional overview of the wells and screenings used for further analysis is shown.

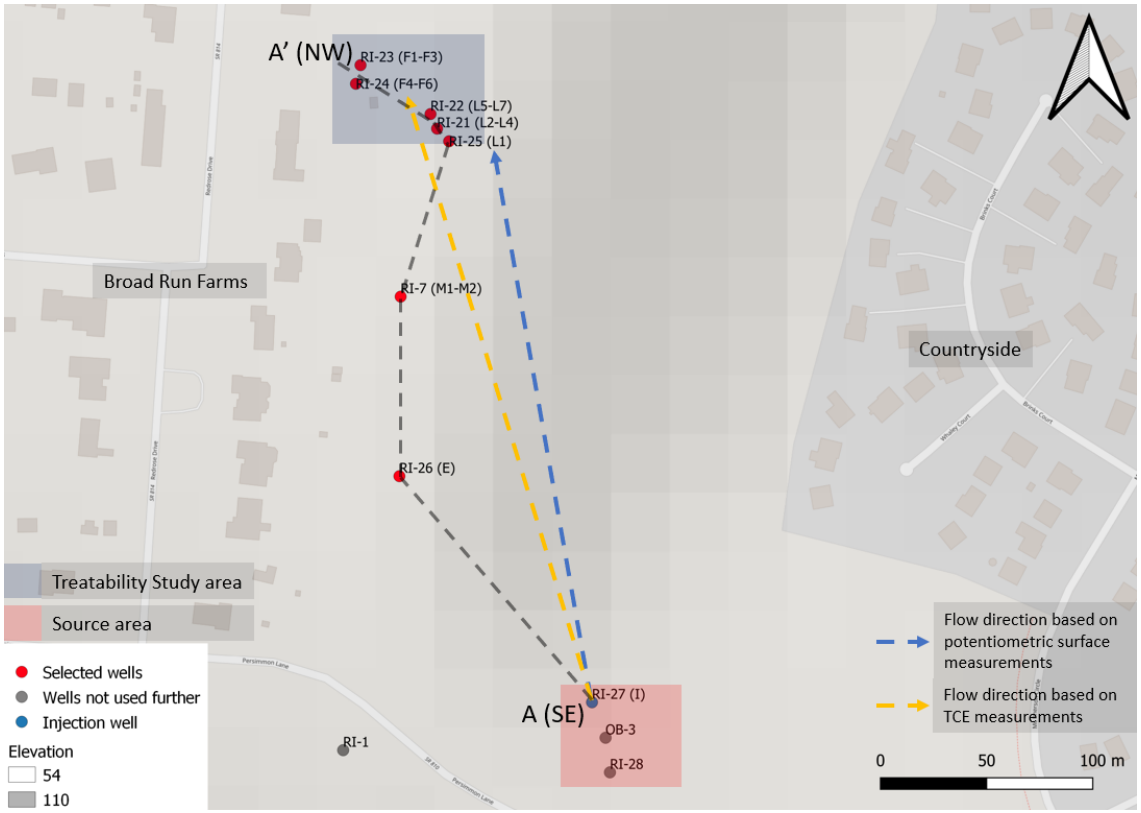

Figure 3.21: Aerial overview of wells chosen for further analysis after evaluation of tracer recoveries. The dashed gray line is a transect line used to develop figure 3.19. The location of the landfill is clearly indicated by the change in elevation.

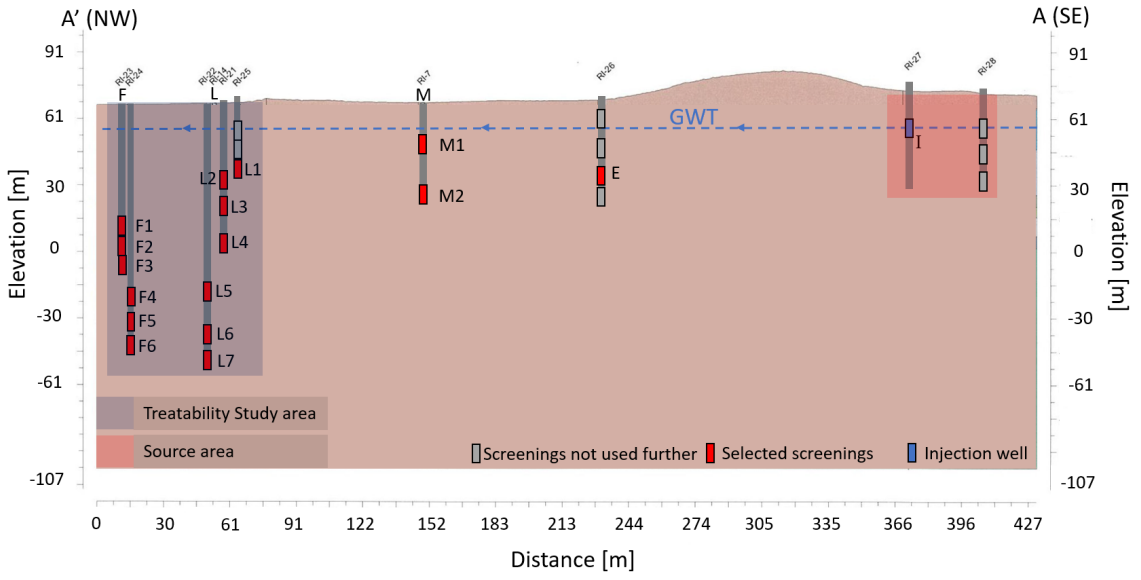

Figure 3.22: Cross-sectional profile of screenings chosen for further analysis after evaluation of tracer recoveries. The cross-sectional profile is based on the dashed gray transect line shown in figure 3.18.

These tracer recoveries matched the estimated flow directions based on TCE and potentiometric surface measurements.

An overview of the tracer data used for further analysis is shown in figure 3.23

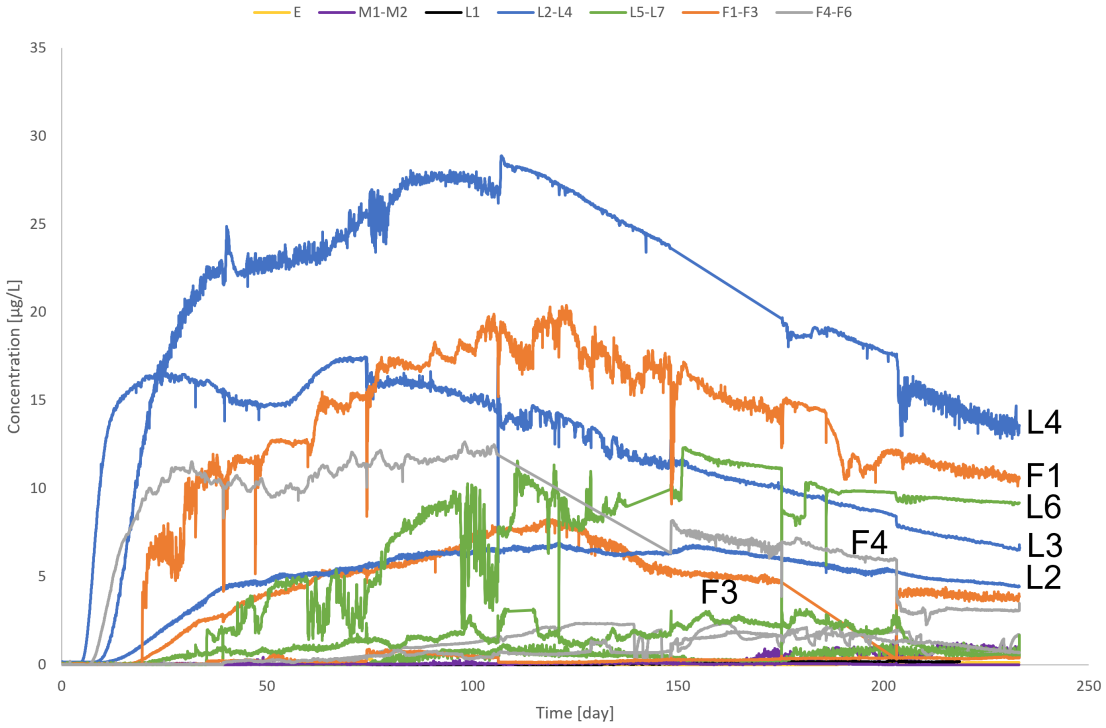

Figure 3.23: Overview of the tracer data used for further analysis. The 7 screenings with the highest concentrations are marked. An aerial and cross-sectional overview of the screening locations is shown in figures 3.21 and 3.22.

Based on the overview screening group L2-L4 and F1-F3 have the highest concentrations, having 3 and 2 of its screenings within the 7 highest concentrations respectively. These were the shallow screenings within the Treatability Study area. This fits with the tendency seen for the TCE cross-sectional profile shown in chapter 2 figure 2.5 where the highest concentrations were seen in approximately the same depth.

Furthermore, an evaluation of the different breakthrough curves showed that multiple domains may be contributing to some of the more complicated breakthrough curves. To describe these breakthrough curves, a model that can describe a multi-domain soil system is required. This model will be further discussed in the following chapter.

Transport Models and Geostatistics 4

The transport models for dealing with the complex tracer data introduced in the previous chapter will be presented in this chapter. It is assumed that 1-dimensional flow occurs between the injection screening and the monitoring screenings, even though the transport, in reality, is 3-dimensional. Furthermore, the geostatistical models used to analyze the goodness of fit between the transport models and the tracer data will be introduced. The models introduced in this chapter are applied using the software Microsoft Excel [Microsoft] unless otherwise implied.

4.1 Advection-Dispersion Equation

The transport of solutes in porous mediums is primarily controlled by the movement of the water in the medium. This means that solute transport is basically the replacement of solute-free water, with water including solute, and eventually replaced by solute-free water again. The concept is shown in figure 4.1. This section is based on [Loll and Moldrup, 2000] unless otherwise indicated.

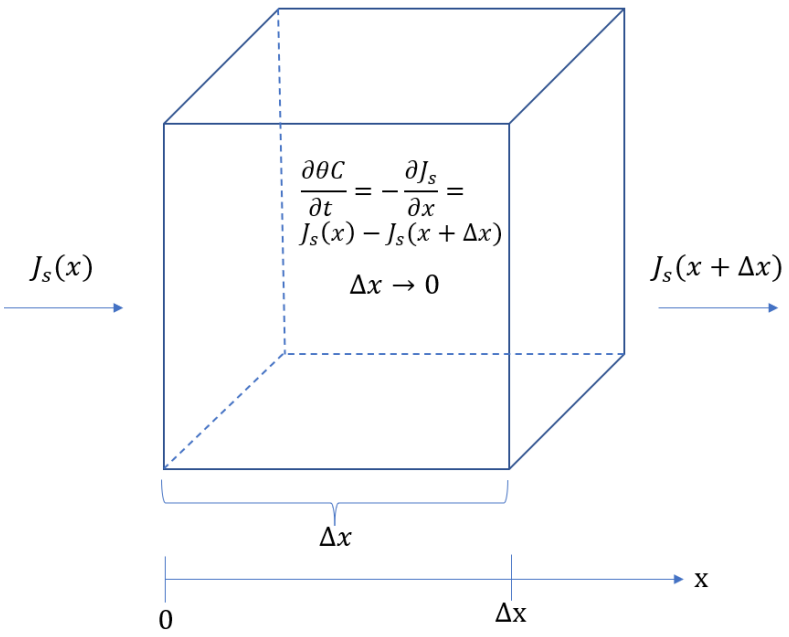

Figure 4.1: Illustration of the change in concentration in a volume of water due to the replacement of water, using the continuity equation.

The transport processes advection and dispersion mainly control the replacement or transport of water and thereby solute. Furthermore, diffusion can, in some soil systems, play a role in the transport of solutes, such as fractured bedrock, which is present at the HLLSS [CLU-IN].

Advection is the solute transport due to water movement, also known as mass transport or convection. The advective flux of a given solute is given by equation (4.1).

$$J_a = v \cdot \theta \cdot C \tag{4.1}$$

J_a	Advective flux [g/(m^2 s)]
v	Pore-water velocity [m/s]
θ	Volumetric water-content $\left[\frac{\text{m}^3 \text{ water—filled pores}}{\text{m}^3 \text{ soil}}\right]$
C	Concentration of solute [g/m^3]

Diffusion is the solute transport due to concentration gradients; basically, the solute is trying to distribute itself equally. This concept is also known as Fick's first law. The diffusive flux of a given solute is given by equation (4.2).

$$J_{dif} = -\theta \cdot D_{dif} \frac{\partial C}{\partial x} \tag{4.2}$$

J_{dif}	Diffusive flux [g/(m^2 s)]
D_{dif}	Diffusion coefficient [m^2/s]
x	Transport direction [m]

Dispersion is the transport or spreading of solute due to inhomogeneity in the soil. The inhomogeneity in the soil causes velocity variations and different flow paths for the water and solute. This concept is also known as mechanical dispersion. The dispersive flux of a given solute is given by equation (4.3).

$$J_{disp} = -\theta \cdot D_{disp} \frac{\partial C}{\partial x} \tag{4.3}$$

J_{disp}	Dispersive flux [g/(m^2 s)]
D_{disp}	Mechanical dispersion coefficient [m^2/s]

Dispersion and diffusion are two very different transport processes. They are, however, often when using the advection-dispersion equation combined into one term. This is because both transport phenomena yield a normal distribution of the mean velocity of the solute. The diffusive and dispersive flux added will be defined as the effective dispersion coefficient, D.

When combining the three transport processes, the total solute flux is found, which is shown in equation (4.4).

$$J_s = -\theta \cdot D\frac{\partial C}{\partial x} + v \cdot \theta \cdot C \tag{4.4}$$

J_s	Total solute flux [g/(m^2 s)]
D	Effective dispersion coefficient ($D = D_{disp} + D_{dif}$) [m^2/s]

As mentioned earlier in the section, the transport of solutes can be described as replacing water within a given volume. For a concentration change to occur within this volume, the concentration going into the volume must differ from the one going out. This also applies to the volumetric water-content within a given volume.

This concept is also known as the continuity equation and is illustrated in figure 4.1, and in equation (4.5).

$$\frac{\partial \theta C}{\partial t} = -\frac{\partial J_s}{\partial x} \tag{4.5}$$

Other processes can also affect solute transport; in the case of the tracer, the following assumptions were made. It is assumed that the tracer does not decay or is produced during the tracer test and that no sorption occurs.

Combining equations (4.4) and (4.5) yields what is known as the advection-dispersion equation and is shown in equation (4.6).

$$\theta\frac{\partial C}{\partial t} = D\frac{\partial^2 C}{\partial x^2}\theta - v\frac{\partial C}{\partial x}\theta \tag{4.6}$$

The main objective of this chapter, as mentioned earlier, is to obtain a model which can describe the complex tracer data obtained from the EPA investigation. This tracer data is a so-called "window" into water and solute transport behavior from the injection well to the monitoring well. The tracer behavior from injection to monitoring wells is therefore left to interpretation based on the results of the monitoring wells. Therefore, it is assumed that the water and solute behavior described through the tracer data is the same from injection to monitoring well. In other words, steady-state water flow is assumed to occur between the injection and monitoring wells meaning that the volumetric water-content, pore-water velocity, and effective dispersion coefficient are constant. By dividing with the volumetric water-content the advection-dispersion equation can be simplified to equation (4.7) for steady-state flow conditions.

$$\frac{\partial C}{\partial t} = D\frac{\partial^2 C}{\partial x^2} - v\frac{\partial C}{\partial x} \tag{4.7}$$

A 1-D and 3-D numerical approach using Modflow [Aquaveo] was considered using the advection-dispersion equation. However, much for the same reason as described for the steady-state conditions, to fully capitalize on the strength of the modflow model, an extensive data set of hydrogeological data would be required. It was assessed that the data for the HLLSS was not sufficient for such complex models, and a more simple model approach would be more appropriate. In appendix B the considerations for the modflow model is further explored.

In the following sections, different models of the advection-dispersion equation are explored.

4.2 Mobile and Immobile Domain Model

The mobile and immobile domain model is a semi-dual-domain model of the advection-dispersion equation, as it includes exchange between two domains, an immobile and mobile domain. In the model, it is assumed that no solute transport occurs within the immobile zone, so the only process occurring in the immobile zone is the exchange with the mobile zone.

CXTFIT2 is a software used for solving steady-state one-dimensional transport problems using the advection-dispersion equation [Simunek et al.], including the mobile and immobile domain model. The software fits solute transport parameters such as pore-water velocity, mechanical dispersion coefficient, and mass transfer coefficient by minimizing the objective function, which is the sum of squared differences between observed and fitted concentrations [Toride et al., 1999].

The mobile and immobile domain advection-dispersion equation is shown in equation (4.8) and (4.9).

$$\theta_m \frac{\partial C_m}{\partial t} = \theta_m D_m \frac{\partial^2 C_m}{\partial x^2} - v\theta_m \frac{\partial C_m}{\partial x} - \alpha(C_m - C_{im}) \tag{4.8}$$

$$\theta_{im} \frac{\partial C_{im}}{\partial t} = \alpha(C_m - C_{im}) \tag{4.9}$$

m	Mobile domain [–]
im	Immobile domain [–]
α	Mass transfer coefficient [s^{-1}]

If equation (4.9) were to be removed and thereby also the mass transfer coefficient term in equation (4.8) the advection-dispersion equation introduced in equation (4.6) is then reobtained.

For simplification, the model introduces some dimensionless parameters for the input file. These are introduced in equations (4.10) and (4.11).

$$\beta = \frac{\theta_m}{\theta} \tag{4.10}$$

β | Partitioning factor between the mobile and immobile domain [–]

$$\rho = \frac{\alpha\zeta}{\theta v} \tag{4.11}$$

ρ | Dimensionless mass transfer coefficient [–]
ζ | Characteristic length [m]

Since the model assumes no movement in the immobile domain, the effluent concentration, c_e, becomes equal to the mobile concentration, c_m.

A conceptual model for the mobile and immobile domain model is shown in figure 4.2.

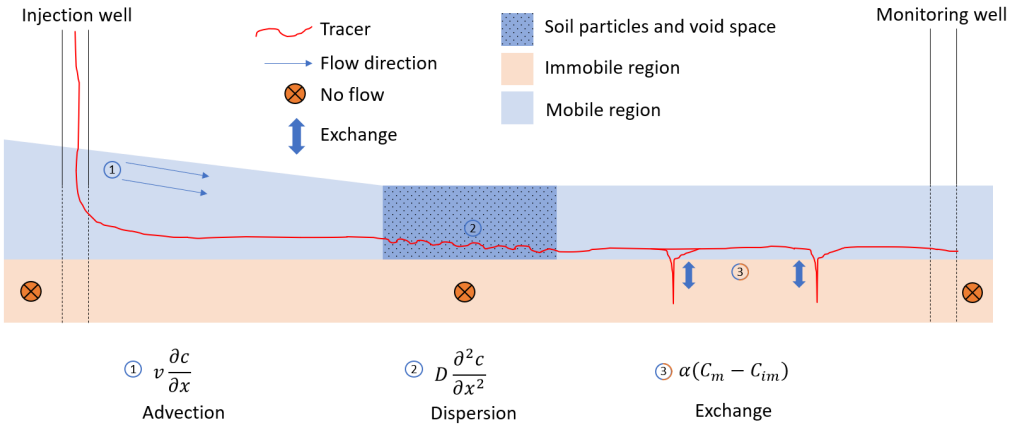

Figure 4.2: Conceptual model for the mobile and immobile domain model. It should be noted that while it appears that the two processes are happening at different locations in the model, this is not the case in reality and is just illustrated as such for easier visualization. Also, the exchange process occurs at pore-scale but is shown at field-scale for easier visualization.

The tracer was injected as quickly as possible to emulate an instantaneous injection. However, that is very hard to achieve, and it is assessed that a pulse release is a more reasonable representation of the tracer release and will be used for the CXTFIT2 software. For the initial input parameters for the CXTFIT2 software, the model QTRACER2 was used [Field, 2002]. QTRACER2 is a model that estimates transport parameters solely based on statistical analysis. By using QTRACER2 as an initial estimator of transport parameters, the likelihood that the CXTFIT2 software achieves the global minimum solution is increased [Field, 2020].

4.3 Dual-domain Model

The dual-domain model of the advection-dispersion equation uses the dual-advection dispersion equation (DADE) to combine different property domains to describe soils with multiple domains [Leij et al., 2012b], similarly to the mobile and immobile domain model. In the dual-domain model, movement occurs in the immobile domain, where the dual-domain model differs from the mobile and immobile domain model. Therefore, both the advection and dispersion processes occur in the immobile domain; hence, it is not an immobile domain in the dual-domain model. Therefore the terms fast and slow flow domains are used when referring to the dual-domain model.

The dual-domain advection-dispersion equation is shown in equation (4.12).

$$\theta_i \frac{\partial C_i}{\partial t} = \theta_i D_i \frac{\partial^2 C_i}{\partial x^2} - \theta_i v_i \frac{\partial C_i}{\partial x} + \alpha(C_j - C_i)(i = 1, 2; j = 2, 1) \tag{4.12}$$

$_i$ and $_j$ | Fast and slow domain [−]

The output concentration, which should match the tracer test as much as possible, is defined. It is unknown if the tracer test concentrations were measured in the fast or slow domain, so the effluent concentration is no longer equal to the concentration in one domain. The effluent concentration is defined as the flux-average concentration in a flowing fluid across both domains and is defined in equation (4.13) [Leij et al., 2012b].

$$C_e = \frac{\theta_i v_i C_i + \theta_j v_j C_j}{\theta_i v_i + \theta_j v_j} \tag{4.13}$$

C_e | Effluent concentration [g/m^3]

A conceptual model of the dual-domain model is shown in figure 4.3.

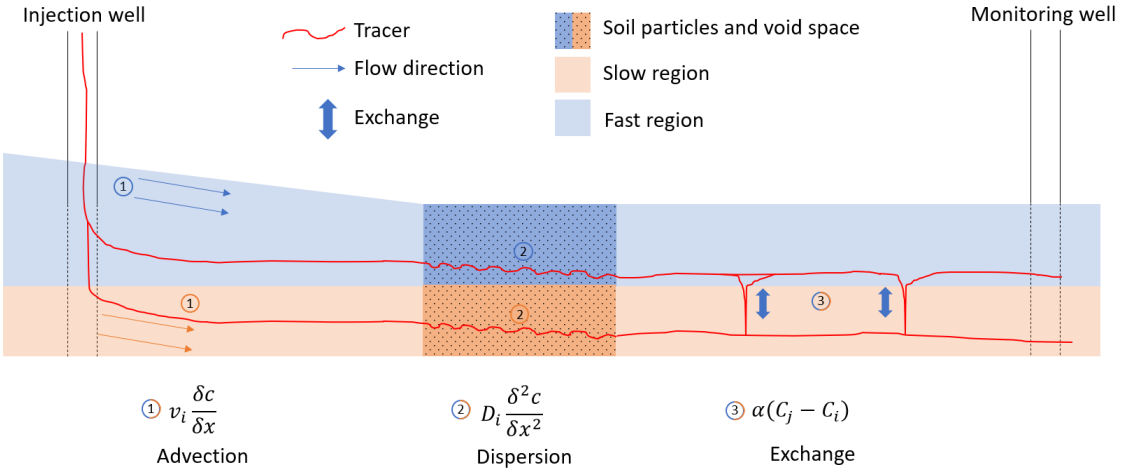

Figure 4.3: Conceptual model for the dual-domain domain model. It should be noted that while it appears that the two processes are happening at different locations in the model, this is not the case in reality and is just illustrated as such for easier visualization. Also, the exchange process occurs at pore-scale but is shown at field-scale for easier visualization.

4.4 Comparison of Mobile Immobile Domain and Dual-domain Models against Tracer Data

The mobile and immobile domain and dual-domain models were tested on the tracer data, showing some limitations. The models were excellent for fitting dual-domain tracer data, but as established in chapter 3 some of the tracer data is relatively complex, requiring a multi-domain model to obtain a decent fit. An example of this is shown for the tracer data from well RI-22S (L5) in figure 4.4

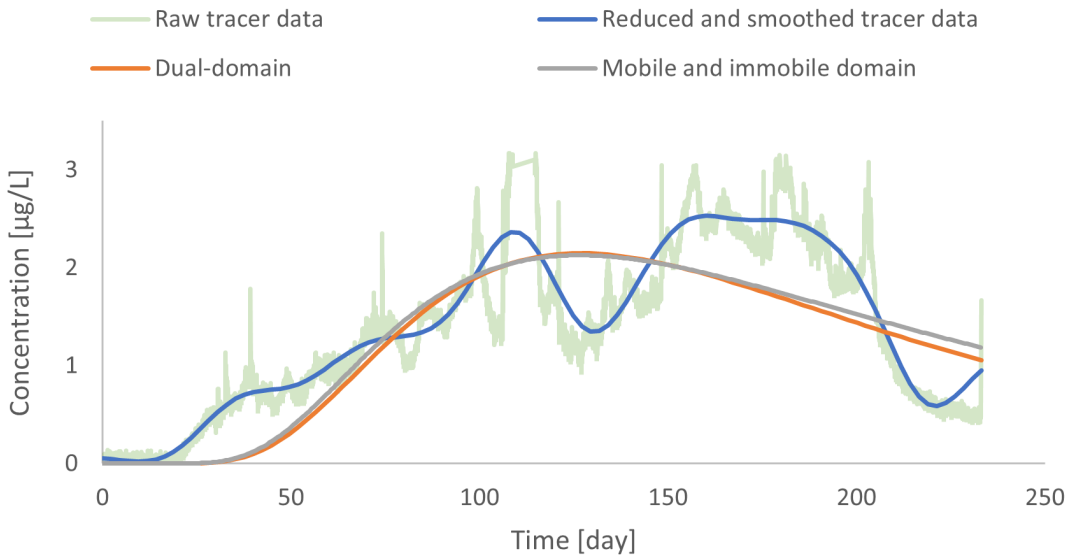

Figure 4.4: Raw tracer data, reduced and smoothed tracer data, and results from the two models. The models were fitted to the reduced and smoothed tracer data. The method for reduction and smoothing of tracer data is further explained in chapter 5. Results are from RI-22S (L5).

Neither model could obtain a decent fit for the raw tracer data or the reduced and smoothed tracer data. Both models are trying to obtain an average fit to the overall data since the amount of flow domains represented is more than the two domains each model uses. Therefore, a multi-domain approach had to be used to try and describe these complex tracer data sets.

4.5 Multi-domain Model

To describe these complex tracer data sets, a multi-domain model is required. For this, a streamtube approach was decided. To understand the concept of streamtubes, the term streamlines first has to be identified. Streamlines are lines tangential to the instantaneous velocity direction. These streamlines can be used to determine the movement of a particle through a given system. The concept of streamlines is further explained in appendix A.

A streamtube is an impermeable tube consisting of these streamlines. In the case of a steady one-dimensional system, the mass flow rate is constant [eFluids]. Therefore, each streamtube is considered an individual flow domain with unique properties, and no exchange will occur between the different flow domains.

The release of tracer is modeled as an instantaneous injection with a constant concentration throughout the injection period and, afterward, a concentration of zero. The injection period is assumed equal to 1 h for all screenings; this was also assumed for modeling in [Field, 2020] at the HLLSS. When dealing with a very short injection period relative to the sampling period of approximately 233 days, the exact value of the injection period is not that important as the variation between the screenings is instead expressed through the inlet concentration.

Since the background concentration is already implemented in the tracer data output, as described in chapter 3, the initial concentration is set to 0. The general analytical solution for such a boundary problem of the advection-dispersion equation introduced in equation (4.7) is shown in equations (4.14) and (4.15) [Leij et al., 2012a].

$$C(t) = \frac{c_0}{2}\Big(\Big[erfc\Big(\frac{L-vt}{\sqrt{4Dt}}\Big) + exp\Big(\frac{vL}{D}\Big)erfc\Big(\frac{L+vt}{\sqrt{4Dt}}\Big)\Big]\Big) \tag{4.14}$$

$for\ 0 < t \leq t_0$

$$C(t) = \frac{c_0}{2}\Big(\Big[erfc\Big(\frac{L-vt}{\sqrt{4Dt}}\Big) + exp\Big(\frac{vL}{D}\Big)erfc\Big(\frac{L+vt}{\sqrt{4Dt}}\Big)\Big]\Big) \tag{4.15}$$
$$-\frac{c_0}{2}\Big(\Big[erfc\Big(\frac{L-v(t-t_0)}{\sqrt{4D(t-t_0)}}\Big) + exp\Big(\frac{vL}{D}\Big)erfc\Big(\frac{L+v(t-t_0)}{\sqrt{4D(t-t_0)}}\Big)\Big]\Big)$$

$for\ t > t_0$

v	Pore-water velocity [m/s]
D	Effective dispersion coefficient [m^2/s]
C	Concentration [μg/L]
c_0	Inlet concentration [μg/L]
t	Time [s]
t_0	Injection time [s]
L	Distance between injection and monitoring well [m]

Equation (4.14) describes the concentration while the tracer is still being injected, while equation (4.15) describes the concentration after the tracer has been injected.

This solution is set up to describe each individual flow domain. Then a so-called combined domain function will be used to describe a final effluent concentration.

A weight factor, ω, is introduced to combine these flow domains into the combined domain function. The weight factor is used to partition each domain. It, therefore, describes the influence each domain has on the overall combined domain function. The sum of the weight factors is always 1 so that mass balance is preserved. The pore-water velocity and effective dispersion coefficient vary with each domain, while the remaining parameters are not domain-dependent. The combined domain function is shown in equations (4.16) and (4.17).

$$C(t) = \sum_{i=1}^{n} \Big(\Big(\frac{c_0}{2} \Big(\Big[erfc\Big(\frac{L - v_i t}{\sqrt{4 D_i t}} \Big) + exp\Big(\frac{v_i L}{D_i} \Big) erfc\Big(\frac{L + v_i t}{\sqrt{4 D_i t}} \Big) \Big] \Big) \Big) \omega_i \Big) \tag{4.16}$$

$for\ 0 < t \leq t_0$

$$C(t) = \sum_{i=1}^{n} \Big(\Big(\frac{c_0}{2} \Big(\Big[erfc\Big(\frac{L - v_i t}{\sqrt{4 D_i t}} \Big) + exp\Big(\frac{v_i L}{D_i} \Big) erfc\Big(\frac{L + v_i t}{\sqrt{4 D_i t}} \Big) \Big] \Big) \tag{4.17}$$

$$- \frac{c_0}{2} \Big(\Big[erfc\Big(\frac{L - v_i (t - t_0)}{\sqrt{4 D_i (t - t_0)}} \Big) + exp\Big(\frac{v_i L}{D_i} \Big) erfc\Big(\frac{L + v_i (t - t_0)}{\sqrt{4 D_i (t - t_0)}} \Big) \Big] \Big) \Big) \omega_i \Big)$$

$for\ t > t_0$

$_i$	i^{th} flow domain [–]
ω	Weight factor [-]

Exchange between the domains is not included in this solution of the advection-dispersion equation. However, while it is not directly implemented into the model, it is still present in the tracer data and, therefore, also affects the model output. This means that the value of the model parameters pore-water velocity and effective dispersion coefficient indirectly expresses this exchange between domains.

A conceptual model of the multi-domain model is shown in figure 4.5.

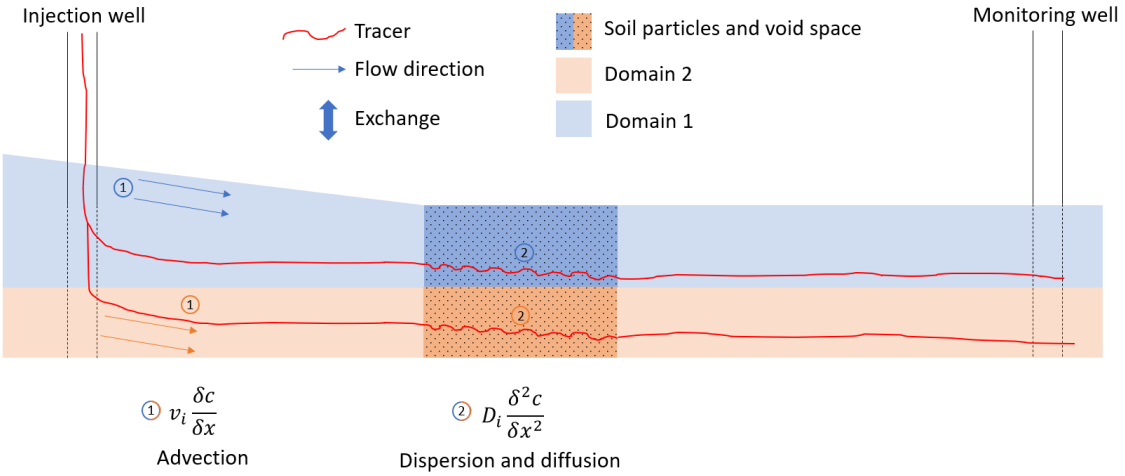

Figure 4.5: Conceptual model for the multi-domain model. It should be noted that while it appears that the two processes are happening at different locations in the model, this is not the case in reality and is just illustrated as such for easier visualization.

An illustration of the model is shown in both chapters 5 and 6.

4.6 Dispersivity as a Validation Tool

Dispersivity describes the relationship between solute spreading due to velocity variations and the average velocity experienced by particles in the pore-water. In other words, dispersivity describes the relationship between the mechanical dispersion coefficient and the pore-water velocity, as shown in equation (4.18) [Loll and Moldrup, 2000]. Dispersivity is, therefore, a relevant parameter to use as a validation tool because it describes the relationship between two of the main transport concepts in the advection-dispersion equation, which are advection and dispersion.

Diffusion and mechanical dispersion were described as one transport type in the effective dispersion coefficient for the multi-domain model. It is assumed that the relationship for dispersivity is still valid even though the effective dispersion coefficient is used instead of the mechanical dispersion coefficient. This is also quite common practice due to dispersion often outweighing diffusion [Loll and Moldrup, 2000].

$$\tau = \frac{D}{v} \tag{4.18}$$

τ | Dispersivity [m]

In [Gelhar and Collins, 1992] 59 different field site results were evaluated in terms of both longitudinal and transverse dispersivities as a function of scale, scale meaning the travel distance. The data were classified into two types of soil: porous (unimodal) and fractured media. The data was also divided into three types of solute transport events: naturally occurring uncontrolled contamination, human-induced uncontrolled contamination, and controlled tracer tests. The results are shown in figure 4.6 [Gelhar and Collins, 1992].

A tendency shown in the data is that at scales 10-1000 meters, the fractured media had higher dispersivity values than the porous (unimodal) media. The data were categorized into three reliability categories, high, intermediate, and low. These were based on factors such as knowledge of mass input history, non-conservative effects of tracer not accounted for, and limited geological knowledge. In cases where the concentration data collected was of high reliability, but other factors could be improved, a reanalysis was conducted, and a new dispersivity value was found [Gelhar and Collins, 1992]. The results are shown in figure 4.7.

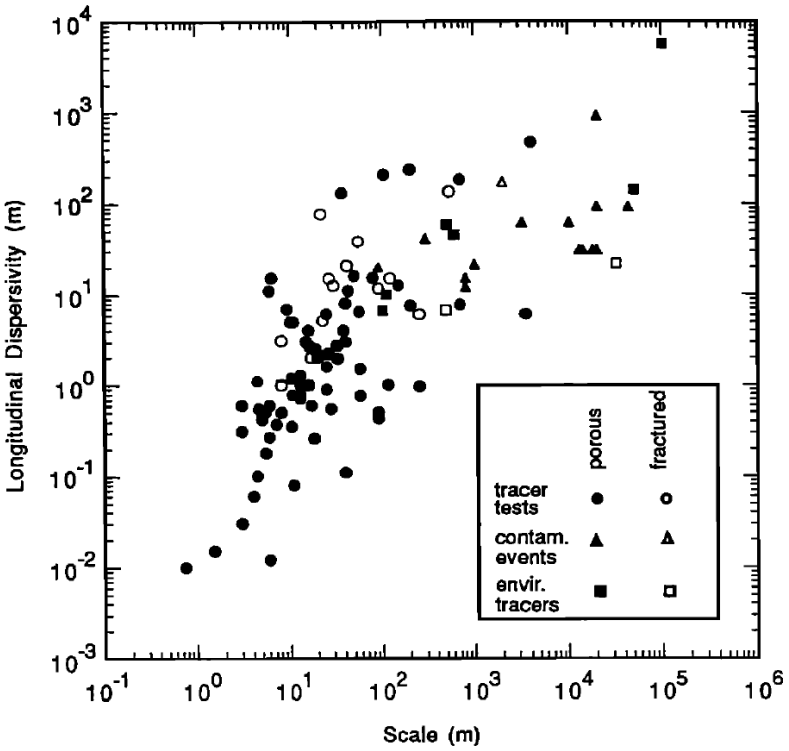

Figure 4.6: Longitudinal dispersivity as a function of distance from injection to detection well. The data is classified by soil type and solute transport event [Gelhar and Collins, 1992].

The site assessed as having high reliability with the largest distance between injection and detection well had, a distance of 250 meters. Most screenings used for analysis were within the Treatability Study area, located approximately 270-320 meters from the Source area, where the tracer was injected. Therefore, having a slightly larger scale than most of the high-reliability data, as also indicated by the scale of the HLLSS, which is shown in figure 4.7.

The results from [Gelhar and Collins, 1992] was also used in [Spitz and Moreno, 1996]. Based on the results, a rule of thumb was estimated that the longitudinal dispersivity is approximately a factor 10 lower than the travel distance. Furthermore, an interval of factor 10 above and below this rule of thumb was added and used as an expected range for dispersivity values. The figure is shown in appendix C figure C.1. This range was added to figure 4.6 and the results are shown in appendix C figure C.2.

As mentioned earlier, the fractured dispersivity values were seemingly higher than for the unimodal soil types. Most of the fractured values are located between the middle and

upper limits of the expected range. Therefore, this interval is defined as typical dispersivity values for fracture media. The lower to the middle limit is defined as typical values for unimodal media. This expected range was also added to figure 4.7 and are the solid and dashed blue lines.

These results were obtained from models primarily using single-domain models of the advection-dispersion equation. This means that for the fractured media soil types, the dispersivity becomes an average of the multi-domain properties within that soil. It is nearly impossible to have a homogeneous fractured media when working with field-scale sizes. This will cause a higher estimated spreading and higher dispersivity, as each domain and the exchange between these domains contribute to more velocity variations, meaning more spreading. This is also indicated by the high dispersivity values for the fractured media as seen in figure 4.6. Therefore, when using the multi-domain model introduced earlier in the chapter, the dispersivity is expected to decrease, especially for the domains representing significant fracture transport.

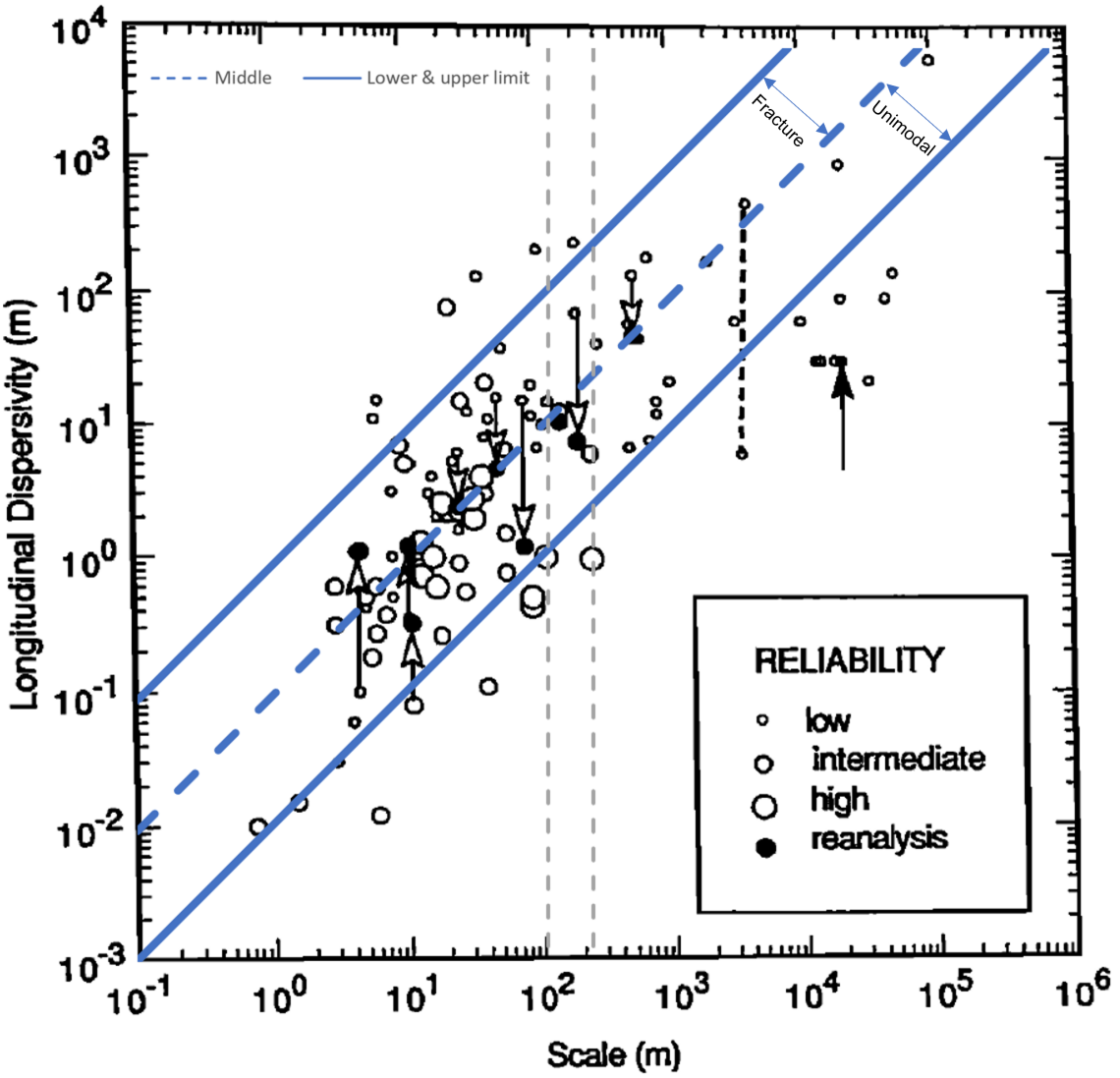

Figure 4.7: Longitudinal dispersivity as a function of distance from injection to detection well. Arrows indicate reported values at tails and corresponding values from reanalyses at heads. The dashed black line connects two dispersivity values determined at the same site; the dashed gray line is the minimum and maximum scale for the screenings used for further analysis at the HLLSS. The solid and dashed blue lines indicate an expected interval when using a single-domain model. The expected interval is divided into two soil types fractured and unimodal. Modified from [Gelhar and Collins, 1992].

This figure will be revisited in chapters 5, 6 and 8 where the results from the FAST-MD procedure will be evaluated to confirm the hypothesis that an increase in domains lowers the dispersivity.

The transverse dispersivity was also investigated in [Gelhar and Collins, 1992]. The results indicated that the longitudinal dispersivity was approximately 10 times higher than the horizontal transverse dispersivity and vertical transverse dispersivity was even lower. This indicates that the spreading of solute is mainly in the main-flow direction, further justifying the implications of using a 1-dimensional model of the advection-dispersion equation.

4.7 Pulse Peak with Power Term Model

The pulse peak with power term model is an empirical model used in the PeakFit software to describe individual peaks identified in the tracer data [Systat Software Inc.]. This is done as part of the FAST-MD procedure to identify the number of domains, their location, and shape. This process is further explained in chapter 5. This specific empirical model was chosen based on an evaluation of the different models offered by PeakFit. The pulse peak with power term model yielded the best results. This is because its shape is similar to that of the right-skewed histogram, which is the typical shape of a breakthrough curve described in chapter 3. This empirical model is quite similar to some of the basic transfer functions introduced in [Jury and Roth, 1990] used for solute transport modeling, further validating its usage. The equation for this model is shown in (4.19).

$$C = \frac{a_0[1 - \exp(-\frac{t-a_1}{a_2})]^{a_3} \exp(-\frac{t-a_1}{a_2})}{a_3^{a_3}(a_3+1)^{-a_3-1}} \tag{4.19}$$

C	Concentration [g/m^3]
t	Time [d]
a_0	Amplitude [g/m^3]
a_1	Pulse initiation [s]
a_2	Width [s]
a_3	Shape [-]

Each of these variables was investigated to understand how they are related to the solute transport parameters from the advection-dispersion model. The variation in output for three different values of each variable is shown in figure 4.8

The amplitude, a_0, changes the concentration peak, meaning it is the equivalent to the inlet concentration, c_0, in the advection-dispersion equation. The pulse initiation, a_1, and shape, a_3, change the breakthrough time of the peak, which would be equivalent to the pore-water velocity. The width, a_2, describes the peak's spreading, which would be equivalent to the effective dispersion coefficient.

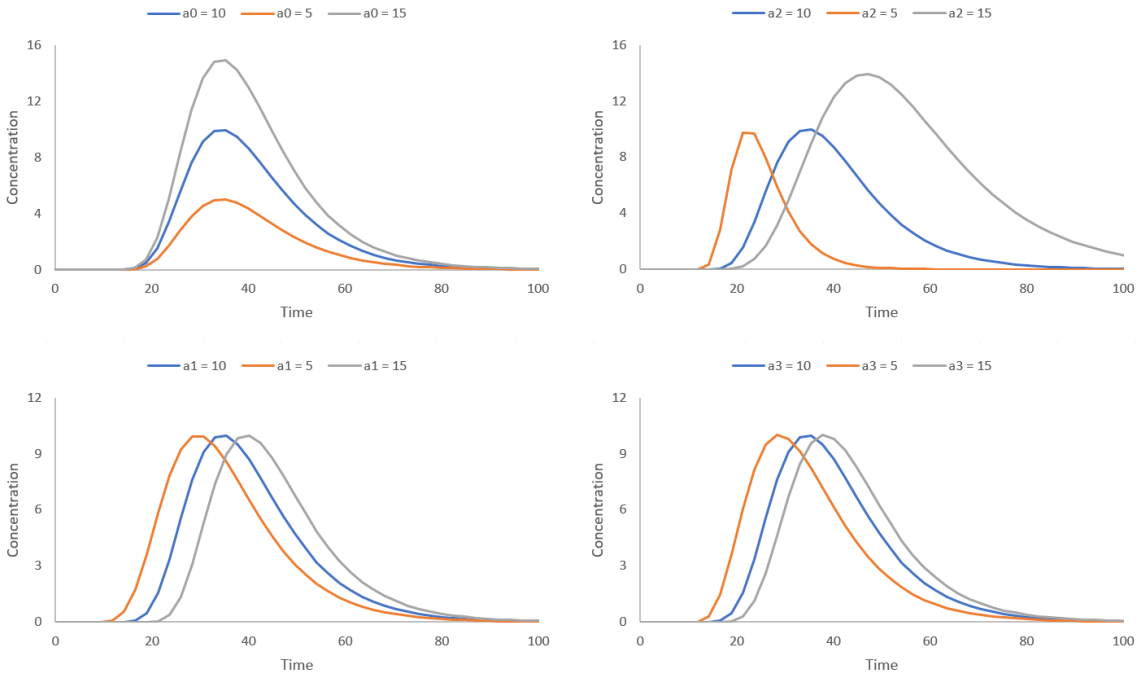

Figure 4.8: Value variation for the 4 variables in the pulse peak with power term model. For the variables kept constant a value of 10 is used.

4.8 Geostatistical Models

Two geostatistical models will be used to evaluate the goodness of fit achieved with the transport models and, thereby, the reliability of the estimated transport parameters.

4.8.1 Nash–Sutcliffe Model Efficiency Coefficient

The Nash–Sutcliffe model efficiency coefficient, hereon referred to as NSE, is widely used a statistical tool to assess the goodness of fit in hydrologic models [McCuen et al., 2006]. In comparison to the more standard coefficient of determination, R^2, the NSE takes into account systematic model bias [Nielsen et al., 2018]. In equation (4.20) the NSE model is shown.

$$NSE = 1 - \frac{\sum_{i=1}^{n}(y_i - c_i)}{\sum_{i=1}^{n}(c_i - \bar{c_i})} \tag{4.20}$$

NSE	Nash–Sutcliffe model efficiency coefficient [–]
y_i	Modeled results at time i [g/m^3]
c_i	Observed results at time i [g/m^3]
$\bar{c_i}$	Mean observed value [g/m^3]

An NSE value of 1 means the model perfectly fits the observed data. An NSE value of 0 means that the model fit is just as good as using the average value of the observed data. Finally, a negative NSE value means that using the average value of the observed data is better than the model fit [Nielsen et al., 2018].

A limitation of the NSE model is that it does not consider the number of model parameters, which is why another geostatistical model is also used.

4.8.2 Akaike's Information Criterion

As mentioned at the end of the NSE model description, the model does not consider the number of model parameters. This is one of the strengths of using Akaike's information criterion, hereon referred to as AIC. It is important to consider the number of model parameters during statistical analysis. In general, the more parameters, the better the overall fit; however, this may cause overconditioning of the model due to too many model parameters [Nielsen et al., 2018]. In equation (4.21) the AIC model is shown.

$$AIC = n(\ln(2\pi) + \ln\left[\frac{\sum_{i=1}^{n}(y_i - c_i)^2}{n-k}\right] + 1) + k \tag{4.21}$$

AIC	Akaike's information criterion [–]
n	Number of observations [–]
y_i	Modeled results at time i [g/m^3]
c_i	Observed results at time i [g/m^3]
k	Number of model parameters [–]

The AIC value varies between $-\infty$ and ∞, where the smaller or more negative the value, the better model prediction [Nielsen et al., 2018].

A limitation in the AIC model is that the output is of relative scale. This means that an isolated AIC value does not say anything about the goodness of fit. Therefore, the AIC model is instead used to compare the goodness of fit between models with the same observation data.

Both the NSE and AIC models are used as they give valuable information about the goodness of fit of the models in different ways that complement each model's limitations.

4.8.3 Residual Sum of Squares

The residual sum of squares is used as a parameter to optimize the goodness of fit between the model and tracer data and is shown in equation (4.22).

$$E = \sum_{i=1}^{n}((y_i - c_i)^2) \tag{4.22}$$

E	Sum of squared residuals [(g/m^3)^2]
y_i	Modeled concentration at i'th time [g/m^3]
c_i	Tracer data concentration at i'th time [g/m^3]

By optimizing the residual sum of squares, the solute transport parameters such as pore-water velocity, effective dispersion coefficient, and inlet concentration are found. The sum of squared residuals is used as the calibration goal, while the solute transport parameters are used as the calibration variable. This method is used in both the initial and final parameter estimation of the FAST-MD procedure introduced in chapter 5.

Summary

In this chapter, different models for describing the tracer data were introduced. It was deemed necessary to use a model of the advection-dispersion equation, which could describe multiple domains. The model used was a streamtube approach where each domain is described individually and then combined with a weight factor in a combined domain function. Exchange between domains is indirectly included in the solute transport parameters; however, the model does not include direct mass transfer between the domains. An empirical model called the pulse peak with power term model was also introduced. The purpose of which is to describe identified peaks in the software PeakFit [Systat Software Inc.]. An application example of both models will be shown in the following chapter and chapter 6.

A validation tool was also introduced using literature values of dispersivity from [Gelhar and Collins, 1992]. A hypothesis was developed that the dispersivity of the multi-domain model would be lower than the literature values because those were mainly obtained with a single-domain model. This validation tool will be used to evaluate the solute transport parameters found with the FAST-MD procedure, which will be introduced in the following chapter.

Two geostatistical models were also introduced. The NSE model was introduced to describe the overall goodness of fit of the data. The AIC model was introduced as a parameter to compare the goodness of fit between models with a different number of model parameters. These model applications will also be introduced in the following chapter and chapter 6.

Development of the Flow And Solute Transport - Multi Domain procedure (FAST-MD)

5

In this chapter, an introduction to the Flow And Solute Transport - Multi Domain procedure, also known as the FAST-MD procedure, will be conducted. The FAST-MD procedure was developed to analyze complex breakthrough curves resulting from transport in porous media with multiple flow domains to obtain water and solute transport parameters.

As illustrated in chapter 2 a more objective way to analyze the tracer data was desired in terms of the number of domains, location, and shape. In chapter 4, it was illustrated that a multi-domain model would be required to handle some of the more complex tracer data sets. With these motivations, the FAST-MD procedure was developed. A short overview of the FAST-MD procedure is shown in figure 5.1.

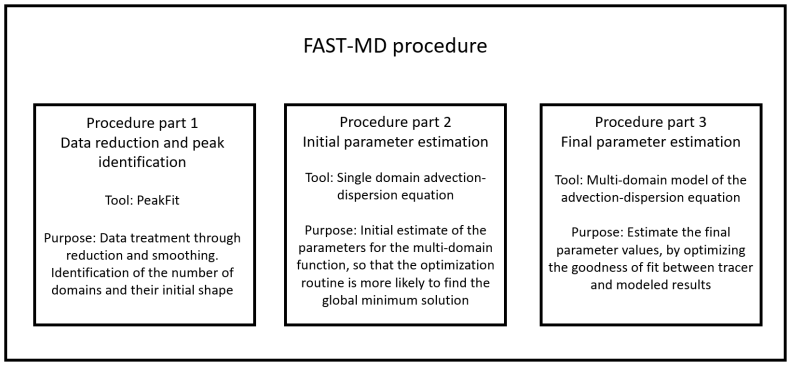

Figure 5.1: Overview of the three procedure parts in the FAST-MD procedure, including tools and purpose.

Process diagrams for each procedure part were made. The results from screening RI-22S (L5) will be used as an example in the process diagrams.

5.1 Part 1. Data reduction and Peak Identification

The purpose of procedure part 1 is to use data reduction and peak identification to obtain a more objective way to analyze the tracer data in terms of the number of domains,

their location, and shape. The software PeakFit is used for procedure part 1 [Systat Software Inc.]. PeakFit is an analysis software used for peak identification in data sets; its application has mainly been used in the scientific fields of spectroscopy, chromatography, and electrophoresis [Systat Software Inc.]. The usage of PeakFit within the hydrogeological field is limited. In [Andreo et al., 2015] and [Groten and E. Calvin Alexander, 2015], PeakFit was used as a tool to separate tracer recoveries when multiple tracer tests were conducted within a short time span of each other in karst systems. PeakFit was also used in [Goldscheider and Drew, eds] for the separation of tracers in laboratory experiments.

Data reduction is conducted due to computational limitations and simulation time optimization concerns. The amount of data points for each monitoring screen is around 11,000. The algorithm used to reduce these data points is the Gaussian weight function. The function calculates a given data point based on an average of surrounding points, where points closer to the given data point is weighted higher than data points further away [Brubaker].
The tracer data is reduced with equal distribution, so the distance between each data point is the same. 100 data points were chosen as it is assessed as an adequate amount of data points so that the results of modeling the tracer data are not changed significantly. This amount of data points significantly reduces computational time when modeling. Furthermore, the number of data points was chosen based upon an evaluation of minimizing data while still retaining the quality of the data set.

Additional data smoothing was done to reduce the amount of variance in the tracer data, removing outliers and noise from the data. In principle, this could be done in one step with the data reduction method, but it has been deemed more effective to do a separate smoothing function afterward [Systat Software Inc.]. This makes identifying peaks more reliable so that the chance that variance in data is mistakenly identified as a peak is minimized. The data was smoothed using the Savitzky-Golay algorithm, which generates local polynomials based on nearly located data points to obtain a local value [Whittaker, 1924]. The degree of smoothing is evaluated by the PeakFit software AI expert, which aims to minimize the noise in the data while still not adversely changing the overall data set [Systat Software Inc.].

Peaks are identified for the reduced and smoothed tracer data set. The shape and position of the peaks are optimized within the PeakFit software using a sum curve of the identified peaks, which is fitted to the reduced and smoothed data set. Furthermore, an optimization of the number of peaks required is conducted by evaluating the importance of the identified peaks. A process diagram of procedure part 1 is shown in figures 5.2, 5.3, and 5.4.

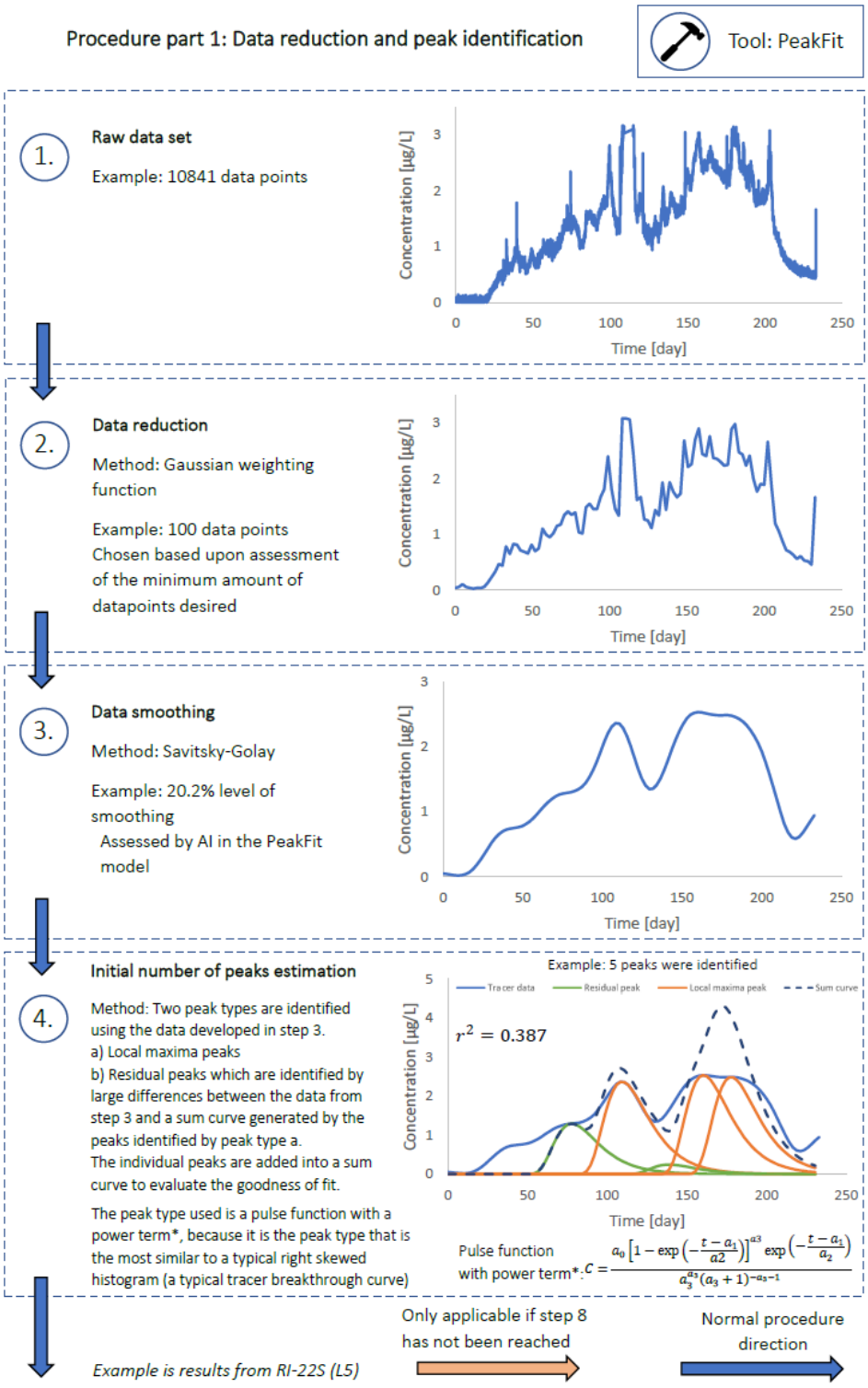

Figure 5.2: Process diagram for procedure part 1, Data reduction and peak identification (1/3).

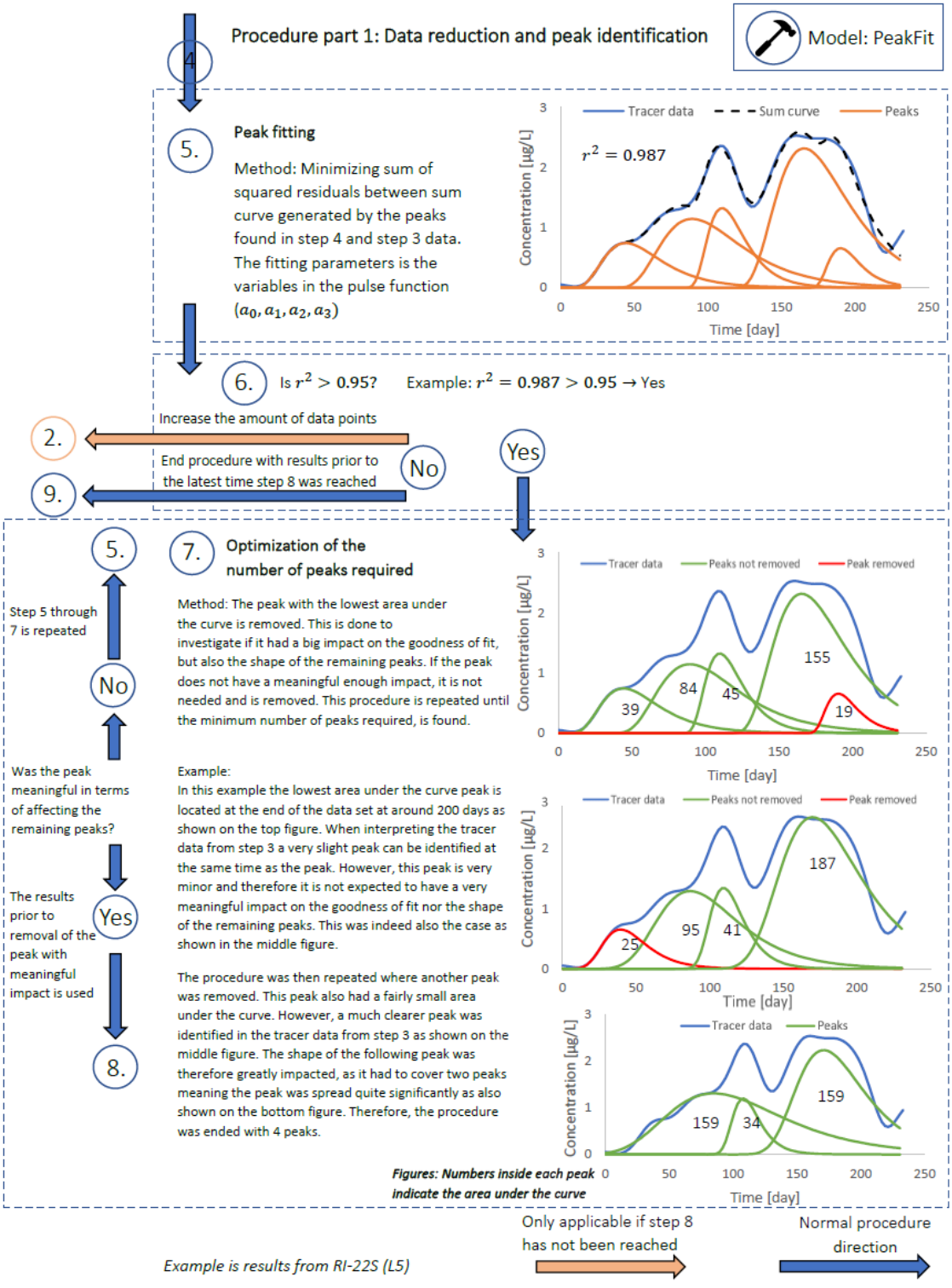

Figure 5.3: Process diagram for procedure part 1, Data reduction and peak identification (2/3).

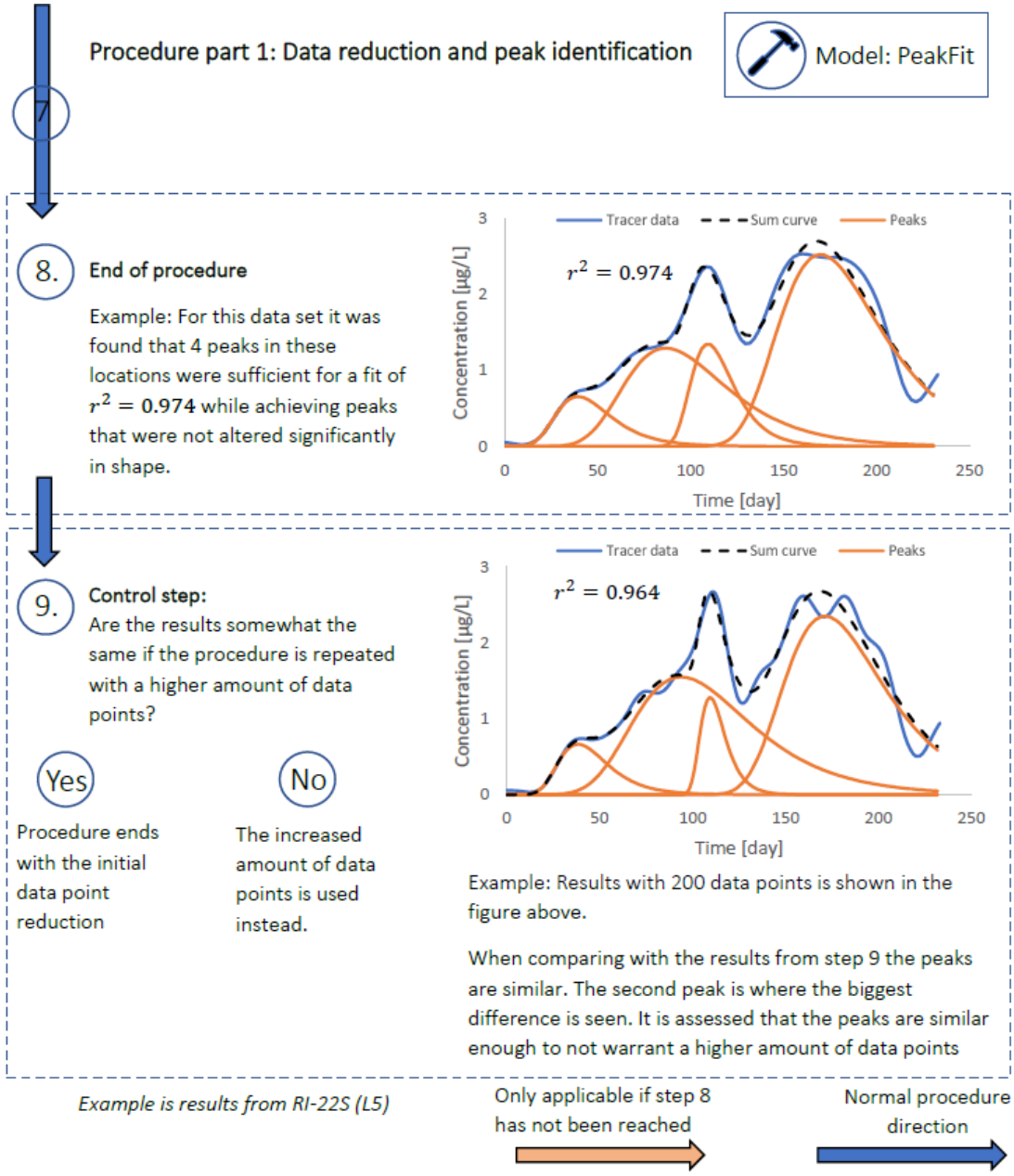

Figure 5.4: Process diagram for procedure part 1, Data reduction and peak identification (3/3).

5.2 Part 2. Initial Parameter Estimation

The purpose of procedure part 2 is to give an initial estimate of the parameters for the multi-domain model so that the optimization routine in procedure part 3 is more likely to achieve the global minimum solution. Each peak identified in procedure part 1 is fitted with the advection-dispersion solution presented in chapter 4 equations (4.14) and (4.15) to obtain initial estimates of the pore-water velocity and effective dispersion coefficient. Furthermore, an initial estimate of the inlet concentration and the weight factors are also obtained. A process diagram of procedure part 2 is shown in figures 5.5

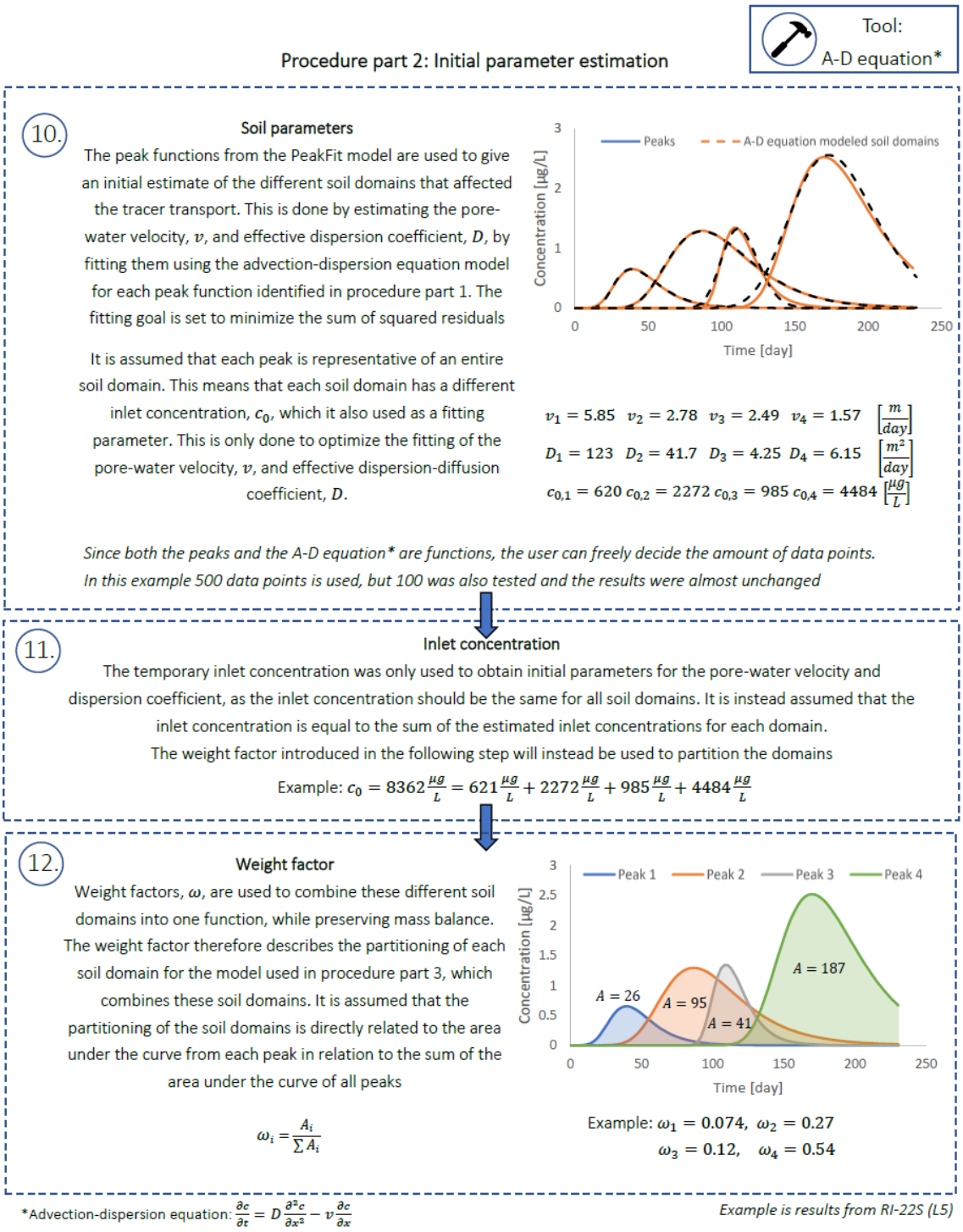

Figure 5.5: Process diagram for procedure part 2, initial parameter estimation (1/1).

5.3 Part 3. Final Parameter Estimation

The purpose of procedure part 3 is to use these initial parameters to obtain the optimized parameters for the tracer data. This is done by minimizing the sum of squared residuals between the combined domain function, obtained from the multi-domain model of the advection-dispersion equation, and the reduced and smoothed tracer data set. The calibration variables are the domain-dependent weight factors, pore-water velocities,

effective dispersion coefficients, and one inlet concentration, which is the same for all domains. A process diagram of procedure part 3 is shown in figures 5.6 and 5.7

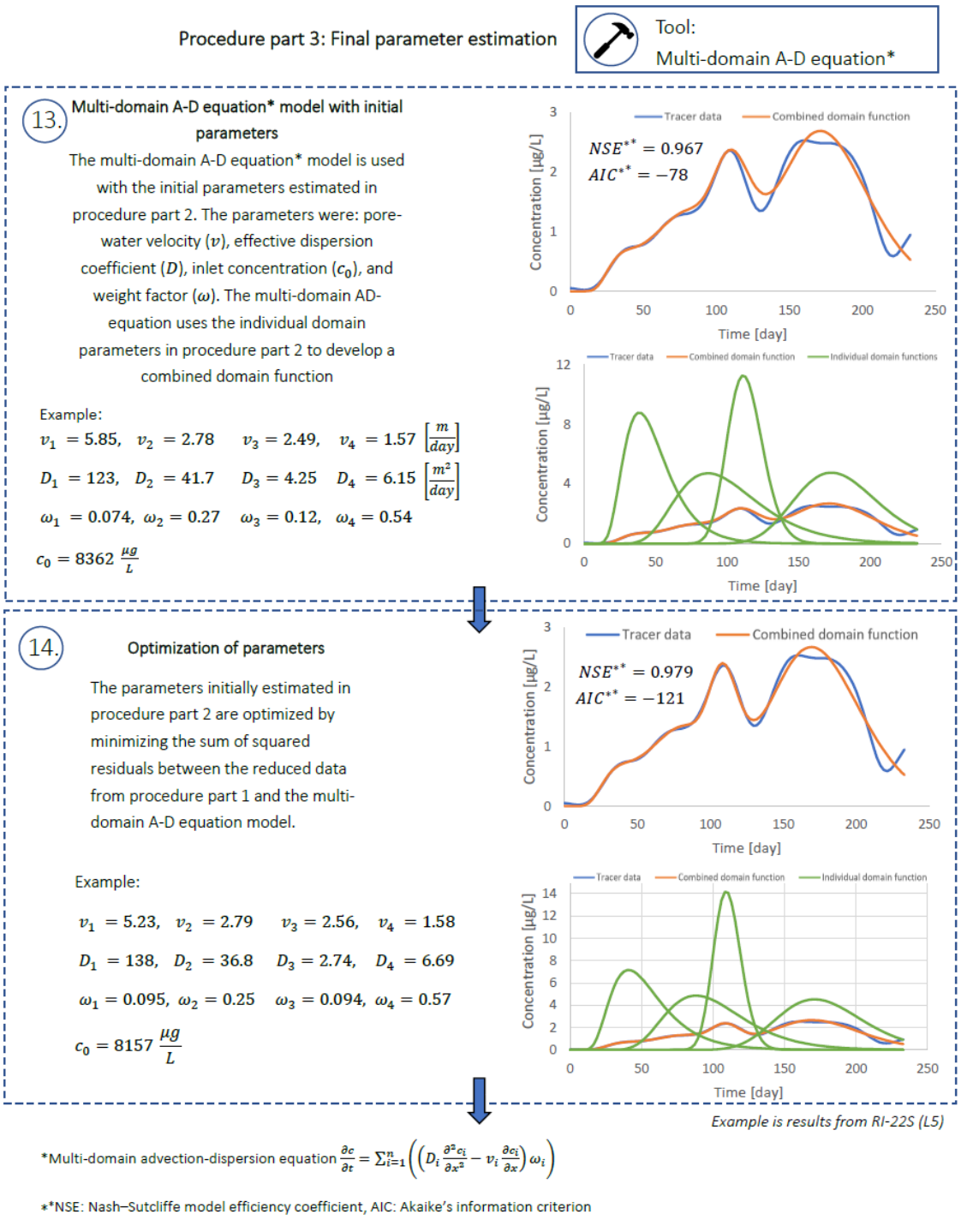

Figure 5.6: Process diagram for procedure part 3, final parameter estimation (1/2).

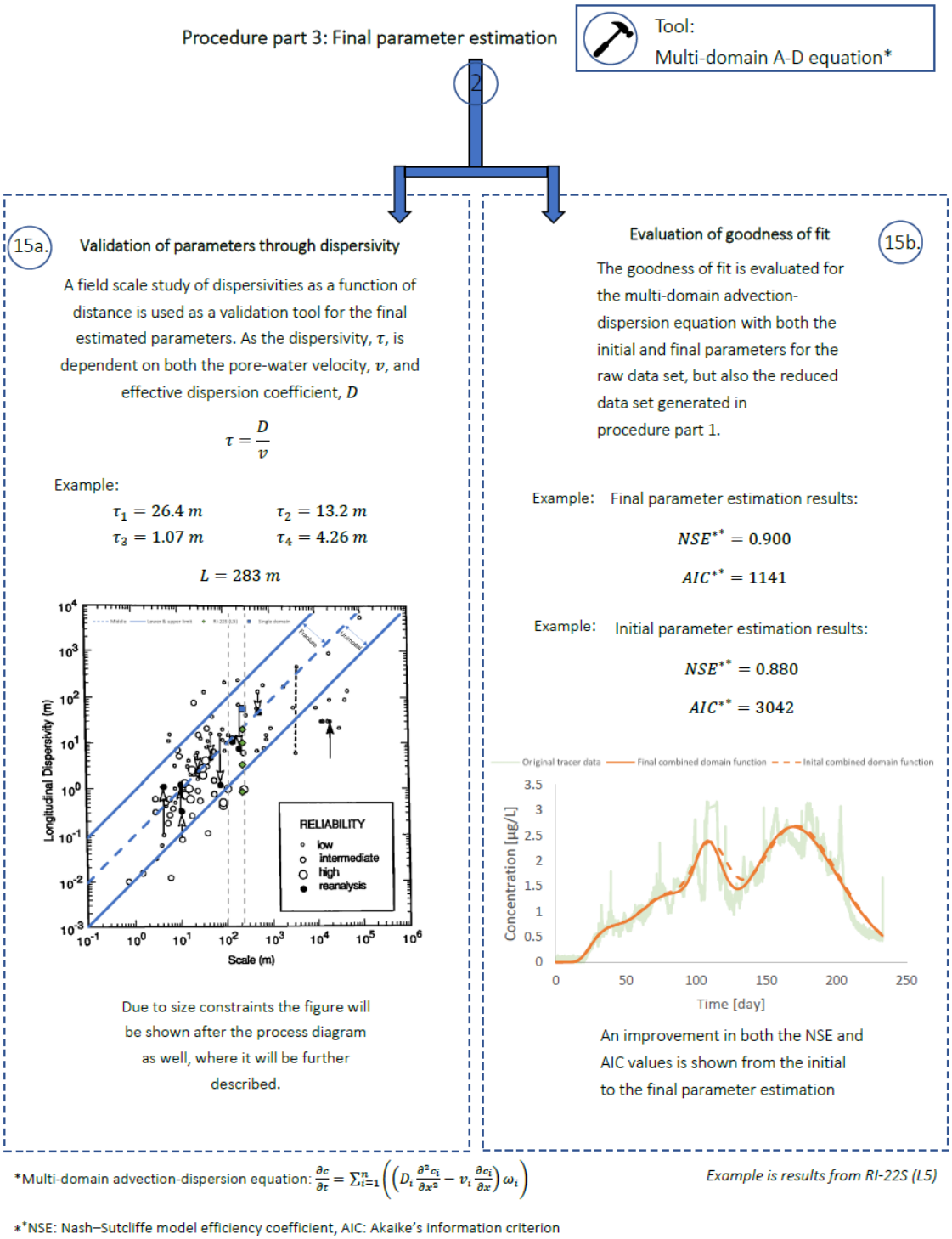

Figure 5.7: Process diagram for procedure part 3, final parameter estimation (2/2).

The validation tool from procedure part 3 is presented again in figure 5.8

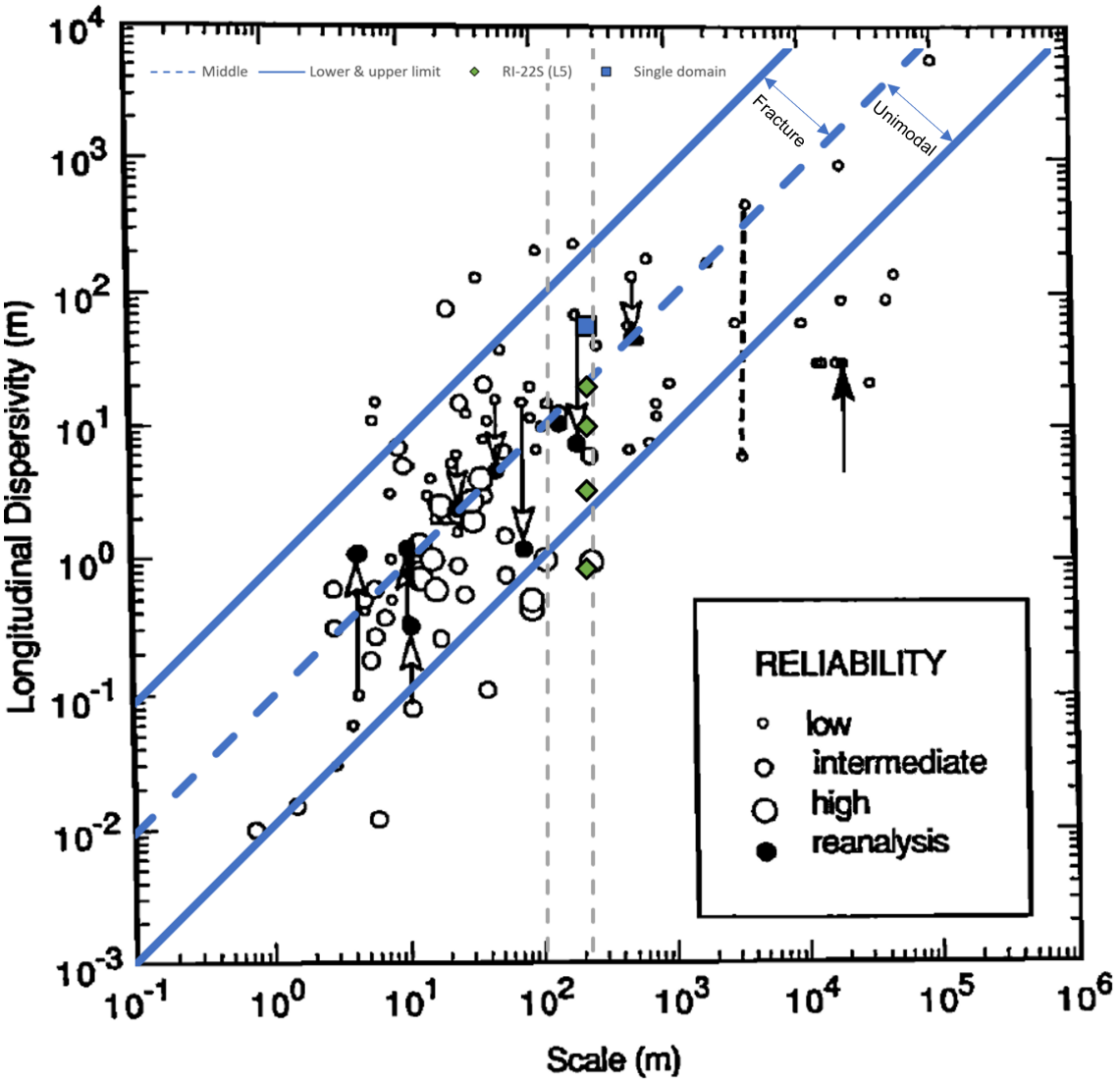

Figure 5.8: Longitudinal dispersivity as a function of distance from injection to detection well. Arrows indicate reported values at tails and corresponding values from reanalyses at heads. The dashed black line connects two dispersivity values determined at the same site. The solid and dashed blue lines indicate an expected interval when using a single-domain model. The expected interval is divided into two soil types fractured and unimodal. Results are from RI-22S (L5). Modified from [Gelhar and Collins, 1992].

The results show a high dispersivity value for the single-domain solution. The value is similar to the literature values for the fractured soil systems (upper end of the expected range), as was also expected. Lower values of dispersivity were found for the multi-domain solution. Three of the dispersivity values are in the lower end of the expected range, similar to the literature values for the porous media (unimodal) soil systems.
One dispersivity value was lower than the expected range. This is expected for this domain as it is domain 3, as shown by the results in the process diagram. This is because domain 3 is the rapid, occurring peak with little tailing after approximately 100 days; hence, low dispersivity was expected. Therefore, the results confirm the hypothesis of lower dispersivity values when increasing the number of domains, validating the FAST-MD procedure. A further discussion of the validation tool using all the results from the FAST-MD procedure will be conducted in chapter 8.

Summary

In this chapter, an overview of the FAST-MD procedure was presented through process diagrams. In figure 5.9 a summary of the procedure is shown.

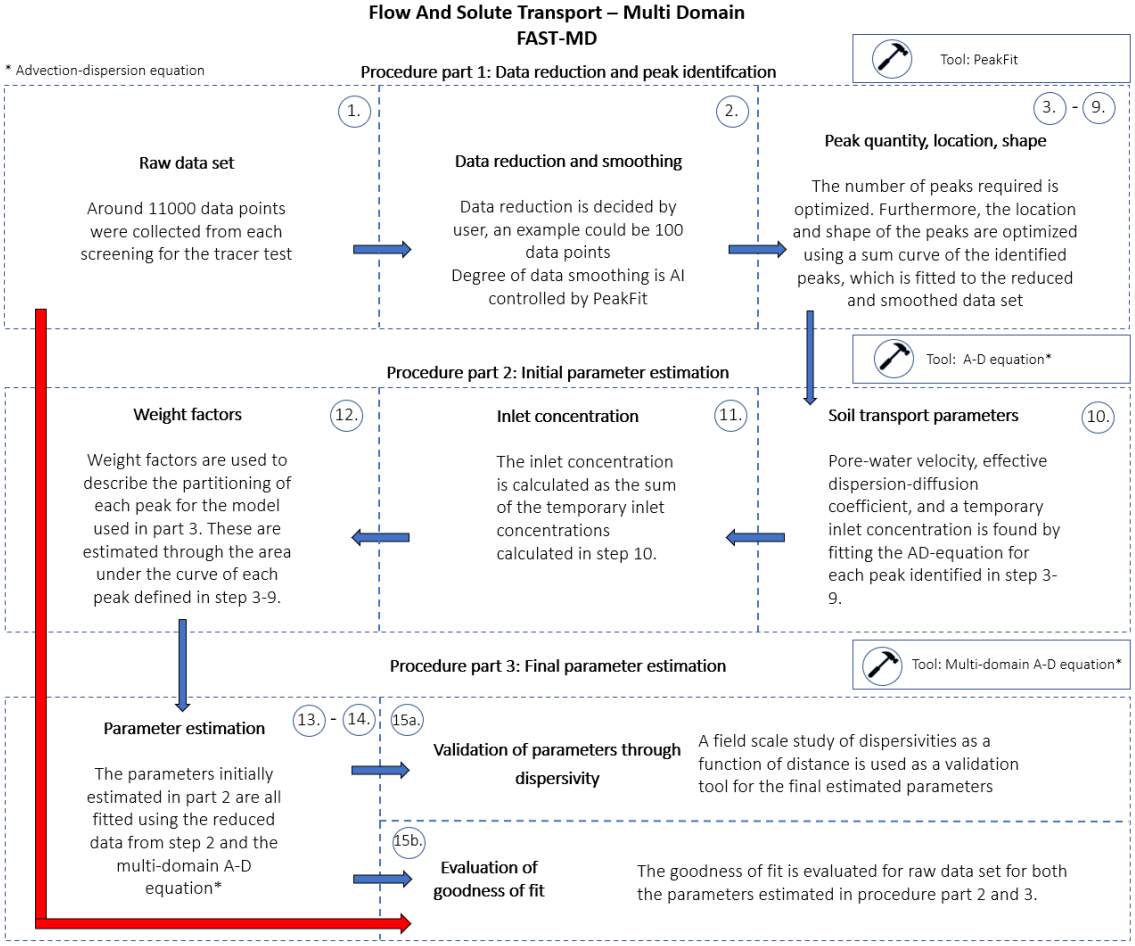

Figure 5.9: Summary of the FAST-MD procedure.

Using the FAST-MD procedure, an example of its usage on a dual-domain and multi-domain tracer data set will be conducted in the following chapter.

Analysis of Tracer Data with the FAST-MD Procedure

6

In this chapter, the FAST-MD procedure shown in chapter 5 will be shortly illustrated on a dual-domain and multi-domain tracer data set. The screenings used are RI-21S (L2) and RI-22I (L6) for the dual-domain and multi-domain tracer data set, respectively. An overview of the screening location of the dual and multi-domain tracer data sets are shown in figures 6.1 and 6.2.

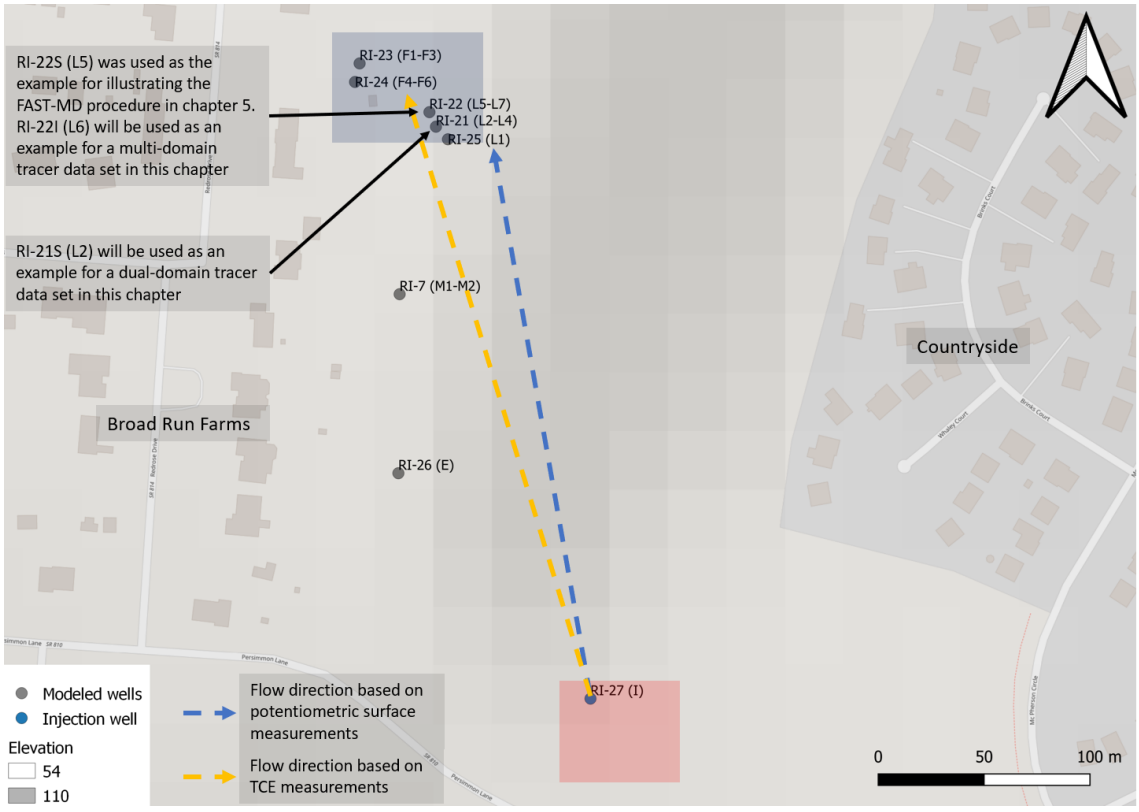

Figure 6.1: Aerial overview of the chosen screenings in relation to the injection well. The dashed gray line is a transect line used to develop figure 6.2. The location of the landfill is clearly indicated by the change in elevation.

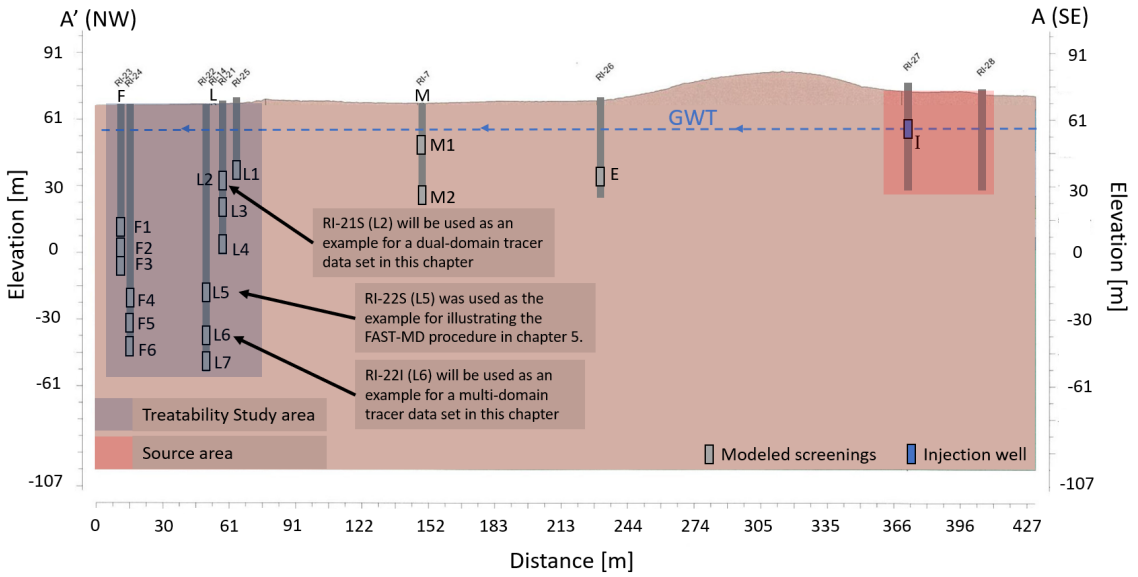

Figure 6.2: Cross-sectional profile showing the screenings location in relation to the injection well. The cross-sectional profile is based on the dashed gray transect line shown in figure 6.1.

6.1 Dual-domain Tracer Data Set

Screening RI-21S (L2) was chosen for the dual-domain tracer data set. The FAST-MD procedure was divided into three procedure parts. Procedure part 1 was data reduction and peak identification, and a short illustration of this procedure part will be shown in the following.

The raw tracer data set is shown in figure 6.3.

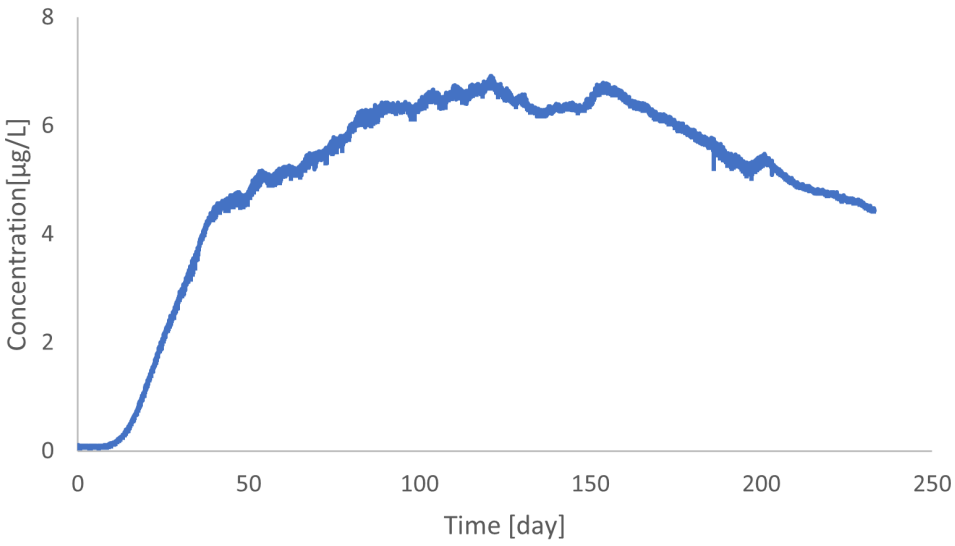

Figure 6.3: Raw tracer data for well RI-21S (L2).

As shown in the figure, the tracer is relatively simple. The fluctuation is very low compared to most of the tracer data collected. Furthermore, there are seemingly only 2-3 peaks in

the data set. The steep slope from around 20 to 50 days could be assessed as a peak. The concentration peaks around 125 and 150 days could also be considered one or two peaks.

The raw tracer data set was reduced to 100 data points and smoothed. The smoothing degree was 20.2%. The reduced and smoothed tracer data is shown in figure 6.4.

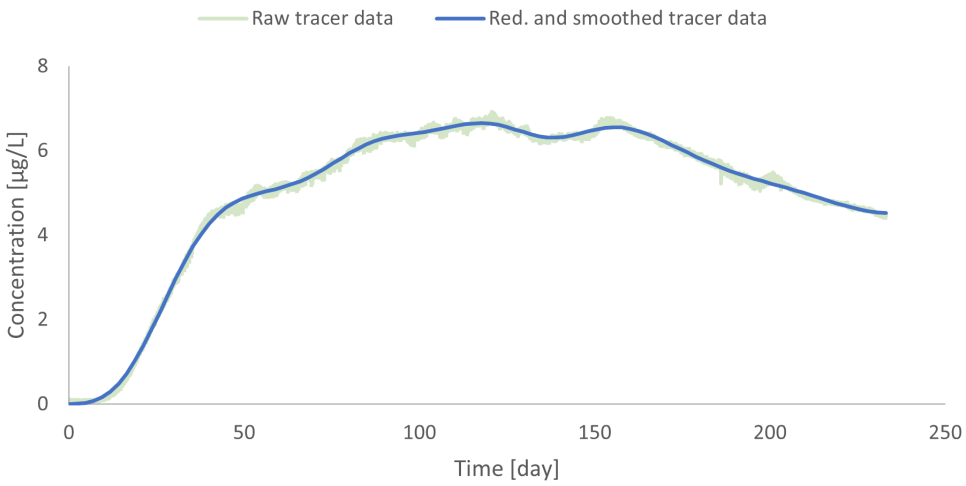

Figure 6.4: Raw and the reduced and smoothed tracer data, for well RI-21S (L2).

The reduced and smoothed tracer data is close to identical to the raw tracer data. This is due to the low fluctuation discussed earlier.

In procedure part 1, step 4 (Initial number of peaks estimation), 2 local maxima peaks and 1 residual peak were identified. At the end of procedure part 1, it was concluded that only 2 peaks were needed to describe the tracer data. The peaks and the sum curve generated by these peaks are shown in figure 6.5.

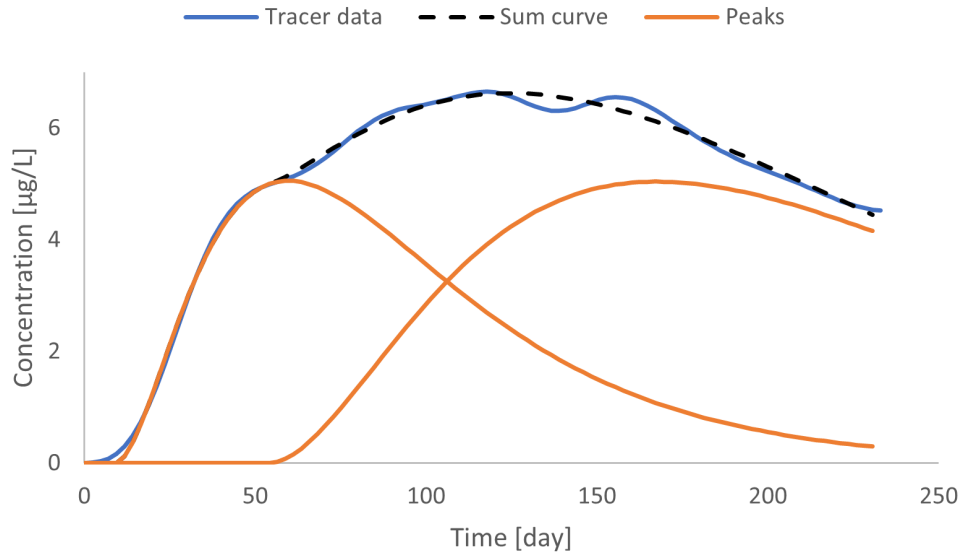

Figure 6.5: Results from procedure part 1 for well RI-21S (L2). The results included are the reduced and smoothed tracer data, the identified peaks, and the sum curve generated by the peaks.

The peaks identified are in good correlation with the assessment of the tracer data. The first peak describes the steep slope data from approximately 20-50 days, while the second peak describes the peak around 125-150 days.

Using the results from procedure part 1, the initial parameter estimation (procedure part 2) was conducted. The results are summarized at the end of this section, together with results from the final parameter estimation (procedure part 3).

The combined domain function using the final estimated parameters from procedure part 3 is shown with the reduced and smoothed tracer data and the raw tracer data in figure 6.6.

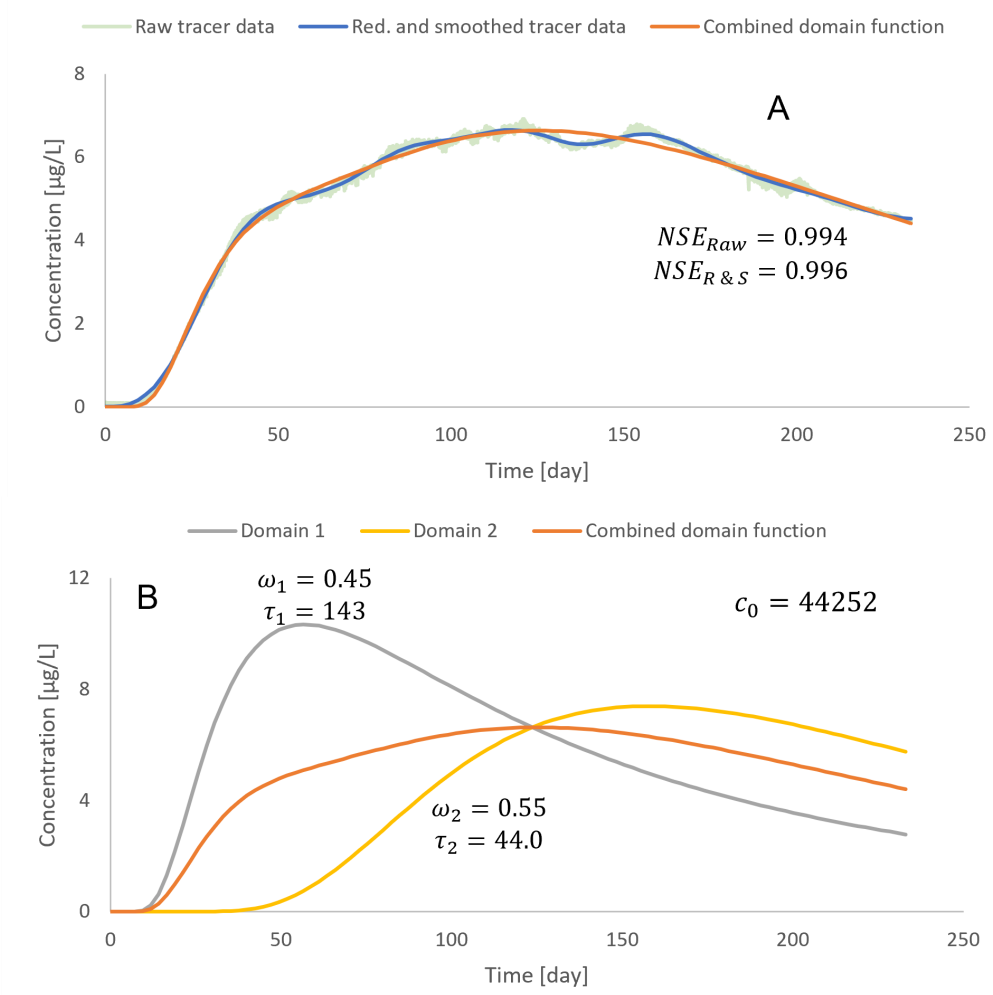

Figure 6.6: Results from the FAST-MD procedure. Figure part A shows the raw tracer data, reduced and smoothed tracer data, and combined domain function using the final parameter estimations. NSE values are between the combined domain function and the two tracer data sets. Figure part B shows the individual domains used for the combined domain function. Results are for screening RI-21S (L2). Dispersivity, τ, is in units m, the inlet concentration, c_0, is in units μg/L.

The combined domain function almost perfectly fits both the raw tracer data and the reduced and smoothed tracer data. The exception is the slight dip in concentration around 125 days. This is also reflected in the NSE values obtained using the estimated parameters. The geostatistical values are summarized in table 6.1.

The domain 1 function is the main contributor to the combined domain function from the start of the tracer test to around 125 days. During those 125 days, the slope of the tracer data changes multiple times. This is due to multiple flow domains contributing to tracer transport during this period, and these are mainly being described through one domain, domain 1. Furthermore, exchange between these flow domains also occurs. These processes are therefore causing a high dispersivity.

Table 6.1: Geostatistical results for the initial and final parameter estimation for the raw tracer data and the reduced and smoothed tracer data for RI-21 (L2).

	Initial parameter estimation	
	Raw tracer data	Reduced and smoothed tracer data
NSE [-]	0.984	0.986
AIC [-]	-1330	-11.3
	Final parameter estimation	
	Raw tracer data	Reduced and smoothed tracer data
NSE [-]	0.994	0.996
AIC [-]	-12374	-133

The overall fit is good when comparing the NSE values for both the initial and final parameter estimations with both tracer data sets. The worst fit is the initial parameters fitted to the raw tracer data. The best fit is the final parameters fitted to the reduced and smoothed tracer data, which is expected. The AIC values can only be compared between identical data sets as the value is a relative measure [Nielsen et al., 2018]. The AIC value is more negative for the final parameters than the initial, meaning a better fit using the final parameter estimation even though more model parameters are used.

The initial and final parameter estimations are shown in table 6.2.

Table 6.2: Initial and final parameter estimations for screening RI-21S (L2). A * indicates that the value is valid for all domains.

	Initial parameter estimation	
Domains	1	2
v [m/d]	2.76	1.12
D [m^2/d]	156	41.6
τ [m]	56.4	37.0
ω [-]	0.33	0.67
c_0 [μg/L]	41341*	
	Final parameter estimation	
Domains	1	2
v [m/d]	1.43	1.11
D [m^2/d]	204	48.6
τ [m]	143	44.0
ω [-]	0.47	0.53
c_0 [μg/L]	44252*	

The parameters for the initial and final parameter estimation are somewhat similar. The most significant change is the pore-water velocity and the effective dispersion coefficient, which increases the dispersivity for domain 1.

The dispersivities obtained from the parameter estimation for RI-21S (L2) are shown in the validation tool introduced in chapter 4 are shown in figure 6.12.

6.2 Multi-domain Tracer Data Set

For the multi-domain tracer data set well, RI-22I (L6) was chosen. The raw tracer data set is shown in figure 6.7.

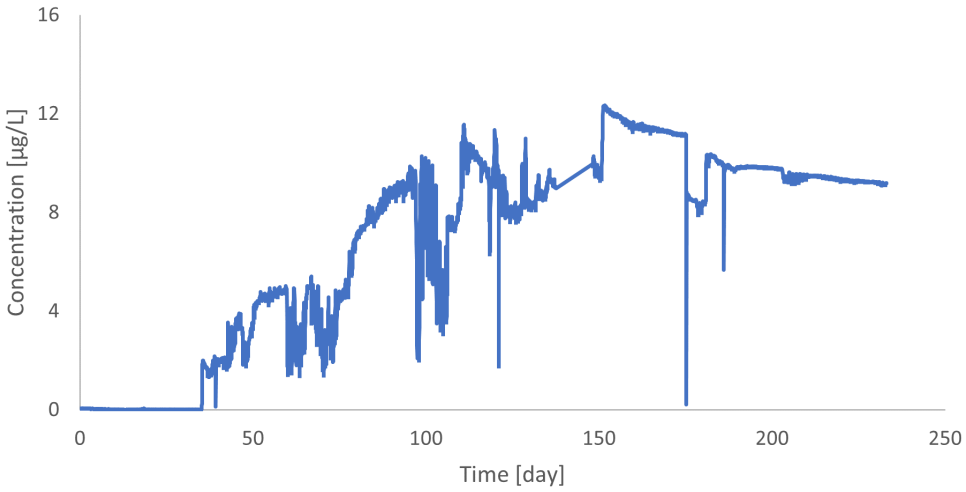

Figure 6.7: Raw tracer data set for well RI-22I (L6).

The tracer data show significant fluctuation, some of which are clearly measurement errors. It is difficult to clearly describe the tracer data in terms of identifying peaks or tendencies in sloops hence the data set being chosen as the multi-domain data set. Data treatment is, therefore, especially important for multi-domain data sets.

The raw tracer data set was reduced to 100 data points and smoothed. The smoothing degree was 20.2%. The reduced and smoothed tracer data is shown in figure 6.8.

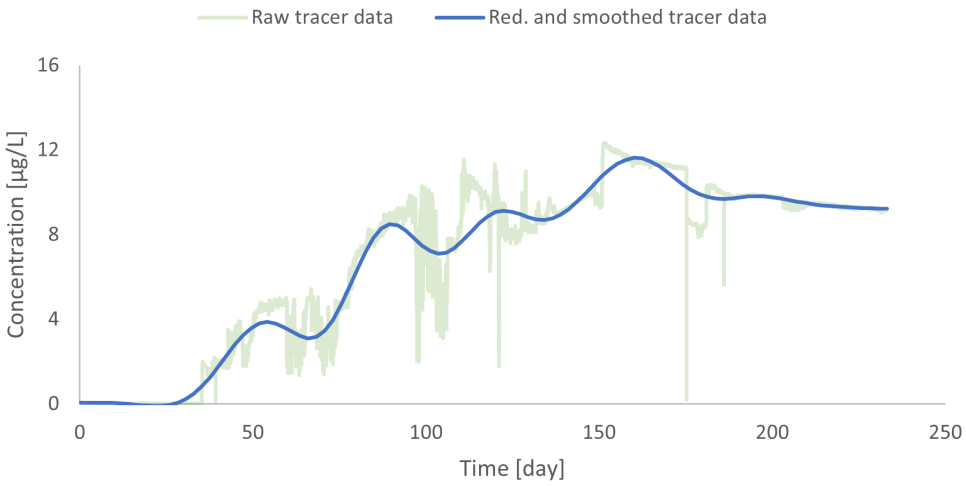

Figure 6.8: Raw and the reduced and smoothed tracer data for well RI-22I (L6).

The tracer data after reduction and smoothing is significantly altered. A much clearer tendency in the tracer data is shown. A fairly steady increase in concentration is shown throughout the tracer test until the concentration reaches its highest at around 160 days. Then the concentration stabilizes into a somewhat constant value. During the steady increase, 4 somewhat clear peaks are seen.

In procedure part 1, step 4 (initial number of peaks estimation), 5 local maxima peaks and 4 residual peaks were identified. At the end of procedure part 1, it was concluded that only 5 peaks were needed to describe the tracer data. The peaks and the sum curve generated by these peaks are shown in figure 6.9.

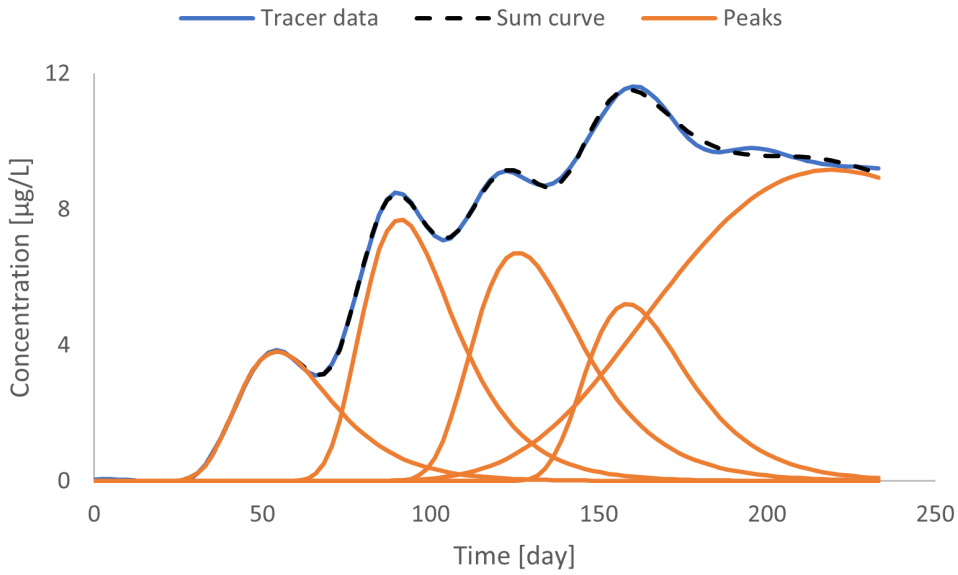

Figure 6.9: Results from procedure part 1 for well RI-22I (L6). The results included are the reduced and smoothed tracer data, the optimized peaks, and the sum curve generated by the peaks.

The 4 peaks in the reduced and smoothed tracer data are represented by one peak each. Furthermore, the final peak represents the somewhat constant concentration at the end of the tracer test.

Using the results from procedure part 1, the initial parameter estimation (procedure part 2) was conducted. The results are summarized at the end of this section, together with results from the final parameter estimation (procedure part 3).

The combined domain function using the final estimated parameters from procedure part 3 is shown with the reduced and smoothed tracer data and the raw tracer data in figure 6.10.

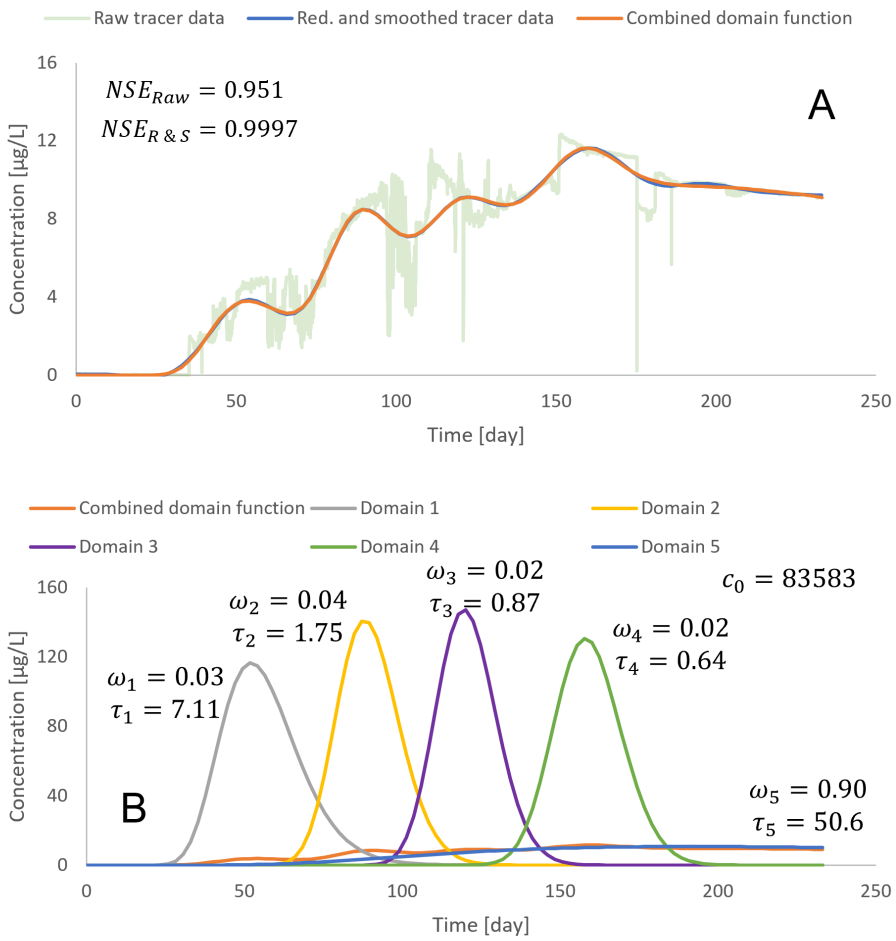

Figure 6.10: Results from the FAST-MD procedure. Figure part A shows the raw tracer data, reduced and smoothed tracer data, and combined domain function using the final parameter estimations. NSE values are between the combined domain function and the two tracer data sets. Figure part B shows the individual domains used for the combined domain function. Results are for screening RI-22I (L6). Dispersivity, τ, is in units m, the inlet concentration, c_0, is in units μg/L.

The combined domain function is close to identical to the reduced and smoothed tracer data, indicating a nearly perfect fit, which is also shown in the NSE value obtained between them. The fit between the combined domain function and the raw tracer data is less good due to the significant fluctuations. The geostatistical values are summarized in table 6.3.

The first four domains have very similar tendencies; they describe a rapid increase and decrease in concentration. This is also reflected in the shape of the peaks having slight tailing and dispersivity values ranging from 0.6-7 m. The contribution of these peaks to the overall tracer mass recovered is low and is also reflected in their combined weight factors being 0.1. The last domain describes the stabilizing concentration starting from around day 180 and lasting until the tracer test is ended. This is the highest contributing domain with a weight factor of 0.9.

Table 6.3: Geostatistical results for the initial and final parameter estimation for the raw tracer data and the reduced and smoothed tracer data.

	Initial parameter estimation	
	Raw tracer data	Reduced and smoothed tracer data
NSE [-]	0.936	0.988
AIC [-]	30348	137
	Final parameter estimation	
	Raw tracer data	Reduced and smoothed tracer data
NSE [-]	0.951	0.9997
AIC [-]	27517	-236

The geostatistical parameters for the multi-domain tracer data set show the same tendencies as the dual-domain tracer data set.

The initial and final parameter estimations are shown in table 6.4.

Table 6.4: Initial and final parameter estimations for well RI-22I (L6). A * indicates that the value is valid for all domains.

	Initial parameter estimation				
Domains	1	2	3	4	5
v [m/d]	4.53	2.87	2.14	1.73	1.17
D [m^2/d]	44.6	9.66	5.19	2.31	11.1
τ [m]	9.85	3.36	2.42	1.34	9.49
ω [-]	0.061	0.12	0.12	0.087	0.61
c_0 [μg/L]	57036*				
	Final parameter estimation				
Domains	1	2	3	4	5
v [m/d]	4.93	3.09	2.34	1.78	0.88
D [m^2/d]	34.2	5.27	1.13	1.13	44.8
τ [m]	6.95	1.71	0.87	0.64	50.8
ω [-]	0.030	0.036	0.015	0.019	0.90
c_0 [μg/L]	83583*				

The pore-water velocities and effective dispersion coefficient values indicate relatively rapid occurring peaks with little spreading, which was also expected when looking at the reduced and smoothed tracer data. The most notable change between the initial parameter estimation and the final parameter estimation is the change in inlet concentration with an increase of approximately 26 000 μg/L. The high concentration at the end of the tracer test is causing this change in inlet concentration. By having a high concentration at the end of the tracer test, the models are left "guessing" how the remainder of the tracer test develops. This is illustrated in figure 6.11 where domain 5 is plotted prior to and post the sampling period for the tracer test, for both the initial and final parameter estimations.

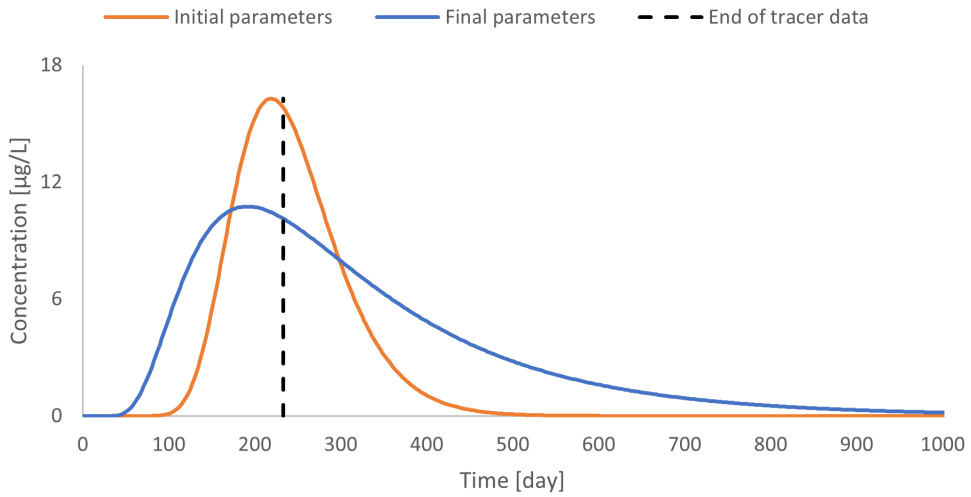

Figure 6.11: Domain 5 for the initial and final parameter sets prior to and post the end of the tracer test.

The final parameter estimation predicts a more spread domain 5 with a slower decline in concentration from the tracer over time, which is also reflected in the increase in the effective dispersion coefficient compared to its initial estimated counterpart. This is also why the weight factor was lowered for the remainder of the domains in the final parameter estimation, as a sort of counter-reaction to the increase in inlet concentration, so that the change for these domains was not as significant.

An analysis of slope tendencies at the end of the raw tracer data could be used to try and predict which parameter estimation is more likely. However, due to how fluctuating the tracer data is, it could be argued that such an analysis does not bring any meaningful insight. It could also be argued that the general tendency in slower-moving flow domains is that the dominating transport process is dispersion meaning the final parameter estimation may be a more accurate representation [Field, 2020]. Overall, the estimated parameters for the first 4 domains are likely an accurate representation of the solute transport process the tracer went through. Still, domain 5 is more uncertain; however, the final parameter estimation may be the more accurate approximation based on typical solute transport behavior in fractured systems.

The dispersivities obtained from the parameter estimation for RI-22I (L6) are shown in the validation tool introduced in chapter 4 are shown in figure 6.12.

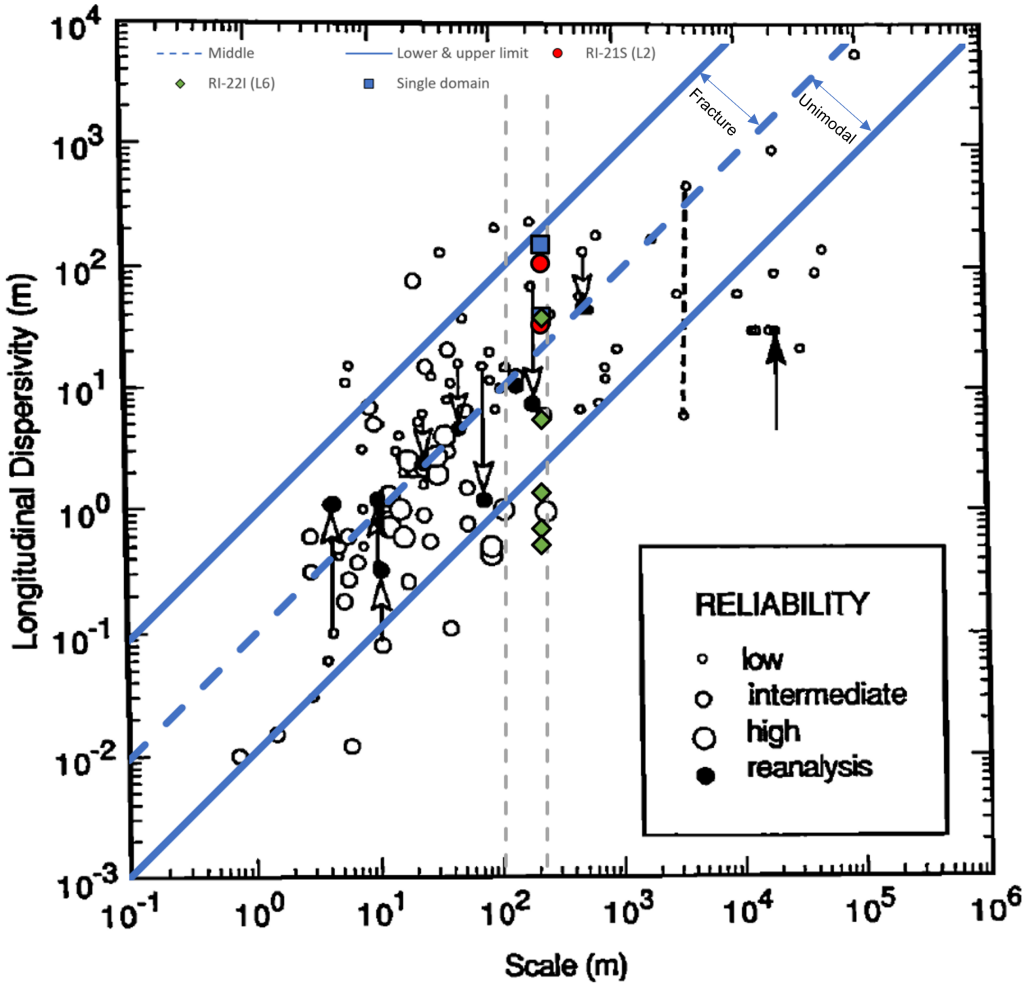

Figure 6.12: Longitudinal dispersivity as a function of distance from injection to detection well. Arrows indicate reported values at tails and corresponding values from reanalyses at heads. The dashed black line connects two dispersivity values determined at the same site; the dashed gray line is the minimum and maximum scale for the screenings used for further analysis at the HLLSS. The solid and dashed blue lines indicate an expected interval when using a single-domain model. The expected interval is divided into two soil types fractured and unimodal. Results are from RI-21S (L2) and RI-22I (L6). The blue squares show the results for the two investigated tracers in this chapter using a single-domain solution, the upper being RI-21S (L2) and the lower being RI-22I (L6). Modified from [Gelhar and Collins, 1992].

The dispersivity values for domain 1 and 2 for RI-21S (L2) is slightly lower than the dispersivity value when using the single-domain solution but still within literature values for fractured media using a single-domain model. Only two domains were used, and therefore a somewhat high amount of spreading was expected for the domains. For RI-22I (L6), three of the five dispersivity values are lower than the expected range of dispersivity values. This was also expected due to the peaks described by these domains being quite abrupt, indicating dominant fracture transport with little spreading.

For the single-domain solution the dispersivity is within the expected range for fractured media dispersivity, when using a single-domain solution. Overall the estimated dispersivities confirm the hypothesis of an increase in domains leading to a decrease in dispersivity, validating the FAST-MD procedure. A further discussion of the validation tool using all the results from the FAST-MD procedure will be conducted in chapter 8.

Overview of Tracer Data Results with the FAST-MD Procedure

7

This chapter shows a brief overview of the results from the FAST-MD procedure for each of the modeled screenings. An overview of the location of the monitoring wells and their screenings are shown in figure 7.1 and 7.2

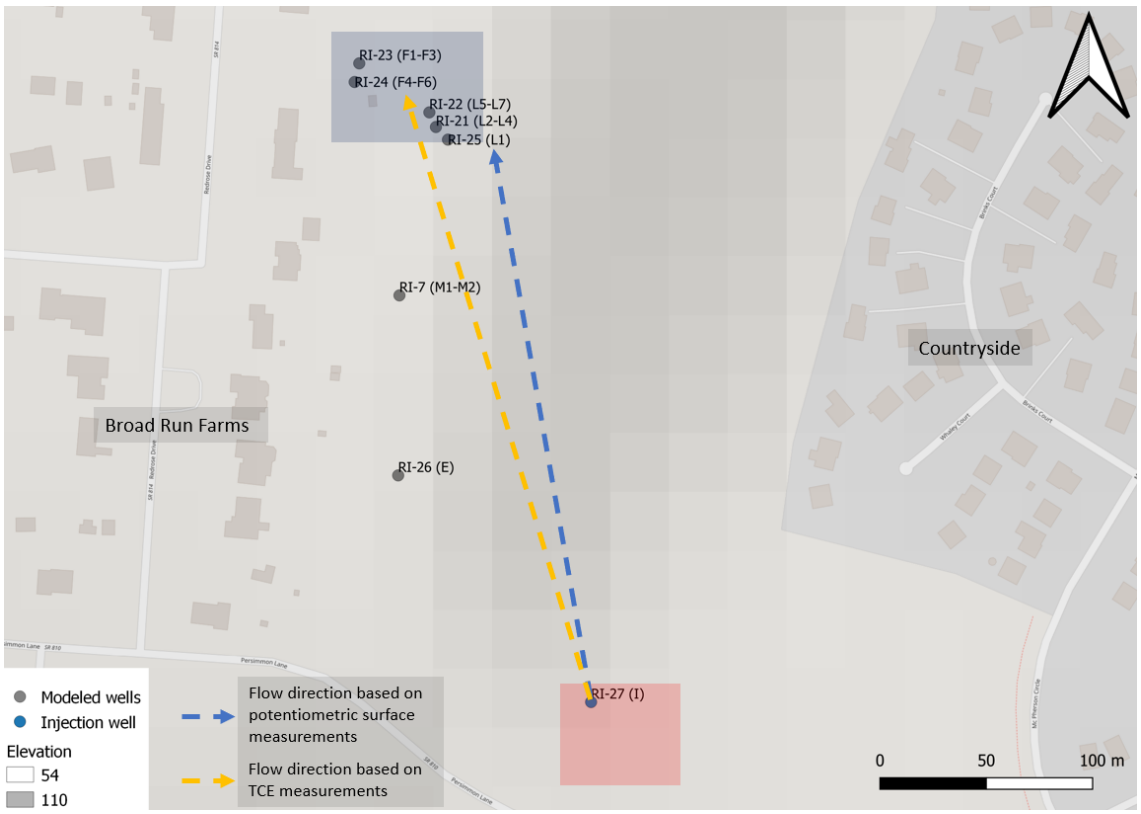

Figure 7.1: Aerial overview of the modeled wells in relation to the injection well. The dashed gray line is a transect line used to develop figure 7.2. The location of the landfill is clearly indicated by the change in elevation.

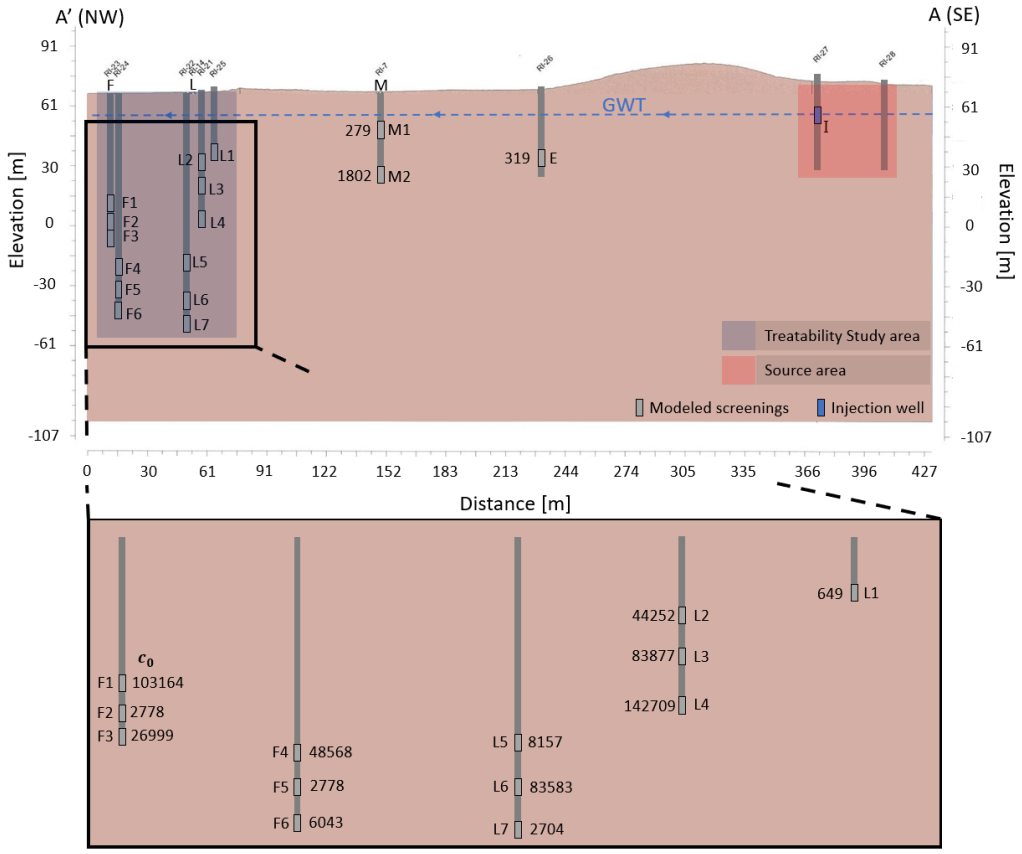

Figure 7.2: Cross-sectional overview of the modeled screenings. The parameter shown at the screenings is the inlet concentration, estimated by the FAST-MD procedure with units [μg/L]. The cross-sectional profile is based on the dashed gray transect line shown in figure 7.1.

The inlet concentration is higher within the Treatability Study area, as indicated in chapter 3 based on the tracer recovery assessments. A tendency is also that the inlet concentration is high for most of the shallow screenings within the Treatability Study area (L2-L4, F1, and F3). A further discussion of tracer distribution is conducted in chapter 8.

RI-26I (E)

In figures 7.3 the combined domain function is shown with the raw tracer data set and the reduced and smoothed tracer data set. Furthermore, the individual domains used for the combined domain function are shown.

Two domains were identified for fitting the data set. Domain 1 describes the peak after 75 days, and domain 2 describes the peak at around 175 days. The peak at 75 days in the raw data set occurred and disappeared rapidly, but the amount of mass recovered was large enough that the reduction and smoothing algorithm included it. The weight factor for this domain was 0.08, indicating that its overall contribution is quite limited. The shape of the peak indicates little spreading, which is also shown by the obtained dispersivity value.

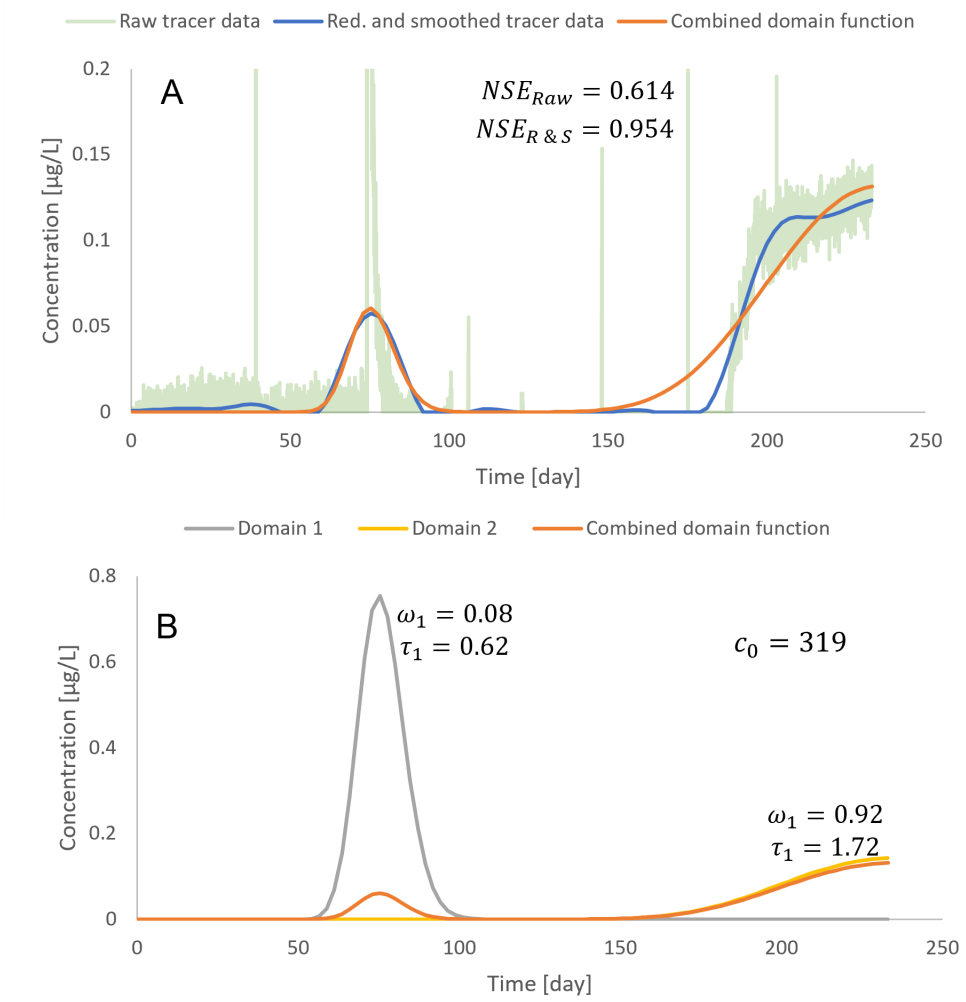

Figure 7.3: Results from the FAST-MD procedure. Figure part A shows the raw tracer data, reduced and smoothed tracer data, and combined domain function using the final parameter estimations. NSE values are between the combined domain function and the two tracer data sets. Figure part B shows the individual domains used for the combined domain function. Results are for screening RI-26I (E). Dispersivity, τ, is in units m, the inlet concentration, c_0, is in units μg/L. An aerial and cross-sectional overview of the screening location is shown in figures 7.1 and 7.2.

The fit between the raw tracer data and the combined domain function is the lowest of all the modeled results. This is caused by the amount of fluctuation seen in the raw tracer data, which is probably caused by measurement uncertainty due to the low concentrations, also indicated by the low inlet concentration of 319 μg/L. The overall fit is still considered good, considering the fit between the reduced and smoothed tracer data and the combined domain function being 0.95.

RI-7S (M1)

In figures 7.4 the combined domain function is shown with the raw tracer data set and the reduced and smoothed tracer data set. Furthermore, the individual domains used for the combined domain function are shown.

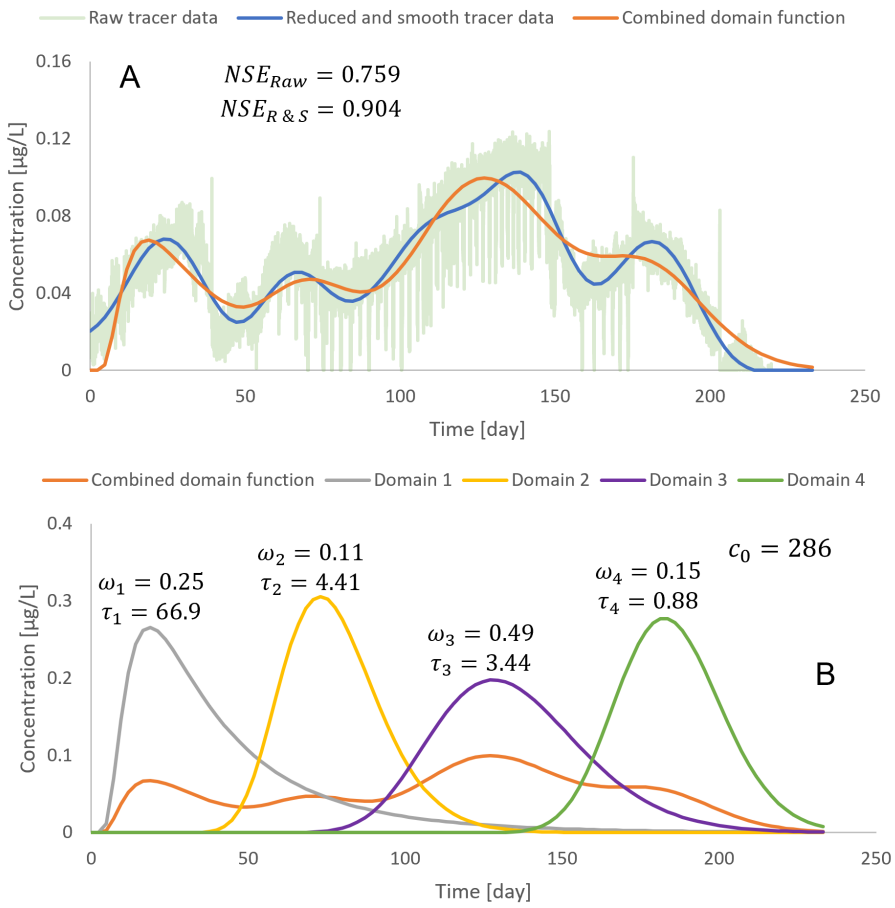

Figure 7.4: Results from the FAST-MD procedure. Figure part A shows the raw tracer data, reduced and smoothed tracer data, and combined domain function using the final parameter estimations. NSE values are between the combined domain function and the two tracer data sets. Figure part B shows the individual domains used for the combined domain function. Results are for screening RI-7S (M1). Dispersivity, τ, is in units m, the inlet concentration, c_0, is in units μg/L. An aerial and cross-sectional overview of the screening location is shown in figures 7.1 and 7.2.

After data reduction and smoothing of the raw tracer data, four peaks were identified, described by a domain each. The raw tracer data shows high fluctuation, presumably due to the low recovery similar to RI-26I (E), also indicated by the low inlet concentration of 286 μg/L. The fit between the reduced and smoothed tracer data and the combined domain function is the lowest of all the modeled results. This is due to the rapid occurrence and disappearance of peaks, which is more difficult for the combined domain function to fit due to the occurrence of tailing from spreading when using the advection-dispersion equation. This is also reflected in the low dispersivity values except for domain 1, which exhibits tailing. The fit is still fairly high though having an NSE of 0.90. Domain 3 is the main contributor to the combined domain function with a weight factor of 0.49, which is also expected based on the high concentration over a long period of time relative to the other peaks in the tracer data.

RI-7D (M2)

In figures 7.5 the combined domain function is shown with the raw tracer data set and the reduced and smoothed tracer data set. Furthermore, the individual domains used for the combined domain function are shown.

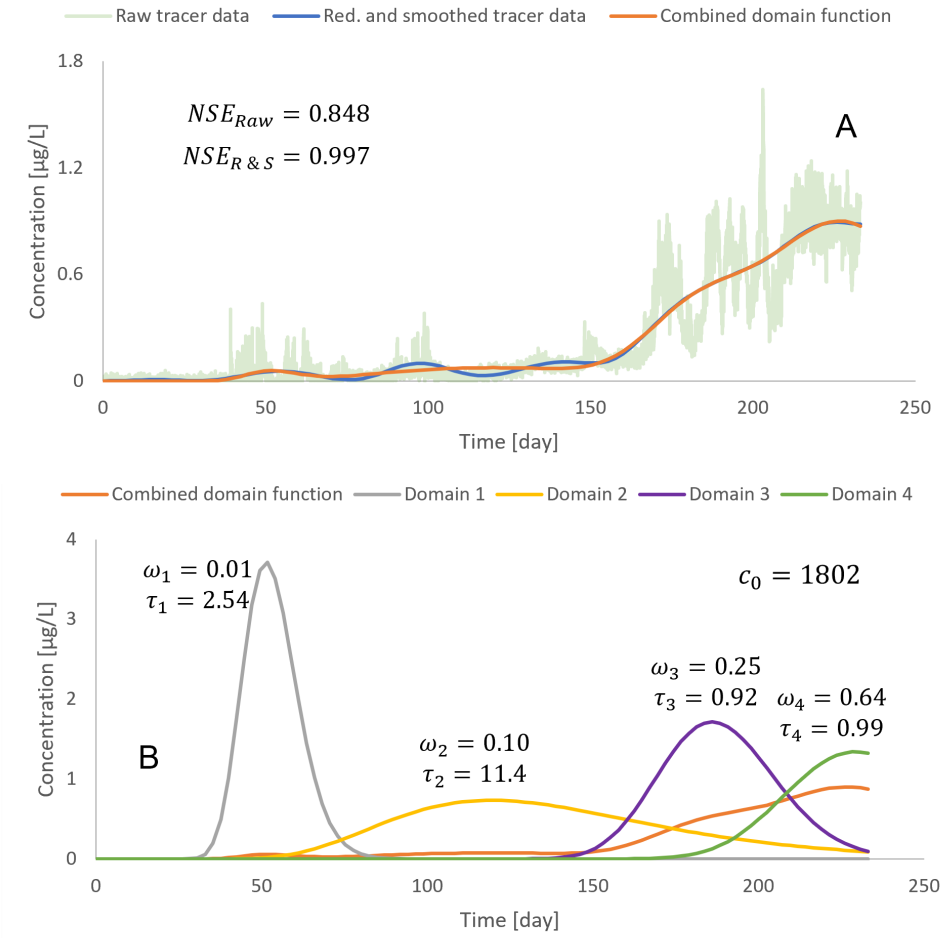

Figure 7.5: Results from the FAST-MD procedure. Figure part A shows the raw tracer data, reduced and smoothed tracer data, and combined domain function using the final parameter estimations. NSE values are between the combined domain function and the two tracer data sets. Figure part B shows the individual domains used for the combined domain function. Results are for screening RI-7D (M2). Dispersivity, τ, is in units m, the inlet concentration, c_0, is in units μg/L. An aerial and cross-sectional overview of the screening location is shown in figures 7.1 and 7.2.

Small concentration peaks were identified around 50 and 100 days when the raw data was reduced and smoothed. These fairly small mass recoveries were enough for PeakFit to identify them as local maxima peaks, and therefore a domain is used to describe each of them. The combined weight factors for the two first domains were 0.11, which is expected due to the low mass recoveries. Domain 1 has an almost normal distribution shape, with very little tailing, which is also reflected in the low dispersivity value of 2.54 m. After 150 days, two domains were used to describe the remainder of the tracer data divided by the change in slope seen at around day 200.

The main contributor to the combined domain function is domain 4, with a weight factor

of 0.64. This is reflected in the highest concentrations measured for the screening at the end of the tracer test. The model predicts that a significant amount of tracer would have been recovered after the tracer test relative to the amount already recovered. The fit between the combined domain function and the reduced and smoothed data is nearly perfect, with an NSE value of 0.997. The fit for the raw tracer data is less good, caused by low concentration fluctuations similar to the previously evaluated screenings.

RI-25D (L1)

For RI-25D (L1), only one peak was identified in procedure part 1 of the FAST-MD procedure, meaning the multi-domain model was not required for this tracer data set. Instead, the single domain model, introduced in chapter 4 equations (4.14) and (4.15) is used. In figure 7.6 the results are shown.

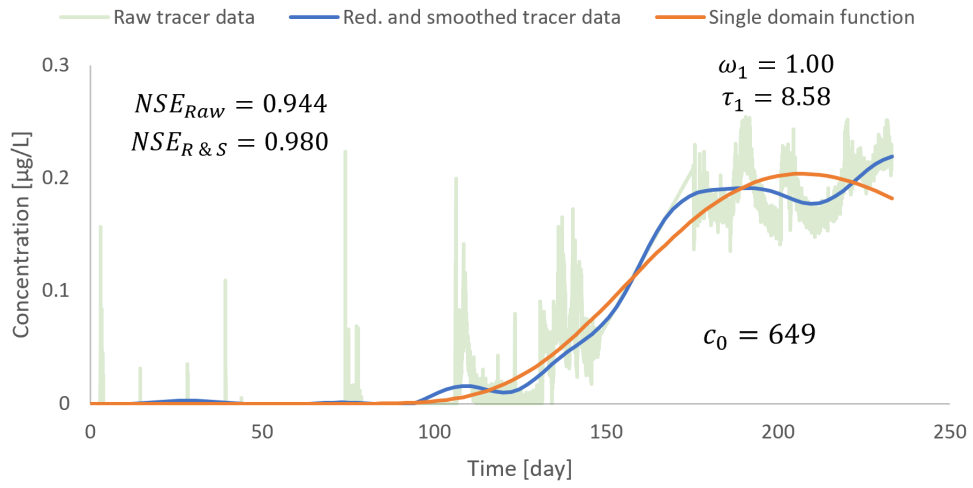

Figure 7.6: Results from the FAST-MD procedure. Figure part A shows the raw tracer data, reduced and smoothed tracer data, and combined domain function using the final parameter estimations. NSE values are between the combined domain function and the two tracer data sets. Figure part B shows the individual domains used for the combined domain function. Results are for screening RI-25D (L1). Dispersivity, τ, is in units m, the inlet concentration, c_0, is in units μg/L. An aerial and cross-sectional overview of the screening location is shown in figures 7.1 and 7.2.

Small concentration peaks occurred within the first 100 days of the tracer test. However, they were not enough for PeakFit to identify as an individual domain. Only one domain was needed to describe the tracer data as the few changes in slope were over short periods and therefore did not warrant an individual domain. This is also reflected in the NSE values for both tracer data, which are high.

RI-21S (L2)

In figures 7.7 the combined domain function is shown with the raw tracer data set and the reduced and smoothed tracer data set. Furthermore, the individual domains used for the combined domain function are shown.

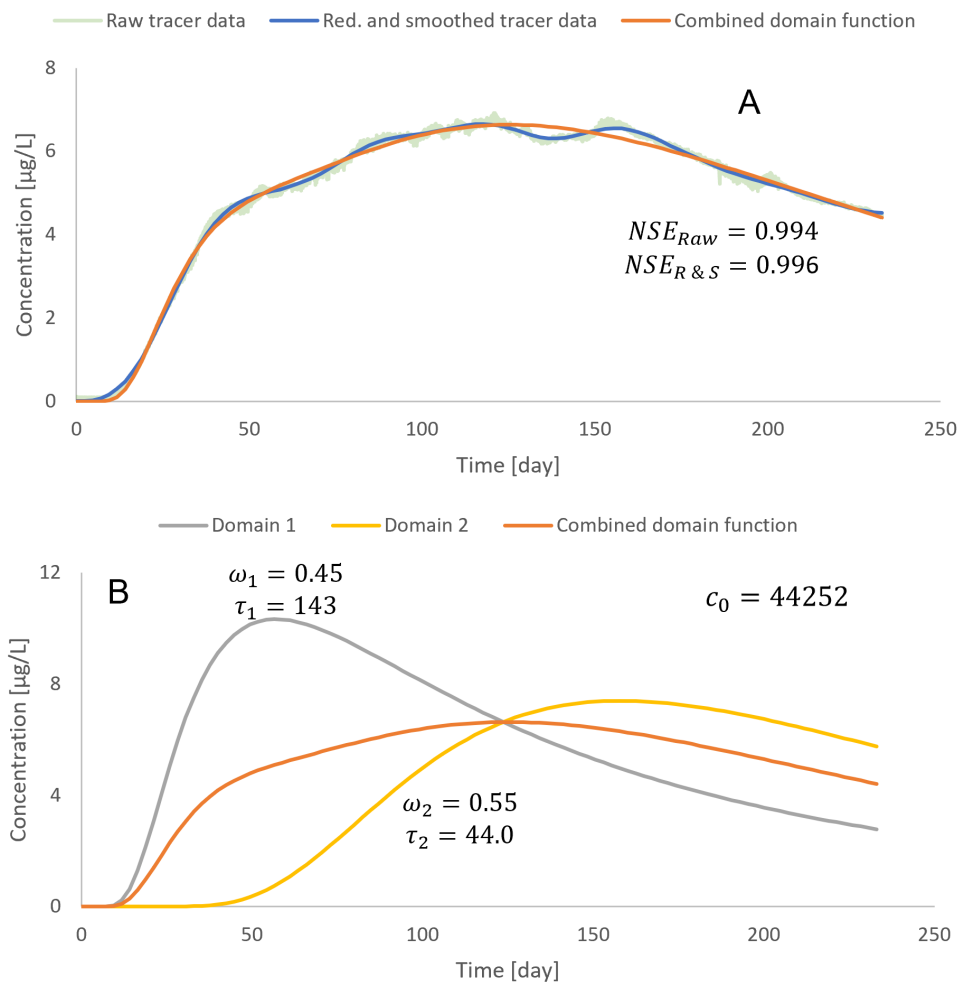

Figure 7.7: Results from the FAST-MD procedure. Figure part A shows the raw tracer data, reduced and smoothed tracer data, and combined domain function using the final parameter estimations. NSE values are between the combined domain function and the two tracer data sets. Figure part B shows the individual domains used for the combined domain function. Results are for screening RI-21S (L2). Dispersivity, τ, is in units m, the inlet concentration, c_0, is in units μg/L. An aerial and cross-sectional overview of the screening location is shown in figures 7.1 and 7.2.

The combined domain function fits both tracer data sets almost perfectly; the only real deviance is seen in the slight dip after approximately 125 days. Two domains were used to describe the tracer data; one for the initial steep slope and then a combination of both domains to describe the remainder of the tracer data. The distribution of the weighting of the domains is almost equal. A more detailed analysis of this screening is conducted in chapter 6, as an example of the FAST-MD procedure used for a dual-domain tracer data set.

RI-21I (L3)

In figures 7.8 the combined domain function is shown with the raw tracer data set and the reduced and smoothed tracer data set. Furthermore, the individual domains used for the combined domain function are shown.

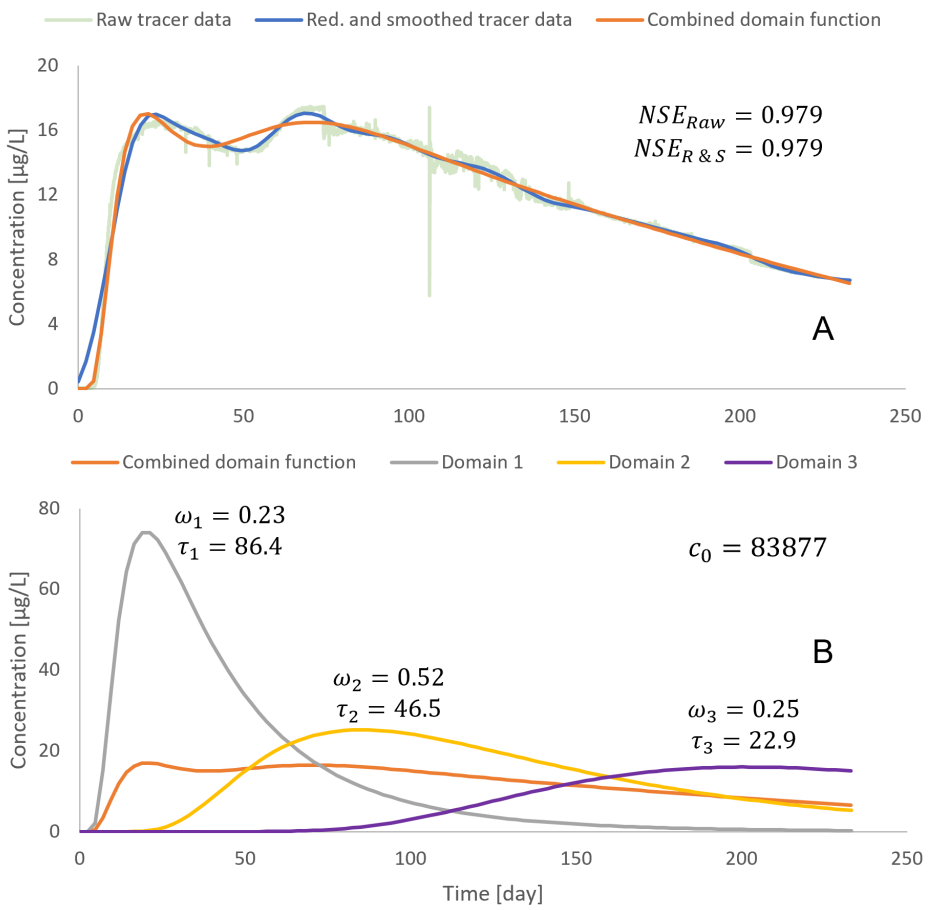

Figure 7.8: Results from the FAST-MD procedure. Figure part A shows the raw tracer data, reduced and smoothed tracer data, and combined domain function using the final parameter estimations. NSE values are between the combined domain function and the two tracer data sets. Figure part B shows the individual domains used for the combined domain function. Results are for screening RI-21I (L3). Dispersivity, τ, is in units m, the inlet concentration, c_0, is in units μg/L. An aerial and cross-sectional overview of the screening location is shown in figures 7.1 and 7.2.

The combined domain function describes the tracer data well. Slight deviations are seen at the beginning of the first peak and during the dip around 50 days. The first domain mainly describes the first peak at around day 25; the second domain describes the second peak after the dip. The remainder of the tracer data is described through domains 2 and 3.

RI-21D

In figures 7.9 the combined domain function is shown with the raw tracer data set and the reduced and smoothed tracer data set. Furthermore, the individual domains used for the combined domain function are shown.

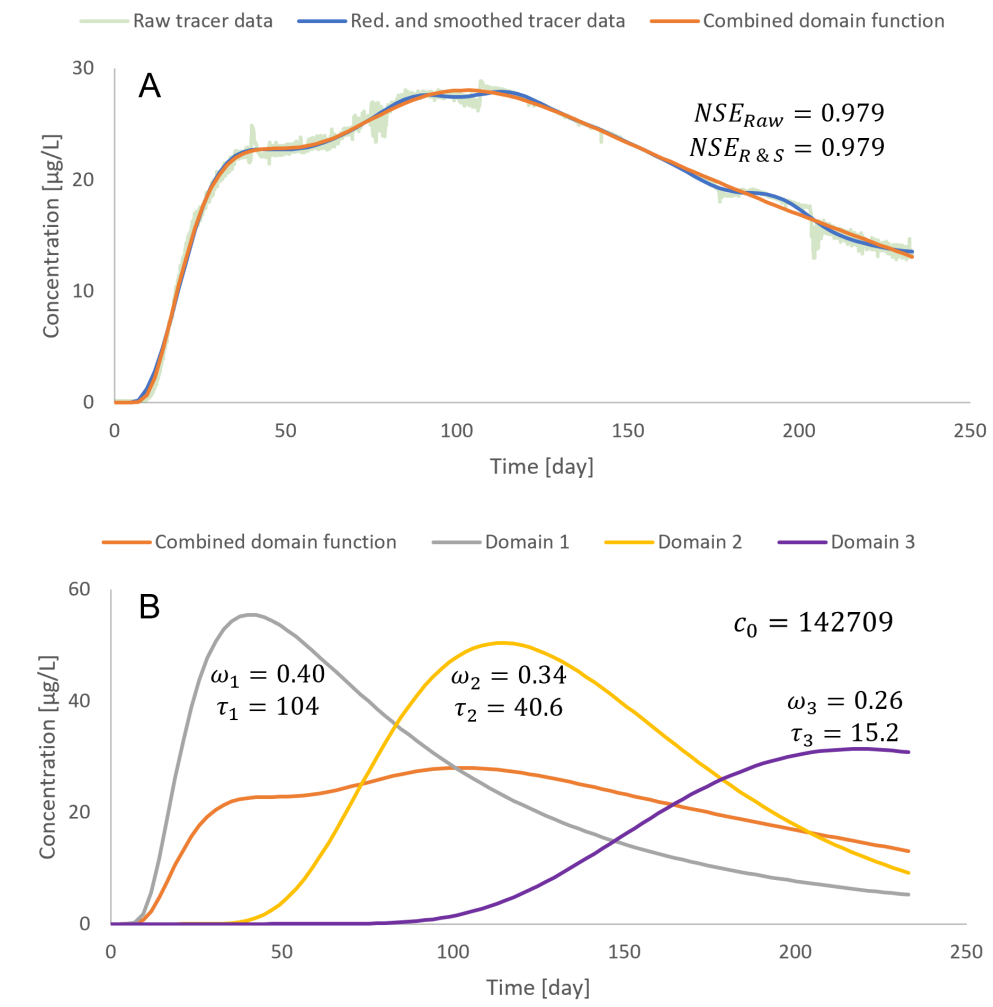

Figure 7.9: Results from the FAST-MD procedure. Figure part A shows the raw tracer data, reduced and smoothed tracer data, and combined domain function using the final parameter estimations. NSE values are between the combined domain function and the two tracer data sets. Figure part B shows the individual domains used for the combined domain function. Results are for screening RI-21D (L4). Dispersivity, τ, is in units m, the inlet concentration, c_0, is in units μg/L. An aerial and cross-sectional overview of the screening location is shown in figures 7.1 and 7.2.

The tracer data and results for RI-21D (L6) are similar to the results of RI-21I. The concentrations for this tracer data are the highest, which is also reflected in the highest inlet concentration at 142 709 μg/L.

RI-22S

In figures 7.10 the combined domain function is shown with the raw tracer data set and the reduced and smoothed tracer data set. Furthermore, the individual domains used for the combined domain function are shown.

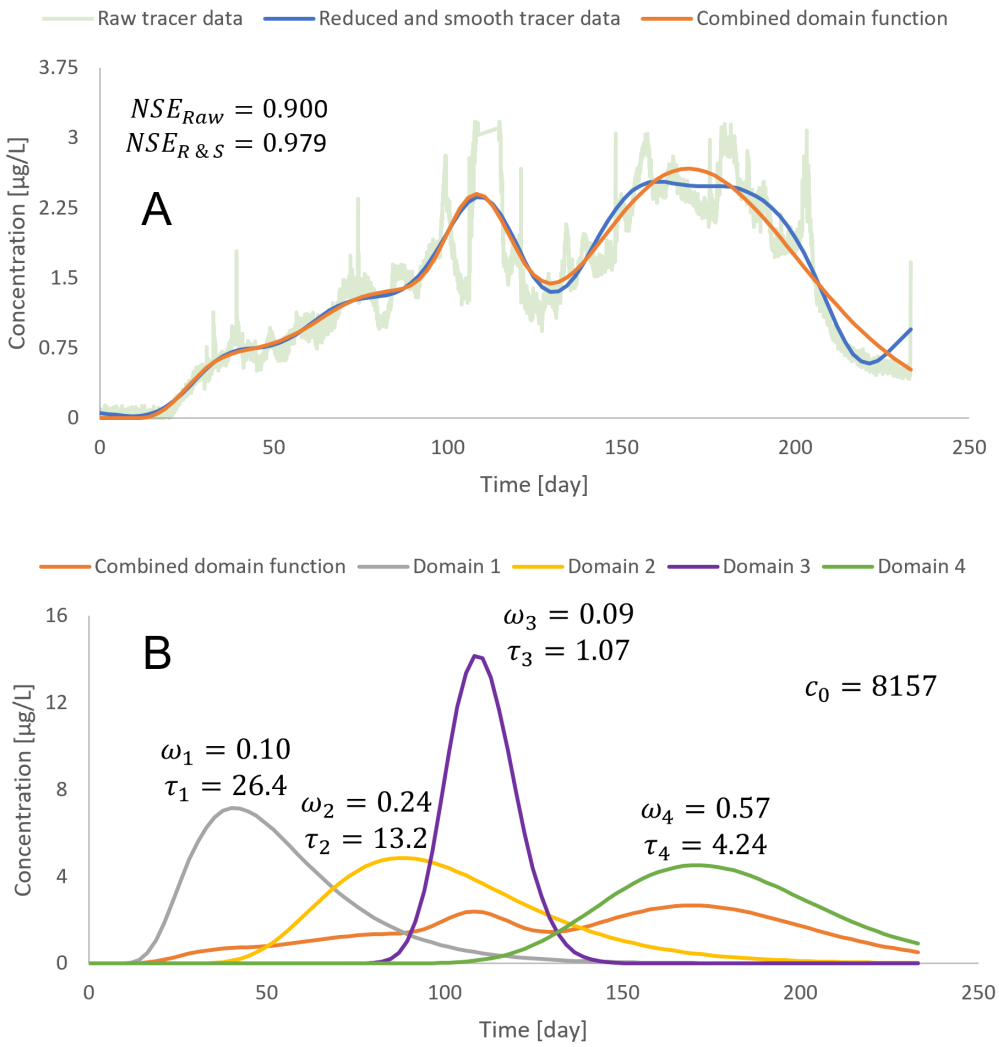

Figure 7.10: Results from the FAST-MD procedure. Figure part A shows the raw tracer data, reduced and smoothed tracer data, and combined domain function using the final parameter estimations. NSE values are between the combined domain function and the two tracer data sets. Figure part B shows the individual domains used for the combined domain function. Results are for screening RI-22S (L5). Dispersivity, τ, is in units m, the inlet concentration, c_0, is in units μg/L. An aerial and cross-sectional overview of the screening location is shown in figures 7.1 and 7.2.

The combined domain function describes the reduced and smoothed data fairly well. The raw tracer data fit is less good, with an NSE of 0.9, but as shown in the figure, the data had many fluctuations and changes in concentration tendencies. The first two domains describe the relatively steady increase in concentration from day 25 to approximately day 80. The first one mainly contributed to the initial increase around 25 days, reflected in its low weight factor of 0.10. The third domain mainly describes the peak in concentration starting at 90 days. It has an almost normal distribution shape, with very little tailing, which is also reflected in the low dispersivity value of 1.07 m. The last domain describes the peak concentration after approximately 125 days. This is the main contributor to the domains with a weight factor of 0.57. This tracer data set was also used as an example of the FAST-MD procedure in chapter 5.

RI-22I

In figures 7.11 the combined domain function is shown with the raw tracer data set and the reduced and smoothed tracer data set. Furthermore, the individual domains used for the combined domain function are shown.

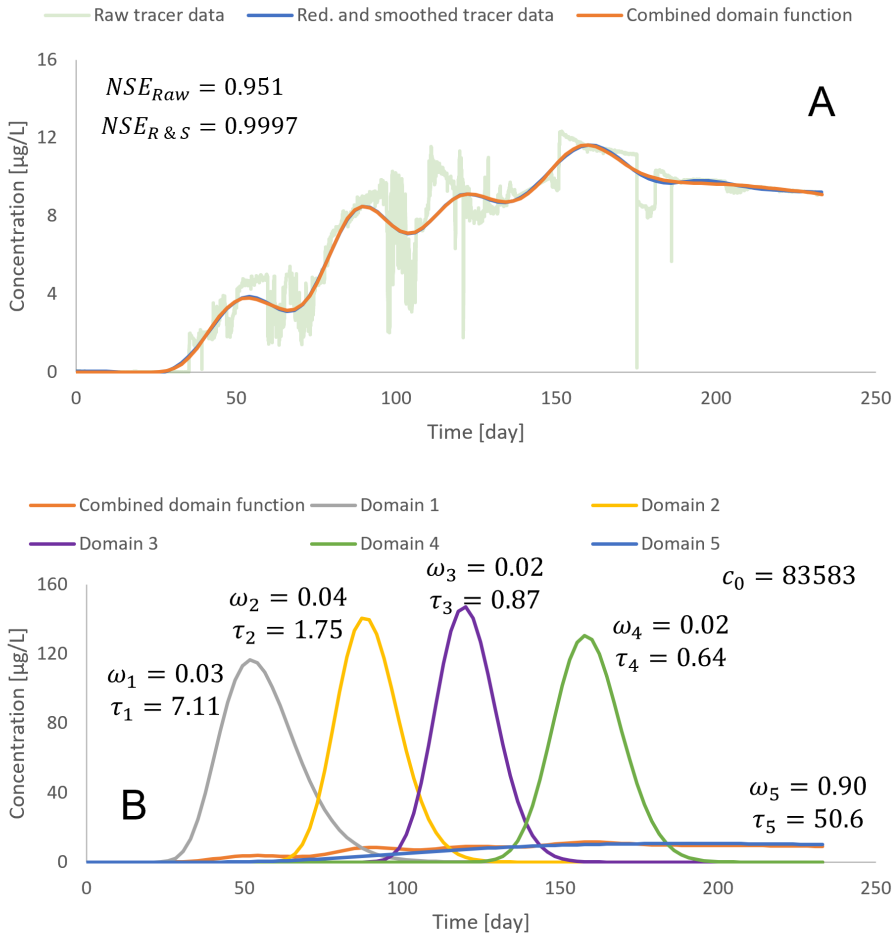

Figure 7.11: Results from the FAST-MD procedure. Figure part A shows the raw tracer data, reduced and smoothed tracer data, and combined domain function using the final parameter estimations. NSE values are between the combined domain function and the two tracer data sets. Figure part B shows the individual domains used for the combined domain function. Results are for screening RI-22I (L6). Dispersivity, τ, is in units m, the inlet concentration, c_0, is in units μg/L. An aerial and cross-sectional overview of the screening location is shown in figures 7.1 and 7.2.

The fit between the combined domain function and the reduced and smoothed function is nearly perfect as almost no deviation is seen, which is also reflected in the NSE value of 0.9997. The fit for the raw tracer data is also good, with an NSE value of 0.951, especially when considering the tracer data fluctuation. The first four domains have very similar tendencies; they describe a rapid increase and decrease in concentration peak. This is also reflected in the shape of the peaks having slight tailing and dispersivity values ranging from 0.6-7 m. The contribution of these peaks to the overall tracer mass recovered is low and is also reflected in their combined weight factors being 0.1. The last domain describes the stabilizing concentration starting from around day 180 and lasting until the tracer test is ended. This is the highest contributing domain with a weight factor of 0.9. A more

detailed description of this tracer data set was conducted in chapter 6, as an example of the FAST-MD procedure used for a multi-domain tracer data set.

RI-22D

In figures 7.12 the combined domain function is shown with the raw tracer data set and the reduced and smoothed tracer data set. Furthermore, the individual domains used for the combined domain function are shown.

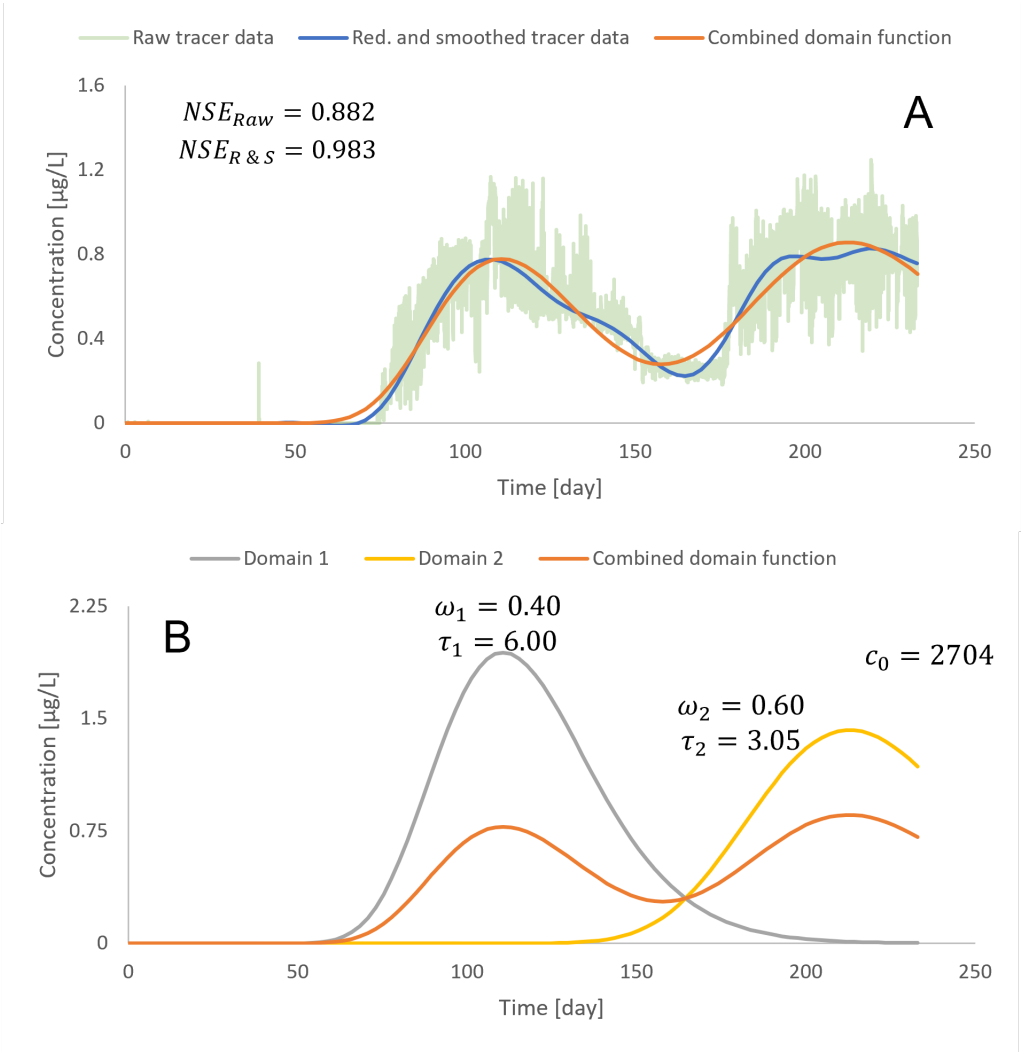

Figure 7.12: Results from the FAST-MD procedure. Figure part A shows the raw tracer data, reduced and smoothed tracer data, and combined domain function using the final parameter estimations. NSE values are between the combined domain function and the two tracer data sets. Figure part B shows the individual domains used for the combined domain function. Results are for screening RI-22D (L7). Dispersivity, τ, is in units m, the inlet concentration, c_0, is in units μg/L. An aerial and cross-sectional overview of the screening location is shown in figures 7.1 and 7.2.

The fit between the raw tracer data and the combined domain function is fairly low compared to most results, with an NSE value of 0.88. However, the data also has a lot of fluctuation, primarily caused by the low concentrations obtained. The fit between the combined domain function and the reduced and smoothed tracer data is good, reaching

an NSE of 0.98. After data reduction and smoothing, two clear peaks were identified, each described by one domain with a relatively equal distribution of 0.4 and 0.6 for domains 1 and 2, respectively.

RI-23S

In figures 7.13 the combined domain function is shown with the raw tracer data set and the reduced and smoothed tracer data set. Furthermore, the individual domains used for the combined domain function are shown.

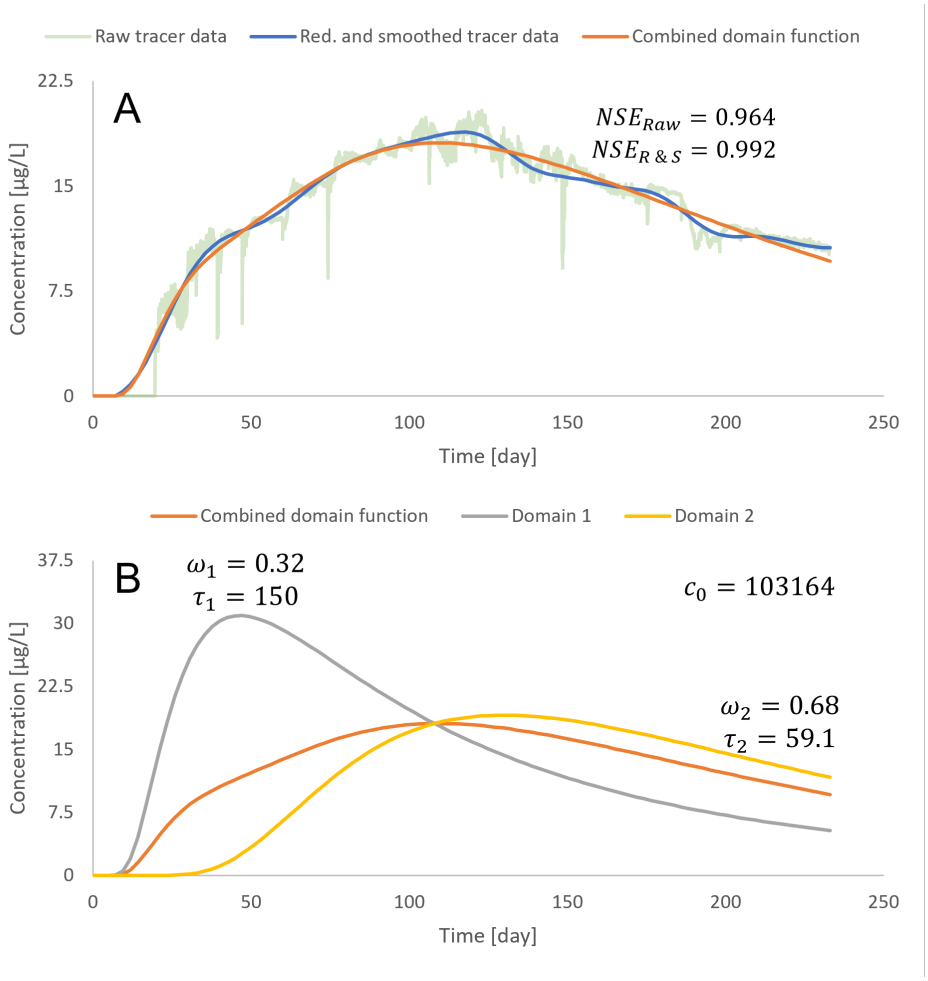

Figure 7.13: Results from the FAST-MD procedure. Figure part A shows the raw tracer data, reduced and smoothed tracer data, and combined domain function using the final parameter estimations. NSE values are between the combined domain function and the two tracer data sets. Figure part B shows the individual domains used for the combined domain function. Results are for screening RI-23S (F1). Dispersivity, τ, is in units m, the inlet concentration, c_0, is in units μg/L. An aerial and cross-sectional overview of the screening location is shown in figures 7.1 and 7.2.

The fit for both tracer data sets has high NSE values. Two domains were identified to describe the tracer data, quite similar to the results for screening RI-21S (L2). One domain mainly describes the early and steep increase in concentration, and the other describes the slower increase and decrease in concentration. The main contributor is domain 2, with a weight factor of 0.68.

RI-23I

In figures 7.14 the combined domain function is shown with the raw tracer data set and the reduced and smoothed tracer data set. Furthermore, the individual domains used for the combined domain function are shown.

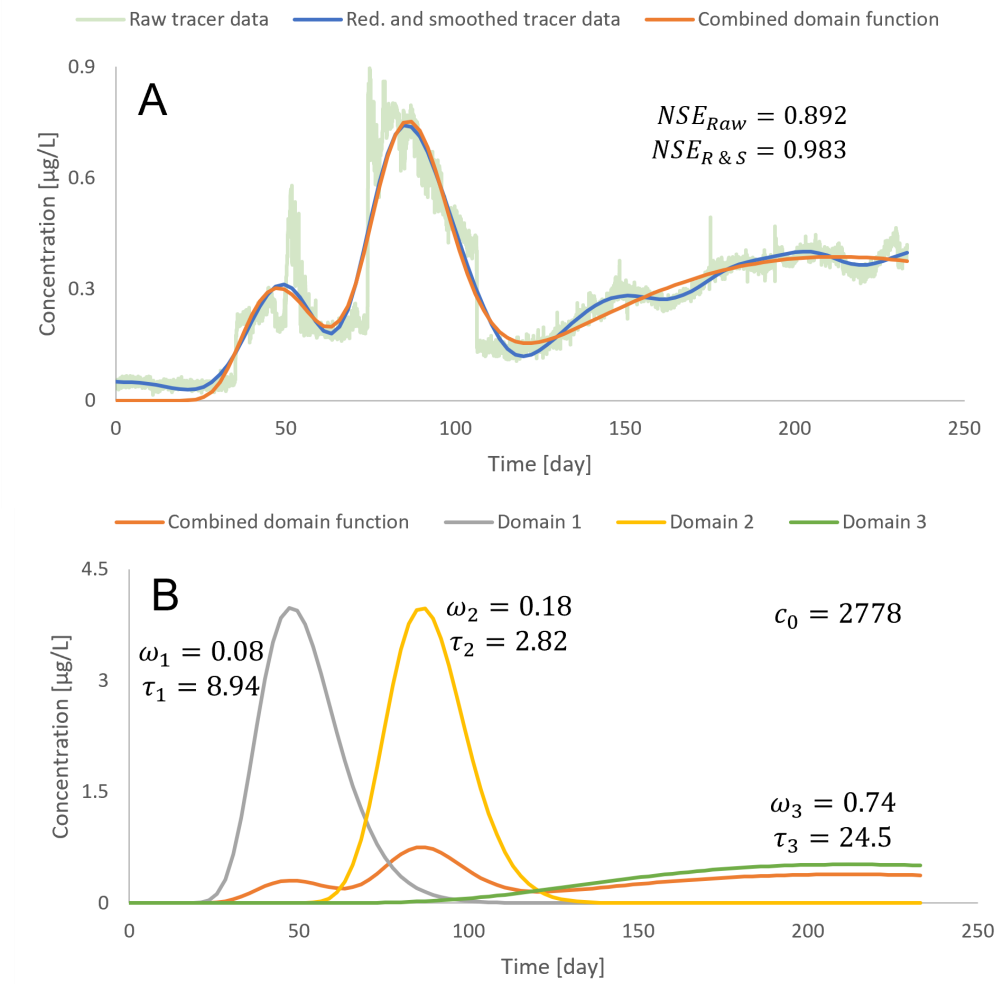

Figure 7.14: Results from the FAST-MD procedure. Figure part A shows the raw tracer data, reduced and smoothed tracer data, and combined domain function using the final parameter estimations. NSE values are between the combined domain function and the two tracer data sets. Figure part B shows the individual domains used for the combined domain function. Results are for screening RI-23I (F2). Dispersivity, τ, is in units m, the inlet concentration, c_0, is in units μg/L. An aerial and cross-sectional overview of the screening location is shown in figures 7.1 and 7.2.

Much like the other tracer data sets with low concentrations, the raw tracer data fit is lowered due to fluctuations. However, the reduced and smoothed tracer data fits well. The main deviations are seen in the low concentrations detected at the beginning of the tracer test and after day 125, where a steady increase in concentration occurs. The first two domains described relatively rapid increasing and decreasing peaks identified after data reduction and smoothing. Similar to the other domains with little tailing and a more normal distribution tendency, these peaks' dispersivity and weight factors are relatively low. The third domain describes the slow increase in concentration after approximately 125

days and until the end of the tracer data. The third domain is also the main contributor with a weight factor of 0.74.

RI-23D

In figures 7.15 the combined domain function is shown with the raw tracer data set and the reduced and smoothed tracer data set. Furthermore, the individual domains used for the combined domain function are shown.

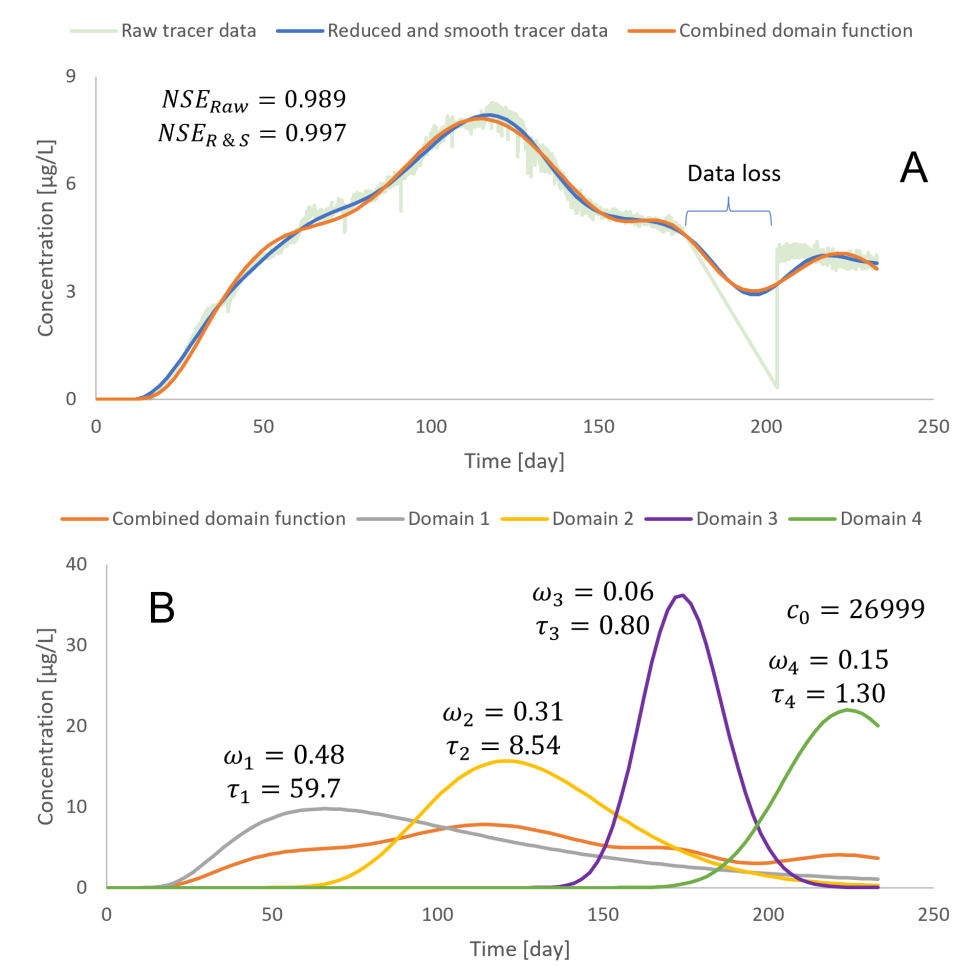

Figure 7.15: Results from the FAST-MD procedure. Figure part A shows the raw tracer data, reduced and smoothed tracer data, and combined domain function using the final parameter estimations. NSE values are between the combined domain function and the two tracer data sets. Figure part B shows the individual domains used for the combined domain function. Results are for screening RI-23D (F3). Dispersivity, τ, is in units m, the inlet concentration, c_0, is in units μg/L. An aerial and cross-sectional overview of the screening location is shown in figures 7.1 and 7.2.

The fit for both the raw and reduced and smoothed tracer data is nearly perfect, with the combined domain function reaching an NSE value of around 0.99 for both fits. The data loss has affected the resulting domains. The reduced and smoothed tracer has a decrease in concentration, which is described by domains 3 and 4. If a linear tendency was assumed between the two parts where the data loss occurred, perhaps it could have been described with one domain. Whether that would have yielded more realistic results

is hard to assess since the concentration in such a time span can vary a lot, as seen with other tracer results. The first domain describes the initial concentration rise until around 50 days. Domain 2 describes the peak in concentration seen at around 125 days. Domain 1 is the main contributor with a weight factor of 0.48.

RI-24S

In figures 7.16 the combined domain function is shown with the raw tracer data set and the reduced and smoothed tracer data set. Furthermore, the individual domains used for the combined domain function are shown.

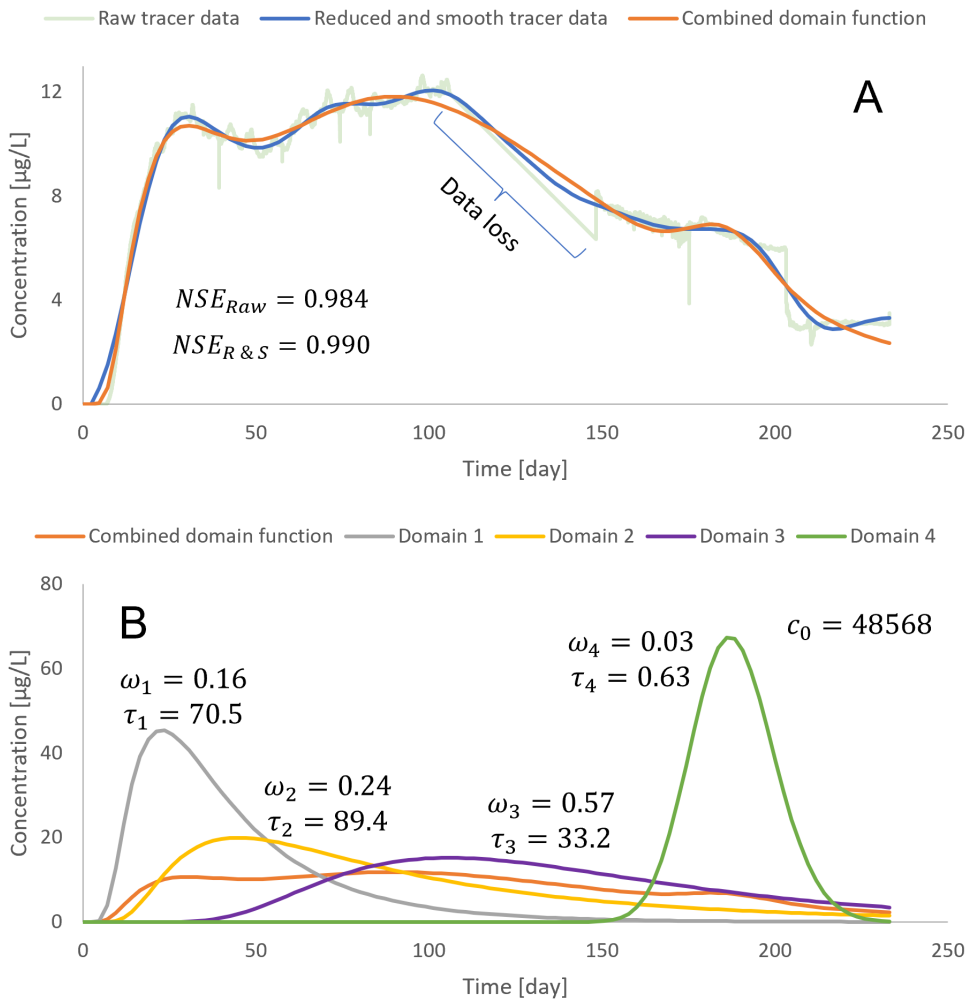

Figure 7.16: Results from the FAST-MD procedure. Figure part A shows the raw tracer data, reduced and smoothed tracer data, and combined domain function using the final parameter estimations. NSE values are between the combined domain function and the two tracer data sets. Figure part B shows the individual domains used for the combined domain function. Results are for screening RI-24S (F4). Dispersivity, τ, is in units m, the inlet concentration, c_0, is in units μg/L. An aerial and cross-sectional overview of the screening location is shown in figures 7.1 and 7.2.

The fit to both tracer data sets with the combined domain function is good, reaching a minimum NSE value of 0.98. Similar to RI-23D (F3), a critical data loss occurred. Domain

1 describes the first peak in concentration after approximately 25 days. Domain 2 describes the second peak in concentration around day 100. Domain 3 describes the general decrease in concentration after 100 days, while domain 4 describes the stabilization in concentration after 160 days and until 205 days. Domain 3 is the main contributor with a weight factor of 0.57. The unfortunate data loss may have altered the results significantly, as it was during the peak concentration of the tracer recovery.

RI-24I

In figures 7.17 the combined domain function is shown with the raw tracer data set and the reduced and smoothed tracer data set. Furthermore, the individual domains used for the combined domain function are shown.

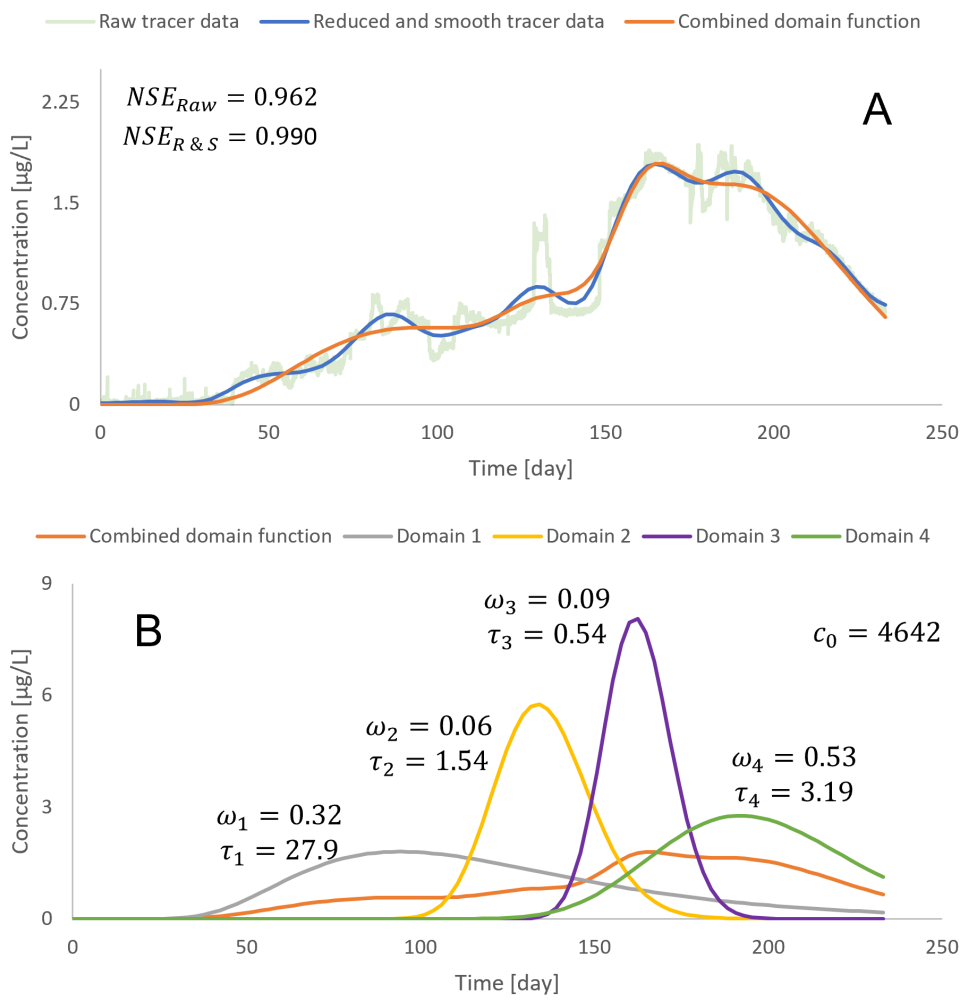

Figure 7.17: Results from the FAST-MD procedure. Figure part A shows the raw tracer data, reduced and smoothed tracer data, and combined domain function using the final parameter estimations. NSE values are between the combined domain function and the two tracer data sets. Figure part B shows the individual domains used for the combined domain function. Results are for screening RI-24I (F5). Dispersivity, τ, is in units m, the inlet concentration, c_0, is in units μg/L. An aerial and cross-sectional overview of the screening location is shown in figures 7.1 and 7.2.

The fit to both tracer data sets with the combined domain function is good, reaching a

minimum NSE value of 0.96, especially when considering the amount of fluctuation in the raw tracer data and a somewhat frequent change in slope. Domain 1 describes the steady increase in concentration from approximately day 25 to 150, causing it to have a significant amount of tailing and a dispersivity of 28 m. Domain 2 describes the small peak after approximately 125 days, and domain 3 describes the one after 160 days. Finally, domain 4 describes the remainder of the tracer data. Domain 4 is the main contributor with a weight factor of 0.53.

RI-24D

In figures 7.18 the combined domain function is shown with the raw tracer data set and the reduced and smoothed tracer data set. Furthermore, the individual domains used for the combined domain function are shown.

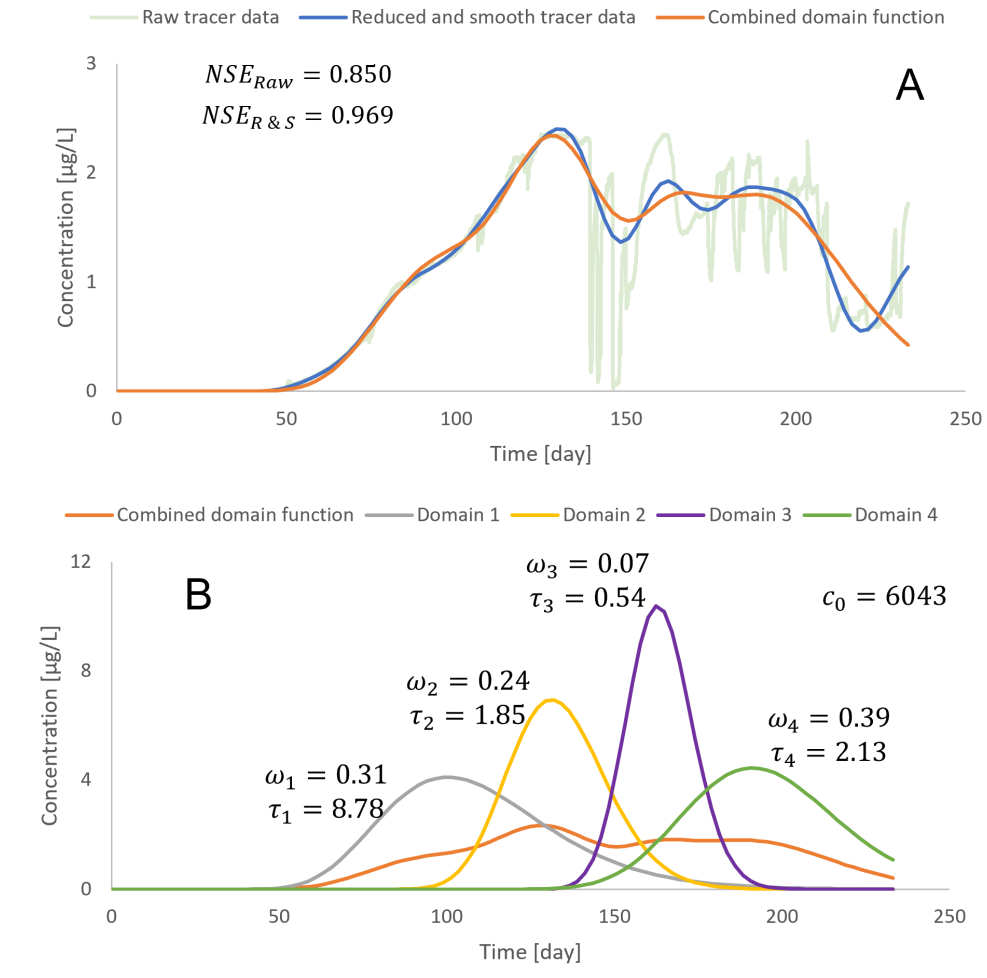

Figure 7.18: Results from the FAST-MD procedure. Figure part A shows the raw tracer data, reduced and smoothed tracer data, and combined domain function using the final parameter estimations. NSE values are between the combined domain function and the two tracer data sets. Figure part B shows the individual domains used for the combined domain function. Results are for screening RI-24D (F6). Dispersivity, τ, is in units m, the inlet concentration, c_0, is in units μg/L. An aerial and cross-sectional overview of the screening location is shown in figures 7.1 and 7.2.

The raw tracer data has a reasonably low fit compared to most of the tracer data, which is also expected when evaluating the amount of fluctuation in the data. The reduced and smoothed data, however, have a decent fit. Domain 1 describes the initial incline in concentration, while domain 2 describes the peak concentration, which develops after approximately 125 days. Domain 3 describes the small peak developing after 150 days, and domain 4 for the peak around 175 days. Domain 2 and 3 are lower tailing domains, which is also expected since the data also shows that tendency with dispersivity values of 1.9 and 0.5 m respectively. The contribution between domains 1 and 4 is relatively close, with weight factors of 0.31 and 0.39, respectively.

An overview of all parameters obtained from the FAST-MD procedure is given in table 7.1.

Table 7.1: Final estimated parameters using the FAST-MD procedure for the tracer data. Notations and units are the same as previously introduced. A "-" indicates that this number of domains were not required for the data set.

Location			Domain 1				Domain 2				Domain 3				Domain 4				Domain 5			
RI name	Given name	c_0	v	D	τ	ω	v	D	τ	ω	v	D	τ	ω	v	D	τ	ω	v	D	τ	ω
RI-26I	E	319	1.87	1.16	0.62	0.080	0.58	1.00	1.72	0.92	-	-	-	-	-	-	-	-	-	-	-	-
RI-7S	M1	279	4.93	325	65.9	0.25	2.71	12.0	4.41	0.11	1.57	5.39	3.44	0.49	1.14	1.05	0.92	0.15	-	-	-	-
RI-7D	M2	1802	3.96	10.1	2.54	0.015	1.50	17.1	11.4	0.10	1.12	1.03	0.92	0.25	0.91	0.90	0.99	0.64	-	-	-	-
RI-25D	L1	649	1.19	10.1	8.48	1	-	-	-	-	-	-	-	-	-	-	-	-	-	-	-	-
RI-21S	L2	44252	1.43	204	143	0.45	1.11	48.6	440	0.55	-	-	-	-	-	-	-	-	-	-	-	-
RI-21I	L3	83877	6.01	519	86.4	0.34	2.00	93.2	46.5	0.52	1.07	24.6	22.9	0.25	-	-	-	-	-	-	-	-
RI-21D	L4	142709	2.58	267	104	0.40	1.93	40.6	21.0	0.34	1.07	16.4	15.2	0.26	-	-	-	-	-	-	-	-
RI-22S	L5	8157	5.23	138	26.4	0.095	2.79	36.8	13.2	0.25	2.56	2.74	1.07	0.094	1.58	6.69	4.24	0.56	-	-	-	-
RI-22I	L6	83583	5.03	35.7	7.11	0.030	3.15	5.50	1.75	0.035	2.34	2.05	0.87	0.016	1.78	1.13	0.64	0.019	0.88	44.6	50.6	0.90
RI-22D	L7	2704	2.40	14.4	6.00	0.40	1.28	3.92	3.05	0.60	-	-	-	-	-	-	-	-	-	-	-	-
RI-23S	F1	103164	2.16	324	150	0.32	1.43	84.5	59.1	0.68	-	-	-	-	-	-	-	-	-	-	-	-
RI-23I	F2	2778	6.10	54.6	8.94	0.076	3.58	10.1	2.82	0.182	1.19	29.1	24.5	0.742	-	-	-	-	-	-	-	-
RI-23D	F3	26999	2.80	167	59.7	0.48	2.42	20.7	8.54	0.31	1.81	1.45	0.80	0.055	1.40	1.82	1.30	0.15	-	-	-	-
RI-24S	F4	48568	7.12	502	70.5	0.16	3.12	279	89.4	0.24	2.17	70.3	33.2	0.57	1.64	1.03	0.63	0.03	-	-	-	-
RI-24I	F5	2778	2.50	69.7	27.9	0.32	2.27	3.48	1.54	0.060	1.89	1.01	0.54	0.088	1.55	4.95	3.19	0.53	-	-	-	-
RI-24D	F6	6043	2.81	24.7	8.78	0.31	2.30	4.26	1.85	0.24	1.88	1.02	0.54	0.069	1.58	3.36	2.13	0.39	-	-	-	-

The NSE values for the final parameter estimation are shown in table 7.2.

Table 7.2: NSE values for the final parameter estimation using the FAST-MD procedure.

Location		Final Parameter estimation	
		Raw	Reduced and smoothed
RI name	Given name	NSE	
RI-26I	E	0.614	0.954
RI-7S	M1	0.759	0.904
RI-7D	M1	0.848	0.997
RI-25D	L1	0.944	0.980
RI-21S	L2	0.994	0.996
RI-21I	L3	0.979	0.979
RI-21D	L4	0.995	0.998
RI-22S	L5	0.900	0.979
RI-22I	L6	0.951	0.9997
RI-22D	L7	0.882	0.983
RI-23S	F1	0.964	0.992
RI-23I	F2	0.892	0.983
RI-23D	F3	0.989	0.997
RI-24S	F4	0.984	0.990
RI-24I	F5	0.962	0.990
RI-24D	F6	0.850	0.969

An overview of the remaining geostatistical parameters for both the initial and final parameters is shown in appendix D.

Summary

In this chapter, an overview of the results from the FAST-MD procedure was shown.

The fit between the reduced and smoothed tracer data and the combined domain function was very high for most screenings. The average NSE value was 0.981, considered a very high average fit. Screening RI-7S (M1) had the lowest NSE value of 0.904.

As expected, for the raw tracer data, a slightly worse fit was found. The lowest fit was for screening RI-26I (E) with an NSE value of 0.614. The average NSE value was 0.907. This is considered a good NSE value considering the amount of fluctuation found in most screenings.

1 screening required 5 domains, 7 screenings required 4 domains, 3 screenings required 3 domains, 4 screenings required 2 domains, and 1 screening required 1 domain. This means that a total of 11 out of the 16 screenings required a multi-domain solution according to the FAST-MD procedure, further validating the need for a multi-domain solution for the tracer data at the HLLSS. The results of the tracer data will in the following chapter be interpreted in terms of transport path and type at the HLLSS, using the presented results from this chapter.

Application of the FAST-MD Procedure Results of the Tracer Test to Evaluate the Hydrogeology at the HLLSS

8

In this chapter, the results from the FAST-MD procedure presented in chapter 7 will be analyzed to gain an overview of the tracers movement. The analysis will mainly focus on the results of domain 1 and the final domain (the slowest domain), as these are assessed as the most important domains for most screenings. Two new parameters are introduced in this chapter for this analysis, and those are the mass recovery and the average velocity.

The mass recovered, m_{rec}, in each well, and screening is a good indicator for the movement of the tracer. To estimate the mass recovery equation (8.1) is used.

$$m_{rec} = (c_0 \cdot t_0 \cdot Q)/m_{inj} \tag{8.1}$$

m_{rec}	Mass recovery [−]
c_0	Inlet concentration [g/m^3]
t_0	Injection time [s]
Q	Discharge [m^3/s]
m_{inj}	Mass injected into the injection well [g]

The inlet concentration for each screening was determined in the FAST-MD procedure, and the results were shown in the previous chapter in table 7.1. The injection period is assumed to be 1 hour for all screenings as described in chapter 4. The mass injected into the injection well was 5.34 kg as described in chapter 3. The discharge was in previous groundwater studies at the HLLSS found to be $6.9 \cdot 10^{-4}$m^3/s [Field, 2020]. This discharge is assumed to be the discharge at all screenings. This is not a realistic assumption; as documented in chapter 7 the tracer data varies significantly in results, and therefore the discharge would also vary. It would be difficult to achieve a realistic estimate of the mass recovery. Many breakthrough curves were still developing when the tracer test ended, which was also shown in chapter 7. Because the tracer data were not fully developed,

the method in equation (8.1) is used, compared to the area under the first moment curve method. This is due to the model trying to predict how the remainder of the breakthrough curve is shaped, and the magnitude of the inlet concentration, therefore, depends on the fully developed breakthrough curve; this is also further explained in chapter 6 figure 6.11. Therefore, the mass recovery estimation aims not to give a realistic estimate but a relative scale to compare the mass recoveries between the screenings.

The average velocity is calculated for each domain. It is estimated based on the breakthrough time for a given domain and the distance between the injection and monitoring well, as shown in equation 8.2.

$$v_{ave} = \frac{L}{t_{bt}} \tag{8.2}$$

v_{ave}	Average velocity [m/s]
L	Distance between injection and monitoring well [m]
t_{bt}	Breakthrough time [s]

The average velocity is used to compare the breakthrough times between screenings and, therefore, gives an estimate of the velocity at which each domain was transported to the monitoring wells.

In figure 8.1 an aerial overview of the location of the wells is shown.

When evaluating the mass recovery, it is shown that the mass recovery is highest within the Treatability Study area, the exception being RI-25 (L1). RI-25 (L1) is a fairly shallow well, presumably causing the low mass recovery. The depth of each screening is shown in figure 8.2. Wells RI-7 (M1-M2) and RI-26 (E) are located west of the estimated flow directions and exhibit low mass recoveries. This indicates that the outskirts of the tracer plume may have passed the wells. Furthermore, this indicates that the main tracer plume was transported toward the Treatability Study area, further validating the estimated flow directions.

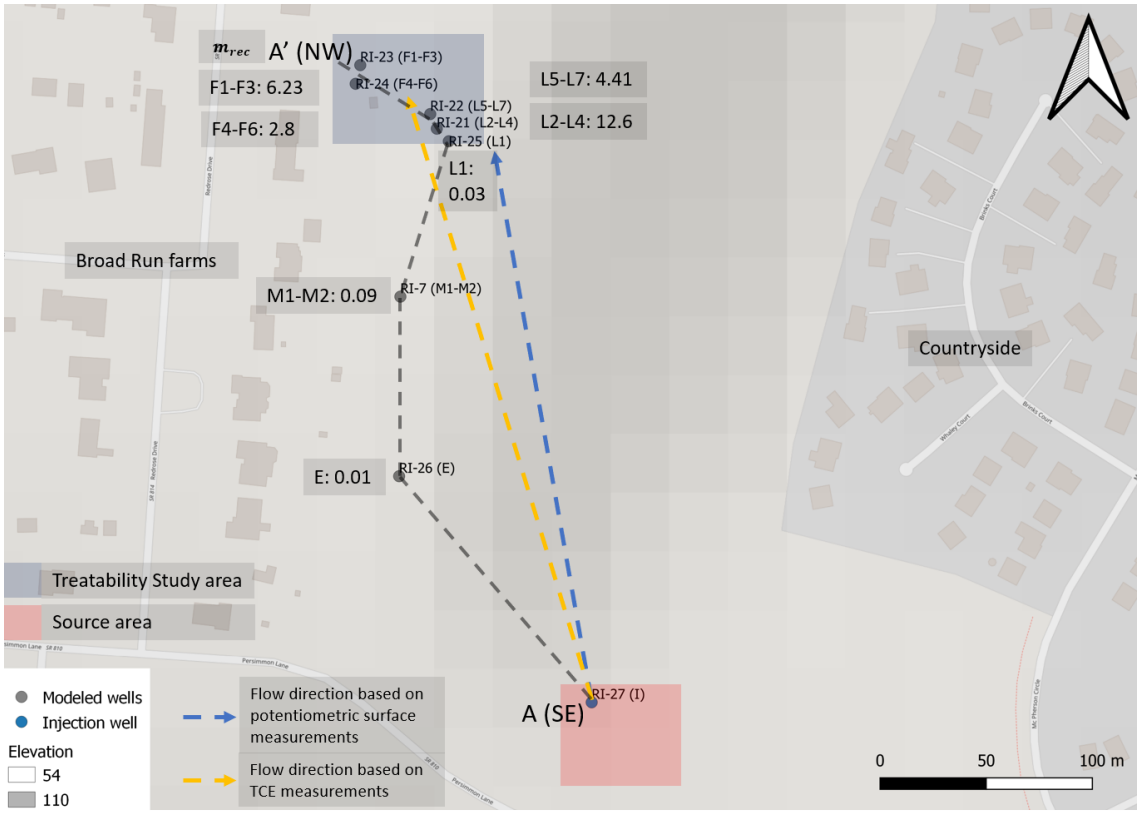

Figure 8.1: Aerial overview showing the location of the modeled wells. The parameter shown at the wells is the summed mass recovery [%] for all screenings within that particular well. The location of the landfill is clearly indicated by the change in elevation. The dashed gray line is a transect line used to develop figures 8.2 and 8.3.

In figure 8.2 a cross-sectional profile of the modeled screenings is shown with some key parameters from domain 1.

Each parameter in the figure above describes how the tracer was transported. The mass recovery describes how much of the tracer was transported through a given screen relative to the other screenings. The weight factor for domain 1 indicates how much of that mass is transported through domain 1. Finally, the average velocity describes how quickly that mass is transported in domain 1. The Treatability Study area is divided into two parts, a shallow and a deep. Wells L1-L4 and F1-F3 are located within the shallow part, while L5-L7 and F4-F6 are located in the deep part.

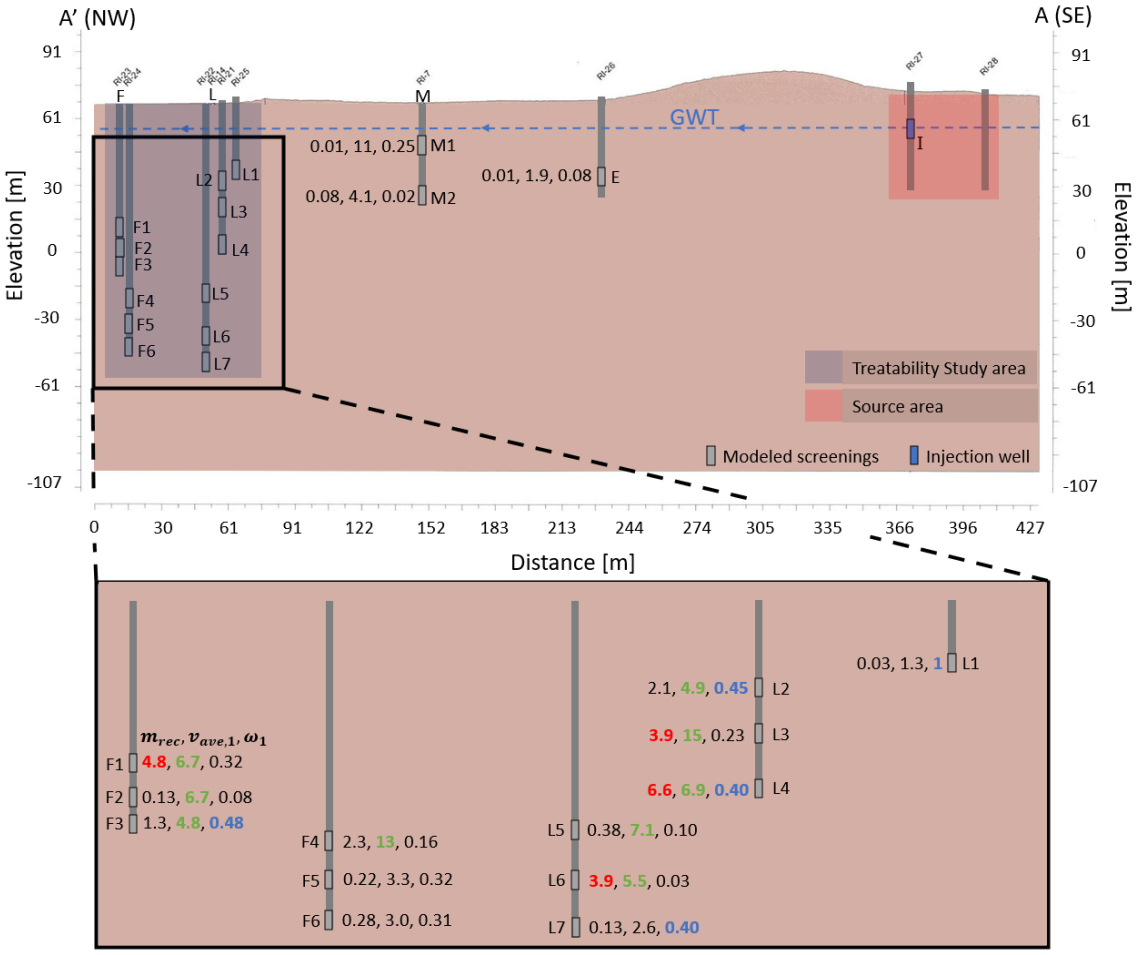

Figure 8.2: Cross-sectional profile showing estimated parameter values for the screenings. The parameters shown at the screenings are in the following order: mass recovery [%], average velocity for domain 1 [m/d], weight factor for domain 1. Values marked in red indicate a mass recovery higher than 3%. Values marked with green indicate an average velocity higher than 4.5 m/d. Values marked with blue indicate a weight factor higher than 0.40. The cross-sectional profile is based on the dashed gray transect line shown in figure 8.1.

The cross-sectional profile shows that a lot of the higher values in terms of both mass recovery, average velocity, and weight factor are situated within the shallow part of the Treatability Study area. This means that the main tracer plume was transported through the shallow part of the Treatability Study area. Furthermore, a significant portion of that mass is transported through domain 1. It is being transported quite rapidly, presumably through mainly fracture-dominated transport, indicated by 4 of the 7 shallow screenings having a weight factor higher than 0.40 and 6 of the 7 having an average velocity higher than 4.5 m/d. Screening L4 is the screening with the highest mass recovery while also having a relatively high average velocity and weight factor and therefore is a substantial contributor to the fast-moving part of the tracer plume.

The total mass recovered for all the screenings was 26% corresponding to 1.40 kg. 72% of that mass was recovered within the shallow screenings of the Treatability Study area. If a direct correlation between mass recovery contribution for each domain and the weight factor of that domain is made, the mass recovered through domain 1 within the shallow screenings of the Treatability Study area was 25% of the total mass recovered. In contrast,

only 27% of the mass was recovered in the deep screenings of the Treatability Study area, while only 2.8% of the mass recovered was within domain 1. This indicates that the tracer was mainly transported through slower domains for the deeper screenings, also emphasized by only having 1 weight factor above 0.40. These mass recoveries are also summarized together with the corresponding results for the final domain in table 8.2.

Other relevant parameters for the FAST-MD procedure results for domain 1 are shown in table 8.1.

Table 8.1: Summarized parameters for the FAST-MD procedure results for domain 1. The parameters in order from left to right is: The distance from injection to monitoring well, the change in depth from injection to screening (using the center of the screening), mass recovery, average velocity, dispersivity, and weight factor.

Location		L	$\Delta depth$	m_{rec}	$v_{ave,1}$	τ_1	ω_1	No. of domains
RI name	Given name	[m]	[m]	[%]	[m/d]	[m]	[-]	[-]
RI-26I	E	142	17	0.01	1.9	0.62	0.08	2
RI-7S	M1	211	0.42	0.01	11	66	0.25	4
RI-7D	M2	211	24	0.08	4.1	2.5	0.02	4
RI-25D	L1	271	10	0.03	1.3	8.5	1	1
RI-21S	L2	277	17	2.1	4.9	143	0.45	2
RI-21I	L3	277	29	3.9	15	86	0.23	3
RI-21D	L4	277	45	6.6	6.9	104	0.40	3
RI-22S	L5	283	68	0.38	7.1	26	0.10	4
RI-22I	L6	283	87	3.9	5.5	7.1	0.03	5
RI-22D	L7	283	100	0.13	2.6	6.0	0.40	2
RI-23S	F1	317	36	4.8	6.7	150	0.32	2
RI-23I	F2	317	45	0.13	6.7	8.9	0.08	3
RI-23D	F3	317	55	1.3	4.8	60	0.48	4
RI-24S	F4	308	69	2.3	13	70	0.16	4
RI-24I	F5	308	80	0.22	3.3	28	0.32	4
RI-24D	F6	308	91	0.28	3.0	8.8	0.31	4

In figure 8.3 a cross-sectional profile of the modeled screenings is shown with some key parameters from the final domain.

A different interval is chosen for the average velocity for this cross-sectional profile compared to the one shown in figure 8.2. This is to illustrate that the change in average velocity between the different screenings is relatively minimal; 13 of the 14 screenings within the Treatability Study have an average velocity between 1-2 m/d, indicating that the later part of the tracer plume was moving with a similar velocity. The weight factors for the shallow screenings within the Treatability Study area show a similar trend to the results for domain 1. For both domain 1 and the final domain, 4 out of the 7 weight factors were above 0.4, indicating a somewhat equal distribution of the tracer mass between these domains.

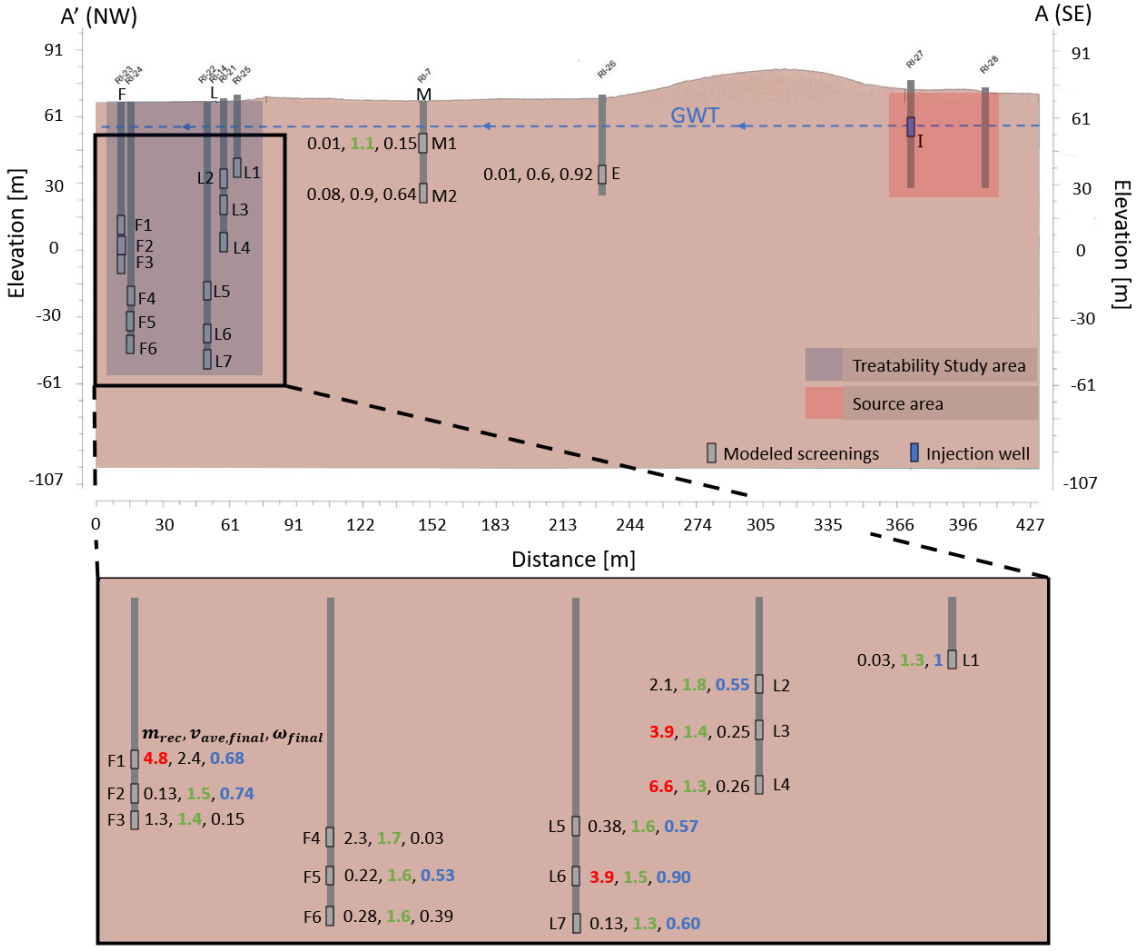

Figure 8.3: Cross-sectional profile showing estimated parameter values for the screenings. The parameters shown at the screenings are in the following order: mass recovery [%], average velocity for the final domain [m/d], weight factor for the final domain. Values marked in red indicate a mass recovery higher than 3%. Values marked with green indicate an average velocity between 1-2 m/d. Values marked with blue indicate an weight factor higher than 0.40. The cross-sectional profile is based on the dashed gray transect line shown in figure 8.1.

For the deeper screenings in the Treatability Study area, 4 out of the 6 screenings have a weight factor above 0.40, whereas, in contrast, only 1 was above 0.40 for domain 1. This indicates that a substantial amount of the mass recovered within the deeper screenings was transported with the final domain. Other relevant parameters for the FAST-MD results for the final domain are shown in table 8.3.

28% of the mass was recovered through the final domain within the shallow screenings of the Treatability Study area. 16% was recovered in the deep screenings. In table 8.2 the different mass recoveries estimated is shown.

Table 8.2: Mass distribution of the 1.40 kg recovered mass from the tracer test, corresponding to a mass recovery rate of 26%.

	Total		Domain 1		Final domain	
	Shallow	Deep	Shallow	Deep	Shallow	Deep
Mass distribution [%]	72	28	25	2.8	28	16

It is shown that a significant portion of the mass was transported towards the shallow screenings. The distribution of the mass between the domains is relatively equal. For the deep screenings, a substantial amount of the mass recovered was recovered within the final domain.

Table 8.3: Summarized parameters for the FAST-MD procedure results for the final domain. The parameters in order from left to right is: The distance from injection to monitoring well, the change in depth from injection to screening (using the center of the screening), mass recovery, average velocity, dispersivity, and weight factor.

Location		L	$\Delta depth$	m_{rec}	$v_{ave,final}$	τ_{final}	ω_{final}	No. of domains
RI name	Given name	[m]	[m]	[%]	[m/d]	[m]	[-]	[-]
RI-26I	E	142	17	0.01	0.61	1.7	0.92	2
RI-7S	M1	211	0.42	0.01	1.1	0.88	0.15	4
RI-7D	M2	211	24	0.08	0.92	0.99	0.64	4
RI-25D	L1	271	10	0.03	1.3	8.5	1	1
RI-21S	L2	277	17	2.1	1.8	44	0.55	2
RI-21I	L3	277	29	3.9	1.4	23	0.25	3
RI-21D	L4	277	45	6.6	1.3	15	0.26	3
RI-22S	L5	283	68	0.38	1.6	4.2	0.57	4
RI-22I	L6	283	87	3.9	1.5	51	0.90	5
RI-22D	L7	283	100	0.13	1.3	3.1	0.60	2
RI-23S	F1	317	36	4.8	2.4	59	0.68	2
RI-23I	F2	317	45	0.13	1.5	25	0.74	3
RI-23D	F3	317	55	1.3	1.4	1.3	0.15	4
RI-24S	F4	308	69	2.3	1.7	0.63	0.03	4
RI-24I	F5	308	80	0.22	1.6	3.2	0.53	4
RI-24D	F6	308	91	0.28	1.6	2.1	0.39	4

8.1 Validation of the FAST-MD Procedure using Literature Values for Hydrogeological Parameters

In chapters, 4 the validation tool for the FAST-MD was introduced. A clear trend when evaluating the tracer data in chapter 7 was that the tracer data with a high number of domains usually consisted of rapidly developed peaks. The domains representing these rapidly developed peaks had low dispersivities. It was hypothesized in chapter 4 that the higher amount of domains used, the lower the dispersivity values would be achieved. Therefore, the dispersivity values were plotted using the validation tool based on the amount of domains used for each screening, the results are shown in figure 8.4.

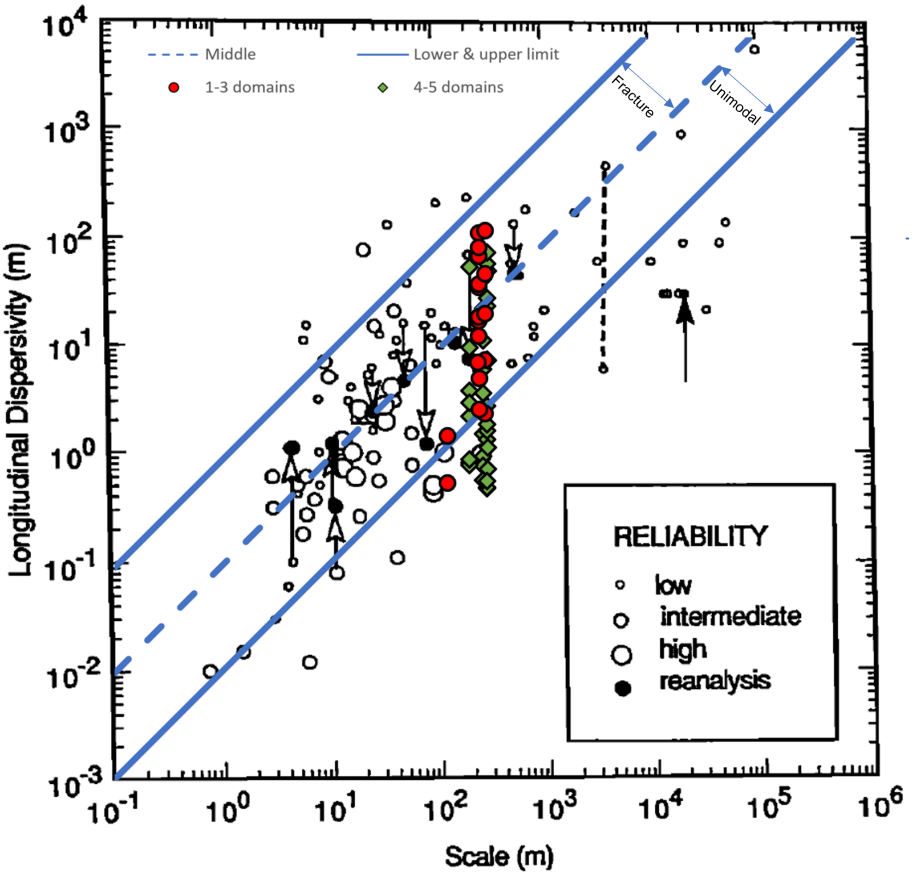

Figure 8.4: Longitudinal dispersivity as a function of distance from injection to detection well. Arrows indicate reported values at tails and corresponding values from reanalyses at heads. The dashed black line connects two dispersivity values determined at the same site. The solid and dashed blue lines indicate an expected interval when using a single-domain model. The expected interval is divided into two soil types fractured and unimodal. Results are all modeled screenings from the FAST-MD procedure. Modified from [Gelhar and Collins, 1992].

The dispersivities for the screenings with 1-3 domains show a somewhat equal distribution between the expected values for fractured and unimodal soil types. This means that some of the dispersivity values were lowered when compared to the literature values for fractured medias, as was expected. For the screenings with 4-5 domains lower values of dispersivity were found. Many being lower than the expected range of dispersivities.

The dispersivities outside the expected range, mainly represent the rapid peaks identified in the tracer data, meaning very low dispersivities were expected for these domains as these represent the rapid fracture movement of the tracer. By describing these peaks with an individual domain, the model no longer has to find an average for the multiple domains, meaning the spreading due to velocity variation decreases. This lowers the spreading as the model no longer has to describe all the different processes in the fractured bedrock, such as rapid movement in fractures, slow movement in the bedrock matrix and exchange between domains, causing variations in velocities and thereby spreading. The hypothesis of lower dispersivity values with an increase of domains was therefore confirmed, which validates the results of the FAST-MD procedure.

To further investigate if the transport type for the tracer was fractured bedrock, an estimate of hydraulic conductivity was conducted. The hydraulic conductivity was chosen as it is one of the most important hydrogeological parameters as it describes a fluid's ability to be transported through a porous medium [Murphy, eds] and [Freeze and Cherry, 1979]. Furthermore, a large amount of measurements of hydraulic conductivity for different soil types have been conducted and summarized. To estimate the hydraulic conductivity, Darcy's law, in combination with the known relationship of the pore-water velocity and effective porosity, is used and is shown in equation (8.3) [Freeze and Cherry, 1979].

$$v \cdot \phi_{eff} = q = -K\frac{dh}{dx} \tag{8.3}$$

v	Pore-water velocity [m/s]
ϕ_eff	Effective porosity [$\frac{\text{m}^3 \text{ pores} > 30 \text{ µm}}{\text{m}^3 \text{ soil}}$]
q	Darcy flux [m/s]
K	Hydraulic conductivity [m/s]
$\frac{dh}{dx}$	Hydraulic gradient [$\frac{\text{m change in head}}{\text{m porous media}}$]

The effective porosity is estimated through modeled results of the tracer data at the HLLSS using the mobile and immobile solution introduced in chapter 4. The values were estimated in [Field, 2020] and ranged from 0.004-0.02 $\frac{\text{m}^3 \text{ pores} > 30 \text{ µm}}{\text{m}^3 \text{ soil}}$, since hydraulic conductivity is one of the most varying hydrogeological parameters [Murphy, eds] a factor 5 variance in effective porosity does not change the result significantly. Therefore a effective porosity of 0.01 $\frac{\text{m}^3 \text{ pores} > 30 \text{ µm}}{\text{m}^3 \text{ soil}}$ was chosen. The hydraulic gradient is based on the potentiometric surface maps and was estimated in chapter 2 using figures 2.13 and 2.14, and was 0.002$\frac{\text{m change in head}}{\text{m porous media}}$. The estimated hydraulic conductivity is shown together with literature values for hydraulic conductivity from different soil types in figure 8.5.

The estimated values are compared to the rock soil types due to the known geology at the HLLSS, where the tracer was injected into the fractured bedrock layer. The values are in the upper spectrum of the "Fractured igneous rocks and metamorphic rocks" type, while somewhat in the middle for the soil types "Karst limestone" and "Permeable basalt". The difference in hydraulic conductivity between domain 1 and the final domain is relatively minimal when considering the scale of magnitude in which a soil can vary in hydraulic conductivity, as illustrated in the figure.

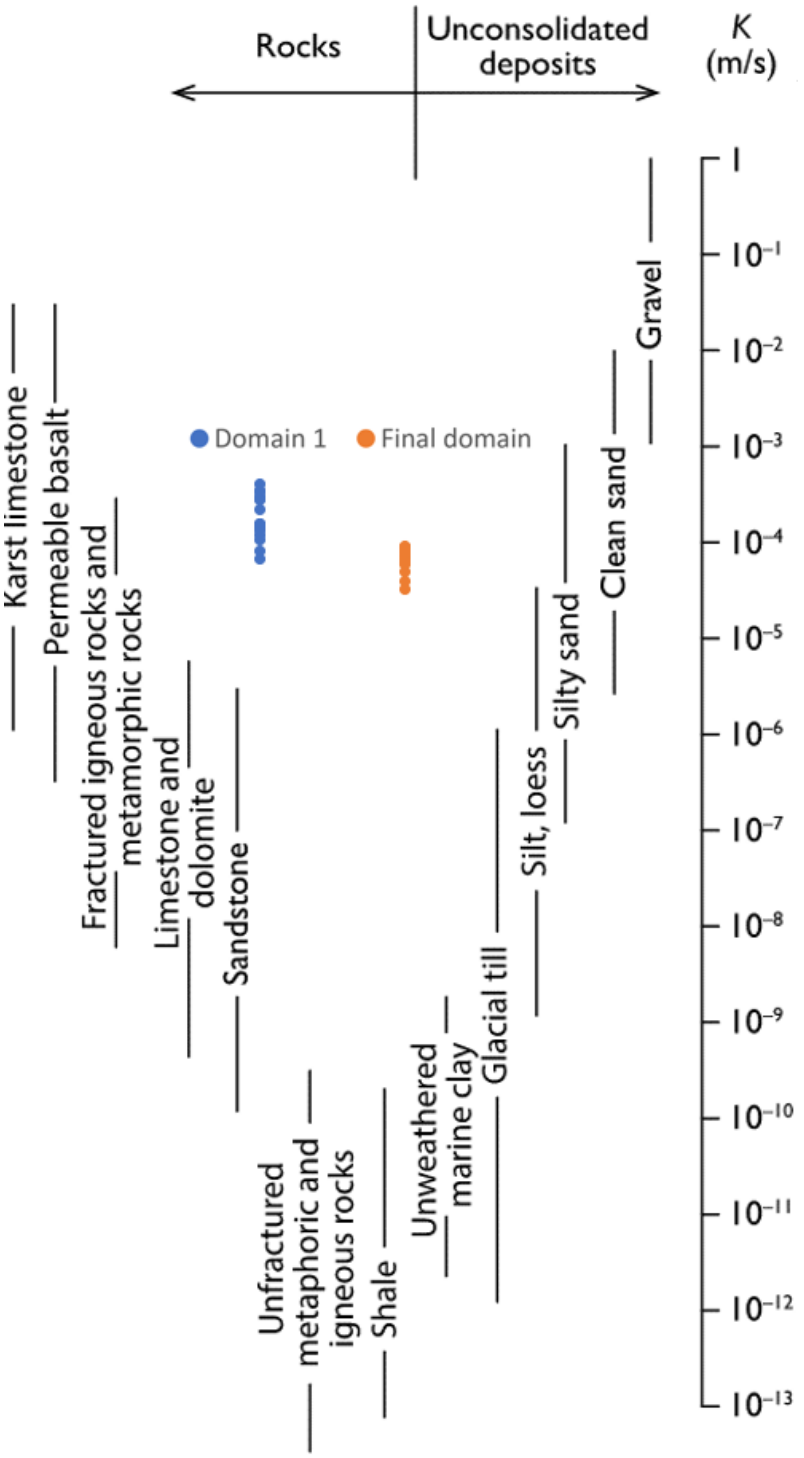

Figure 8.5: Estimated hydraulic conductivities for domain 1 and the final domain for each screening. Also, literature values for hydraulic conductivity from different soil types are shown. Modified from [Freeze and Cherry, 1979].

The hydraulic conductivities estimated are quite uncertain due to the method by which the effective porosity and hydraulic gradient were found. However, considering the magnitude at which the parameters would have to differ for a meaningful change in results in terms of soil type, based on the figure, the estimate may be considered reasonable to obtain an idea of the soil type. Furthermore, the literature values for hydraulic conductivity shown in the

figure are from soil samples, which is a significantly smaller scale than the approximately 300 meters the tracer was transported for most of the screenings. This is also why such a significant variation in magnitude is seen for the literature values. A sample may be well connected or poorly connected throughout the entire sample, yielding so-called extreme outlier hydraulic conductivity values.

In comparison, the hydraulic conductivities estimated is an average hydraulic conductivity from the injection well to the monitoring wells. Over such a distance, it is nearly impossible that the tracer was only transported through one well-connected fracture or solely through the bedrock matrix. Therefore, less variation is seen in the estimated hydraulic conductivities.

It is assessed that while uncertainties in the estimation of the hydraulic conductivity and that the scale at which the compared values were sampled or estimated is significantly different, the estimate can still be used as a confirmation of the fact that the tracer indeed was transported through a soil yielding typical values for a fractured rock soil type.

In table 8.4 the estimated hydraulic conductivities are shown.

Table 8.4: Hydraulic conductivity using the estimated effective porosity and hydraulic gradient, for both domain 1 and the final domain of each screening.

Location		Domain 1	Final domain
RI name	Given name	K [m/s]	K [m/s]
RI-26I	E	$1.1E^{-4}$	$3.4E^{-5}$
RI-7S	M1	$2.85E^{-4}$	$6.60E^{-5}$
RI-7D	M2	$2.29E^{-4}$	$3.37E^{-5}$
RI-25D	L1	$6.91E^{-5}$	$6.91E^{-5}$
RI-21S	L2	$8.3E^{-5}$	$6.4E^{-5}$
RI-21I	L3	$3.5E^{-4}$	$6.2E^{-5}$
RI-21D	L4	$1.5E^{-4}$	$6.2E^{-5}$
RI-22S	L5	$3.0E^{-4}$	$9.1E^{-5}$
RI-22I	L6	$2.9E^{-4}$	$5.1E^{-5}$
RI-22D	L7	$1.4E^{-4}$	$7.4E^{-4}$
RI-23S	F1	$1.3E^{-4}$	$8.3E^{-5}$
RI-23I	F2	$3.5E^{-4}$	$6.9E^{-5}$
RI-23D	F3	$1.6E^{-4}$	$8.1E^{-5}$
RI-24S	F4	$4.1E^{-4}$	$9.5E^{-5}$
RI-24I	F5	$1.5E^{-4}$	$9.0E^{-5}$
RI-24D	F6	$1.6E^{-4}$	$9.1E^{-5}$

Summary

This chapter found that the tracer's main transport path was through the shallow screenings located in the Treatability Study area. A total of 72% of the mass recovered was transported through these screenings. The distribution between fast (domain 1) and slow domain (final domain) transport of the tracer was pretty equal for the shallow screenings. Almost all of the remaining tracer mass was recovered at the deep screenings within the Treatability Study area. The fast domain transport was generally slower than for the shallow screenings. Furthermore, a small amount of the tracer mass recovered at the deep

screenings was transported through the fast domain. The slower domain was the main contributor to the mass recovered at the deeper screenings.

Using literature values from field-scale studies and soil samples for dispersivity and hydraulic conductivity, respectively, a validation of the estimated parameters and transport type was achieved. The hypothesis that an increase in domains yielded lower dispersivity values was confirmed. The low dispersivity values were from domains showing significant fracture transport, validating their low values in dispersivity. The estimated hydraulic conductivities were within the range of literature values for fractured rock soil types, further validating the assessment of fractured bedrock transport being dominant for the transport of the tracer.

Scientific Summary of the new FAST-MD Procedure for Tracer Data Analysis, and its Application with TCE Contamination

9

In this chapter, a summary of the results obtained with the tracer data from the EPA using the Fast-MD procedure will be presented. Furthermore, these results will be related to the TCE contamination at the Hidden Lane Landfill Superfund Site, referred to as the HLLSS.

The HLLSS was a previously unpermitted landfill that was closed by court order in 1984, one of the reasons being that in 1976 an inspection was done where containers marked "poison and toxic" was found. In 1989 trichloroethylene (TCE) was found in drinking water wells of the Broad Run Farms community, located west of the HLLSS, with concentrations way higher than the maximum threshold set by the EPA. A remedial investigation conducted by the EPA was therefore started. In 2018 the EPA conducted TCE measurements in the groundwater at the HLLSS, from which an estimated TCE plume was found. Furthermore, an estimated Source area and Treatability Study area were defined [Field, 2020]. These are shown in figure 9.1. The transport of TCE was found to be through a fractured bedrock layer located approximately 5-10 meters below the surface. A tracer test was conducted in 2019 to obtain a better understanding of the transport of water and by associate chemicals like TCE from the Source area to the Treatability Study area through this fractured bedrock system [Field, 2020]. In chapter 2, a more detailed description of the HLLSS site is conducted, while the tracer experiment is described further in chapter 3.

9.1 Flow Direction and Tracer Recoveries at the HLLSS

In figure 9.1 an aerial overview of potentiometric surface measurements (A), the TCE plume (B), and the tracer experiment (C) is shown.

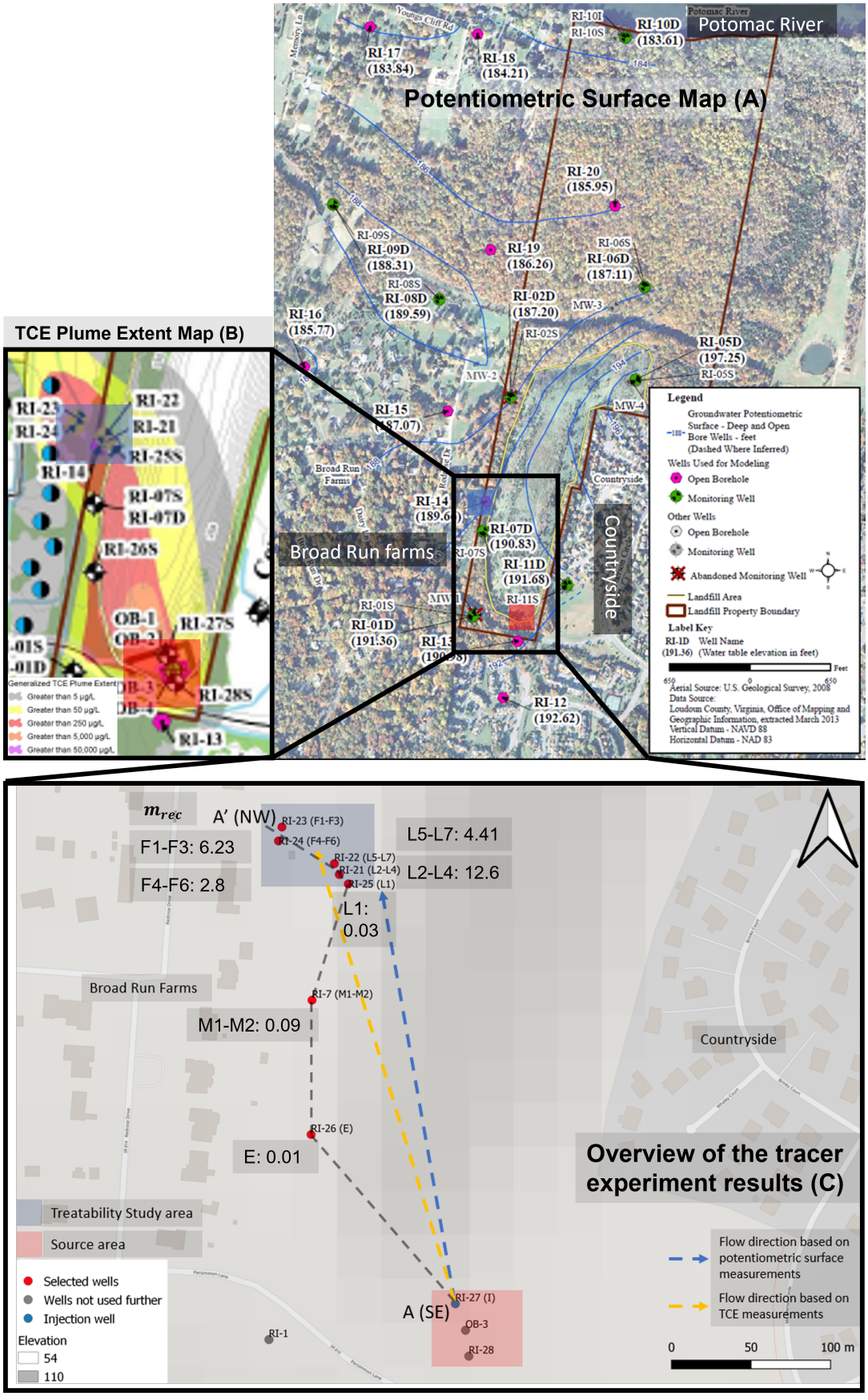

Figure 9.1: Potentiometric Surface map (A), TCE Plume Extent Map (B), and Overview of the tracer experiment results (C). The parameter shown at the wells is the summed mass recovery [%] for all screenings within that particular well. The mass recovery estimation is further explained in chapter 8 in equation (8.1). The dashed gray line is a transect line used to develop figure 9.10.

The Potentiometric Surface Map (A) was used to obtain an overall estimate of groundwater flow direction in the near vicinity of the HLLSS. The two potentiometric surface maps used can also be found in chapter 2 figures 2.13 and 2.14. When evaluating the map, it was assessed that the general flow direction was mainly north and slightly westward. The assessed flow direction is marked as the dashed blue arrow on the Overview of the tracer experiment results (C). The TCE Plume Extent Map (B) shows that the plume moves from the Source area northwest towards the Treatability Study area. The entire TCE Plume Extent Map is shown in chapter 2 figure 2.5. The assessed flow direction based on the TCE Plume is marked with the dashed yellow arrow on the Overview of the tracer experiment results (C).

The Overview of the tracer experiment results (C) shows that the wells located south of the injection well (marked with gray) are not used further. This is due to their weak tracer recovery, meaning very little of the tracer migrated south of the injection well. Furthermore, when evaluating the mass recovery, it is shown that the mass recovery is highest within the Treatability Study area, the exception being RI-25 (L1). RI-25 (L1) is a fairly shallow well, presumably causing the low mass recovery. The depth of each screening will be shown later in the chapter. Wells RI-7 (M1-M2) and RI-26 (E) are located west of the estimated flow directions and exhibit low mass recoveries. This indicates that the outskirts of the tracer plume may have passed the wells. This indicates that the main tracer plume mass went towards the Treatability Study area, further validating the estimated flow directions.

It should be considered that no monitoring wells for the tracer test were located east of the injection well. However, none of the drinking water wells located within the Countryside community located east of the injection well have shown high concentrations of TCE. In contrast, multiple drinking water wells in the Broad Run Farms community located west of the injection well have shown high concentrations of TCE [EPA, 2015a].

The flow directions are somewhat uncertain based on visual estimates of measurement tendencies. Therefore, these flow directions are not expected to be certain estimates but more a ballpark figure of the expected tendency in the flow direction. However, four different methods were evaluated, and all show the same tendency a northwest movement of water and chemicals from the Source area towards the Treatability Study area. The four methods are the potentiometric surface measurements, TCE measurements, tracer measurements, and drinking water well measurements. Therefore, it is assessed that the estimated flow direction of northwest, from the Source area to the Treatability Study area, is a good estimate. Also, the tracer test successfully mimicked the estimated transport path of the TCE.

The tracer data with an intermediate or strong recovery were used for further analysis and are marked with red in figure 9.1. A more detailed explanation of the categorizing of recovery types for the screenings is conducted in chapter 3. An overview of the raw tracer data used for further analysis is shown in figure 9.2.

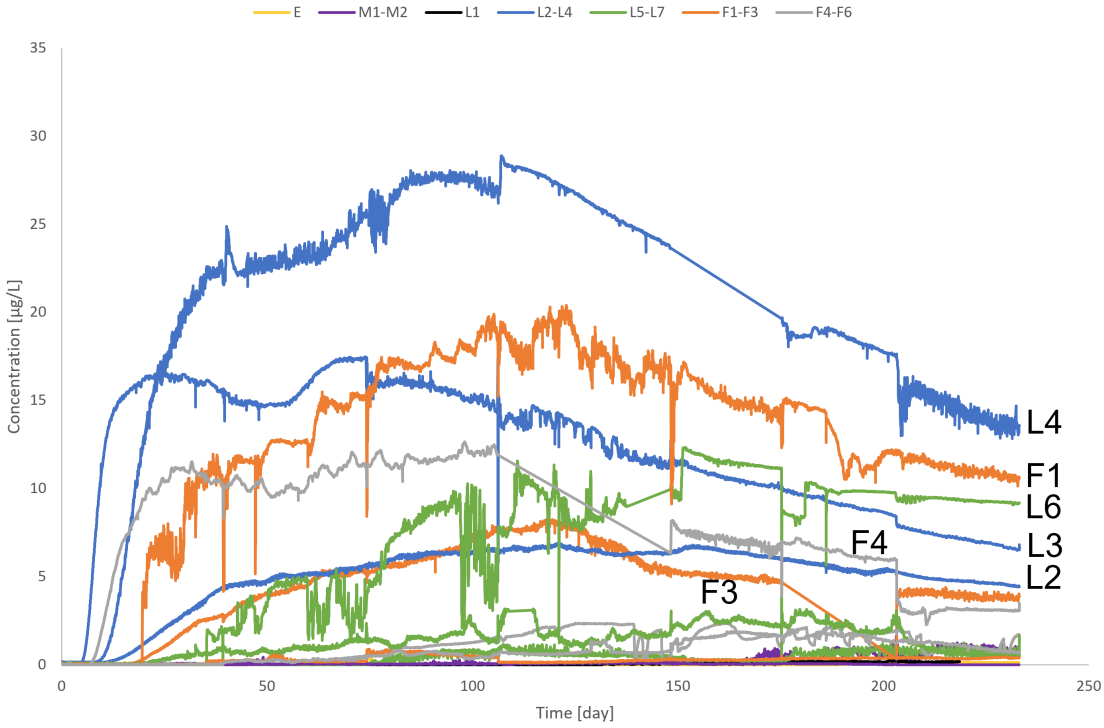

Figure 9.2: Overview of raw tracer data used for further analysis. The seven tracer data sets that yielded the highest concentrations are marked, while the remainder will be shown in more detail in figure 9.3. An aerial overview of the screening location is shown in figures 9.1.

The seven tracer data sets that yielded the highest concentrations are all located within the Treatability Study area. Furthermore, all three screenings located within well RI-21 (L2-L4) are represented, while two of the three screenings within well RI-23 (F1-F3) are represented. These two wells had the highest mass recovery rate at 12.6% and 6.23% for wells RI-21 (L2-L4) and RI-23 (F1-F3), respectively.

The tracer data consists of approximately 11000 data points, and most data sets show a significant amount of fluctuation. To analyze such big and fluctuating data sets, data treatment is required.

9.2 Development and Steps in FAST-MD Procedure

Both data reduction and smoothing of the tracer data are done as part of procedure part 1 of the Fast-MD procedure, and the results are shown in figure 9.3. In chapter 5 a further explanation of the Fast-MD procedure can be found.

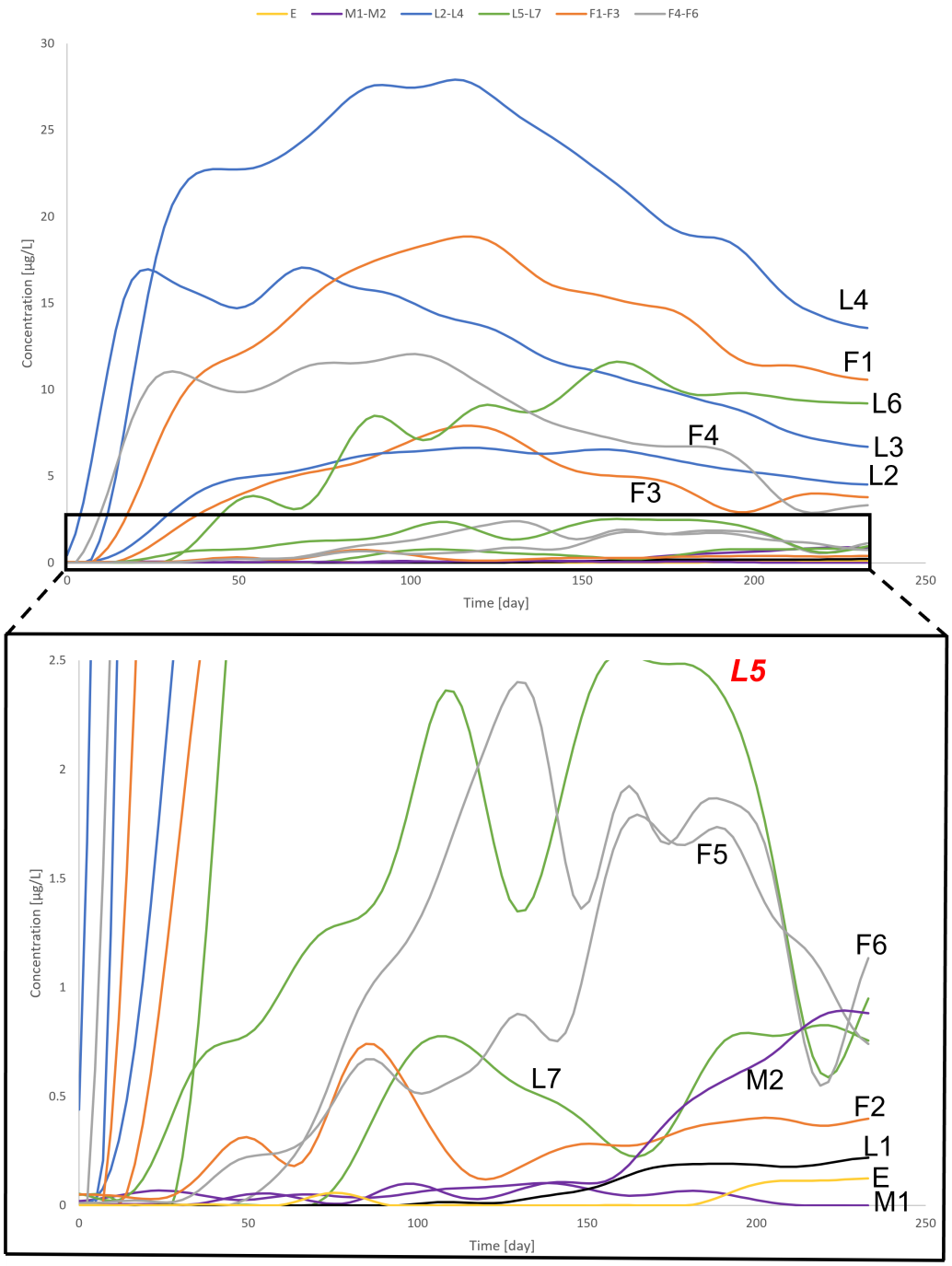

Figure 9.3: Overview of tracer data used for further analysis after reduction in data points and smoothing as part of the FAST-MD procedure, which is further explained in chapter 5. The screening marked with red is the one used to demonstrate part of the FAST-MD procedure later in this section. An aerial overview of the screening location is shown in figures 9.1.

Comparing figures 9.2 and 9.3, the tracer data still shows the same tendencies even though the data was reduced to a 100 data points. Furthermore, the clear fluctuation in the raw tracer data is no longer present due to the smoothing algorithm. However, some of the tracer data sets are still fairly complex, showing multiple peaks in concentration. A multi-domain model of the advection-dispersion equation is used to handle such complex tracer data. The solution can be found in chapter 4 in equations (4.16) and (4.17). A short

demonstration of the FAST-MD procedure will be shown for screening RI-22S (L5). A more detailed description of the FAST-MD procedure for this screening is also shown in chapter 5.

An overview of the three procedure parts in the FAST-MD procedure is shown in figure 9.4.

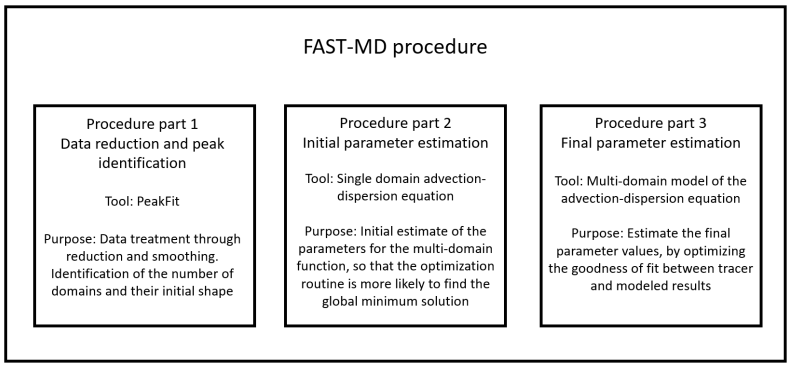

Figure 9.4: Overview of the three procedure parts in the FAST-MD procedure, including tools and purpose.

The purpose of procedure part 1 is, the data treatment method already demonstrated, and to identify the number of domains required for the multi-domain model of the advection-dispersion equation. Furthermore, the purpose is also to give an initial estimate of their position and shape. The software PeakFit is used for procedure part 1 [Systat Software Inc.]. The software identifies local maxima and residual peaks based on the reduced and smoothed tracer data set. These are then fitted to the reduced and smoothed data set using a sum curve of the identified peaks.

The number of peaks required is optimized by removing the peak with the lowest area under the curve and then refitting the peaks. If the goodness of fit or general shape of the peaks is significantly altered, the peak is assessed as having a meaningful impact and is not removed. If no significant change is seen, the peak can be removed. This process is further explained in chapter 5 figure 5.3. In figure 9.5 the results of the FAST-MD procedure part 1 is shown.

The results show that four domains are required to describe the reduced and smoothed tracer data set. The first peak describes the initial increase in concentration after approximately 25 days. The second peak describes the continued increase in concentration until around 90 days. The third peak describes the rapid peak occurring from approximately day 100 till 125. Finally, the fourth peak is used to describe the remainder of the tracer data set where a final peak occurs.

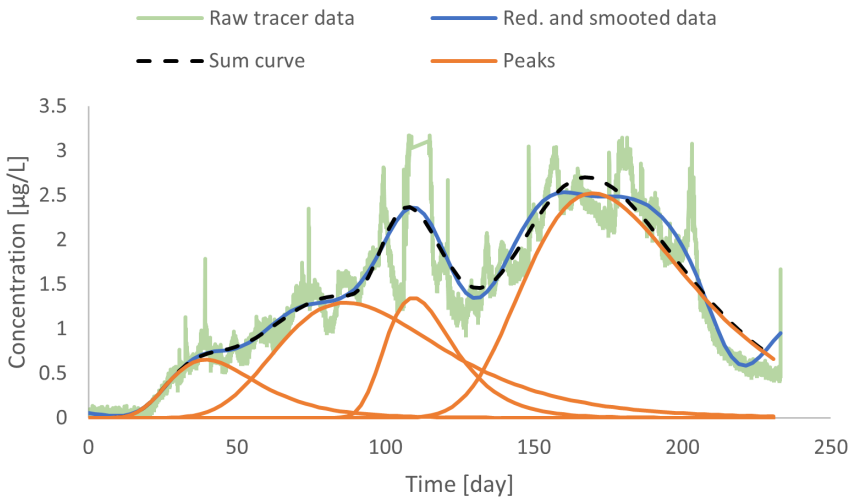

Figure 9.5: Results from procedure part 1 of the FAST-MD procedure, showing the fit between the sum curve of the identified peaks and the reduced and smoothed data set. Results are from screening RI-22S (L5).

In figure 9.6 the results of the FAST-MD procedure part 2 is shown.

The purpose of procedure part 2 is to obtain an initial estimate of the parameters for the multi-domain model so that when the optimization routine is run, in procedure part 3, the likelihood of achieving the global minimum solution is increased. The peaks identified in procedure part 1 is fitted with the advection-dispersion equation solution presented in chapter 4 and (4.14) and (4.15). A more detailed overview of procedure part 2 can be found in chapter 5 figure 5.5.

As calibration variables, three parameters are used: pore-water velocity, v, the effective dispersion coefficient, D, and the inlet concentration, c_0. This means that a different inlet concentration is used for each domain, as illustrated in figure 9.6 part A. A different inlet concentration for each domain is unrealistic and does not make sense from a hydrogeological standpoint. This estimate is only done to generate estimates for the final optimization of pore-water velocity and effective dispersion coefficient in terms of the peak shapes.

In figure part B the inlet concentration shown is the sum of the inlet concentrations shown in figure part A and is used for all the domains. The weighting factors are distributed based on the area under the curve of each peak shown in figure part A, in relation to the total area under the curve of all the peaks. Using these initial parameters, the results of the multi-domain solution are shown in figure part C, which gives a good fit, especially for the reduced and smoothed tracer data set.

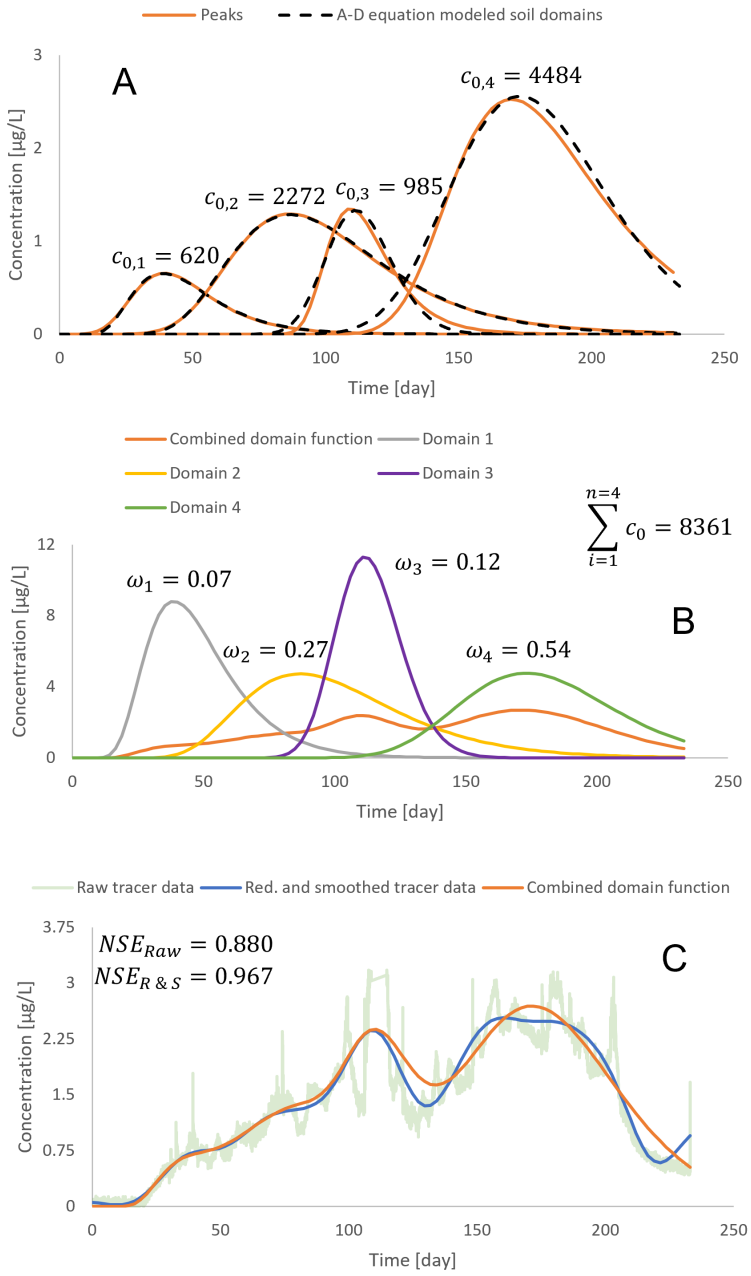

Figure 9.6: Results from procedure part 2 of the FAST-MD procedure. In figure part A the individual fitting of peaks is shown. In figure part B, the individual domains are shown. Figure part C shows the fit for the combined domain function using the initial parameters. Results are from screening RI-22S (L5). Units for the inlet concentration are the same as the y-axis.

The purpose of procedure part 3 is to use these initial parameters to obtain the optimized parameters for the tracer data. This is done by minimizing the sum of squared residuals between the combined domain function and the reduced and smoothed tracer data set. The calibration variables are the domain-dependent weight factors, pore-water velocities, and effective dispersion coefficients. As well as the inlet concentration, which is not domain-dependent. A more detailed description of procedure part 3 is conducted in chapter 5 figures 5.6 and 5.7. In figure 9.7 the results of the FAST-MD procedure part 3 is shown.

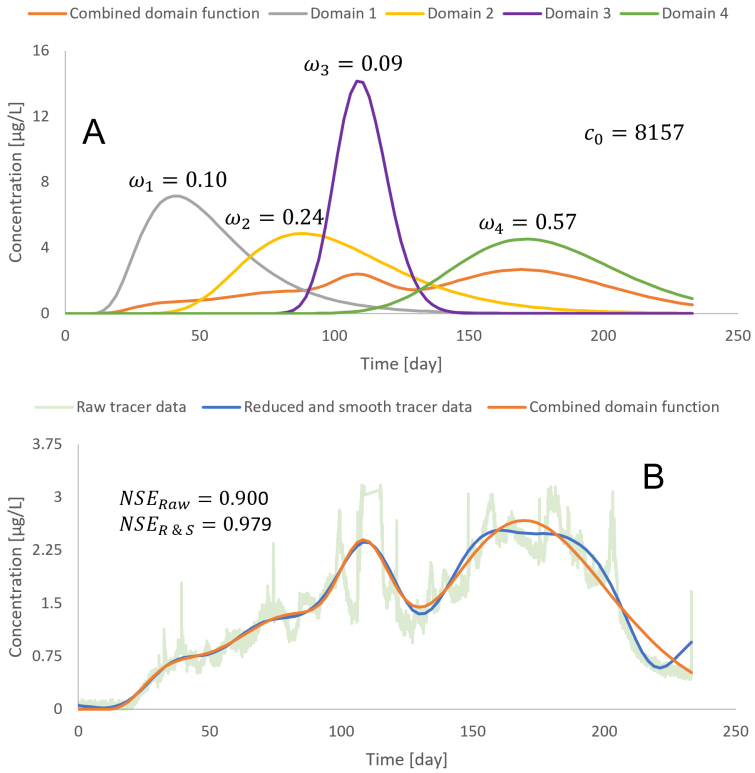

Figure 9.7: Results from procedure part 3 of the FAST-MD procedure. In figure part A the individual domains are shown. Figure part B shows the fit between the combined domain function and the tracer data sets. Results are from screening RI-22S (L5). Units for the inlet concentration is the same as the y-axis.

The individual and the combined domain function did not change much from the initial parameter estimate; however, a slight improvement in the fit is shown. This was also expected since the fit was already good. The fit of the raw tracer data is not as good, but when considering the amount of fluctuation that is also expected.

9.3 Initial Validation based on Dispersivity and Hydraulic Conductivity

The results from the FAST-MD procedure were evaluated using a validation tool based on literature values for dispersivity obtained with a single-domain model; the results are shown in figure 9.8. The validation tool is further explained in chapter 4.

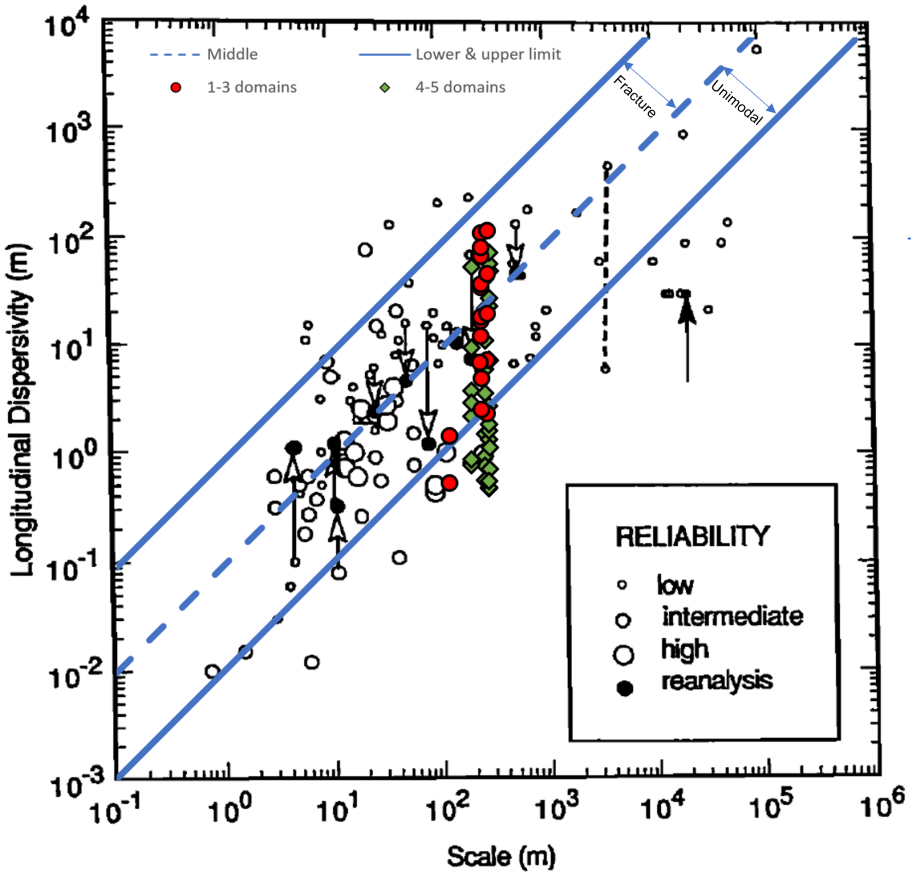

Figure 9.8: Longitudinal dispersivity as a function of distance from injection to detection well. Arrows indicate reported values at tails and corresponding values from reanalyses at heads. The dashed black line connects two dispersivity values determined at the same site. The solid and dashed blue lines indicate an expected interval when using a single-domain model. The expected interval is divided into two soil types fractured and unimodal. Results are all modeled screenings from the FAST-MD procedure. Modified from [Gelhar and Collins, 1992].

The dispersivities for the screenings with 1-3 domains show a somewhat equal distribution between the expected values for fractured and unimodal soil types. This means that some of the dispersivity values were lowered when compared to the literature values for fractured medias, as was expected. For the screenings with 4-5 domains, lower values of dispersivity were found. Many are lower than the expected range of dispersivities when using a single domain solution. The dispersivities outside the expected range mainly represent the rapid peaks identified in the tracer data, meaning very low dispersivities were expected for these domains as these represent the rapid fracture movement of the tracer. This was also the hypothesis, and the estimated parameters for the FAST-MD procedure are therefore validated. An further analysis of the dispersivity values is conducted in chapter 8 figure 8.4.

Using the estimated pore-water velocities from the FAST-MD procedure and Darcy's law, an estimate of the saturated hydraulic conductivity for each screening was found. Hydraulic conductivity is one of the most important hydrogeological parameters as it describes a fluid's ability to be transported through a porous medium [Murphy, eds]. The effective porosity is estimated through modeled results at the HLLSS [Field, 2020]. The hydraulic gradient is based on the potentiometric surface maps. A more detailed description of the

calculation can be found in chapter 8 equation (8.3). The estimated hydraulic conductivity is shown together with literature values for hydraulic conductivity from different soil types in figure 9.9.

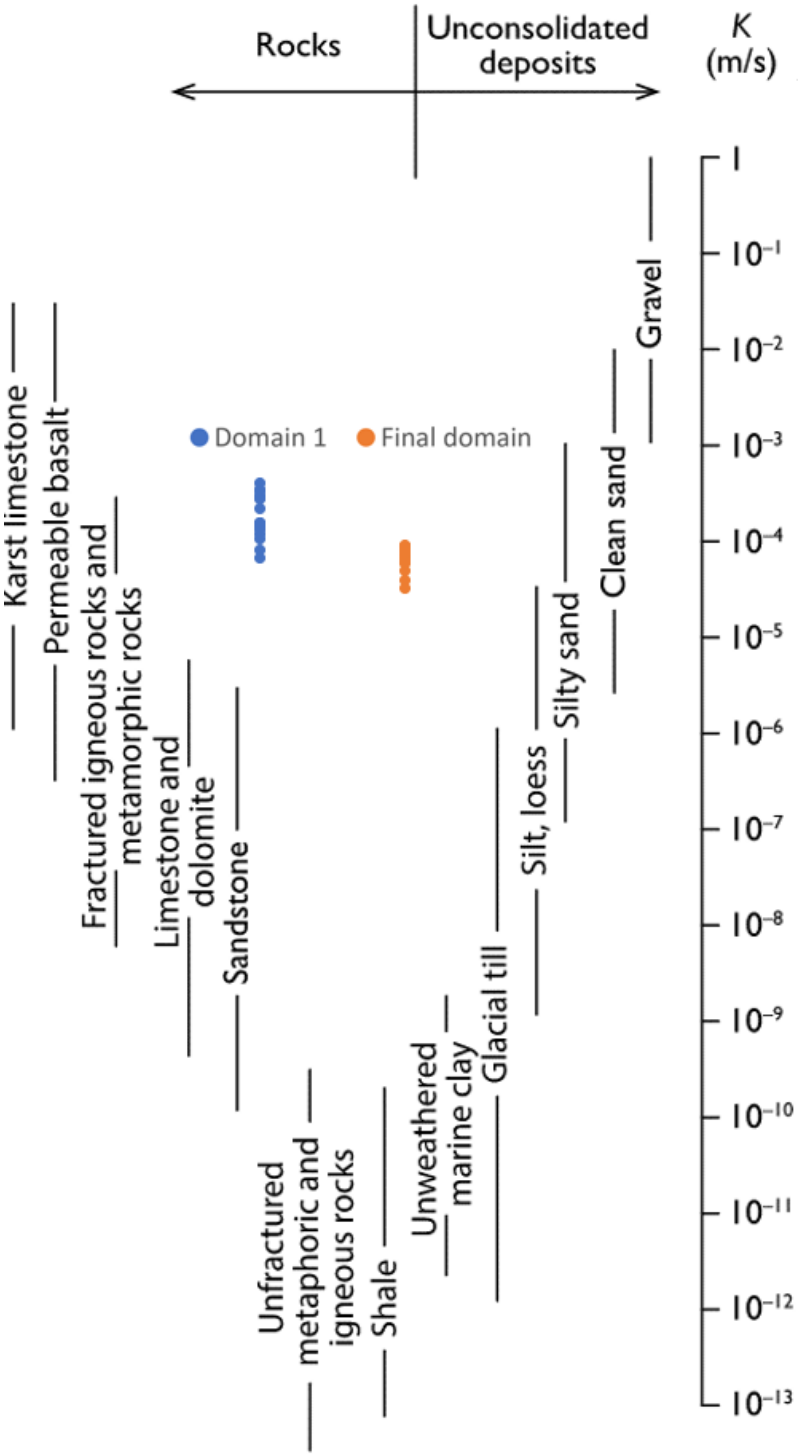

Figure 9.9: Estimated hydraulic conductivities for domain 1 and the final domain for each screening. Also, literature values for hydraulic conductivity from different soil types are shown. Modified from [Freeze and Cherry, 1979].

The estimated values are compared to the rock soil types due to the known geology at the

HLLSS, where the tracer was injected into the fractured bedrock layer. The values are in the upper spectrum of the "Fractured igneous rocks and metamorphic rocks" type, while somewhat in the middle for the soil types "Karst limestone" and "Permeable basalt". The difference in hydraulic conductivity between domain 1 and the final domain is relatively minimal when considering the scale of magnitude in which a soil can vary in hydraulic conductivity, as illustrated in the figure. A further description of the considerations regarding the hydraulic conductivities is conducted in chapter 8 figure 8.5.

9.4 Site Application using Hydrogeology and Pollution

Using the results from the FAST-MD procedure, a cross-sectional profile with some of the key parameters is shown in figure 9.10. A brief overview of the FAST-MD results for all of the tracer data can be found in chapter 7.

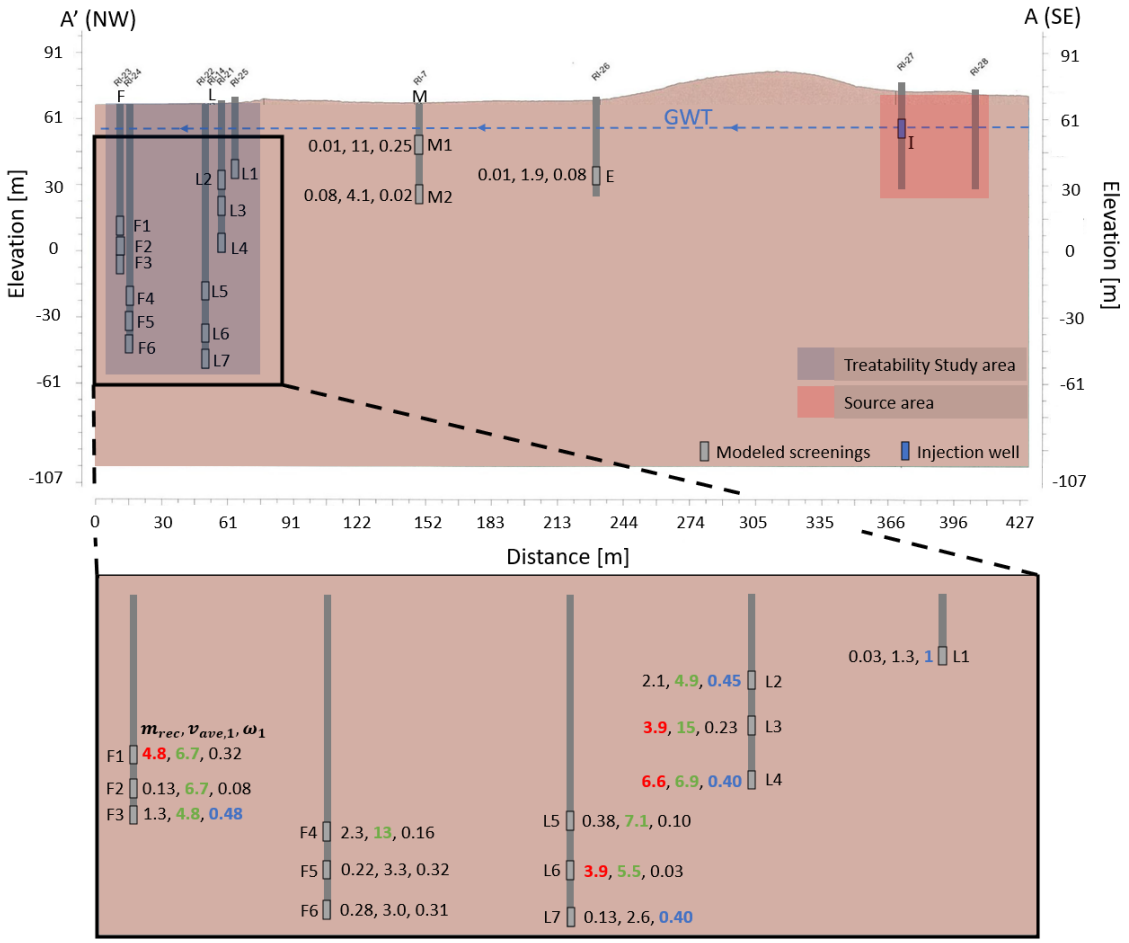

Figure 9.10: Cross-sectional profile showing estimated parameter values for the screenings. The parameters shown at the screenings are in the following order: mass recovery [%], average velocity for domain 1 [m/d], weight factor for domain 1. Values marked in red indicate a mass recovery higher than 3%. Values marked with green indicate an average velocity higher than 4.5 m/d. Values marked with blue indicate an weight factor higher than 0.40. The cross-sectional profile is based on the dashed gray transect line shown in figure 9.1. The calculation of the average velocity is shown in chapter 8 in equation 8.2.

The cross-sectional profile shows that a lot of the higher values in terms of both mass recovery, average velocity, and weight factor are situated within the shallow part of the

Treatability Study area. This means that the main tracer plume was transported through the shallow part of the Treatability Study area. Furthermore, a significant portion of that mass is transported through domain 1, and it is being transported quite rapidly, presumably through mainly fracture-dominated transport. Further analysis of the key parameters obtained from the FAST-MD procedure can be found in chapter 8. Some additional parameters is shown in table 9.1.

Table 9.1: Summarized parameters for the FAST-MD procedure results for domain 1. The parameters in order from left to right is: The distance from injection to monitoring well, the change in depth from injection to monitoring well (using the center of the screening), mass recovery, average velocity, dispersivity, and weight factor.

Location		L	$\Delta depth$	m_{rec}	$v_{ave,1}$	τ_1	ω_1	No. of domains
RI name	Given name	[m]	[m]	[%]	[m/d]	[m]	[-]	[-]
RI-26I	E	142	17	0.01	1.9	0.62	0.08	2
RI-7S	M1	211	0.42	0.01	11	66	0.25	4
RI-7D	M2	211	24	0.08	4.1	2.5	0.02	4
RI-25D	L1	271	10	0.03	1.3	8.5	1	1
RI-21S	L2	277	17	2.1	4.9	143	0.45	2
RI-21I	L3	277	29	3.9	15	86	0.23	3
RI-21D	L4	277	45	6.6	6.9	104	0.40	3
RI-22S	L5	283	68	0.38	7.1	26	0.10	4
RI-22I	L6	283	87	3.9	5.5	7.1	0.03	5
RI-22D	L7	283	100	0.13	2.6	6.0	0.40	2
RI-23S	F1	317	36	4.8	6.7	150	0.32	2
RI-23I	F2	317	45	0.13	6.7	8.9	0.08	3
RI-23D	F3	317	55	1.3	4.8	60	0.48	4
RI-24S	F4	308	69	2.3	13	70	0.16	4
RI-24I	F5	308	80	0.22	3.3	28	0.32	4
RI-24D	F6	308	91	0.28	3.0	8.8	0.31	4

To obtain more knowledge of the location and orientation of the major fractures in the bedrock between the Source area and the Treatability Study area, the EPA conducted gamma logging measurements. These were used to determine stratifications within the bedrock. The results are shown in figure 9.12. Furthermore, a cross-sectional profile of the TCE plume is also shown in the figure. The transect line used to create these cross-sectional profiles is shown in figure 9.11.

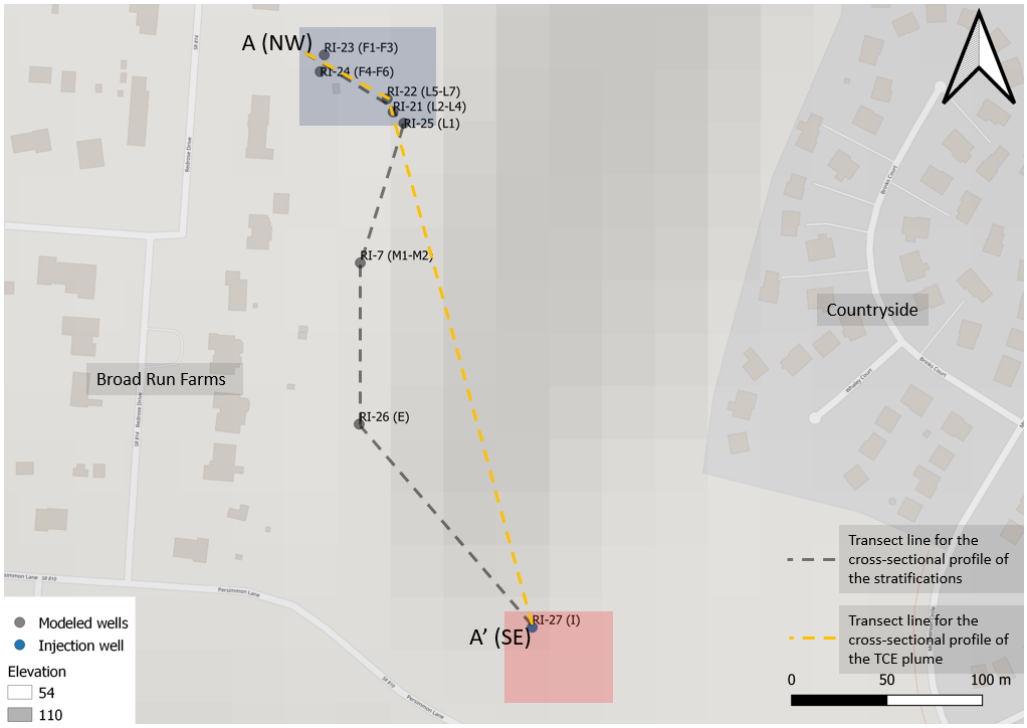

Figure 9.11: Aerial overview of the two transect lines used for the cross-sectional profiles in figure 9.12. The location of the landfill is clearly indicated by the change in elevation.

The three highest mass recoveries from the tracer test are all located within the estimated main TCE plume transport path. These screenings are located within two stratifications, a dark blue and light brown layer. The dark blue layer is also connected to the injection well. These three screenings have a somewhat high average velocity and weight factor for domain 1. This indicates that a substantial amount of mass is transported rapidly through fractures that might be the identified dark blue and light brown layers. This may also be the case for the TCE plume based on the similarity in results. The transport of the dissolved TCE and the tracer is mainly controlled by groundwater movement as sorption, biodegradation, and vapor migration were assessed as having a slight influence on the transport of both chemicals at the HLLSS as established in chapters 2 and 3, further validating the comparison between the dissolved TCE and the tracer transport.

Furthermore, the amount of domains for these three screenings is 2-3. This means that a somewhat low amount of exchange through diffusion between different soil property domains occurred; otherwise, a higher amount of domains would probably have been required to describe these tracer data sets. This further emphasizes that the tracer transport has primarily been dominated by fracture transport for these three screenings.

When comparing these cross-sectional maps, an uncertainty is that they are not generated from entirely the same area. However, it is generally within the same orientation north-westbound. Therefore it is assessed as a reasonable comparison. Also, when comparing the key bedding units marked with red on the TCE Plume Map (A) with the stratifications seen in the Stratification Map (B), the two are very similar, validating the assessment that the comparison between the maps is valid.

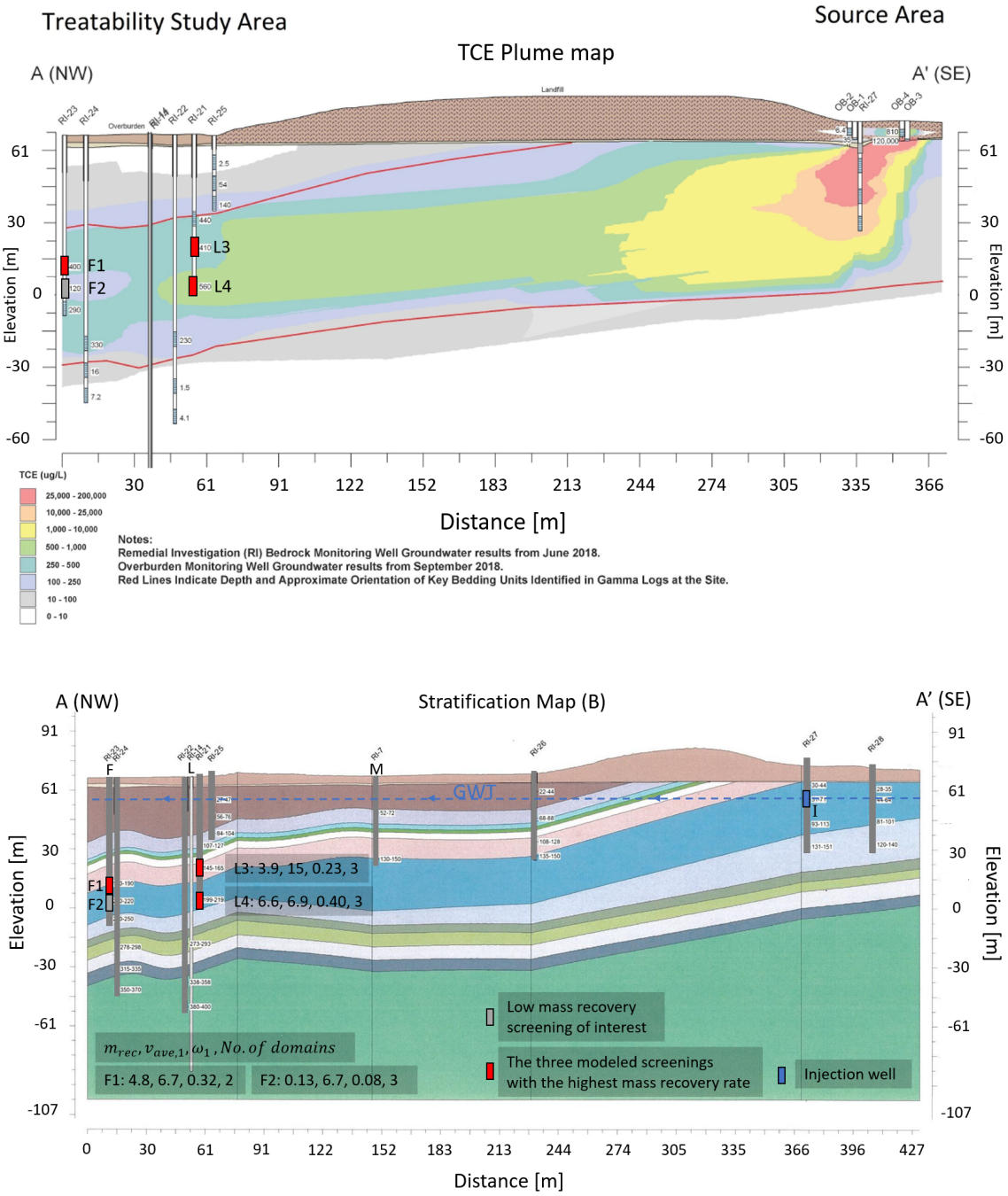

Figure 9.12: Figure part (A) shows a cross-sectional profile of the TCE concentration from the Source area to the Treatability Study area based on measurements in 2019. Modified from [EPA, 2019]. Figure part (B) shows a cross-sectional profile of the different stratifications in the bedrock from the Source Area to the Treatability Study area. Modified from [Field, 2020]. Additionally the three screenings with the highest mass recovery rates are shown. The cross-sectional profiles is based on the transect lines shown in figure 9.11.

Another interesting tendency is that screening F2 has a low mass recovery compared to the other screenings located within the same well or depth. The recovery was so low that it was assessed as an intermediate tracer recovery. TCE concentrations also decrease in the near vicinity of F2, presumably caused by the measurements of TCE at this screening. This indicates that perhaps some fracture orientations are causing a significant amount of mass to bypass the screening, as shown by both the TCE and tracer measurements. This

further validates the assessment that the dissolved TCE and tracer plume had similar transport paths. However, the stratification map does not indicate a change in geology. This could be due to the fracture being small causing the gamma logs measurement to not detect it, or that the fracture orientation was different from the estimated flow direction, as the system, in reality, is 3-dimensional.

Conclusion 10

A geohydrological overview of the Hidden Lane Landfill Superfund Site (HLLSS) was conducted. An estimated Source area and Treatability area were defined. Governing flow directions based on TCE and potentiometric surface measurements from the Source area showed a north-west flow direction towards the Treatability Study area. Sixteen screenings were identified as having an intermediate or strong recovery from the tracer experiment. These screenings validated the governing flow directions as the strong tracer recoveries were located within the Treatability Study area.

A robust, rapid, objective and semi-automated procedure (FAST-MD) was developed for analyzing the tracer data. Using the software PeakFit a procedure for data treatment of tracer data and an objective semi-automated routine for identifying individual flow domains were developed. Furthermore, an initial estimate of the shape of the individual flow domain was found and proved somewhat accurate compared to the final estimated results. Using the results from PeakFit, a model for rapid estimation and automated calibration of the individual flow domains using the multi-domain solution of the advection-dispersion equation was developed.

The FAST-MD procedure was initially validated by showing that tracer dispersivities for the identified individual flow domains became close to or lower than literature levels for unimodal soil systems. In comparison, if a tracer data set was treated as a single-domain, the dispersivities were dramatically higher and, as expected, close to those estimated literature levels for fractured systems. Thus, the FAST-MD procedure seems able to realistically identify the dominating individual flow domains within a complex geological setting like those found at the HLLSS.

Application of the parameter values from the FAST-MD procedure found that the main tracer mass was recovered in the shallow part of the Treatability Study area of the HLLSS through a few dominant transport domains. It was found that the distribution of tracer mass within the shallow part of the Treatability Study area was somewhat equally distributed between rapid and slow movement. Similar results were found when comparing the results to TCE measurements and a model of the geological stratifications, further validating the results from the FAST-MD procedure.

10.1 Future Perspectives

For future usage and modifications of the FAST-MD procedure, a point of improvement could be step 7: Optimization of the number of peaks required. This step is part of procedure part 1: Data reduction and peak identification. Currently, an assessment of the change in shape for the other peaks is made when the peak with the lowest area under the curve is removed. Instead, the change in parameter values for the pulse peak with power term model could be evaluated. A threshold could be set for the maximum change in chosen parameters, further objectifying the procedure. A parameter of interest would be a_2 as it describes the width of the peak and thereby the amount of tailing for the peak, which would be the equivalent to the effective dispersion coefficient in the multi-domain solution of the advection-dispersion equation. A parameter of less interest would be a_0 as it describes the amplitude of peak, equivalent to the inlet concentration in the multi-domain solution of the advection-dispersion equation. This is because the inlet concentration is not a domain-dependent parameter, and an inlet concentration for all domains is estimated later in the FAST-MD procedure. Another modification could be implementing exchange between the domains in the FAST-MD procedure, which would lead to more accurate estimates of the solute transport parameters.

It would be interesting to evaluate the FAST-MD procedure on a larger scale site, such as the Hanford Site [EPA, c], to see if the same tendencies in terms of the relation between dispersivity and the number of domains found in this thesis would be yielded. Furthermore, it would be interesting to evaluate the FAST-MD procedure when multiple tracers are present, as could be the case at the Hanford Site. This is because other studies have used PeakFit, which is the tool used for procedure part 1 of the FAST-MD procedure, to separate different tracers occurring in the same time span [Andreo et al., 2015] and [Groten and E. Calvin Alexander, 2015]. This could perhaps be implemented as an extra tool in the FAST-MD procedure.

Another interesting aspect would be to utilize the FAST-MD procedure to construct plume maps. This would be of interest as the travel distance and concentration could be calculated for each domain to identify the plume's fast and slow-moving parts. The FAST-MD procedure could also be used for risk assessment models in the same context. The breakthrough time for the different domains could be estimated to obtain a more complete picture of the plumes distribution and transport to a given recipient. This is vital information when dealing with risk assessments, as the breakthrough times of the different domains could be relevant depending on the concentration distribution of the chemical in the different domains and the sensitivity of the recipient.

References

Andreo, Bartolomé, Carrasco, Francisco, Durán, Juan José, Jiménez, Pablo and LaMoreaux, James W., 2015. *Hydrogeological and Environmental Investigations in Karst Systems.* Environmental Earth Sciences 1, Springer, Berlin, Germany.

Aquaveo. URL https://www.aquaveo.com/software/gms-modflow.

Biggar, J. W. and Nielsen, D. R., 1962. *Miscible Displacement: II. Behavior of Tracers.* Soil Sci. Soc. Am. J. 26(2): 125-128.

Brubaker, Marcus. CSC320 Tutorial Notes. URL https://www.google.com/url?sa=t&rct=j&q=&esrc=s&source=web&cd=&ved=2ahUKEwiZyPikud32AhUUEEQIHa2tCsYQFnoECA0QAw&url=http%3A%2F%2Fpeople.csail.mit.edu%2Fhasinoff%2F320%2Fsliding-notes.pdf&usg=AOvVaw0iiDD-HxfzWNnnKBKmQNMk.

Cascarano, Ryan Nicholas, 2018. *Use of Fluorescein Dye for Characterizing Water and Solute Flux Across the Groundwater – Surface Water Interface.* Master's Thesis at Western Michigan University.

Chen, Honguan, 2018. *Streamline Tracing and Sensitivity Calculation in Fractured Reservoir with Complex Geometry: Field Application to History matching and Flood Optimization.* Dissertation at Texas A&M University.

CLU-IN. URL https://clu-in.org/issues/default2.focus/sec/Fractured_Rock/cat/Overview/.

Delvin, J.F., 2020. *Groundwater Velocity.* The Groundwater Project, Guelph, Ontario, Canada.

ECHA. URL https://echa.europa.eu/da/registration-dossier/-/registered-dossier/18690/5/1.

eFluids. URL https://www.princeton.edu/~asmits/Bicycle_web/streamline.html.

Enviroforensics. URL https://www.enviroforensics.com/blog/investigation-accuracy-tracer-testing/.

EPA, 2015a. *Final Remedial Investigation Report. Hidden Lane Superfund Site. Sterling, Virginia.* EA Engineering, Science, and Technology, Inc., PBC. EA Project No. 14530.13, Revision 3, 1311 Continental Drive, Suite K Abingdon, Maryland 21009.

EPA, 2015b. *Final Remedial Investigation Report. Hidden Lane Superfund Site. Sterling, Virginia, Appendix C.* EA Engineering, Science, and Technology, Inc., PBC. EA Project No. 14530.13, Revision 3, 1311 Continental Drive, Suite K Abingdon, Maryland 21009.

EPA, 2019. *Supplemental Remedial Investigation Report. Hidden Lane Superfund Site. Sterling, Virginia.* EA Engineering, Science, and Technology, Inc., PBC. Project No. 14530.13, Version: FINAL, 1311 Continental Drive, Suite K Abingdon, Maryland 21009.

EPA, a. URL `https://www.epa.gov/newsreleases/epa-updates-superfund-national-priorities-list-clean-pollution-address-public-health-0`.

EPA, b. URL `https://www.usgs.gov/centers/sawsc/science/characterization-subsurface-bedrock-fractures-gmh-electronics-epa-superfund/`.

EPA, c. URL `https://www.epa.gov/fedfac/hanford-site-spotlight`.

EPA, d. URL `https://www.epa.gov/superfund/superfund-human-exposure-dashboard`.

EPA. URL `https://www.epa.gov/superfund`.

Field, Malcolm S., 2002. *The Qtracer2 Program for Tracer-Breakthrough Curve Analysis for Hydrological Tracer Tests.* EPA/600/R-02/001 and EPA/600/CR- 02/001, Washington D.C.

Field, M.S., 2003. *Tracer-Test Planning Using the Efficient Hydrologic Tracer-Test Design (EHTD) Program.* EPA/600/R-03/034 and EPA/600/CR-03/034, U.S. Environmental Protection Agency, Washington D.C.

Field, M.S., 2020. *Tracer-Test Results for the Hidden Lane Landfill Superfund Site, Sterling, Va., June 2019 - December 2019: Technical Report EPA/600/R-XX/XXX [Unpublished draft].* U.S. Environmental Protection Agency, Washington D.C., United States of America.

Freeze, R. Allan and Cherry, John A., 1979. *Groundwater.* Prentice-Hall, Englewood Cliffs, NJ 07632.

Gao, Bin, 2022. *Emerging Contaminants in Soil and Groundwater Systems (1st ed.).* Elsevier, Amsterdam, Netherlands.

Gelhar, L. W. and Collins, M. A., 1992. *A Critical Review of Data on Field-Scale Dispersion in Aquifers.* Water Resources Research 28(7): 1955-1974.

Gerke, Kirill M., Sidle, Roy C. and Mallants, Dirk, 2013. *Criteria for selecting fluorescent dye tracers for soil hydrological applications using Uranine as an example.* Journal of Hydrology and Hydromechanics 61(7): 13pp.

Goldscheider, Nico and Drew(eds), David, 2007. *Methods in Karst Hydrogeology.* International Association of Hydrogeologist (26), CRC Press, Boca Rotan, United States of America.

Grenier, Christophe, Fourno, Andre, Mouche, Emmanuel, Delay, Frédérick and Benabderrahmane, Hakim, 2005. *Assessment of Retention Processes for Transport in a Fractured System at Äspö (Sweden) Granitic Site: From Short-Time Experiments to Long-Time Predictive Models.* Dynamics of Fluids and Transport in Fractured Rock. Geophysical Monograph Series 162: 117-128.

Groten, Joel T. and E. Calvin Alexander, Jr., 2015. *Karst Hydrogeologic Investigation of Trout Brook, Dakota County, Minnesota.* Conference: National Cave and Karst Research Institute Symposium 5, DOI: http://dx.doi.org/10.5038/9780991000951.1012.

Huling, Scott G. and Weaver, James W., 1991. *Ground Water Issue, Dense Nonaqueous phase liquids.* Ground Water Issue EPA/540/4-91-002.

Hægland, Håkon, 2009. *Streamline methods with application to flow and transport in fractured media.* Doctor Scientiarum Thesis, University of Bergen.

Jarai Mon, Markus Flury and B.Harsh, James, 2006. *Sorption of four triarylmethane dyes in a sandy soil determined by batch and column experiments.* Geoderma 133(3): 217-224.

Jury, William A. and Roth, Kurt, 1990. *Transfer Functions and Solute Movement through Soil.* Birkhauser Verlag, Basel, Switzerland.

Kresic, Neven and Stevanovic, Zoran, 2009. *Groundwater Hydrology of Springs, Engineering, Theory, Management and Sustainability.* Butterworth-Heinemann, Oxford, United Kingdom.

Leij, Feike J., Sciortino, Antonella, Huang(eds.), Pan Ming, Li(eds.), Yuncong and Sumner(eds.), Malcolm E., 2012a. *Chapter 7 Solute Transport, Handbook of Soil Sciences Properties and Processes, (2nd ed.).* CRC Press, Boca Raton, United States of America.

Leij, Feike J., Toride, Nobuo, Field, Malcolm S. and Sciortino, Antonella, 2012b. *Solute transport in dual-permeability porous media.* Water Resources Research 48(4), DOI: https://doi.org/10.1029/2011WR011502.

Loll, P. and Moldrup, P., 2000. *Soil Characterization and Polluted Soil Assessment.* Course book for: Environmental Soil Science and Geostatistics, Aalborg University, Aalborg.

Martin, C.J., 2011. *Appendix E—Overview of Hanford Hydrogeology and Geochemistry.* Hanford Site Groundwater Monitoring for 2011 DOE/RL-2011-118, Rev. 0, U.S. Department of Energy, Washington D.C., United States of America.

Matringe, Sébastien F., Juanes, Ruben and Tchelepi, Hamdi A., 2007. *Streamline Tracing on General Triangular or Quadrilateral Grids.* SPE Journal 12(2): 217-233.

McCuen, Richard H., Knight, Zachary and Cutter, A. Gillian, 2006. *Evaluation of the Nash–Sutcliffe Efficiency Index.* Journal of Hydrologic Engineering 11(6).

Microsoft. URL `https://www.microsoft.com/da-dk/microsoft-365/excel`.

Miljøstyrelsen. URL `https://mst.dk/affald-jord/jordforurening/generationsforureningerne/`.

Minnesota Department of Health. Trichloroethylene (TCE) and Your Health. URL `https://www.health.state.mn.us/communities/environment/hazardous/topics/tce.html#health`, cited September the 08th 2021.

Murphy(eds), Brian L. and Morrison(eds), Robert D., 2015. *Introduction to Environmental Forensics (3rd ed.).* Academic Press, Cambridge, USA.

Nielsen, D. R. and Biggar, J. W., 1961. *Miscible Displacement in Soils: I. Experimental Information.* Soil Sci. Soc. Am. J. 25(1): 1-5.

Nielsen, Jesper, Karup, Dan, Jonge, Lis W. De, Ahm, Malte, Bentzen, Thomas R., Rasmussen, Michael R. and Moldrup, Per, 2018. *Can the volume ratio of coarse to fine particles explain the hydraulic properties of sandy soil?* Soil Sci. Soc. Am. J. 82(5): 1093-1100.

NIST. URL `https://webbook.nist.gov/cgi/cbook.cgi?ID=C79016&Mask=2000&Type=KOVATS-RI-NON-POLAR-ISOTHERMAL`.

Pan, H., Freeston, D.H. and O'Sullivan, M.J., 1991. *Tracer Test Design For The Rotorua Geothermal Field.* 13th New Zealand Geothermal Workshop 1991: 105-113.

Pollock, David W., 1988. *Semianalytical Computation of Path Lines for Finite-Difference Models.* Groundwater 26(6): 743-750.

QGIS. URL `https://www.qgis.org/en/site/`.

Simunek, J., van Genuchten, M.Th., Sejna, M., Toride, N. and Leij, F. J. STANMOD for Windows, Version: 2.xx, December 2003. URL `https://www.pc-progress.com/en/Default.aspx?stanmod`.

Spitz, K. and Moreno, J., 1996. *A Practical Guide to Groundwater and Solute Transport Modeling.* John Wiley & Sons, Inc., New York, United States of America.

Systat Software Inc. URL `https://systatsoftware.com/peakfit/`.

The Center for Public Integrity. URL `https://publicintegrity.org/environment/human-exposure-uncontrolled-at-114-superfund-sites/`.

Toride, Nobuo, Leij, Feike J. and van Genuchten, M. Th., 1999. *The CXTFIT Code for Estimating Transport Parameters from Laboratory or Field Tracer Experiments Version 2.1.* U.S. Salinity Laboratory, Research Report. No 137.

Wexler, Philip, 2014. *Encyclopedia of Toxicology (3rd ed.).* Elsevier Inc., Amsterdam, Netherlands.

Whittaker, Sir Edmund Taylor, 1924. *The Calculus Of Observations.* London etc. Blackie and Son limited, London, United Kingdom.

Streamline A

The streamline method has received interest as an attractive and successful method for solving problems such as flow visualization, model optimization, and more [Matringe et al., 2007], [Chen, 2018]. One of the first scientific papers on streamlines was [Pollock, 1988], which methods on developing streamlines using a cartesian grid is referenced in many other streamline papers as the base for methods developed later on [Chen, 2018], [Matringe et al., 2007], [Hægland, 2009]. Streamlines can be regarded as a subset of particle tracking as the streamlines are computed from particle tracking [Hægland, 2009]. Particle tracking is a relatively simple concept. Tracking a specific particle in a flow field can be achieved using the directional velocity components and a given time step in a finite difference model. By connecting these particle tracking points, streamlines are computed. To achieve these streamlines, interpolation within the control volumes must be done. There are multiple ways of achieving this; one of the simpler methods is simple linear interpolation. An advantage using this interpolation method is that velocity components in all three directions can be incorporated into each control volume to determine the streamline [Pollock, 1988].

The method described in the following is based on [Pollock, 1988].

In figure A.1 a sketch of a control volume with flow in and out is illustrated.

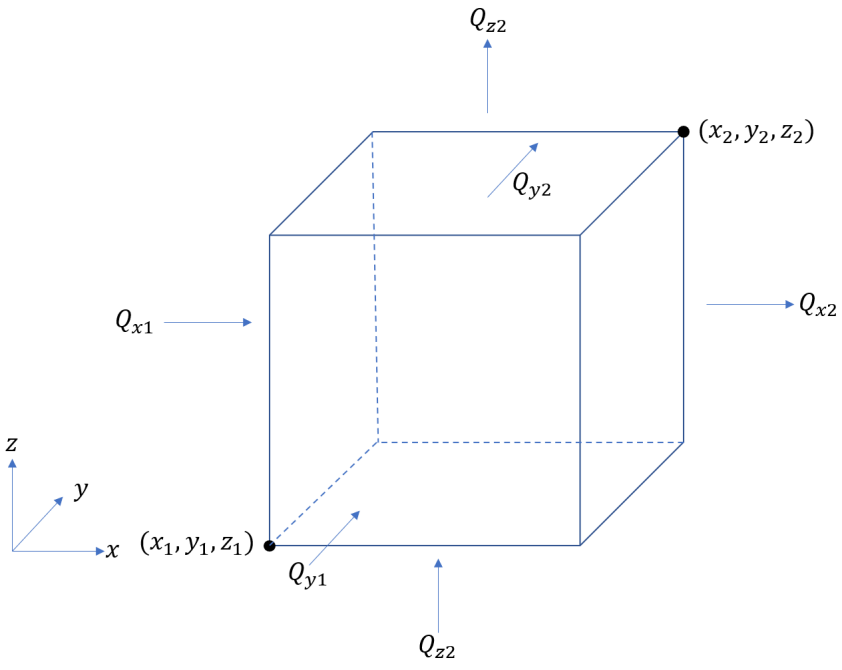

Figure A.1: Sketch of a control volume with flow in and out and the different cell phases illustrated.

The velocity component for each cell phase are shown in the following equations:

$$v_{x1} = \frac{Q_{x1}}{(n\Delta y\Delta z)} \tag{A.1}$$

$$v_{x2} = \frac{Q_{x2}}{(n\Delta y\Delta z)} \tag{A.2}$$

$$v_{y1} = \frac{Q_{y1}}{(n\Delta x\Delta z)} \tag{A.3}$$

$$v_{y2} = \frac{Q_{y2}}{(n\Delta x\Delta z)} \tag{A.4}$$

$$v_{z1} = \frac{Q_{z1}}{(n\Delta x\Delta y)} \tag{A.5}$$

$$v_{z2} = \frac{Q_{z2}}{(n\Delta x\Delta y)} \tag{A.6}$$

v_{ij}	Velocity component in the i^{th} direction and the j^{th} cell phase $[\frac{\text{m}}{\text{s}}]$
Q_{ij}	Flow component in the i^{th} direction and the j^{th} cell phase $[\frac{\text{m}^3}{\text{s}}]$
n	Porosity $\left[\frac{\text{cm}^3 \text{ pores}}{\text{cm}^3 \text{ soil}}\right]$
$\Delta x, y, z$	Length of the different cell phases $[m]$

By implementing the velocity components in the conservation of mass expression, equation (A.7) is obtained.

$$\frac{(nv_{x2} - nv_{x1})}{\Delta x} + \frac{(nv_{y2} - nv_{y1})}{\Delta y} + \frac{(nv_{z2} - nv_{z1})}{\Delta z} = \frac{Q_s}{\Delta x\Delta y\Delta z} \tag{A.7}$$

v_{ij}	Velocity component in the i^{th} direction and the j^{th} cell phase $[\frac{\text{m}}{\text{s}}]$
n	Porosity $\left[\frac{\text{cm}^3 \text{ pores}}{\text{cm}^3 \text{ soil}}\right]$
$\Delta x, y, z$	Length of the different cell phases $[m]$
Q_s	Change in flow due to storage or drainage $[\frac{\text{m}^3}{\text{s}}]$

To obtain the streamlines the velocity at a given position within the control volume needs to computed. As mentioned earlier simple linear interpolation is used for this. In the following equation the velocity as a function of position is shown:

$$v_i = A_i(i - i_1) + v_{i1} \tag{A.8}$$

v_i	Velocity at a given position for the i^{th} direction $[\frac{\text{m}}{\text{s}}]$
A_i	Velocity gradient for the i^{th} direction $[s^{-1}]$
i	Position in the the i^{th} direction $[m]$
$(x, y, z)_1$	Position of cell phase 1 the i^{th} direction $[m]$
v_{i1}	Velocity at cell phase 1 for the i^{th} direction $[\frac{\text{m}}{\text{s}}]$

The velocity gradient, A_i, is calculated using the difference in velocity between cell phase 1 and 2 divided by the cell length.

The particle moving through the control volume is expressed in equation (A.9)

$$\left(\frac{dv_i}{dt}\right)_p = \frac{dv_i}{di}\left(\frac{di}{dt}\right)_p \tag{A.9}$$

$\left(\frac{dv_i}{dt}\right)_p$	Change in particle velocity in i^{th} direction over a change in time $[\frac{\text{m}}{\text{s}}/s]$
$\frac{dv_i}{di}$	Change in velocity in i^{th} direction over a change in position in i^{th} direction $[\frac{\text{m}}{\text{s}}/m]$
$\left(\frac{di}{dt}\right)_p$	Change in particle position in the i^{th} direction over a change in time $[\frac{\text{m}}{\text{s}}]$

By differentiating, substituting, and integrating with equations (A.8) and (A.9) the travel time it takes for the particle to enter and leave a control volume can be computed and is shown in equation (A.10).

$$\Delta t_i = A_i^{-1} \cdot \ln(v_{i2}/v_{ip}) \tag{A.10}$$

Δt_i	Time for the particle to leave the cell in the i^{th} direction $[s]$
A_i	Velocity gradient for the i^{th} direction $[s^{-1}]$
v_{i2}	Velocity for the i^{th} direction at cell phase 2 $[\frac{\text{m}}{\text{s}}]$
v_{ip}	Velocity of the particle in the i^{th} direction when entering the control volume $[\frac{\text{m}}{\text{s}}]$

Through substitution of equation (A.8) in equation (A.10) the exit position of the particle from a given control volume can be computed using equation (A.11).

$$i_e = i_1 + A_i^{-1}(v_{ip}e^{A_i \Delta t_e} - v_{i1}) \tag{A.11}$$

i_e	Exit position in the i^{th} direction $[m]$
i_1	Position of cell phase 1 in the i^{th} direction $[m]$
A_i	Velocity gradient for the i^{th} direction $[s^{-1}]$
v_{ip}	Velocity of the particle in the i^{th} direction when entering the control volume $[\frac{\text{m}}{\text{s}}]$
Δt_e	Time for the particle to leave the control volume $[s]$
v_{i1}	Velocity for the i^{th} direction at cell phase 1 $[\frac{\text{m}}{\text{s}}]$

A.1 Example of a Multi-cell Problem with No Flow Boundaries

On figure A.2 the example is shown.

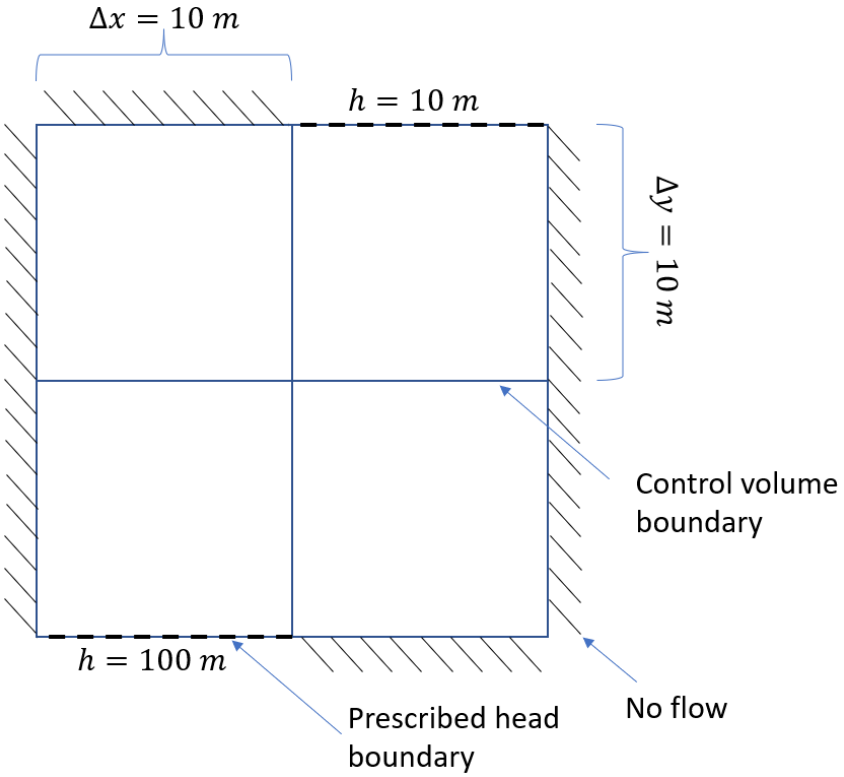

Figure A.2: Sketch of the multi-cell problem.

The velocity components are computed using the software GMS. In figure A.3, the velocity distribution obtained is shown.

Using the same methods described above, the streamlines are calculated for three different particles. The starting positions of the particles are on the upper prescribed head boundary. One very close to the left edge, one in the middle, and one very close to the right edge. The position of the particle was calculated at five different travel times equally distributed based on the travel time to exit a cell. The results are shown in figure A.4.

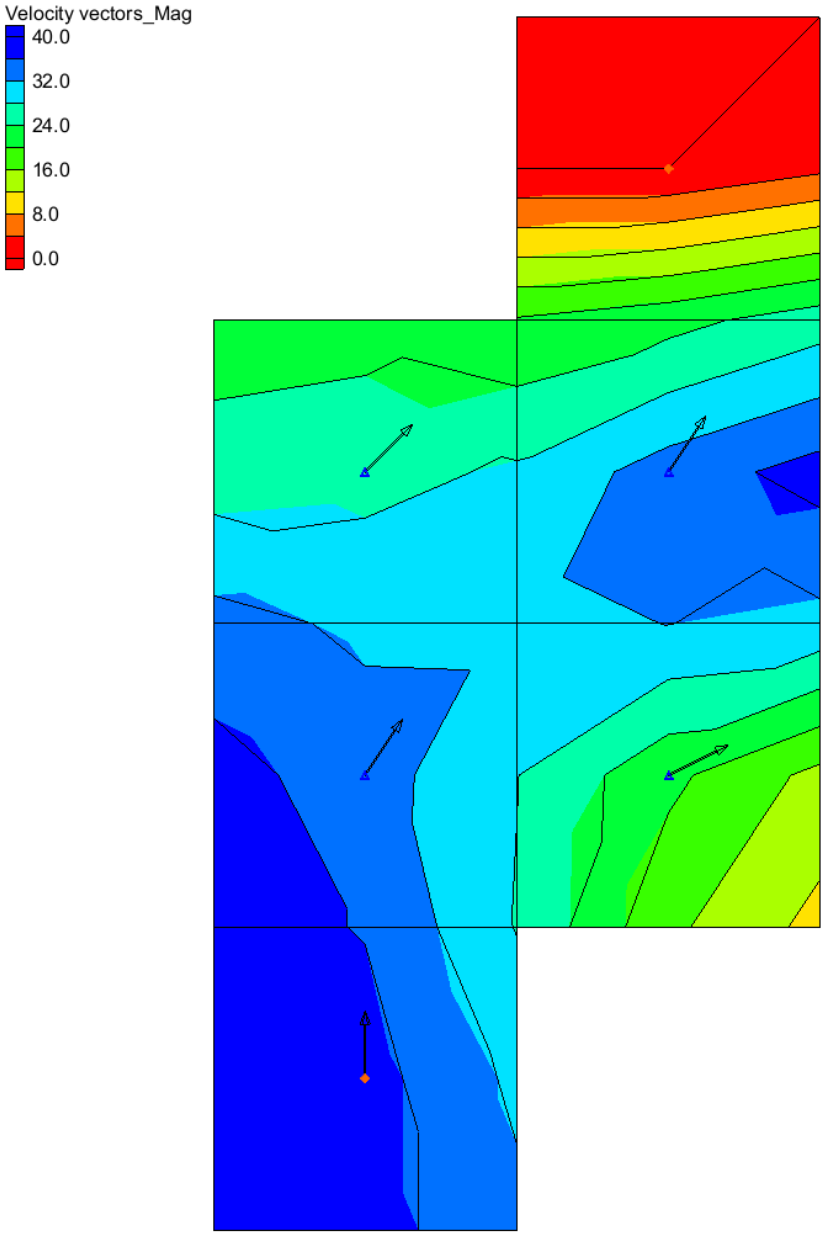

Figure A.3: Velocity components for the multi-cell problem.

When comparing figure A.3 and A.4 it is shown that the travel time fits with the magnitudes of the velocity components, e.g., having the lowest velocity magnitudes in the right part results in the highest travel time for the right starting particle. The results also shows the strength of the streamline method, as it illustrates that the difference in travel times can be several magnitudes in difference for particles within the same control volume. The certainty of the model will depend on the reliability of the velocity components computed using other models.

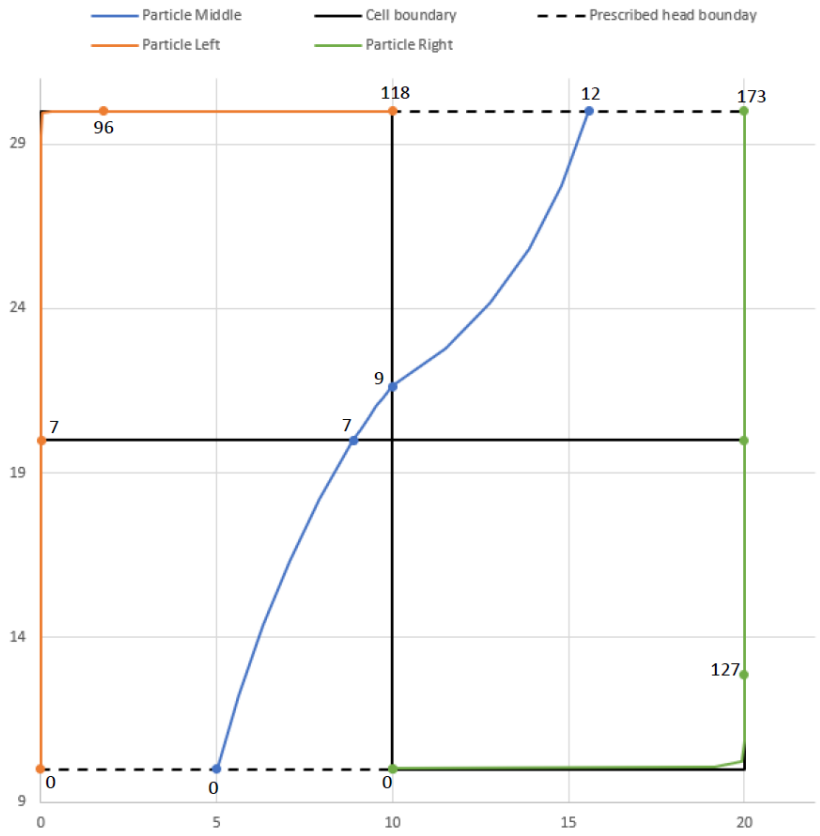

Figure A.4: Streamlines for the multi-cell problem. The numbers next to the datapoints is travel time in units hours.

Modflow Model B

B.1 1-Dimensional Model

In this section, the software Modflow [Aquaveo] will be used to develop a numerical model. The model is set up as an "infinitely" long channel which is one control volume wide and one control volume deep, with no flow boundaries along the side and a prescribed head boundary in each end. The length of the actual model is set to 1000 meters as it is assessed that the prescribed head boundaries will not affect the model area. The injection and monitoring wells are then placed in the middle of the channel.

The flow model is a 1-dimensional steady-state model, which means the scale of the hydraulic gradient and the hydraulic conductivity independently is not relevant so long as the product of the two gives the desired darcy velocity (or pore-water velocity) as shown in Darcy's Law. Therefore the prescribed head boundaries are set to 10 and 5 meters respectively, resulting in a hydraulic gradient of 0.005 $\frac{\text{m change in head}}{\text{m porous media}}$ and the porosity is set to 0.3 $\frac{\text{cm}^3 \text{ pores} > 30 \text{ µm}}{\text{cm}^3 \text{ soil}}$. The hydraulic conductivity is then calculated using darcy's law, where the pore-water velocity is set equal to the one achieved in the CXTFIT2 model. The head distribution for the flow model is shown in figure B.1.

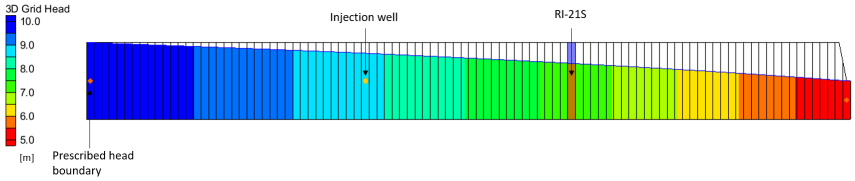

Figure B.1: Head distribution for the flow model.

To simulate the tracer test, the software MT3DMS was used, which uses the advection-dispersion equation.

The time discretization was calibrated using the results from the mobile-immobile model with GRG-non linear solver in excel, where the calibration goal was set as the sum of the root square error between the mobile-immobile model and the Modflow model.

The spatial discretization was tested at 5 and 10 meters. The result did not change significantly, and the spatial discretization was set equal to 10 meters to save computational time.

In figure B.2 the distribution of the tracer in the different control volumes at different simulation times.

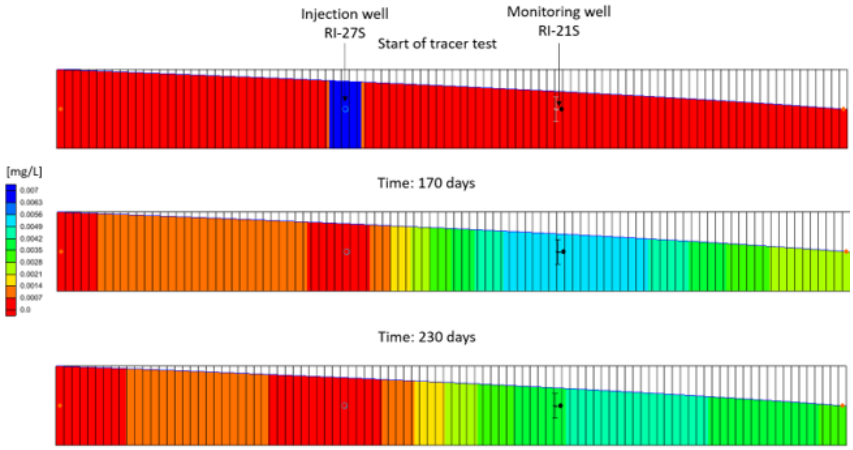

Figure B.2: Distribution of the tracer in the different control volumes at different simulation times.

As shown in the figure, the tracer does not reach the upper prescribed head boundary, meaning the boundary does not affect the tracer by causing "backlash" of the tracer if it were to reach it. Since the flow model is steady-state, the same is true for the lower prescribed boundary due to constant flow distribution.

The breakthrough curve for the Modflow model can now be estimated for each control volume. The results are shown in figure B.3.

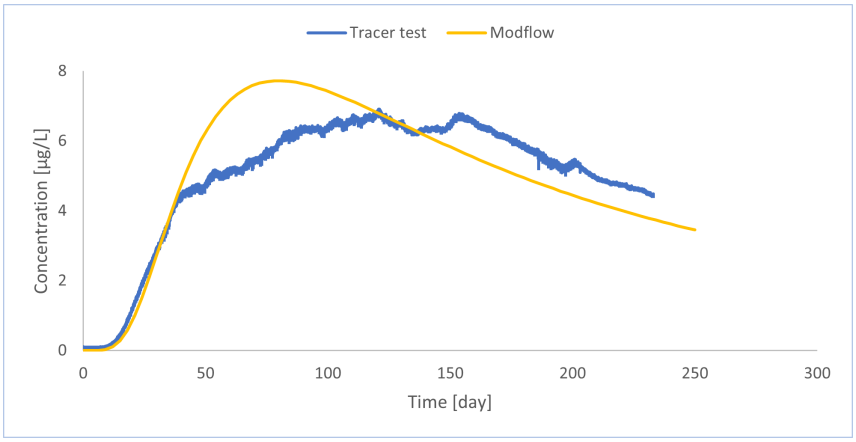

Figure B.3: Results using the Modflow for screening R1-21S (L2).

The results of the parameter estimation are shown in table B.1.

Table B.1: Calibrated parameters for the 1-D modflow model for well RI-21S (L2).

Symbol	Parameter	Value
d	Dispersivity [m]	207
D	Dispersion coefficient [m^2/s]	157
v	Pore-water velocity [m/d]	0.76
v_d	Darcy-velocity [m/d]	0.23
c_0	Injection concentration [kg/m^3]	3.503
t_0	Injection time [s^{-1}]	48
L	Distance between injection and monitoring well [m]	277
Δx	Spatial discreatization [m]	10
Δt	Time discreatization [d]	2
ϕ	Porosity $\left[\frac{cm^3 \text{ pores}}{cm^3 \text{ soil}}\right]$	0.3
$\frac{\Delta h}{\Delta x}$	Hydraulic gradient $\left[\frac{\text{m change in head}}{\text{m porous media}}\right]$	0.005
K	Hydraulic conductivity [m/d]	46

A 3-dimensional modflow model was also set up, using the concept particle tracking described in appendix A which is further explored in the following section.

B.2 3-Dimensional Model

A conceptual model approach using the software GMS [Aquaveo] will be used to try and replicate the tracer test results using the particle tracking method.

The boundary conditions of the model are described in the following. On the west side, a no-flow boundary condition was used. This boundary condition is based on the USGS map of the watershed boundary; hence it can be used as a no-flow boundary.

The north and east sides of the model area have prescribed head boundaries. The north is the Potamic River. Water level measurements in the Potamic River were used at the two sites nearest the HLSS. The water level stations were Little Falls Pumping Station and Point of Rocks. The average water level for each station over five years from 2016-2021 was calculated. The average of these mean water levels was used as the boundary condition and is 55.75 m.

A stream is connected from the Potamic River to the east side of the model area. The water level of the stream was unknown. However, it is assumed that the stream's water level is controlled by the water level of the Potamic River due to the significantly higher flow in the Potamic River. Therefore, it is assumed that the water level in the stream is equal to the water level in the Potamic River plus the difference in elevation from the Potamic River to the end of the general head boundary. The elevation change is 7.3 m, the general head boundary at the end of the stream is assessed to be 63 m. Along the stream, GMS interpolates the head along the boundary.

To close out the boundary in the south is a bit more complicated. Currently, a prescribed head boundary based on groundwater elevation measurements is used. This is a less than ideal boundary condition since groundwater levels change and have also changed 1.3 m at this measurement well just the year after. The boundary conditions and the model area are illustrated in figure B.4.

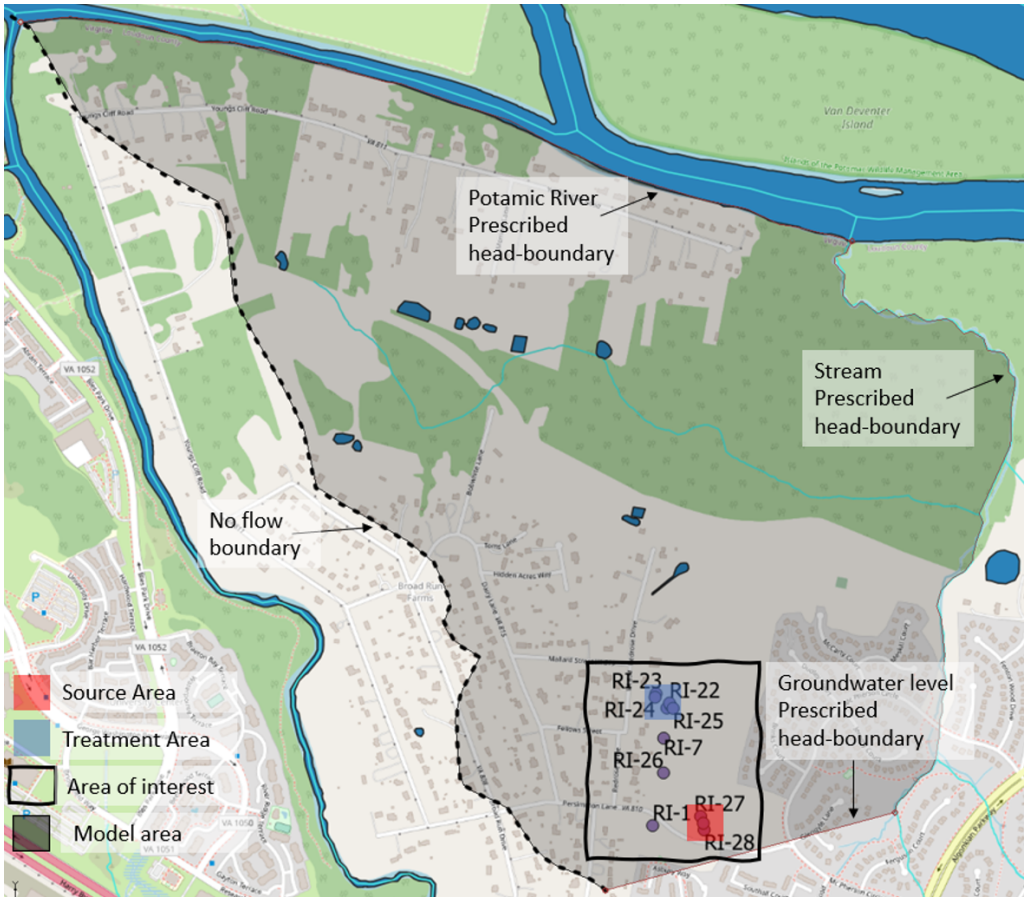

Figure B.4: Boundary conditions for the 3-dimensional modflow model.

A world map elevation tool from GMS was used for the surface elevation. The finest resolution of 3.7 m was used for the map and is then interpolated into the GMS top layer grid as the top elevation. The top elevation grid is shown in figure B.5.

The grid shows that the elevation is highest in the south and decreases towards the Potamic River. Also, the landfill is seen in the southeast part of the model area.

Using geological boring logs, the elevation of the top of bedrock was found for several wells. The values for the bedrock elevation were interpolated using IDW interpolation with the software QGIS. However, the wells are primarily focused around the landfill. The lag of wells in the remainder of the model area was problematic with the interpolation since data points in the western part of the model area are limited. This led to the elevation of the bedrock exceeding the surface elevation in some areas, mainly near the Potamic River. The wells used and interpolation results in is shown in figure B.6 when just interpolating around the area covered by the wells.

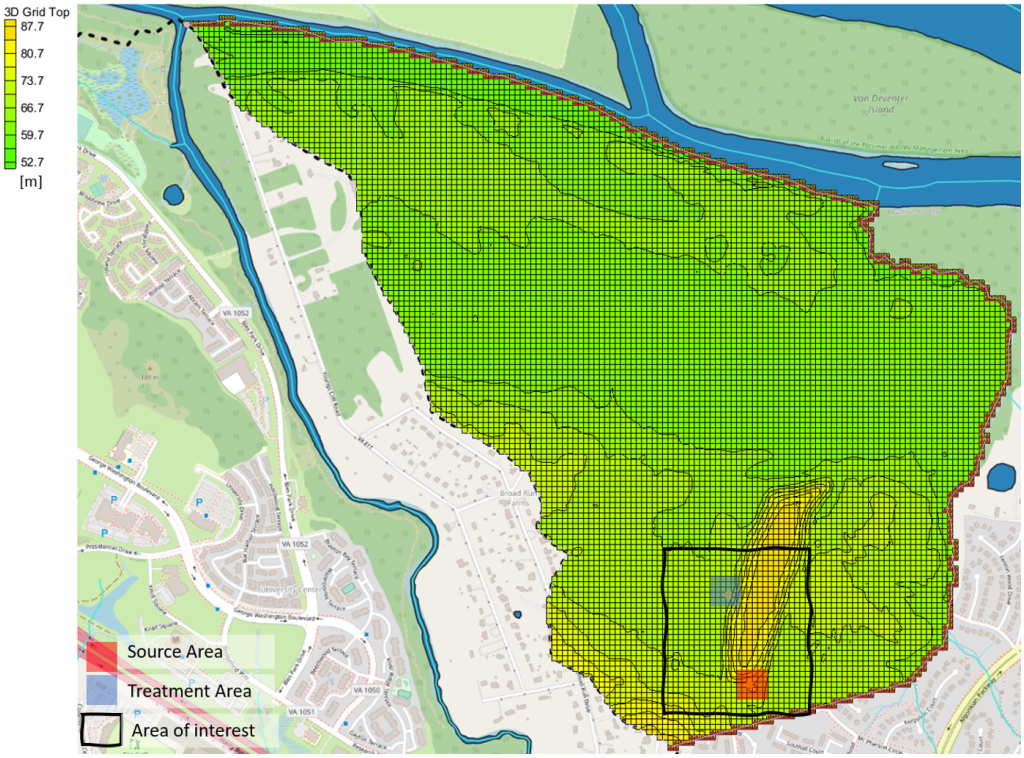

Figure B.5: Surface elevation implemented in the 3-dimensional modflow model.

The bedrock elevation is somewhat similar to the surface elevation, except for the extended height due to the landfill, decreasing northward towards the Potamic River. Based on the similarities in elevation, it is assumed that the bedrock follows the same tendency for the remainder of the model area as the surface elevation. Therefore, four artificial "wells" are introduced along the Potamic River boundary with an elevation for the bedrock of 54 m, and a new IDW interpolation was conducted. This drastically reduced the number of errors due to the bedrock having a higher elevation than the surface. The remainder of the errors were manually corrected by adjusting the bedrock elevation using neighboring cells' values. The grid for the bedrock elevation is shown in figure B.7.

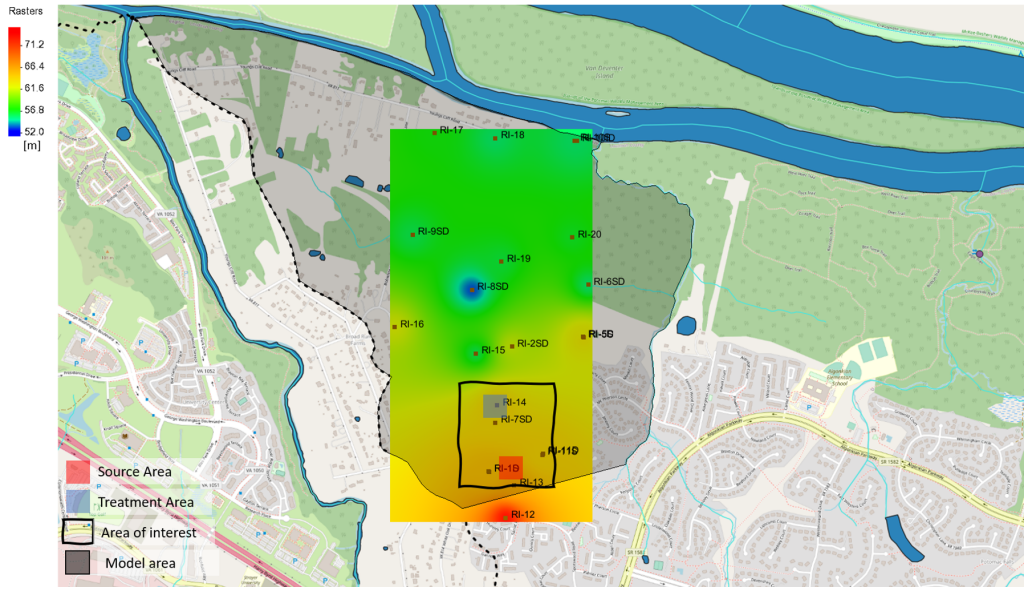

Figure B.6: Bedrock surface based on interpolation from well data.

Using these boundaries, a simple transport model was constructed to understand how the boundaries work in the model. The resulting head distribution of a steady-state simulation using this model is shown in figure B.8. Also, a forward particle tracking simulation was conducted using 20 particles starting at the injection well of the tracer test, RI-27, in the Source Area. A backward particle tracking simulation was conducted from well RI-21 in the Treatment Area.

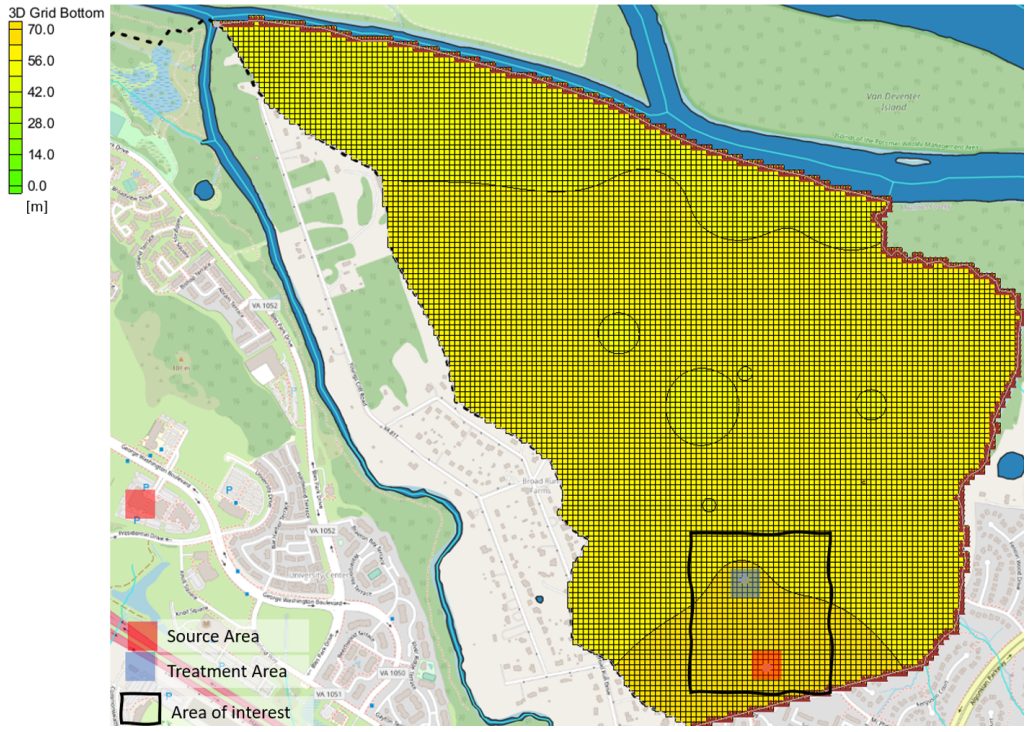

Figure B.7: Bedrock surface implemented into the modflow grid.

The figure shows a high head distribution in the southeast corner of the model and then

decreases in the northwest, making the flow direction northwest. This is similar to the contour maps and the tracer test results, indicating that the boundary conditions give a similar representation of the model area as was already known. The particle tracking results show a similar flow pattern. The particles from the source area do not reach the treatment area or vice versa from the treatment area to the source area. However, this was not expected as this is a simple model with limited input, and also, the number of particles simulated was not that high.

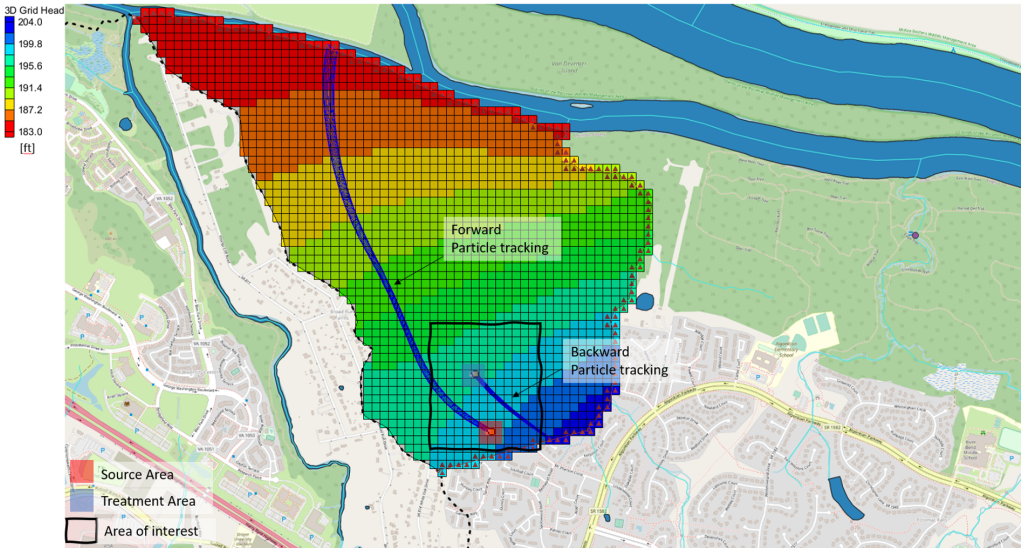

Figure B.8: Head distribution for the 3-dimensional modflow model, with particle tracking from both injection and monitoring well.

Literature values of Dispersivity

C

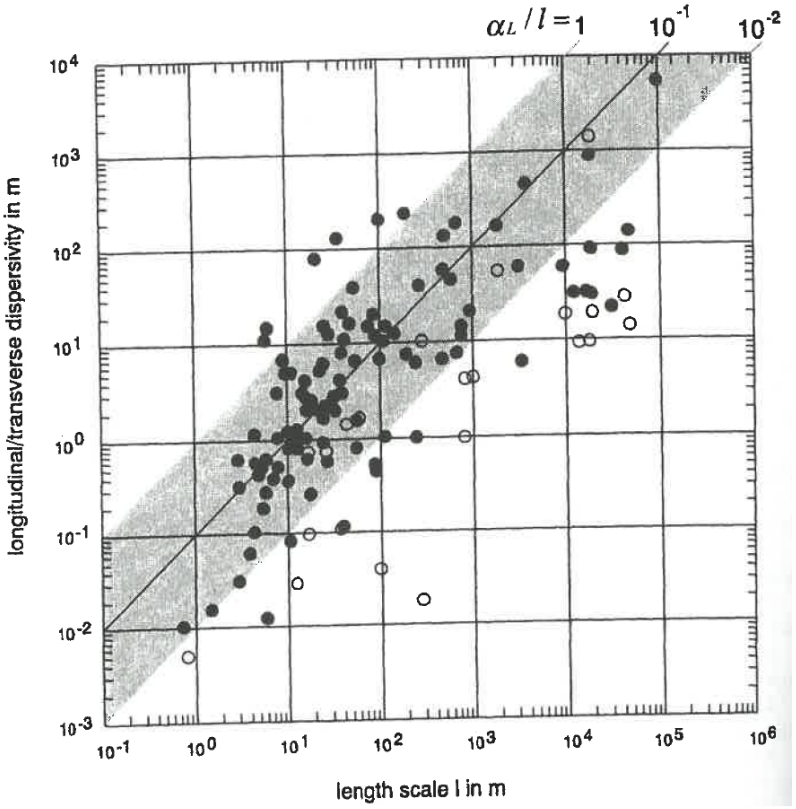

Figure C.1: Longitudinal dispersivity versus scale of observation from [Gelhar and Collins, 1992], with an expected range of dispersivity values based on these results [Spitz and Moreno, 1996].

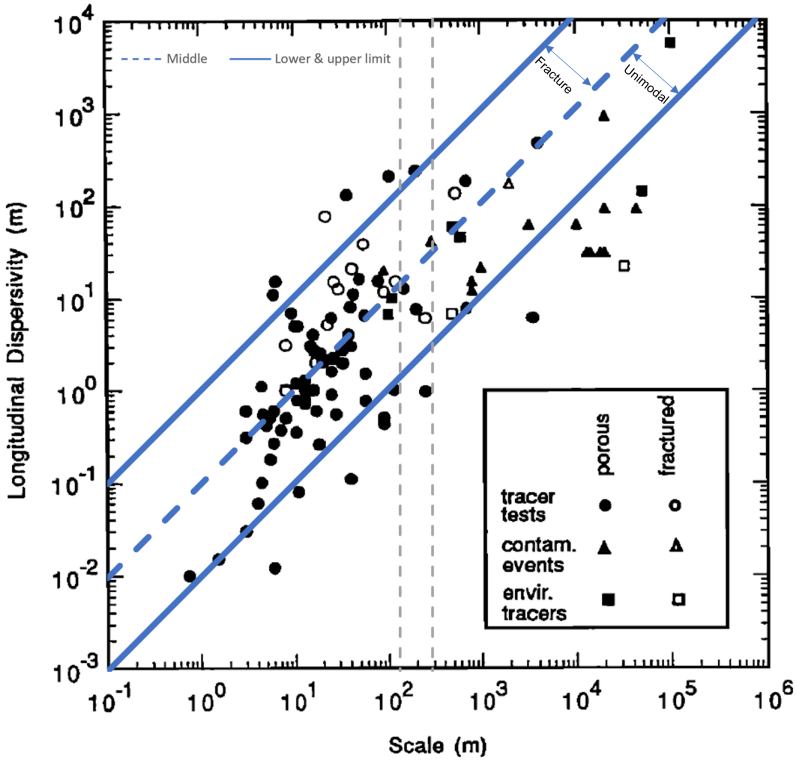

Figure C.2: Longitudinal dispersivity versus scale of observation identified by type of observation and type of aquifer. With the interval defined in figure C.1 implemented. Modified from [Gelhar and Collins, 1992].

Geostatisctical Parameters from the FAST-MD Procedure

D

In table D.1 the geostatistical parameters from the FAST-MD procedure is summarized.

Table D.1: Geostatistical parameters for the initial and final parameter estimation using the FAST-MD procedure. IPE is short for Initial parameters estimation, FPE final parameter estimation, Raw is the raw tracer data, R & S is the reduced and smoothed tracer data.

		IPE				FPE			
Location		Raw		R & S		Raw		R & S	
RI name	Given name	NSE	AIC	NSE	AIC	NSE	AIC	NSE	AIC
RI-26I	E	0.605	-44369	0.941	-625	0.614	-44634	0.954	-646
RI-7S	M1	0.727	-61379	0.872	-617	0.759	-62761	0.904	-643
RI-7D	M1	0.706	-9434	0.723	-58.9	0.848	-16494	0.997	-503
RI-25D	L1	0.941	-56811	0.979	-591	0.944	-57309	0.980	-594
RI-21S	L2	0.984	-1330	0.986	-11	0.994	-12374	0.996	-133
RI-21I	L3	0.940	30510	0.943	274	0.979	18760	0.979	177
RI-21D	L4	0.985	25625	0.986	262	0.995	14997	0.998	70
RI-22S	L5	0.880	3042	0.967	-78	0.900	1141	0.979	-121
RI-22I	L6	0.936	30348	0.988	137	0.951	27517	0.9997	-236
RI-22D	L7	0.708	-6121	0.770	-79	0.882	-16220	0.983	-337
RI-23S	F1	0.953	33778	0.971	259	0.964	30777	0.992	139
RI-23I	F2	0.808	-24970	0.894	-278	0.892	-31336	0.983	-457
RI-23D	F3	0.971	8854	0.975	91	0.989	-1731	0.997	-107
RI-24S	F4	0.969	17410	0.976	171	0.984	10857	0.990	82
RI-24I	F5	0.958	-15515	0.986	-228	0.962	-16575	0.990	-261
RI-24D	F6	0.838	6888	0.963	-66.9	0.850	6032	0.969	-84

Comparing the NSE values of the initial and final parameter estimation the values are higher for the final parameter estimation, as should be the case. The difference between the initial and final parameters is relatively small for most screenings, indicating that the initial parameter estimation procedure was successful. All of the AIC values were more negative or smaller for the final parameter estimation, indicating that the even tho more parameters was used for the final parameter estimation, the improvement of the fit was significant enough